UNIVERSIDAD DE CONCEPCIÓN
FACULTAD DE CIENCIAS FÍSICAS Y MATEMÁTICAS
DEPARTAMENTO DE FÍSICA

Resonant Absorption of The Kink Mode in a Coronal Plasma Slab via 2D Hybrid-PIC Simulations: Multifluid and Kinetic Descriptions

A dissertation presented to Universidad de Concepción in partial fullfilment of the requirements for the degree of PhD in Physical Sciences

Author: Hugo Alexis Carril Pardo
Advisors: Dr. Roberto Elías Navarro Maldonado
Dr. Jaume Terradas Calafell

March 30, 2026
Concepción, Chile

The content of this thesis is based on two papers writen during the PhD. They are listed below.

- H. A. Carril, J. Terradas, R. E. Navarro, A. F. Viñas, M. Goossens. "Resonant Absorption and Fluctuations via Hybrid Simulations on Coronal Loops. I. Plasma Multifluid Description". In: *ApJ* 986.1, 40 (June 2025), p. 40. DOI: 10.3847/1538-4357/adceac.

- H. A. Carril, A. F. Viñas, J. Terradas, R. E. Navarro, M. Goossens. "Resonant Absorption and Fluctuations via Hybrid Simulations on Coronal Loops. II. Kinetic Description". In: *ApJ* 999.2 (March 2026), p. 191. DOI: 10.3847/1538-4357/ae394e.

Abstract

We investigate the resonant absorption kink oscillations in a plasma slab with linearly inhomogeneous particle densities. Different thicknesses of the layers and angles of the background magnetic field to the plane of the slab are studied via 2D−3V PIC-hybrid simulations.

We identify the resonant absorption of the large-scale mode in the inhomogeneous layers and compare its damping rate with a single fluid, linear MHD estimation. Scales in the order of the proton inertial length are achieved in most of the simulated cases, particularly in the case of thinner layers and for moderately magnetized slabs. Quasi-perpendicular fluctuations consistent with Kinetic Alfvén Waves (KAWs) are generated at the layers only when resonant absorption occurs.

The KAWs interact non-linearly and generate a parallel electric field, which subsequently produces density structures and accelerates protons. This causes strong heating and flat-topped distribution. We derive an analytical estimate for this parallel field that reproduces the most relevant signals of the dispersion relations during and after resonant absorption. The transverse particle dynamics are driven by the cross-field drift, causing the transverse temperature to oscillate and grow exponentially due to small-scale fluctuations. Therefore, the proton distribution functions are largely shaped non-resonantly by the KAW activity.

Resumen (Spanish)

Investigamos la absorción resonante de oscilaciones *kink* en un plasma de protones tipo lámina con densidades de partícula linearmente inhomogéneas. Se estudian diferentes grosores de capas y ángulos del campo magnético de fondo con respecto al plano de la simulación por medio de simulaciones 2D−3V PIC-híbridas.

Identificamos la absorción resonante del modo de escalas más grandes en las capas inhomogéneas y comparamos su tasa de amortiguamiento con una estimación de teoría MHD de un sólo fluido. Las fluctuaciones alcanzan escalas en el orden de la longitud inercial del protón en la mayoría de los casos simulados. Particularmente, en el caso de capas más delgadas y para *slabs* moderadamente magnetizados. Sólo cuando la absorción resonante ocurre, se generan fluctuaciones cuasi-perpendiculares en las capas, consistentes con Ondas de Alfvén Cinéticas (KAWs).

Las KAWs interactúan de forma no-lineal y generan un campo eléctrico paralelo, que subsecuentemente genera estructuras en densidad y acelera protones. Esto causa fuerte calentamiento y distribuciones tipo *flat-top*. Derivamos una estimación analítica para este campo paralelo que reproduce las señales más relevantes de la relación de dispersión durante y después de la absorción resonante. El *drift* $\mathbf{E} \times \mathbf{B}$ domina la dinámica transversal de partícula. Esto causa que la temperatura transversal oscile y crezca exponencialmente por fluctuaciones de escalas pequeñas. Por lo tanto, la dinámica de las KAWs deforma de manera importante la función de distribución de los protones por medio de interacciones no-resonanates.

Agradecimientos (Spanish)

Suele costarme expresar con presición lo que pienso y lo que siento. Desde que inicié el doctorado en el 2020, este ha sido un viaje largo y con muchos cambios que probablemente aún estoy procesando en distintos niveles. Este camino no lo recorrí solo: estuve acompañado por muchas personas, sin las cuales esto habría sido considerablemente más árido.

Comienzo agradeciendo a mi director de tesis, Roberto Navarro, por haberme aceptado como su estudiante y por la confianza depositada en mis capacidades. Valoro especialmente su apoyo en la concreción de oportunidades académicas, entre ellas la pasantía realizada durante el doctorado.

La pasantía en la Universitat de les Illes Balears (UIB) en Palma fue significativa para esta investigación. Por ello, agradezco a Jaume Terradas por aceptar trabajar conmigo y recibirme en el grupo de Física Solar de la UIB. Así como también a Adolfo Figueroa-Viñas por su rol en este proceso. A ambos agradezco su amabilidad, orientación y por las discusiones e ideas compartidas, fundamentales en etapas clave de la investigación.

Extiendo este reconocimiento a los coautores de los trabajos realizados durante esta investigación y que están compilados en esta tesis. Las conversaciones, comentarios y experiencias compartidas fueron una parte importante de mi formación académica y científica. También agradezco a los miembros de la comisión evaluadora por su tiempo y disposición para la revisión de este trabajo.

Agradezco la cálida acogida de los demás integrantes del grupo de Física Solar

durante la estadía en Palma: Roberto, José Lluís, Elie, Manuel e Isabell, así como de Llorenç, Varsha, Guillem, Sergio, Andreu y Matheus, con quienes compartí de manera más frecuente. Gracias por esas conversaciones en el ritual café de la mañana, la hora de almuerzo y las juntas que contribuyeron a que esta experiencia fuera mucho más grata.

Asimismo, agradezco a mis compañeros y compañeras de oficina en la Universidad de Concepción (UdeC), en la oficina 305 de la CFM desde el 2020, en la UIB en el despacho 108 en el Departament de Física y luego en el despacho en ParcBIT, por el ambiente cordial y respetuoso en los espacios compartidos. Le agradezco también al personal de la UdeC. En particular, a Julia Herrera por su amabilidad y consideración, y a Nilsa García y a Soledad Daroch, por su paciencia, ayuda y enorme disposición en los procesos administrativos del doctorado. También al personal administrativo de la UIB, en particular a María José Ferrà por su disposición y ayuda durante distintos trámites burocráticos asociados a la pasantía.

A lo largo del doctorado, fue fundamental contar con el acompañamiento de amistades que estuvieron presentes. Valoro el apoyo de Jorge, incluso en momentos en que mis delirios me hacían dudar. A Danilo, por su buen ánimo y su forma positiva de ver las cosas, así como por la oportunidad de colaborar académicamente. A Carlos, que ha estado desde hace un buen tiempo, y cuyas conversaciones sobre vocación, fueron fundamentales para que hoy me encuentre en este punto.

También agradezco a David, Pedro, Nicolás, Vicente, Nicol, Martín, Nayda y Nelson, con quienes compartí distintos espacios: desde almuerzos y cafés post-almuerzo hasta salidas más distendidas. Esos momentos han sido un soporte importante en estos años. Asimismo, a Franco, Salomón, Sergio y Jorge, con quienes hemos seguido en contacto a pesar de la distancia.

En el tramo final del doctorado, sumé amistades que han sido importantes. Agradezco a Jordan por su presencia y haber creído en mí en momentos difíciles, y a Javier y Jonathan por su compañía y los momentos compartidos. A los tres valoro haberlos conocido y su disposición a acompañarme en esa última etapa. En distintas formas y momentos encontré compañía, escucha y apoyo que resultaron significativos.

La pasantía también fue una oportunidad para conocer y compartir con más personas. En la UIB destaco a Ruiling y Juan Antonio, así como a Fernando e Yseut por su cercanía. Además, hubo actividades que permitieron mantenerme cuerdo en ese tiempo: el grupo de capoeira Ginga Mundo de Mallorca, con los instructores Algodão y Anum, y los compañeros de entreno Encrenca, Coquinho, Timón, Positiva y Girasol; y el grupo folklórico Rissaga Ball de Bot, con la profesora Rosa y todo el grupo de estudiantes. De ambos espacios recibí una cálida bienvenida.

Finalmente, agradezco a mi familia por el apoyo brindado en estos años, sobre todo cuando estuve lejos de casa. A mis padres por el respaldo constante, la disciplina, y el valor del trabajo y el estudio inculcados, que han sido fundamentales en el doctorado. A Vanessa, agradezco las risas y su cercanía en estos años. A Claudio, agradezco la convivencia compartida y una influencia temprana que contribuyó a mi interés por la ciencia. Por supuesto, extiendo este agradecimiento a toda mi familia por su presencia y apoyo.

Financial Support

This work has been funded by ANID (Asociación Nacional de Investigación y Desarrollo) Chile through ANID DOCTORADO-NACIONAL 2020 fellowship No. 21202472. This work was also supported by FONDECyT Grants No. 1240281 and 1240697, by the Spanish Ministry of Science and Innovation MICIU/AEI/10.13039/501100011033/ via the I+D+i project PID2023-147708NB-I00, and by the European Union via FEDER (Fondo Europeo de Desarrollo Regional). The development of this work was also possible to IAC3 (Institute of Applied Computing and Community Code) and the FCFM (Facultad de Ciencias Físicas y Matemáticas, Universidad de Concepción).

Contents

List of Figures

Chapter 1

Introduction

1.1 Background and motivation

Resonant absorption is a process in which electromagnetic (EM) energy is converted into plasma energy with a mode conversion on the resonant layer where the incident EM wave phase speed matches that of the local plasma modes [1–3]. Resonant absorption operates in plasmas with inhomogeneities in density, proton bulk-velocity, and/or the background magnetic field [4–6]. Due to these inhomogeneities, globally large-scale modes, whether driven or excited, can locally resonate and transfer energy into narrow regions via wave-wave coupling [7, 8]. This causes small-scale fluctuations, damping of the global mode [7, 9], and plasma heating [10, 11].

The damping rate of global kink-modes involving fast waves [9, 12], and for slow and Alfvén waves [12] have been determined for the oscillation localized in the inhomogeneous regions of the plasma. The damping time-rate depends sensitively on the density profile across the transition layer [13]. During the damping, models predict that the global kink transverse oscillations become local azimuthal [9, 12, 13] or normal Alfvénic motions [14, 15] concentrated in the inhomogeneous layers. Such localized motions generate enhanced parallel vorticity [16, 17].

Resonant absorption of kink modes has been demonstrated to be a robust process in complex, pressure-balanced configurations, such as multi-stranded loops [7],

sheared flows [18], and non-linear 3D single-fluid MHD simulations of magnetized plasmas slabs with external driver [19, 20], and in cylindrical columns [18, 21–24]. Resonant absorption may coexist with Kelvin-Helmholtz instabilities (KHI), supplying energy at small-scales for it to occur [22, 23]. It is observed that resonant absorption generates small-scale, transverse fluctuations at the resonant layers.

In solar corona structures, strong transverse inhomogeneities in density and temperature allow for processes such as resonant absorption and phase-mixing [25]. Observational research find transverse oscillations in coronal structures whose amplitudes decay in time and space (e.g. TRACE [26, 27]; Hinode [28]; CoMP and AIA/SDO [4, 29–31]; IRIS [32]). Thus, the propagation of waves launched by the Sun is affected by the presence of such inhomogeneities.

Observed damping lengths and times are consistent with resonant absorption of kink modes into Alfvénic modes in coronal loops [9, 33, 34], threads and filaments [9, 35], and in the quiescent corona [29, 36]. A statistical study on individual coronal loops reinforces this interpretation via correlations between the measured oscillation frequency and wave-power [36]. Analyses of data on solar prominences from IRIS, and Hinode and SOT indicate signatures of resonant absorption, such as heating, and transverse and azimuthal displacements [32]. Numerical MHD simulations show that density gradients generated by a KHI can trigger additional resonant absorption [22]. Thus, resonant absorption may be a relevant process operating in coronal environments.

Resonant absorption concentrates energy into progressively smaller spatial scales around the regions of resonance. In this process, fluctuations may reach spatial scales in the order of the proton Larmor radius or the proton inertial length, channeling energy to particles. Here, dissipative and kinetic effects become necessary to

describe the physics of the plasma, such as non-thermal features and wave-particle interactions. These effects are not accounted by single-fluid MHD theory. Therefore, a kinetic approach would allow us to describe the microscopic physics and reveal further processes when flucuations reach kinetic scales.

Particle in Cell (PIC)-hybrid works have identified only qualitative features of resonant absorption [37, 38]. They reported nonpropagating structures of enhanced particle density, caused by cross-field modulation of the global fluctuations [37, 39]. Simulations using 2D−3V Vlasov-hybrid schemes showed that finite-amplitude KAWs grow from global Alfvén waves in the regions of inhomogeneity. Fluctuations reach scales in the order of the proton Larmor radius via phase-mixing [40–42]. These works are relevant because they suggest mechanisms in which finite-amplitude KAWs can be generated in inhomogeneous plasmas at kinetic-scales from global, large-scale fluctuations.

Moreover, observational research links KAWs with plasma energization, distribution heating, and particle acceleration in low-β inhomogeneous plasmas such as in the solar corona, coronal loops, and magnetospheric plasma-sheet [43–45]. Such energization implies the presence of wave-particle interactions. In this regard, Vasquez [38] suggests resonant wave-particle interactions leading to parallel heating via transit-time damping in a low-β plasma. Distribution functions are not explored in this work. These findings motivate a kinetic research of resonant absorption as a potential channel for energy from large-scale, kink oscillations to KAWs toward small-scales.

Finite-amplitude Alfvén waves and KAWs in plasmas may cause complex, nonlinear effects and further wave-particle interactions. Pairs of counterpropagating Alfvén waves can couple, generating a parallel electric field under specific conditions of the amplitudes of the magnetic field fluctuations [46, 47]. The coupling generates

nonpropagating density cavities where particles are accelerated depending on the combined polarizations, resulting in fluctuations with characteristic spectral signatures in wavenumber and frequency [47]. This process may be of interest in coronal and magnetospheric plasmas.

In inhomogeneous, low-β environments, stationary finite-amplitude Alfvén waves may also couple to ion-acoustic fluctuations. The coupling can produce density modulations via non-linear ponderomotive forces and ion parallel heating by Landau damping [48]. Interactions between finite-amplitude KAWs or Alfvén waves, and ponderomotive forces may expel ions, generating kinetic-scale cavities. This process leads to regions of enhanced density in magnetospheric plasmas [49–52]. Similar studies focus on ponderomotive forces and the formation of cavities in the context of turbulence in coronal plasmas [53, 54]. Generally, magnetic fluctuations are stronger in cavities [54], while regions of enhanced particle density have been correlated with temperature enhancement [51, 54]. Heating has been inferred from the study of magnetic field spectral fluctuations, which exhibit a spectral break [53].

Non-linear processes may involve the transverse dynamics. In low-β plasmas, fluctuations have frequencies smaller than the ion cyclotron frequency Ω_i, and waves satisfy non-resonant conditions [55]. Non-resonant interactions have been investigated for finite-amplitude Alfvén waves. The configurations consider a monochromatic wave and a spectrum of random-phased waves [56–58]. This interaction has been described as driven by the cross-field drift $\mathbf{E}\times\mathbf{B}$ [59]. Another approach to this process is from particle motion, finding pitch-angle scattering [56–58], which leads to effective heating [60]. Kinetic Alfvén waves also interact non-resonantly [61, 62], and their dynamics are dominated by the cross-field drift in the low-β regime [63]. Simulations of resonant absorption suggest that particles show scattering in velocity

space in the directions parallel ($\parallel$) and transverse ($\perp$) to the background magnetic field, $v_\parallel - v_\perp$ [38]. This may be interpreted as pitch-angle scattering, though the underlying mechanism is not clearly specified.

Therefore, there is evidence of processes accounted by a kinetic description occurring in inhomogeneous and coronal plasmas. They may be triggered when fluctuations reach small enough scales due to resonant absorption. Further, different species contribute differently to the dynamics. Such processes are not accounted by single-fluid MHD theories. In this thesis, we study the resonant absorption of kink oscillations of an inhomogeneous plasma using a kinetic model to study the multifluid and kinetic pictures of the process when fluctuations are transported toward kinetic scales.

1.2 Objectives

The main objective of the present research is to study a known MHD process via a kinetic model, which introduces different physical processes that cannot be accouted for by a fluid model of an inhomogeneous plasma when fluctuations reach scales in the order of the proton inertial length. This is achieved via two objectives: **1.** To provide a multifluid characterization of resonant absorption in a 2D slab, comparing quantitative and qualitative features with known results from MHD theories and to determine the nature of the fluctuations which grow around the magnetic field lines that are resonant with an excited perturbation. **2.** To characterize the physical processes that are triggered by resonant absorption when small scales are reached by fluctuations in a 2D slab, and to provide a kinetic picture via the description of the distribution functions at the zones of resonance of this system. This analysis

is conducted for different layer thicknesses of the slabs, and different angles of the background magnetic field with respect to the plane of the simulation.

The specific objectives are described below.

1. **Multifluid characterization of resonant absorption in a slab**

   1.1. To identify qualitative features of resonant absorption

   To identify qualitative features of resonant absorption, such as the development of small-scale structure and fluctuations in the inhomogeneous regions of the slab in scalar (density) and vector quantities (transverse bulk-velocity and magnetic field components); the refraction of waves propagating in the plasma; and the vorticity enhancement in the direction parallel to the background field. Vector quantities are rotated to the axes aligned with the background magnetic field.

   1.2. To estimate the damping time-rate due to resonant absorption

   To estimate the damping time-rate in the bulk velocity components. This requires determining the oscillation frequency of the plasma associated to the excited kink oscillations and the damping time of the said quantities. This damping time-rate is compared with a prediction from linear MHD theory for slab geometry with oblique magnetic field, and in the approximation of thin inhomogeneous layers.

   1.3. To determine the spatial scales reached by resonant absorption

   To identify quantities in which small-scale structures are developed due to resonant absorption and tracking their time evolution in order to compare the scales reached by the fluctuations using characteristic kinetic lengths. This is achieved via spatial spectral decomposition.

1.4. To characterize the small-scale fluctuations

To analyse fluctuations related to small-scale structures through a spectral decomposition, and to determine the polarization in the plasma physics sense, spatial structure, cross-correlation, and dispersion relation. Features are compared with theoretical properties of linear waves. The analysis is restricted to a region where fluctuations are localized.

2. Underlying physical processes and kinetic features

2.1. To study of the correlation between density fluctuations and the electric field parallel to the background field

To analyse the parallel electric field and density fluctuations spectrally through wavenumber decomposition. The analysis allows us to characterize the formation of density small-scale structures where resonant absorption occurs, and to establish milestones in the evolution of the plasma.

2.2. To determine the origin of the parallel electric field fluctuations in the slab

To find a physical mechanism relating the excitation of the waves at the regions where resonant absorption occurs, density structures, and the parallel electric field, considering the spectral decomposition of density and vector quantities in the parallel direction.

2.3. To study of proton phase-space portraits related to the directions parallel and transverse to the background magnetic field

To construct projections of phase-space at zones where resonant absorption occurs and the parallel velocity to identify wave-particle interactions

associated with the excited small-scale waves. These projections also allows us to determine how density structures are formed at particle level.

This is done in the same way with the transverse velocity, and allows us to determine the wave-particle interactions in the perpendicular direction.

2.4. To study of temperatures in the parallel and transverse directions

To characterize the evolution of the temperatures in zones of relevance, where resonant absorption occurs, in the directions parallel and transverse to the background magnetic field. This allows us to determine how energy from global scales is channeled to particles, and the structure of the disribution functions.

2.5. To study of temperature ratios

To track the evolution of the temperature ratios in regions of relevance, where resonant absorption occurs. These ratios allows us to discern whether there is a direction in which the plasma is preferentially energized. They also allow us to characterize parameters related to sources of free energy, such as temperatures anisotropy and gyrotropy.

1.3 Methodology

The main objective of this research is achieved via numerical simulations using a 2D−3V PIC hybrid code of a magnetized, inhomogeneous 2D slab plasma composed by kinetic protons and massless, fluid electrons written in `Fortran 90`.

We choose a 2D-space setting, because it allows for waves and particles to move in different directions within the plane of the simulation, in constrast to a 1D setting.

This is necessary for resonant absorption to occur. With regard of computational resources, it is less demanding than a spatially 3D configuration. The slab configuration is a first approximation to study resonant absorption in a coronal loop.

The PIC-hybrid model is suitable for our purposes, because we are focused on the low-frequency kinetics of protons while ignoring further details of the electrons dynamics. The code is modified using as a basis a code originally developed by A. F. Viñas [48, 64–67]. The code uses a non-sympletic algorithm that bounds energy fluctuations in computing particle motion. Digital filtering with compensation is applied on the moments of the distribution function to eliminate small-scale, noisy, non-physical fluctuations and to retain physical information at large-scale fluctuations. Further details of the model are provided in Chapter 5. The code is implemented to use `OpenMP` parallelization for `Fortran`.

`Fortran` data from simulations are loaded by the `Julia` library `FortranFiles.jl` [68] (used in specific objectives **1** and **2**, particularly in **2.4** and **2.5**). Spectral analysis is achieved via the use of the library `FFTW.jl` [69] (used in specific objectives **1.1** to **2.2**). Finally, distribution functions and phase-space portraits are constructed with histograms using particle data through the library `StatsBase.jl` [70] (used in specific objective **2.3**). Fit to data is carried out with the library `LsqFit` [71] (used in specific objectives **1.2**, **2.4**, and **2.5**). The language `Julia` and all of the required libraries have MIT license.

1.4 Outline of the document

The document is organized as follows. Chapter 2 shows a brief review of coronal plasmas and coronal loops, the fluid theoretical framework, and the fluid equilibrium

state. Chapter 3 presents the background for kinetic theory and interpret the distribution functions, and discusses the equilibrium distribution function. Chapter 4 presents the characterization of Alfvén and kinetic Alfvén waves, and non-linear coupling studied in this research. Chapter 5 describes the model of the 2D−3V PIC-hybrid simulation, the initialization of the inhomogeneous plasma, and the corresponding numerical implementations. Chapter 6 describes the identification of resonant absorption in the results of our simulations, using as a basis the existing MHD features of the phenomenon. Chapter 7 presents the characterization of the fluctuations excited in the plasma after the resonant absorption of the excited perturbation. In Chapter 8, the kinetic processes induced by resonant absorption in the direction parallel to the background magnetic field are studied. Chapter 9 studies the kinetic processes related to the dynamics transverse to the background magnetic field. Finally, we present the conclusions of this work in Chapter 10.

Chapter 2

Coronal Observations and Fluid Framework

The solar corona is the outermost layer of the solar atmosphere. It is a tenuous plasma compared with the lower atmosphere [72]. The coronal plasma is highly ionized and strongly interacts with the magnetic field of the Sun, rendering the structure of the solar corona as highly inhomogeneous [73, 74].

The solar corona has several structures characterized by the magnetic field morphology and the local conditions of the surrounding plasma [75]. Among them, there are coronal loops, which are the structures of interest for our research. In these environmental conditions, these strongly magnetized and inhomogeneous structures enable processes such as resonant absorption. In this process, the global mode acting on the structure is damped and transfers energy to localized regions.

Fluid theory has been largely used to model large-scale plasma phenomena. In this Chapter, we present fluid-related theory that is required for this work. We use linear MHD theory to derive the exponential damping rate of the global mode undergoing resonant absorption [7, 15, 76]. Multifluid theory is used to define a pressure-balanced equilibrium state for the system we are investigating. This allows us to isolate the evolution of resonant absorption from any other possible process. The multifluid approach is used because the plasma has two components (protons and electrons), and the largest spatial scales of the system are defined on fluid scales.

2.1 Coronal Plasma Background

Typically, the coronal temperature is in the order of $2-2.5\times10^6$ K, considering both active and inactive regions [75], whereas the magnetic field strength is $1-4$ G [77] with particle density in the order of 10^8-10^9 cm^{-3} [78]. These parameters yield a plasma $\beta = 8\pi nT/B_0^2$ in the order of $\beta \sim 10^{-4}-10^{-1}$. Thus, the solar corona is typically a strongly magnetized plasma.

The collisionality of the coronal plasma is characterized by a mean free path ~ 1 Mm for protons and electrons, and collision time ~ 10 s for protons and 0.25 s for electrons [79]. Whereas the gyration radii are ~ 1 m for protons and ~ 0.022 m for electrons, and inertial lengths ~ 20 m for protons and 0.5 m for electrons, assuming a proton-electron plasma with quasi-neutrality. Its collisionality is larger than that of the solar wind [80]. Nonetheless, the electromagnetic-scales remain dominant over collision scales.

2.1.1 Coronal Loops

Among the structures in the solar corona, there are coronal loops [81, 82]. Coronal loops are arch-shaped structures in the solar corona that are visible in the X-ray band. These structures are anchored at the chromosphere and exhibit high luminosity because they are composed of magnetic flux-tubes where the plasma is strongly confined and isolated from the surrounding environments [73] (see Fig. 2.1).

Detailed observational research provides further characterization of coronal loops. Measurements show that the particle density and the background magnetic field along coronal loops [83] are nearly uniform over an extension of ~ 40 Mm around the apex of the structures. The particle density around the apex has a lower bound,

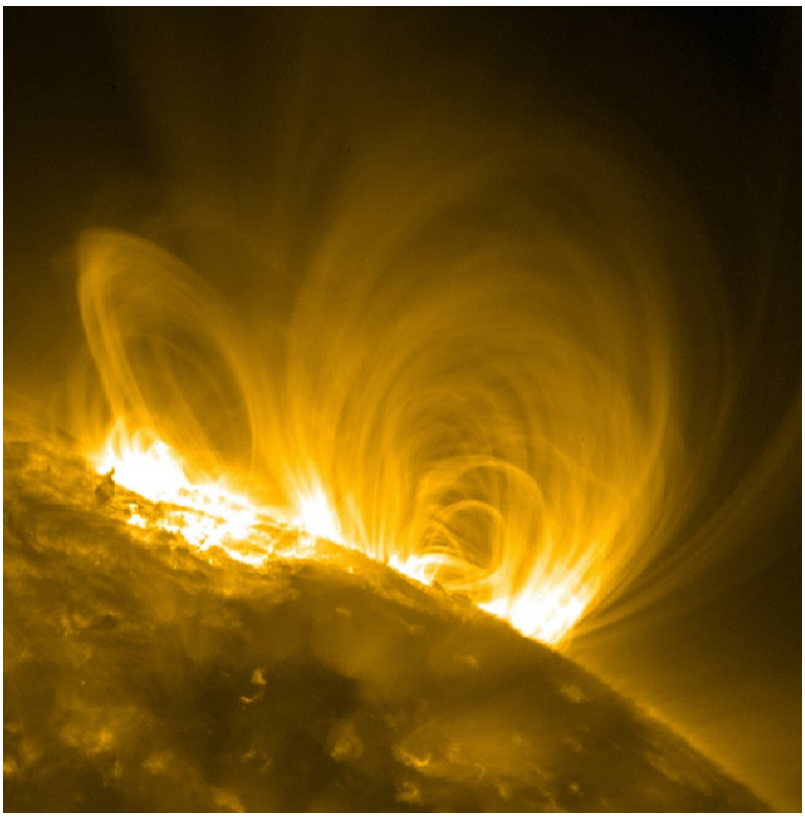

Figure 2.1: Coronal loops bundles. Image from SDO, 171 Å filter. Figure from Reale [73].

typically in the order of 10^8 cm^{-3} [73, 74, 83–85], which allows for the largest proton inertial length to be in the order of $v_A/\Omega_p = c/\omega_{pp} \simeq 23$ m (where $v_A = B_0/\sqrt{4\pi m_p n_0}$ is the Alfvén speed, $\Omega_p = q_p B_0/m_p c$ is the proton cyclotron frequency, and $\omega_{pp} = \sqrt{4\pi q_p^2 n_0/m_p}$ is the proton plasma frequency), and electron inertial length ~ 0.5 m. These spatial scales, which are related to particle motion, are much smaller than all the characteristic lengths of a coronal loop, considering its full axial length, radius, and density gradient. Both scale-ranges have effects on each other. Therefore, if only the fluid scales are modeled, as in MHD theory, physics triggered at particle

scales is missing from the global picture.

The background magnetic field magnitude is typically in the order of 10 G [83, 84]. In this region, the temperature is in the range of 10^5 K in cool loops to more than 10^7 K in flaring loops [73]. Accordingly, the parameter beta lies within the range for generic coronal plasmas ($\beta \sim 10^{-4} - 10^{-2}$). Its collisionality is roughly the same as that presented above.

Violent events such as flares in active regions perturb these structures in the solar corona. Coronal loops are dynamic. Their geometry and luminosity, based on temperature, and density, vary in time [86]. The dynamics of these structures have been observed and studied via image-based analyses with wavelength in the band of 171 Å (Extreme Ultra-Violet range of observation) using data from TRACE [26, 87] and SDO [31, 82, 84, 88]. The images generated with data obtained at this band have limited resolution. Instrumentation on board SDO has spatial resolution in the order of 0.5 Mm at 1 AU [73, 86, 89]; and more recently SolO, with spatial resolution in the order of $100 - 200$ km at the perihelion $0.3 - 0.55$ AU [90, 91]. This resolution is determined by the design of the optical instrumentation on board and the size of the sensors in the 171 Å band [92–94].

The oscillations of the loops have been described as standing, transverse waves, asymmetric with respect to the axis of the loop, where the body oscillates as a whole with respect to said axis, and having nodes at the feet of the loops [26, 87].

2.2 Resonant Absorption in MHD

In here, kink oscillations and their damping due to resonant absorption based on Goossens [95] are recalled. Both are treated under a linearized, single-fluid MHD

approach.

2.2.1 Kink Oscillations

The oscillations of coronal loops are consistent with the kink mode predicted by MHD linear theory [87, 96]. Typically, these oscillations are observed to become rapidly damped in time [26, 30, 31, 84] or to persist for several oscillation cycles [82, 88]. Kink oscillations in coronal loops are observed by setting slits along the structures. Then the slits are tracked in time (see Fig. 2.2).

Damped standing kink oscillations are of interest. They have been studied with regard to the damping of fluctuations in connection to coronal heating [10, 11, 86]. The problem has been theoretically modelled via single-fluid MHD theory, considering a dense slab (in Cartesian coordinates [15]) or column (in cylindrical coordinates [9]) immersed in a tenuous medium. Equations are linearized and obtain the oscillation frequency and the damping rate for exponentially damped oscillations of the global scale kink perturbations by resonant absorption at the interface, considering thin and thick inhomogeneous layers [9, 13, 14, 33, 98]. Standing kink oscillations can be obtained without other approximations by solving the linearized equations for the Lagrangian displacement $\boldsymbol{\xi}$ along the density gradient. In particular, the Klein-Gordon equation for the lagrangian displacements is solved by Terradas [99], specifying initial conditions in the displacements, $\boldsymbol{\xi}(0) = \mathbf{0}$, and in the fluid velocity, $\partial\boldsymbol{\xi}/\partial t|_{t=0} = \mathbf{v}$. Damped oscillations are obtained analytically. Kink oscillations may involve different single-fluid MHD modes in a fluid plasma such as Alfvén, and fast and slow modes [12]. Fluctuations generated during resonant absorption inherit properties of these modes [17]. In particular, Alfvénic fluctuations involve zero displacements along the background magnetic field.

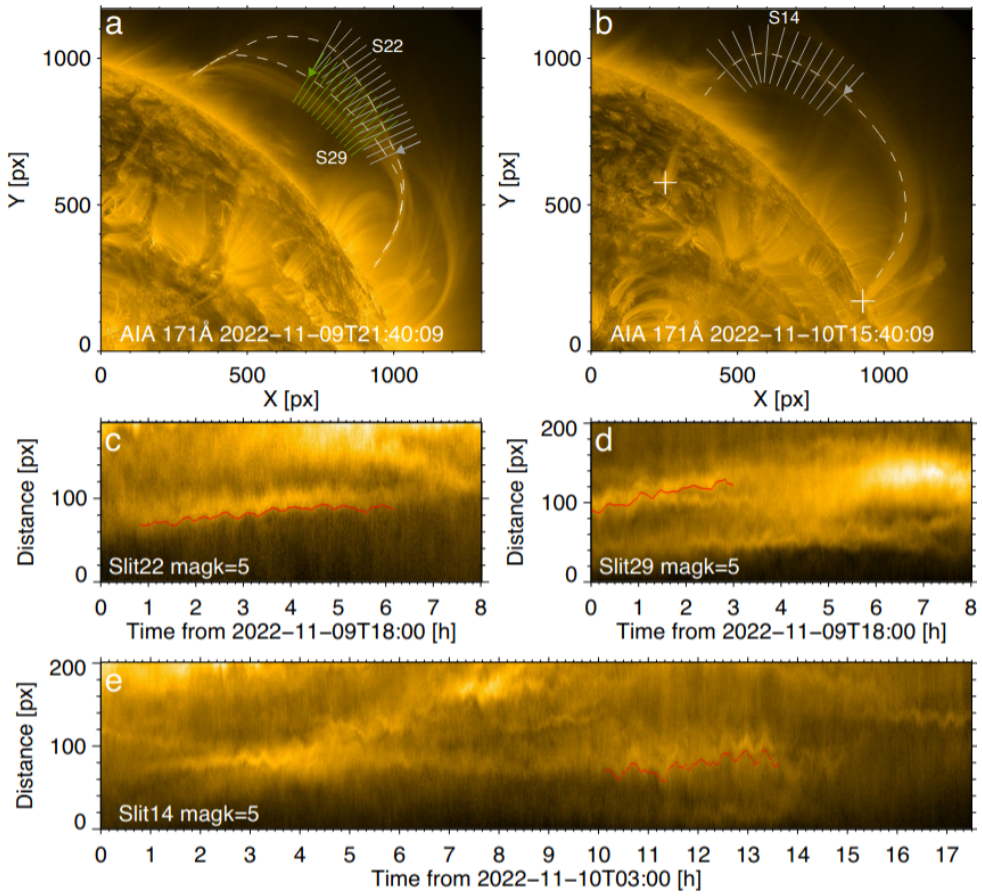

Figure 2.2: Analysis of kink oscillations in coronal loops using data from SDO. Identification of coronal loops and partition into slits, labeling specific slits S22, S29, and S14 [(a) to (c)]. Frames (c) to (e) show the evolution of three slits in time. Figure from Zhong et al. [97].

2.2.2 Damping by Resonant Absorption

The damping time-rate caused by resonant absorption can be obtained from the single-fluid, ideal MHD equations [100],

$$\frac{\partial \rho}{\partial t} + \nabla \cdot (\rho \mathbf{u}) = 0, \tag{2.2.1}$$

$$\rho \frac{\partial \mathbf{u}}{\partial t} + \rho \mathbf{u} \cdot \nabla \mathbf{u} = -\nabla p + \frac{1}{c} \mathbf{j} \times \mathbf{B}, \tag{2.2.2}$$

$$\frac{\partial p}{\partial t} + \nabla \cdot (p \mathbf{u}) = 0,$$

$$\nabla \cdot \mathbf{B} = 0,$$

$$\nabla \times \mathbf{B} = \frac{4\pi}{c} \mathbf{j}, \tag{2.2.3}$$

$$\frac{1}{c} \frac{\partial \mathbf{B}}{\partial t} = -\nabla \times \mathbf{E}, \tag{2.2.4}$$

$$\mathbf{E} + \mathbf{u} \times \mathbf{B} = 0,$$

via a perturbative analysis considering Fourier-Laplace transformations. We are interested in the problem solved in rectangular geometry. Calculations follow the procedure shown in Goossens [95]. Perturbed quantities are

$$\rho = \rho_0 + \rho_1,$$

$$\mathbf{u} = \mathbf{u}_0 + \mathbf{u}_1,$$

$$\mathbf{B} = \mathbf{B}_0 + \mathbf{B}_1,$$

$$p = p_0 + p_1,$$

where quantities with subscript 0 are equilibrium quantities, and subscript 1 are perturbations. Equilibrium quantities are non-uniform in principle. The Lagrangian

displacement $\boldsymbol{\xi}$ is related to the perturbative bulk-velocity as $\mathbf{u}_1 = \partial\boldsymbol{\xi}/\partial t$. Equations are written in terms of the displacement $\boldsymbol{\xi}$. The system of MHD equations is reduced to the following set [95].

$$\begin{aligned}
\rho_1 &= -\nabla\cdot(\rho_0\boldsymbol{\xi})\,,\\
\rho_0\frac{\partial^2\boldsymbol{\xi}}{\partial t^2} &= -\nabla p_1 + \frac{1}{4\pi}\left[(\nabla\times\mathbf{B}_0)\times\mathbf{B} + (\nabla\times\mathbf{B})\times\mathbf{B}_0\right],\\
\mathbf{B}_1 &= \nabla\times(\boldsymbol{\xi}\times\mathbf{B}_0)\,,\\
p_1 &= -\nabla\cdot(p_0\boldsymbol{\xi})\,.
\end{aligned}$$

The total pressure P' is introduced in the analysis, which involves the gas and the magnetic pressures. The zeroth and first orders are given by

$$\begin{aligned}
P' &= P'_0 + P'_1\\
&= \left[p_0 + \frac{B_0^2}{8\pi}\right] + \left[p_1 + \frac{\mathbf{B}_0\cdot\mathbf{B}_1}{4\pi}\right],
\end{aligned}$$

where $P'_1 = p_1 + \mathbf{B}_1\cdot\mathbf{B}_0/4\pi$. By introducing P' and reordering terms in the momentum equation, it is found that

$$\begin{aligned}
\rho_0\frac{\partial^2\boldsymbol{\xi}}{\partial t^2} &= -\nabla P'_1 + \frac{1}{4\pi}\left\{\mathbf{B}_0\cdot\nabla\mathbf{B}_1 + \mathbf{B}_1\cdot\nabla\mathbf{B}_0\right\}\\
&= -\nabla P'_1 + \frac{1}{4\pi}\left[\mathbf{B}_0\cdot\nabla\right]^2\boldsymbol{\xi}.
\end{aligned}$$

The plasma is restricted to 2 dimensions on the plane xy. Thus, no fluctuations propagate along z. We set inhomogeneities only along x (see Fig. 2.3). The density profile is defined piece-wise with homogeneous regions with densities ρ_{in} [region (**I**)] and ρ_{en} [region (**II**)] such that $\rho_{\text{in}} > \rho_{\text{en}}$. Both regions are connected with inhomoge-

neous regions of width l in x [region (**III**)]. The background magnetic field $\mathbf{B}_0$ and the equilibrium pressure p_0 are defined as uniform. The field $\mathbf{B}_0$ is defined as being perpendicular to the density gradient, in the plane yz. Generally, this field is defined as $\mathbf{B}_0 = B_0\,[\sin\varphi\widehat{\mathbf{y}} + \cos\varphi\widehat{\mathbf{z}}]$. This configuration is shown in Fig. 2.3.

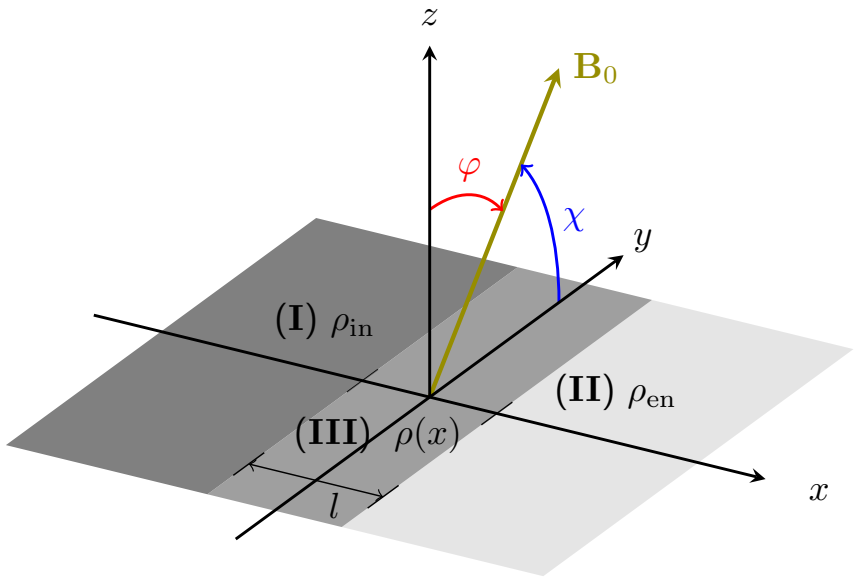

Figure 2.3: Scheme of the inhomogeneous plasma we consider for the calculation of the damping time-rate with a 2D plasma in the $xy-$plane. Regions (**I**), (**II**), and (**III**) are indicated (gray shades). The background magnetic field $\mathbf{B}_0$ (green) is defined on the $yz-$plane. Angles φ (red) and χ (blue) are indicated.

The vector quantities are decomposed in a base aligned with respect to the background magnetic field $\mathbf{B}_0$ following the rotation matrix (A.1.4). Since the rotations lead to $\widehat{\mathbf{e}}_{\perp,1} = -\widehat{\mathbf{x}}$, the dependencies and direction x are maintained in the analysis. Considering that the system has only propagation along y, the wavevector $\mathbf{k} = k_y\widehat{\mathbf{y}}$

becomes

$$\begin{aligned}\mathbf{k} &= k_{\parallel}\widehat{\mathbf{e}}_{\parallel} + k_{\perp,2}\widehat{\mathbf{e}}_{\perp,2} \\ &= k_y \left[\sin\varphi\widehat{\mathbf{e}}_{\parallel} - \cos\varphi\widehat{\mathbf{e}}_{\perp,2}\right]. \end{aligned} \tag{2.2.5}$$

The linearized equations in terms of $\boldsymbol{\xi}$ are Fourier-Laplace transformed with initial condition adiabatically turning perturbations on. In these conditions, perturbed quantities acquire the explicit dependency

$$A(x,y,t) = A'(x)\exp\left\{i\left[k_{\parallel}y\sin\varphi + k_{\perp,2}y\cos\varphi - \omega t\right]\right\},$$

where the frequency $\omega = \omega_R + i\gamma$ is complex. Here, ω_R is the oscillation frequency and γ is the growth/damping rate of the fluctuations. This means that the amplitude of physical quantities in this system exponentially grows or decays in time. We are interested in the resonant absorption of Alfvénic waves. Accordingly, parallel Lagrangian displacement and pressure variations along $\mathbf{B}_0$ are regarded as negligible. Accordingly, the components of the momentum equation become

$$\rho_0\left(\omega^2 - \omega_A^2\right)\xi_x = \frac{\mathrm{d}P_1'}{\mathrm{d}x}, \tag{2.2.6}$$

$$\rho_0\left(\omega^2 - \omega_A^2\right)\xi_{\perp,2} = ik_{\perp,2}P_1', \tag{2.2.7}$$

where $\omega_A = \mathbf{B}_0\cdot\mathbf{k}/\sqrt{4\pi\rho_0}$ is the Alfvén frequency, and is actually a function of x. The character of Alvénic waves also involves incompressibility, $\nabla\cdot\boldsymbol{\xi} = 0$ [15, 101].

The following equation is obtained

$$\frac{\mathrm{d}}{\mathrm{d}x}\left[\frac{1}{\rho_0\left(\omega^2-\omega_A^2\right)}\frac{\mathrm{d}P_1'}{\mathrm{d}x}\right]=\frac{k_{\perp,2}^2P_1'}{\rho_0\left(\omega^2-\omega_A^2\right)}. \tag{2.2.8}$$

The total pressure P_1' is solved for regions (**I**) and (**II**), where the Alfvén frequencies are homogeneous. Inside the region (**III**), the perturbation is resonant with the plasma. For a monothonically increasing or decreasing density profile, there is a single point x that is resonant with the perturbation, $x = x_A$. The problem is further solved by assuming that the transition layer is thin. Thus, it is reduced to a small neighborhood around $x = x_A$. Without loss of generality, the density ρ_{in} is set for $x < x_A$ and ρ_{en} for $x > x_A$. In such a case, the solutions for regions (**I**) and (**II**) are continuous. This condition avoids divergent pressure gradients. The pressure field is given by [95]

$$P_{1,\mathrm{in}}'=Ae^{k_{\perp,2}(x-x_A)},$$
$$P_{1,\mathrm{en}}'=Ae^{-k_{\perp,2}(x-x_A)}.$$

From Equation (2.2.6) the corresponding lagrangian displacements in x are given by

$$\xi_{x,\mathrm{in}}=\frac{k_{\perp,2}A}{\rho_0\left(\omega^2-\omega_{A,\mathrm{in}}^2\right)}e^{k_{\perp,2}(x-x_A)}, \tag{2.2.9}$$
$$\xi_{x,\mathrm{en}}=-\frac{k_{\perp,2}A}{\rho_0\left(\omega^2-\omega_{A,\mathrm{en}}^2\right)}e^{-k_{\perp,2}(x-x_A)}. \tag{2.2.10}$$

The displacements (2.2.9) and (2.2.10) allow to solve Equation (2.2.8), which leads to the jump condition for displacements [9, 14, 15]. This condition allows

us to obtain the dispersion relation of large-scale fluctuations by the resonant layer including its damping rate. Integration is made around $x = x_A$ by assuming a thin layer.

$$\xi_x(x_A^+) - \xi_x(x_A^-) = \int_{x_A^-}^{x_A^+} \frac{k_{\perp,2}^2 P_1'}{\rho_0 \left(\omega^2 - \omega_A^2\right)} \mathrm{d}x. \tag{2.2.11}$$

The denominator is expanded around $x = x_A$ up to first order. At the zone of resonance, the frequency ω is the Alfvén frequency at $x = x_A$, $\omega = \omega_A(x_A)$. Considering the dependency of ω_A on x, it is found that

$$\omega^2 - \omega_A^2(x) \approx (x - x_A) \frac{\omega_A^2(x_A)}{\rho_0(x_A)} \left| \frac{\mathrm{d}\rho_0}{\mathrm{d}x} \right|_{x_A}. \tag{2.2.12}$$

With this change of variables, it is found that the integral in Equation (2.2.11) is singular at $x = x_A$ and has a simple pole. By following the integration procedure in Appendix A.2 and using the result of Equation (A.2.4), Equation (2.2.11) becomes the jump condition for displacements

$$\xi_x(x_A^+) - \xi_x(x_A^-) = -i\pi \frac{k_{\perp,2}^2 P_1'(x_A)}{\omega_A^2(x_A) \left| \mathrm{d}\rho_0/\mathrm{d}x \right|_{x_A}}. \tag{2.2.13}$$

This integral along with the explicit dependencies of the of the displacements at both sides of the resonant layer (2.2.9) and (2.2.10), lead to the dispersion relation for waves exhibiting damping due to resonant absorption at the section x_A at the inhomogeneous layer [12, 95]. Due to the thin layer approximation, the exact location

of x_A is not of relevance.

$$1+\frac{\rho_{\rm en}\left(\omega^2-\omega_{A,\rm en}^2\right)}{\rho_{\rm in}\left(\omega^2-\omega_{A,\rm in}^2\right)}=i\pi\frac{|k_{\perp,2}|\,\rho_{\rm en}\left(\omega^2-\omega_{A,\rm en}^2\right)}{\omega_A^2(x_A)\,|{\rm d}\rho_0/{\rm d}x|_{x_A}}. \tag{2.2.14}$$

The damping rate is solved with the approximation of weakly damped waves, $|\gamma|\ll|\omega_R|$. This means that $\omega^2\simeq\omega_R^2+2i\gamma\omega_R$. In solving for the complex frequency ω, it is assumed that $\omega_A(x_A)$ can be approximated to a frequency ω_k, given by

$$\omega_k^2\equiv\frac{\rho_{\rm in}\omega_{A,\rm in}^2+\rho_{\rm en}\omega_{A,\rm en}^2}{\rho_{\rm in}+\rho_{\rm en}}.$$

which is the frequency for kink oscillations in the case of a sharp transition between both regions (**I**) and (**II**). By using the explicit definition of the local Alfvén frequency, the damping rate is obtained.

$$\frac{\gamma}{\omega_R}=-\frac{\pi}{8}\frac{(\rho_{\rm in}-\rho_{\rm en})^2}{(\rho_{\rm in}+\rho_{\rm en})}\frac{|k_y\cos\varphi|}{|{\rm d}\rho_0/{\rm d}x|_{x_A}}. \tag{2.2.15}$$

The damping time-rate is computed as a ratio of times, where $\tau_{\rm P}=2\pi/\omega_R$ is the oscillation period, and $\tau_{\rm D}=1/|\gamma|$ is the damping time. Thus,

$$\frac{\tau_{\rm D}}{\tau_{\rm P}}=\frac{4}{\pi^2}\frac{(\rho_{\rm in}+\rho_{\rm en})}{(\rho_{\rm in}-\rho_{\rm en})^2}\frac{|{\rm d}\rho_0/{\rm d}x|_{x_A}}{|k_y\cos\varphi|}.$$

We note that the angle φ is related to the angle χ, which is its complementary angle. Thus, $\cos\varphi=\sin\chi$. The angle χ is defined as $\chi=\arctan\left[B_{0z}/B_{0y}\right]$ (see angle χ in Fig. 2.3). The density profile used throughout this research is introduced to

compute the explicit form of the damping time-rate.

$$\rho_p(\mathbf{r},0) = \begin{cases} \rho_{\text{en}}, & |x-x_0| \geq x_+, \\ \sigma(x)\left[\dfrac{\rho_{\text{in}}-\rho_{\text{en}}}{l}\right]\Big[(x-x_0)+\ \sigma(x)x_+\Big]+\rho_{\text{en}}, & x_- \leq |x-x_0| < x_+, \\ \rho_{\text{in}}, & |x-x_0| \leq x_- \end{cases} \tag{2.2.16}$$

where $\sigma(x) = \text{sign}(x_0 - x)$, l is the width of the linear transition from ρ_{en} to ρ_{in}, $x_\pm = R \pm l/2$, and R is the distance from the center of the slab x_0 to the middle point of the linear transition, as shown in Fig. 2.4. This density profile has two zones

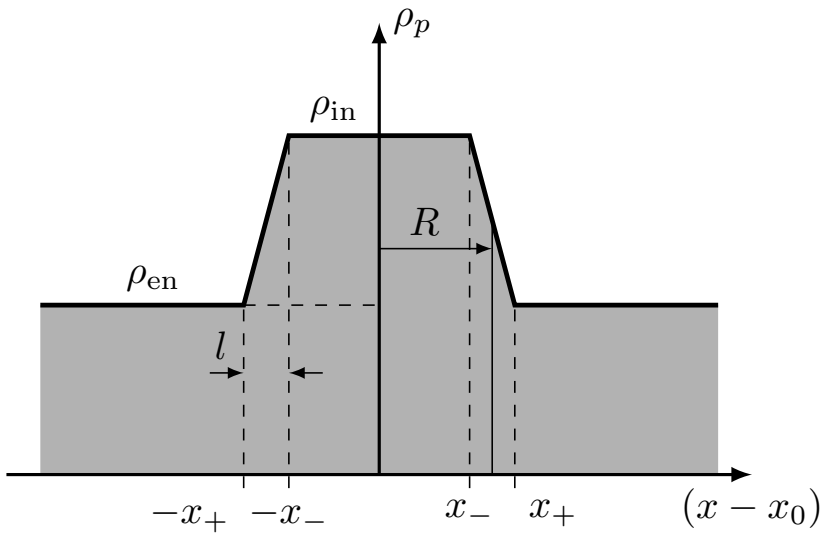

Figure 2.4: Section of the mass-density profile of protons for a section y in the initial condition. Figure from Carril et al. [39] .

where resonant absorption occurs, one on each layer. By taking one of the resonant

layers with wavenumber $k_y = \pi/L_y$, the damping time-rate is obtained

$$\frac{\tau_{\mathrm{D}}}{\tau_{\mathrm{P}}} = \frac{1}{|\sin\chi|}\frac{4}{\pi^3}\frac{\rho_{\mathrm{in}}+\rho_{\mathrm{en}}}{|\rho_{\mathrm{in}}-\rho_{\mathrm{en}}|}\frac{L_y/R}{l/R}. \tag{2.2.17}$$

2.3 Multifluid Equilibrium for an Inhomogeneous Plasma

The density gradient in the plasma requires to introduce an equilibrium condition at the largest spatial scales. The equilbibrium condition allows dynamics only triggered by the perturbation. For this purpose, a pressure-balanced equilibrium is set. We consider a plasma composed of protons and electrons. Macroscopically, this plasma consists of two fluids. Therefore, the equilibrium condition of the slab is set through a multifluid approach.

2.3.1 Equations of the Model

The multifluid equations are derived from the kinetic equation for each of the species s composing the plasma. For this research, we consider the mass conservation, the momentum conservation laws [102] for a collisionless plasma, and the non-relativistic Ampère-Maxwell equation, in a quasi-neutral plasma.

$$\frac{\partial n_s}{\partial t} + \nabla\cdot[n_s\mathbf{u}_s] = 0, \tag{2.3.1}$$

$$\frac{\partial \mathbf{u}_s}{\partial t} + \mathbf{u}_s\cdot\nabla\mathbf{u}_s = \frac{q_s}{m_s}\left[\mathbf{E}+\frac{\mathbf{u}_s\times\mathbf{B}}{c}\right] - \frac{1}{n_s m_s}\nabla\cdot\mathbb{P}_s, \tag{2.3.2}$$

$$\nabla\times\mathbf{B} = \frac{4\pi}{c}\mathbf{j}, \tag{2.3.3}$$

$$\sum_s q_s n_s = 0, \tag{2.3.4}$$

where n_s and $\mathbf{u}_s$ are the particle density and the bulk-velocity $\mathbf{u}_s$ of the species s respectively, q_s is the charge of the species s, and $\mathbf{j}$ is current density of the plasma. The pressure tensors of all of the species are assumed to be isotropic, so that $\mathbb{P}_s = p_s\mathbb{I}$. Furthermore, by using the thermodynamic definition of temperature for all of the species with initially isotropic, Maxwellian distributions and the definition of the diagonal components of the pressure tensors, it is found that the pressure p_s is given by the ideal gas equation of state

$$p_s = n_s T_s, \tag{2.3.5}$$

where T_s contains information from the Boltzmann constant.

2.3.2 Equilibrium Conditions

The aim is to define a multifluid static equilibrium condition to initialize the plasma given arbitrary density n_s and temperature T_s profiles. Under these conditions, the dynamic equations are reduced to

$$\begin{aligned} \nabla \cdot [n_s \mathbf{u}_s] &= 0, \\ m_s n_s \mathbf{u}_s \cdot \nabla \mathbf{u}_s &= q_s n_s \left[\mathbf{E} + \frac{\mathbf{u}_s \times \mathbf{B}}{c} \right] - \nabla p_s. \end{aligned} \tag{2.3.6}$$

We assume the dependency $n_s = n_s(x)$, so that all of the quantities depend only on x. Therefore, the continuity equation implies that $u_{sx} = 0$ for all s. Because of the dependency on x, the advection term in the momentum equation is zero. By

summing over all of the species of the plasma, the momentum equation leads to

$$\mathbf{E}\left[\sum_s q_s n_s\right] + \frac{1}{c}\left[\sum_s q_s n_s \mathbf{u}_s\right] \times \mathbf{B} - \nabla \sum_s p_s = 0.$$

The term associated to the electric field is zero due to quasi-neutrality. The term in the magnetic forcing corresponds to the current density, $\mathbf{j}$. Thus,

$$\frac{1}{c}\mathbf{j} \times \mathbf{B} - \nabla \sum_s p_s = 0. \tag{2.3.7}$$

The Maxwell-Ampère law is used in the limit of non-relativistic dynamics (2.3.3). Accordingly, the magnetic forcing becomes,

$$\frac{1}{c}\mathbf{j} \times \mathbf{B} = \frac{1}{4\pi}\left[\nabla \times \mathbf{B}\right] \times \mathbf{B} = \frac{1}{4\pi}\left\{\mathbf{B} \cdot \nabla \mathbf{B} - \frac{1}{2}\nabla B^2\right\}. \tag{2.3.8}$$

Because of the dependency on x, it is necessary that the magnetic field $\mathbf{B}$ has only components y and z. Therefore, only the gradient of the magnetic energy is non-zero in Equation (2.3.8), and the momentum equation (2.3.7) becomes,

$$\nabla\left\{\frac{B^2}{8\pi} + \sum_s p_s\right\} = \nabla\left\{\frac{B^2}{8\pi} + \sum_s n_s T_s\right\} = 0. \tag{2.3.9}$$

The magnetic field of this equilibrium configuration, the background magnetic field $\mathbf{B} = \mathbf{B}_0$ is fixed as uniform in the plasma. Since the field $\mathbf{B}_0$ has components in y and z, for convenience it is defined as

$$\mathbf{B}_0 = B_0\left[\sin\varphi\widehat{\mathbf{y}} + \cos\varphi\widehat{\mathbf{z}}\right]. \tag{2.3.10}$$

The system we study is 2D and defined on the plane xy. For the angle $\varphi = 90^{\text{o}}$, the magnetic field is fully contained in the $xy-$ plane. The uniformity of $\mathbf{B}_0$ is used in order to have an analytical approximation (condition required for the procedure in section 2.2) to compare with the simulation data.

2.3.3 Proton Temperature Profile

Equation (2.3.9) is applied to a magnetized plasma composed of protons and electrons with a background magnetic field as in Equation (2.3.10), and an inhomogeneous proton temperature distribution T_p such that it compensates the proton density profile n_p, given. The electron temperature T_e is given, and due to quasi-neutrality, $n_e = n_p$. Equation (2.3.9) implies that the argument of the gradient is a uniform quantity in the plasma. We consider a reference point where the density is known: the maximum of ion density, n_0, and set a reference proton temperature T_{0p}, given. Therefore, the constancy of the argument in Equation (2.3.9) leads to the proton temperature distribution for any point x in the plasma.

$$T_p(x) = \frac{n_0}{n_p(x)} \left\{ T_{0p} + T_{e0} - T_e(x) \frac{n_p(x)}{n_0} \right\}.$$

A brief discussion is provided regarding the electron temperature distribution T_e. Electron dynamics occur at time-scales much shorter than the proton dynamics and related kinetic processes. Accordingly, electrons are nearly at instantaneous equilibrium conditions [103]. Another assumption for electrons is that they are isothermal, implying that electrons rapidly redistribute energy leading to large thermal conductivity. Thus, space fluctuations of temperature are negligible [104, 105]. Accoridngly, in this research we set a constant, uniform electron temperature $T_e = T_{e0}$. Thus, the

temperature profile used in this research is given by

$$T_p(x) = \frac{n_0}{n_p(x)} \left\{ T_{0p} + T_{e0} \left[1 - \frac{n_p(x)}{n_0} \right] \right\}. \tag{2.3.11}$$

This temperature profile provides an equilibrium of the fluid quantities. It defines the proton temperature everywhere in the space domain and establishes a thermally inhomogeneous plasma.

Chapter 3

Kinetic and Particle Frameworks

Fluid theories are not valid when fluctuations reach scales in the order of the ion Larmor radius or ion inertial length [106]. Waves may interact with the plasma by resonating with specific populations of particles, depending on their velocity, or may shape the distribution function via wave-particle interactions. When collisions are frequent, perturbations are relaxed [107] and the plasma can be described using macroscopic, averaged quantities as a fluid with local thermal equilibria [108].

In the case of a collisionless or weakly collisional plasma, the particle distributions deviate from the thermal equilibrium [105]. This requires including kinetic effects in the model. The phenomena predicted by kinetic theory can significantly influence macroscopic scales [109].

This Chapter provides a review of the formalism underlying the particle distribution function from individual particle dynamics to the statistical, single-particle distribution function, including the Debye shielding and the Vlasov-Maxwell system of equations. This is the basis to build and analyze distribution functions using particle data from simulations. We further use this formalism to study the particle distribution for the equilibrium for the pressure-balanced equilibrium state derived in Chapter 2 and its validity based on Brunner [110]. This framework allows us to connect the macroscopic, MHD equilibrium with the microscopic, kinetic equilibrium.

3.1 Particle Distribution Function

3.1.1 Microscopic Description

A microscopic description of a plasma considers each particle i of a species s composing the plasma. Each of these particles follows trajectories with instantaneous positions $\mathbf{r}_{i,s}(t)$ and velocities $\mathbf{v}_{i,s}(t)$. In a collisionless plasma, particle positions and trajectories evolve by the equations of motion considering the Lorentz force (in CGS units),

$$\frac{\mathrm{d}\mathbf{r}_{i,s}}{\mathrm{d}t} = \mathbf{v}_{i,s}, \tag{3.1.1}$$

$$\frac{\mathrm{d}\mathbf{v}_{i,s}}{\mathrm{d}t} = \frac{q_s}{m_s}\left[\mathbf{E}'^{\mathrm{M}} + \frac{\mathbf{v}_{i,s}\times\mathbf{B}'^{\mathrm{M}}}{c}\right]. \tag{3.1.2}$$

The fields $\mathbf{E}^{\mathrm{M}}$ and $\mathbf{B}^{\mathrm{M}}$ are the electromagnetic fields self-consistent with the collection of particle distributions. The apostrophe means that they are the fields due to all of the particles but i. The microscopic quantities due to all of the particles of the plasma correspond to mean values and short-scale, fast varying fluctuations [105].

Such a system of particles of the species s is fully characterized in the microscopical sense by the function [109]

$$N_s(\mathbf{r},\mathbf{v},t) = \sum_i \delta\left[\mathbf{r}-\mathbf{r}_{i,s}(t)\right]\delta\left[\mathbf{v}-\mathbf{v}_{i,s}(t)\right]. \tag{3.1.3}$$

The function N_s indicates whether any of the $\overline{N}_s$ particles of the species s is at the coordinates $(\mathbf{r},\mathbf{v})$. It is intrinsically discontinuous, unbounded, and leads to a complex description of the plasma.

This distribution allows us to obtain the source terms, and charge and current

densities. Thus, the Maxwell equations of the microscopic fields are

$$\begin{aligned}
\nabla \cdot \mathbf{E}^{\mathrm{M}} &= 4\pi \sum_s q_s \int N_s \mathrm{d}^3 v, \\
\nabla \cdot \mathbf{B}^{\mathrm{M}} &= 0, \\
\nabla \times \mathbf{E}^{\mathrm{M}} &= -\frac{1}{c}\frac{\partial \mathbf{B}^{\mathrm{M}}}{\partial t}, \\
\nabla \times \mathbf{B}^{\mathrm{M}} &= \frac{4\pi}{c} \sum_s q_s \int \mathbf{v} N_s \mathrm{d}^3 v + \frac{4\pi}{c}\frac{\partial \mathbf{E}^{\mathrm{M}}}{\partial t}.
\end{aligned}$$

The time-evolution for the functions N_s is obtained from the particle equations of motion (3.1.1) and (3.1.2) [109]. This yields

$$\frac{\partial N_s}{\partial t} + \mathbf{v} \cdot \nabla N_s + \frac{q_s}{m_s}\left[\mathbf{E}'^{\mathrm{M}} + \frac{\mathbf{v} \times \mathbf{B}'^{\mathrm{M}}}{c}\right] \cdot \nabla_v N_s = 0. \tag{3.1.4}$$

In order to solve the dynamics of this plasma, it is necessary to solve the coupled equations of motion of each particle. Therefore, a simpler approach is required while retaining microscopic information of the plasma. This is made via a statistical approach.

3.1.2 The Debye Shielding

The notion of shielding is required to continue with the statistical approach for a plasma. We follow the standard discussion for the Debye shielding [111, 112]. We consider a uniform distribution of charged particles space, thermal plasma with zero net charge, and a test charge slowly introduced into the plasma. The interparticle interaction is due to the Coulomb force.

In the transient stage, the particles close to the test charge will move according

to their respective electrical charge until a stationary equilibrium is achieved. The reaction of the plasma to counteract the electric field of this perturbation is labeled as shielding [113]. The resulting electrostatic potential of the test charge is affected by the plasma.

By considering each of the species of the plasma as a fluid of temperatures T_s, densities n_s, and charges q_s. The closure in Equation (2.3.5) is considered. The multifluid momentum equations (2.3.6) for the case of slowly varying dynamics obtains the Boltzmann relation [111],

$$n_s = n_{s0} e^{-q_s \phi / T_s},$$

where ϕ is the total electrostatic potential. This potential is solved via the Poisson equation, considering the contribution of each species and the test charge. In the limit of a small perturbative potential $|q_s \phi| \ll T_s$, the electrostatic potential in the plasma is given by [112, 113]

$$\phi \propto \frac{e^{-r/\lambda_D}}{r},$$

where λ_D is the total Debye length given by

$$\frac{1}{\lambda_{\mathrm{D}}^2} = \sum_s \frac{1}{\lambda_{\mathrm{D}s}^2} \tag{3.1.5}$$

$$\lambda_{\mathrm{D}s} \equiv \sqrt{\frac{T_s}{4\pi n_{0s} q_s^2}}. \tag{3.1.6}$$

The interpretation is that for $r \gg \lambda_{\mathrm{D}}$, the potential is close to zero. That is, the potential of the test charge has been shielded. Whereas for $r \ll \lambda_{\mathrm{D}}$, the potential is

similar to that of the test charge alone. This interpretation is valid as long as there is a large number of charges within a sphere of radius λ_{D} [111]. Accordingly, it can be interpreted as the distance of closest approach in Coulomb scattering [105].

The Debye length must be much smaller than the size of the system for the shielding to be dynamically relevant. This is a fundamental definition of a plasma [105, 107]. This length is small compared with the fluid scales in MHD plasmas and is not present in the model. It is introduced through quasi-neutrality. On the contrary, the Debye length appears in kinetic theory and is necessary to establish the collinsionless character of the plasma.

This length defines another fundamental property of a plasma. For a distribution of particles, the mean interparticle distance is related to $n_0^{-1/3}$, where n_0 is the particle density. It is associated to collisions. By definition, a plasma verifies the condition $1 \gg 1/n_0\lambda_{\mathrm{D}}^3$ [105], meaning that the characteristic length of the electrostatic interaction is dominant over the collision distance. It is also interpreted as having a large number of particles within a sphere of radius λ_{D}.

3.1.3 Statistical Description - Phase-space Density

The statistical description is a bridge between the macroscopic and the microscopic descriptions of a plasma. For this purpose, we consider a plasma composed by N particles of different species, described by a $6N-$dimensional phase-space. Following Ichimaru [114], given a macroscopic state of the plasma, there are ν_R, arbitrarily large, microscopical possible realizations.

The $N-$distribution function F_N is defined in terms of the phase-space coordinates $\boldsymbol{\zeta}_{i,s} \equiv (\mathbf{r}_{i,s}, \mathbf{v}_{i,s})$ for the particle i of the species s. This distribution depends

on all of the particle coordinates,

$$F_N = F_N\left(\ldots, \boldsymbol{\zeta}_{i-1,s}, \boldsymbol{\zeta}_{i,s}, \boldsymbol{\zeta}_{i+1,s}, \ldots; \ldots, \boldsymbol{\zeta}_{j-1,u}, \boldsymbol{\zeta}_{j,u}, \boldsymbol{\zeta}_{j+1,u}, \ldots; \ldots, t\right).$$

It is defined on an infinitesimal volume $\prod_{j,\alpha} \mathrm{d}\boldsymbol{\zeta}_{j,\alpha}$ in phase-space containing ν_d microscopic configurations as

$$F_N \prod_{j,\alpha} \mathrm{d}\boldsymbol{\zeta}_{j,\alpha} = \lim_{\nu_R \to \infty} \frac{\nu_\mathrm{d}}{\nu_R}.$$

The function F_N is normalized to the unity and satisfies the Liouville equation. That is, the conservation of the distribution function F_N in phase-space [109].

$$\frac{\mathrm{d}F_N}{\mathrm{d}t} = \frac{\partial F_N}{\partial t} + \sum_i \mathbf{v}_i \cdot \nabla_i F_N + \sum_i \mathbf{a}_i \cdot \nabla_{\mathbf{v}_i} F_N = 0,$$

where $\mathbf{a}_i$ is the acceleration of the particle i.

The introduction of F_N allows the compuation statistical averages of any macroscopic quantity of the plasma. Reduced distribution functions of the species s, for a specific number of particles, are obtained by integrating over the phase-space coordinates of the remaining particles.

3.1.4 Single-particle Distribution Function

We aim to construct a formalism for a collisionless plasma. The one-particle distribution function of the species s, f_s^1, is obtained by integrating F_N over the phase-space

of all of the particles except for one particle of the species s.

$$f_s^1\left(\mathbf{r}_{1,s}, \mathbf{v}_{1,s}, t\right) = V \int F_N\left(\boldsymbol{\zeta}_{1,s}, \boldsymbol{\zeta}_{2,s}, \ldots, t\right) \prod_{j=2,s} \mathrm{d}\boldsymbol{\zeta}_{j,s} \prod_{i,\alpha \neq s} \mathrm{d}\boldsymbol{\zeta}_{i,\alpha},$$

where V is the volume occupied by the system of particles.

The distribution function f_s^1 is equivalently interpreted as the statistical average of the function (3.1.3) for the species s with distribution function F_N [109].

$$\langle N_s \rangle = \int F_N N_s(\mathbf{x}, \mathbf{v}, t) \prod_{j,\alpha} \mathrm{d}\boldsymbol{\zeta}_{j,\alpha}.$$

The expansion of the summatory of the distribution (3.1.3) leads to $\overline{N}_s$ identical contributions, corresponding to the number of particles of the species s. The integration yields

$$\begin{aligned}
\int F_N N_s(\mathbf{x}, \mathbf{v}, t) \prod_{j,\alpha} \mathrm{d}\boldsymbol{\zeta}_{j,\alpha} &= \overline{N}_s \int F_N \delta\left[\mathbf{r} - \mathbf{r}_{1,s}\right] \delta\left[\mathbf{v} - \mathbf{v}_{1,s}\right] \prod_{j,\alpha} \mathrm{d}\boldsymbol{\zeta}_{j,\alpha} \\
&= \overline{N}_s \int F_N\left(\boldsymbol{\zeta}, \boldsymbol{\zeta}_{2,s}, \ldots, t\right) \prod_{j=2,s} \mathrm{d}\boldsymbol{\zeta}_{j,s} \prod_{i,\alpha \neq s} \mathrm{d}\boldsymbol{\zeta}_{i,\alpha} \\
&= \overline{n}_s f_s^1(\mathbf{r}, \mathbf{v}, t)
\end{aligned}$$

where $\overline{n}_s$ and $\boldsymbol{\zeta} = (\mathbf{r}, \mathbf{v})$ and is the average particle density. Here we introduce the equivalence $f_s \equiv f_s^1$. Therefore, this single-particle distribution provides a complete statistical description of the plasma at the one-particle level.

Higher-order functions of N_s can be obtained, which contain simultaneous information of two or more particles. Following Goldston [105] and Krall and Trivelpiece [109], the evolution of the reduced distribution f_s can be obtained by av-

eraging (3.1.4) over the $6N-$phase-space with the distribution F_N. This procedure introduces two-particle correlations $\langle N_s N_u \rangle$. The equations for these correlations are obtained from Equation (3.1.4). In time, the resulting equation requires correlations $\langle N_s N_u N_v \rangle$. By repeating the same procedure, higher-order correlations are required to solve the dynamics of the distribution f_s. The system of equations is the BBGKY hierarchy, and its solution requires establishing a closure relation [107].

To proceed, the notion of statistical correlation is introduced. Correlations quantify the degree to which the state of a particle at phase-space coordinates $\boldsymbol{\zeta}$ in a system is affected the presence of all of the other particles [109]. Considering that a plasma verifies $1 \gg 1/n_0\lambda_{\mathrm{D}}^3$, charges may move close to each other up to a distance $\sim \lambda_{\mathrm{D}}$ particles are affected by Coulomb scattering only at distances $\sim \lambda_{\mathrm{D}}$ due to collective shielding (subsection 3.1.2). Thus, particles are statistically uncorrelated or weakly correlated, since the interaction is mediated by the fields generated by the whole particle distribution rather than between individual particles.

We consider second-order correlations, $f_{su}^2 \equiv f_{su}$. This distribution can be expanded as

$$f_{su}\left(\boldsymbol{\zeta}, \boldsymbol{\zeta}', t\right) = f_s(\boldsymbol{\zeta}, t) f_u(\boldsymbol{\zeta}', t) + g_{us}\left(\boldsymbol{\zeta}, \boldsymbol{\zeta}', t\right).$$

The first term corresponds to the limit of zero statistical correlation. The second term quantifies the probability of finding particles being attracted near neighbours rather than repelled [109]. It is possible to show that the function g depends strongly on the ratio $1/n_0\lambda_{\mathrm{D}}^3$, and thus it can be neglected. Higher-order correlations involve higher powers of this ratio and are similarly neglected.

Thus, particles in a collisionless plasma are approximately statistically uncorre-

lated. To a good approximation, it can be treated as an ideal gas. These approximations render the single-particle distribution f_s as a sufficient and tractable statistical description of the system.

3.1.5 The Vlasov-Maxwell System of Equations

In a collisionless plasma, the equation for the distribution function f_s is obtained by the statistical average of the equation ruling the function N_s, Equation (3.1.4). The result is the Vlasov equation [109, 115],

$$\left[\frac{\partial}{\partial t} + \mathbf{v}\cdot\nabla + \frac{q_s}{m_s}\left(\mathbf{E} + \frac{1}{c}\mathbf{v}\times\mathbf{B}\right)\cdot\nabla_v\right] f_s = 0. \tag{3.1.7}$$

The electromagnetic fields $\mathbf{E}$ and $\mathbf{B}$ are the statistical averages of the microscopic fields $\mathbf{E}^{\mathrm{M}}$ and $\mathbf{B}^{\mathrm{M}}$, respectively. These are the average fields caused by all of the particle distributions. Their evolution is obtained by statistically averaging over the microscopic Maxwell equations,

$$\nabla\cdot\mathbf{E} = 4\pi\rho_c, \tag{3.1.8}$$

$$\nabla\cdot\mathbf{B} = 0, \tag{3.1.9}$$

$$\nabla\times\mathbf{E} = -\frac{1}{c}\frac{\partial\mathbf{B}}{\partial t}, \tag{3.1.10}$$

$$\nabla\times\mathbf{B} = \frac{4\pi}{c}\mathbf{j} + \frac{4\pi}{c}\frac{\partial\mathbf{E}}{\partial t}. \tag{3.1.11}$$

This procedure provides the source terms of charge and current density in terms of the single-particle distribution function, rather than in terms of all of the particle

data.

$$\rho_c = \sum_s q_s n_s \int f_s \mathrm{d}^3 v, \tag{3.1.12}$$

$$\mathbf{j} = \sum_s q_s n_s \int \mathbf{v} f_s \mathrm{d}^3 v. \tag{3.1.13}$$

The Vlasov-Maxwell system (3.1.7)–(3.1.13) evolves self-consistently.

3.2 Exact Equilibrium Distribution Functions

The fluid equilibrium condition given by the pressure-balanced structure established in section 2.3 does not necessarily describe a kinetic equilibrum/stationary state. Therefore, it is necessary to connect the fluid and the kinetic equilibria by constructing a proton distribution function such that it obeys the temperature profile in Equation (2.3.11).

In here, we follow a similar procedure of Brunner [110] to obtain a distribution function f_p to first-order approximation to the exact equilibrium function f_p^E built via the constants of motion of the system [116–119]. For this purpose, we calculate the equilibrium electric field associated with an arbitrary density profile from the equilibrium fluid equation for electrons (2.3.6), pressure (2.3.5), and assuming zero bulk velocity, $\delta \mathbf{u}_e = \mathbf{0}$. The density and temperature profiles are inhomogeneous,

$$\begin{aligned} \mathbf{E}_0 &= -\nabla\phi \\ &= -\widehat{\mathbf{x}} \frac{\partial}{\partial x} \left[\frac{1}{2} \frac{m_p v_A^2 \beta_e}{q_p} \ln\left(\frac{n_p}{n_0}\right) \right]. \end{aligned} \tag{3.2.1}$$

3.2.1 Particle Lagrangian and Constants of Motion

In here, we assume that particles interact only through the mean electric and magnetic fields, neglecting the presence of electromagnetic fluctuations that arise due to particle thermal motion of charged particles [120–122]. Therefore, the one-particle Lagrangian is enough to describe particle motion.

The one-particle Lagrangian

$$\mathcal{L}_p = \frac{1}{2} m_p v^2 - q_p \phi + q_p \frac{\mathbf{A}_0 \cdot \mathbf{v}}{c}, \tag{3.2.2}$$

is used to derive the proton equations of motion, where $\mathbf{A}_0$ is the vector potential associated with the background field in Equation (2.3.10), given by $\mathbf{A}_0 = xB_0\,(-\cos\varphi\widehat{\mathbf{y}} + \sin\varphi\widehat{\mathbf{z}})$. The Lagrangian (3.2.2) does not depend explicitly on y or z, so that the momenta in y and z are conserved quantities. From the respective equations of motion, we find that

$$\frac{\mathrm{d}v_y}{\mathrm{d}t} = x\Omega_p \cos\varphi, \tag{3.2.3}$$

$$\frac{\mathrm{d}v_z}{\mathrm{d}t} = -\,x\Omega_p \sin\varphi. \tag{3.2.4}$$

Integration of Equations (3.2.3) and (3.2.4) leads to two constants of motion W_y and W_z.

$$W_y = v_y - x\Omega_p \cos\varphi, \tag{3.2.5}$$

$$W_z = v_z + x\Omega_p \sin\varphi. \tag{3.2.6}$$

We combine the constants of motion from Equations (3.2.5) and (3.2.6), and redefine them as the gyrocenter position X, following other works that use a similar analysis [110, 123–125].

$$X = x + \frac{1}{\Omega_p}\left[-v_y \cos\varphi + v_z \sin\varphi\right] \equiv \frac{1}{\Omega_p}\left[-W_y \cos\varphi + W_z \sin\varphi\right]. \tag{3.2.7}$$

Since the Lagrangian does not depend explicitly on time, the total proton energy $\mathcal{E}_p$ is another constant of motion,

$$\mathcal{E}_p = \frac{1}{2} m_p v^2 + q_p \phi, \tag{3.2.8}$$

where ϕ is the electrostatic potential derived in Equation (3.2.1).

3.2.2 Exact Equilibrium

With these constants of motion, we build a Maxwellian-like distribution for f_p^E [110, 124],

$$f_p^E(X,\mathcal{E}_p) = \frac{\mathcal{N}_p(X)}{\pi^{3/2}v_{\mathrm{th}p}^3(X)}\exp\left[-\frac{\mathcal{E}_p(X,\mathbf{v})}{T_p(X)}\right]. \tag{3.2.9}$$

This function is an exact equilibrium for an arbitrary inhomogeneous density and temperature profiles in the guiding center, and the background magnetic field in Equation (2.3.10). The function $\mathcal{N}_p$ is not exactly the particle density, and it is defined such that the zeroth moment of f_p^E is the density profile in the initial instant.

3.2.3 First order Approximation

The first order approximation of the distribution $f_p^E(\mathcal{E}_p, X)$ of a stationary state of the Vlasov-Maxwell system (3.1.7)–(3.1.13) is estimated via a Taylor series expansion in X with respect to $X = x$ taking $|-v_y\cos\varphi + v_z\sin\varphi| \simeq v_{\mathrm{th}p}$, up to first order in the smallness parameter r_p/l_{ih} where $r_p = v_{\mathrm{th}p}/\Omega_p$ is the proton gyroradius, and l_{ih} is the inhomogeneity characteristic length [110, 123],

$$f_p^E(X,\mathbf{v}) \simeq f_p^E(x,\mathbf{v}) + \frac{\partial f_p^E}{\partial x}\frac{1}{\Omega_p}\left[-v_y\cos\varphi + v_z\sin\varphi\right]. \tag{3.2.10}$$

By computing the zeroth moment of the distribution function, we obtain the function $\mathcal{N}_p$ valid up to first-order expansion in the smallness parameter (3.2.10),

$$\int f_p^E\left[X,\mathcal{E}_p(X,\mathbf{v})\right]\mathrm{d}^3v \simeq \int f_p^E\left[x,\mathcal{E}_p(x,\mathbf{v})\right]\mathrm{d}^3v = n_p(x).$$

Thus,

$$\mathcal{N}_p(x) = n_p(x) \exp\left\{ \frac{\beta_e}{\beta_p(x)} \ln\left[\frac{n_p(x)}{n_0} \right] \right\}. \tag{3.2.11}$$

Now we proceed to evaluate the terms of the distribution (3.2.10) using Equations (3.2.1), (3.2.8), and (3.2.11). The zeroth-order term yields the distribution

$$\begin{aligned} f_p^E(x, \mathbf{v}) &= \frac{\mathcal{N}_p(x)}{\pi^{3/2} v_{\mathrm{th}p}^3(x)} \exp\left\{ -\frac{v^2}{v_{\mathrm{th}p}^2(x)} - \frac{\beta_e}{\beta_p(x)} \ln\left[\frac{n_p(x)}{n_0} \right] \right\} \\ &= \frac{n_p(x)}{\pi^{3/2} v_{\mathrm{th}p}^3(x)} \exp\left[-\frac{v^2}{v_{\mathrm{th}p}^2(x)} \right], \end{aligned} \tag{3.2.12}$$

which corresponds to an inhomogeneous Maxwellian distribution function with arbitrary density and temperature profiles. We redefine the zeroth-order term as f_p. The derivative yields

$$\frac{\partial f_p^E}{\partial x} = f_p \frac{1}{n_p} \frac{\partial n_p}{\partial x} \left[1 - \frac{3}{2} \left(1 + \frac{\beta_e}{\beta_p} \right) + \frac{1}{\beta_p} \frac{v^2}{v_A^2} \left(1 + \frac{\beta_e}{\beta_p} \right) \right].$$

A comparison is made between the zeroth-order term, which corresponds to the distribution in Equation (3.2.12), and the first order-term. We estimate the velocities v_y and v_z such that the largest value of the first-order term is obtained. For the parameters of interest, we find that these velocities may be as large as $4v_{\mathrm{th}p}$, which is at the tail of the proton distributions. In any case, by taking this value or in the order of $v_{\mathrm{th}p}$, the zeroth order term is dominant. We provide a discussion in Chapter 5 about the closeness of the distribution $f_p^E(x, \mathbf{v})$ to the exact distribution

for the parameters we use in this research.

Chapter 4

Alfvén and Kinetic Alfvén Waves, and Non-linear Coupling

Alfvén waves are pervasive in astrophysical plasmas, particularly in the solar atmosphere and in the solar wind [4, 126, 127]. They involve incompressible, electromagnetic fluctuations and propagate parallel to the background magnetic field [128].

As Alfvén waves reach sufficiently small spatial scales, they may acquire quasi-perpendicular propagation, develop a significant electrostatic component, and become right-hand polarized [129, 130]. With such features, they become kinetic Alfvén waves (KAWs).

Finite amplitude Alfvén waves and Kinetic Alfvén waves may couple and generate stationary, non-propagating structures. Particularly, the counterpropagating Alfvén waves [47]. In this Chapter, we review features of circularly polarized Alfvén and kinetic Alfvén waves that are relevant to this work. In particular, we use circularly polarized Alfvén waves to generate a large-scale perturbation. Also, we describe the non-linear coupling that motivates the analysis presented in a subsequent Chapter.

4.1 Circularly Polarized Alfvén Waves

4.1.1 Multifluid Dispersion Relation

A plasma composed of fluid electrons and protons is studied for parallel propagations along the background magnetic field $\mathbf{B}_0 = B_0\hat{\mathbf{x}}$. Equations (2.3.1) to (2.3.5). Following Terradas, Viñas, and Araneda [48], the dispersion relation for parallel propagating waves is obtained. Fields are assumed to be harmonic.

$$\delta\mathbf{u}_{s,\perp} = u_{s,\perp 0}e^{i\left(k_\parallel x-\omega t\right)}, \tag{4.1.1}$$

$$\delta\mathbf{B}_\perp = B_{\perp 0}e^{i\left(k_\parallel x-\omega t\right)}, \tag{4.1.2}$$

for the species s, which involve only perpendicular fluctuations. The notation $A_\perp = A_y + iA_z$ has been used. From the induction law, the electric field is obtained,

$$\delta\mathbf{E}_\perp = -\,i\frac{\omega}{k_\parallel c}\delta\mathbf{B}_\perp. \tag{4.1.3}$$

The magnetic forcing to first order in the perturbations is given by

$$\delta\mathbf{u}_{s,\perp}\times\mathbf{B}_0 = -\,iB_0\delta\mathbf{u}_{s,\perp}. \tag{4.1.4}$$

The momentum conservation equation (2.3.2) is evaluated to first order in the perturbations using Equations (4.1.1) to (4.1.4). We assume no pressure gradients, because these fluctuations carry no density fluctuations

$$\omega\delta\mathbf{u}_{s,\perp} = \Omega_s\frac{\omega}{k_\parallel}\frac{\delta\mathbf{B}_\perp}{B_0} + \Omega_s\delta\mathbf{u}_{s,\perp},$$

where $\Omega_s = q_s B_0/m_s c$ is the cyclotron frequency of the species s. This equation leads to the the amplitude $u_{s,\perp 0}$ in terms of the magnetic field amplitude $B_{\perp 0}$

$$u_{s,\perp 0} = \left[\frac{\Omega_s}{\omega - \Omega_s}\right] \frac{\omega}{k_\parallel} \frac{B_{\perp 0}}{B_0}. \tag{4.1.5}$$

In the following calculations, a plasma composed of protons and electrons is assumed. The waves of interest involve very low frequencies such that $|\Omega_e| \gg |\omega|$. The plasma is assumed to verify quasi-neutrality, $n_{0p} = n_{0e} = n_0$. The dispersion relation is obtained by computing the transverse current density $\mathbf{j}_\perp$ from the species density current

$$\begin{aligned} \mathbf{j}_\perp &= q_p n_0 \left[u_{p,\perp 0} - u_{e,\perp 0}\right] e^{i\left(k_\parallel x - \omega t\right)} \\ &= q_p n_0 \frac{\omega}{k_\parallel} \left[\frac{\omega}{\omega - \Omega_p}\right] \frac{\delta \mathbf{B}_\perp}{B_0}, \end{aligned} \tag{4.1.6}$$

and from the Ampère law (2.3.3),

$$\begin{aligned} \mathbf{j}_\perp &= \frac{c}{4\pi} \nabla \times \delta \mathbf{B}_\perp \\ &= -\frac{c}{4\pi} k_\parallel \delta \mathbf{B}_\perp. \end{aligned} \tag{4.1.7}$$

The dispersion relation is obtained by equating Equations (2.3.3) and (4.1.7),

$$\frac{\omega^2}{\Omega_p^2} \frac{\Omega_p^2}{k_\parallel^2 v_{Ap}^2} + \frac{\omega}{\Omega_p} - 1 = 0, \tag{4.1.8}$$

where $v_{Ap} = B_0/\sqrt{4\pi n_0 m_p}$ is the Alfvén speed. The obtained frequency depends on the sign of $\omega = \sigma_\omega \omega_0$ ($\omega_0 > 0$), which determines the sense of polarization of the wave, being left-hand polarized in the plasma sense for $\sigma_\omega > 0$ and right-hand

polarized for $\sigma_\omega < 0$ [48, 130]

$$\frac{\omega}{\Omega_p} = \sigma_\omega \frac{k_\parallel^2 v_{Ap}^2}{2\Omega_p^2} \left\{ -1 \pm \sigma_\omega \sqrt{1 + \frac{4\Omega_p^2}{k_\parallel^2 v_{Ap}^2}} \right\}. \tag{4.1.9}$$

A similar definition is introduced for the sign of $k_\parallel$, $k_\parallel = \sigma_k k_0$, where $k_0 > 0$. This frequency (4.1.9) makes the bulk velocity (4.1.5) self-consistent with the plasma. Therefore, a superposition of such waves introduced as a perturbation of a plasma in equilibrium is also self-consistent.

4.1.2 Superposition of Circularly Polarized Waves

The dispersion relation (4.1.8) is also valid for superpositions of waves. In particular, it is valid for a standing wave (superposition of counter-propagating waves). The following construction is based on the work of Terradas, Viñas, and Araneda [48]. For left-hand polarization, the monochromatic wave is characterized by the following components, using the relation (4.1.5) and the dispersion relation (4.1.8). The bulk-velocity components are set to follow left-hand polarization for forward propagation ($\sigma_\omega > 0$, $\sigma_k > 0$),

$$\begin{aligned}
\delta u_{p,y} &= u_0 \sin\left(k_0 x - \omega_0 t\right), \\
\delta u_{p,z} &= -\, u_0 \cos\left(k_0 x - \omega_0 t\right), \\
\delta B_y &= -\, u_0 \frac{B_0}{v_{Ap}^2} \frac{\omega_0}{k_0} \sin\left(k_0 x - \omega_0 t\right), \\
\delta B_z &= u_0 \frac{B_0}{v_{Ap}^2} \frac{\omega_0}{k_0} \cos\left(k_0 x - \omega_0 t\right).
\end{aligned}$$

The bulk-velocity components are set to represent left-hand polarization for backward propagation. ($\sigma_\omega > 0$, $\sigma_k < 0$),

$$\begin{aligned}
\delta u_{p,y} &= -\, u_0 \sin\left(k_0 x + \omega_0 t\right), \\
\delta u_{p,z} &= -\, u_0 \cos\left(k_0 x + \omega_0 t\right), \\
\delta B_y &= -\, u_0 \frac{B_0}{v_{Ap}^2} \frac{\omega_0}{k_0} \sin\left(k_0 x + \omega_0 t\right), \\
\delta B_z &= -\, u_0 \frac{B_0}{v_{Ap}^2} \frac{\omega_0}{k_0} \cos\left(k_0 x + \omega_0 t\right).
\end{aligned}$$

It is possible to perform a superposition of waves such that,

$$\begin{aligned}
\delta u_{p,y} &= 2u_0 \sin\left(k_0 x\right) \cos\left(\omega_0 t\right), \\
\delta u_{p,z} &= -\, 2u_0 \sin\left(k_0 x\right) \sin\left(\omega_0 t\right), \\
\delta B_y &= 2u_0 \frac{B_0}{v_{Ap}^2} \frac{\omega_0}{k_0} \cos\left(k_0 x\right) \sin\left(\omega_0 t\right), \\
\delta B_z &= 2u_0 \frac{B_0}{v_{Ap}^2} \frac{\omega_0}{k_0} \cos\left(k_0 x\right) \cos\left(\omega_0 t\right).
\end{aligned}$$

The same calculation is repeated for right-hand polarization waves. By applying the same superposition, the following fluctuations are found

$$\begin{aligned}
\delta u_{p,y} &= 2u_0 \sin\left(k_0 x\right) \cos\left(\omega_0 t\right), \\
\delta u_{p,z} &= 2u_0 \sin\left(k_0 x\right) \sin\left(\omega_0 t\right), \\
\delta B_y &= 2u_0 \frac{B_0}{v_{Ap}^2} \frac{\omega_0}{k_0} \cos\left(k_0 x\right) \sin\left(\omega_0 t\right),
\end{aligned}$$

$$\delta B_z = -\,2u_0 \frac{B_0}{v_{Ap}^2} \frac{\omega_0}{k_0} \cos\left(k_0 x\right) \cos\left(\omega_0 t\right).$$

4.1.3 Construction Initial States

From the above obtained superposition of counter-propagating left- and right-hand polarized waves, it is possible to further build a superposition of these stationary fluctuations. From the dispersion relation (4.1.9) it is clear that the frequencies ω_0 are not the same for left- and right-hand polarized waves. However, if the wavenumber k_0 is set to be small enough, both frequencies tend to be identical. Therefore, it is possible to perform a superposition such that

$$\begin{aligned}
\delta u_{p,y} &= 4u_0 \sin\left(k_0 x\right) \cos\left(\omega_0 t\right), \\
\delta u_{p,z} &= 0, \\
\delta B_y &= 4u_0 \frac{B_0}{v_{Ap}^2} \frac{\omega_0}{k_0} \cos\left(k_0 x\right) \sin\left(\omega_0 t\right), \\
\delta B_z &= 0.
\end{aligned}$$

The initial state is obtained by setting $t = 0$, for which all of the components are zero except one,

$$\delta u_{p,y}(x) = u_0 \sin\left(k_0 x\right), \tag{4.1.10}$$

with bulk-velocity fluctuations transverse to the background magnetic field. The prescription of this initial condition excites kink oscillations in the plasma [99].

4.2 Kinetic Alfvén Waves

For the study of Kinetic Alfvén waves (KAWs), we consider two approaches: linearized two-fluid model and Vlasov-Maxwell. The two-fluid equations are found to represent appropriately signals observed in the dispersion relation from simulation data. The kinetic approach would be suitable because it considers the kinetics of the system. This difference suggests that the kinetic effects of the linear waves per se are accurately explained by a fluid model of the waves. We note that the calculations presented here provide an approximate model of the waves, since they consider uniform plasmas.

Properties of KAWs based on literature are also presented below.

4.2.1 Two-Fluid Approach

A 2D plasma without resistivity is considered for calculations on the plane xy. Ohm's law is obtained from multifluid equations, ignoring non-linear advective terms, quasi-neutrality, and a plasma composed of protons and electrons [108, 131].

$$\frac{m_e}{n_p q_p^2}\frac{\partial \mathbf{j}}{\partial t} = \frac{1}{n_p q_p}\nabla p_e - \frac{1}{n_p q_p c}\mathbf{j}\times\mathbf{B} + \mathbf{E} + \frac{1}{c}\mathbf{u}\times\mathbf{B}. \tag{4.2.1}$$

Other equations used in this model [130] are Equation (2.2.1), the parallel component of the momentum equation along the background field $\mathbf{B}_0$ (2.2.2), the equation for the compressibility, $\nabla\cdot\mathbf{u}$ [divergence of Equation (2.2.2)], and an equation for

the vorticity, $\boldsymbol{\omega} = \nabla \times \mathbf{u}$ [curl of Equation (2.2.2)],

$$\rho \frac{\partial}{\partial t} (\nabla \cdot \mathbf{u}) = - \nabla^2 p + \frac{1}{c} \nabla \cdot (\mathbf{j} \times \mathbf{B}) , \tag{4.2.2}$$

$$\rho \frac{\partial \boldsymbol{\omega}}{\partial t} = \frac{1}{c} \nabla \times (\mathbf{j} \times \mathbf{B}) . \tag{4.2.3}$$

The Ampère (2.2.3) and induction (2.2.4) laws are used. The system of equations is completed with an equation for the magnetic field $\mathbf{B}$ by obtaining the curl of Equation (4.2.1),

$$\frac{\partial \mathbf{B}}{\partial t} - \lambda_e^2 \nabla^2 \frac{\partial \mathbf{B}}{\partial t} = \nabla \times (\mathbf{u} \times \mathbf{B}) - \frac{1}{n_p q_p} \nabla \times (\mathbf{j} \times \mathbf{B}) , \tag{4.2.4}$$

where $\lambda_e = c/\omega_{pe}$ is the electron inertial length, and $\omega_{pe} = \sqrt{4\pi n_e q_p^2 / m_e}$ is the electron plasma frequency. The system is completed with an equation for the current density $\mathbf{j}$ from the curl of Equation (4.2.4),

$$\frac{4\pi}{c} \frac{\partial \mathbf{j}}{\partial t} - \frac{4\pi}{c} \lambda_e^2 \nabla^2 \frac{\partial \mathbf{j}}{\partial t} = \nabla \times \left\{ \nabla \times (\mathbf{u} \times \mathbf{B}) - \frac{1}{n_p q_p} \nabla \times (\mathbf{j} \times \mathbf{B}) \right\} . \tag{4.2.5}$$

The dispersion relation for KAWs in this model is obtained by first-order perturbative theory in the same way as in subsection 2.2.2, but with homogeneous quantities. We focus on the direction parallel to the background magnetic field $\mathbf{B}_0$ (2.3.10). Equations (4.2.4) and (4.2.5) become respectively

$$\frac{\partial B_{1\parallel}}{\partial t} - \lambda_e^2 \nabla^2 \frac{\partial B_{1\parallel}}{\partial t} = \left[\mathbf{B}_0 \cdot \nabla u_{1\parallel} - B_0 (\nabla \cdot \mathbf{u}_1) \right] - \frac{1}{n_p q_p} \mathbf{B}_0 \cdot \nabla j_{1\parallel}, \tag{4.2.6}$$

$$\frac{4\pi}{c} \frac{\partial j_{1\parallel}}{\partial t} - \frac{4\pi}{c} \lambda_e^2 \nabla^2 \frac{\partial j_{1\parallel}}{\partial t} = \mathbf{B}_0 \cdot \nabla \omega_{1\parallel} + \frac{1}{n_p q_p} \frac{c}{4\pi} \mathbf{B}_0 \cdot \left(\nabla^2 B_{1\parallel} \right) . \tag{4.2.7}$$

The linearized system of equations is Fourier-transformed in space and time, with dependencies

$$A(x,y,t) = A' \exp\left\{ i \left[k_\parallel y \sin\varphi + k_{\perp,2} y \cos\varphi + k_{\perp,1} x - \omega t \right] \right\}.$$

The dispersion relation in these conditions yields

$$\left\{ 1 + \lambda_e^2 k^2 - \frac{v_A^2 k_\parallel^2}{\omega^2} \right\} \times \left\{ \left[1 + \lambda_e^2 k^2 \right] \left[\frac{\omega^2}{v_A^2 k^2} - \frac{n_p T_p}{v_A^2} \right] - \left[1 - \frac{k_\parallel^2 n_p T_p}{\omega^2} \right] \right\} = \frac{v_A^2 k_\parallel^2}{\omega^2} \left\{ \frac{\omega^2}{\Omega_p^2} - \frac{n_p T_p k^2}{\Omega_p^2} \right\}. \tag{4.2.8}$$

By introducing the proton inertial length λ_p in the wavenumbers, it is found that the ratio $\lambda_e^2/\lambda_p^2 = m_e/m_p$. Thus, all of the terms involving the electron inertial length are neglected. Other approximations are introduced [130]. The limit of quasi-perpendicular propagation, $|k_x| \gg |k_y|$. This condition implies that $|k_{\perp,1}| \gg \left|k_\parallel\right|, |k_{\perp,2}|$. Therefore, $k^2 \simeq k_x^2$. Because of the order of magnitude of the frequencies we are working with, $|\omega| \ll \Omega_p$. Thus, the dispersion relation (4.2.8) leads to the frequency for KAWs in the two-fluid model,

$$\omega_{\mathrm{KAW}} = v_A k_\parallel \sqrt{1 + \frac{k_x^2 v_A^2}{2\Omega_p^2} \beta_p}, \tag{4.2.9}$$

where $\beta_p = 2 n_p T_p / v_A^2$. In this calculation, the effect of the electron temperature has been neglected. The group velocity is obtained by evaluating the gradient of the

frequency ω_{KAW} (4.2.9) in wave-vector space,

$$\mathbf{v}_{g,\text{KAW}} = \nabla_{\mathbf{k}}\omega_{\text{KAW}} = \omega_{\text{KAW}}\left\{\frac{1}{1+\frac{k_x^2 v_A^2}{2\Omega_p^2}\beta_p}\frac{k_x v_A^2}{2\Omega_p^2}\beta_p\widehat{\mathbf{x}} + \frac{1}{k_y}\widehat{\mathbf{y}}\right\}. \tag{4.2.10}$$

4.2.2 Vlasov-Maxwell Approach

The plasma is collisionless and magnetized with background field (2.3.10). Protons and electrons are assumed to have Maxwellian distribution equilibrium functions $f_{0s}(\mathbf{v})$ (3.2.12) with homogeneous densities and temperatures. The Vlasov-Maxwell system (3.1.7)–(3.1.13) is perturbed to first order with respect to the equilibrium configuration, and Fourier-Laplace transformed considering an adiabatically perturbed system [107]. The system of equations is then reduced to the form [132]

$$\check{\mathbf{D}}(\omega,\mathbf{k})\cdot\delta\mathbf{E}_1 = 0, \tag{4.2.11}$$

where $\delta\mathbf{E}_1$ are first order perturbations of the electric field in Fourier-Laplace variables, and $\check{\mathbf{D}}$ is the dielectric tensor, which contains the dispersion properties of the plasmas as functions of the complex frequency $\omega = \omega_r + i\gamma$, and the wave-vector $\mathbf{k}$. We are interested in the limit of quasi-perpendicular propagation, $|k_{\perp,1}| \gg \left|k_{\parallel}\right|, |k_{\perp,2}|$ and zero flux parallel to $\mathbf{B}_0$ in the equilibrium state [132]. Also, the limit of small frequencies is considered, $|\omega| \ll \Omega_s$. Following Lysak and Lotko [129], these approximations lead to a decoupled fast mode. Further approximations are non-relativistic fluctuations, $v_A^2/c^2 \ll 1$, and large parallel wavenumbers, $k_{\parallel}^2\lambda_{\text{De}}^2 \ll 1$, where $\lambda_{\text{De}} = v_{\text{the}}/2\omega_{pe}$ is the electron Debye length. This reduces the dielectric

tensor to

$$\begin{bmatrix} \frac{c^2}{v_A^2}\frac{1}{b_p}\left[1-e^{-b_p}I_0\left(b_p\right)\right]-\frac{k_\parallel^2 c^2}{\omega^2} & \frac{k_\parallel k_{\perp,1}c^2}{\omega^2} \\ \frac{k_\parallel k_{\perp,1}c^2}{\omega^2} & \frac{e^{-b_e}}{k_\parallel^2\lambda_{\mathrm{D}}^2}I_0\left(b_e\right)\left[1+\zeta_e Z(\zeta_e)\right]-\frac{k_{\perp,1}^2c^2}{\omega^2}, \end{bmatrix}$$

where $b_s = k_x^2\rho_s^2/2$, $\rho_s = v_{\mathrm{th}s}/\Omega_s$ is the Larmor radius of the species s, $\zeta_e = \omega/k_\parallel v_{\mathrm{th}e}$ is the resonance factor, I_0 is the modified Bessel function of order zero, and Z is the plasma dispersion function [133]. Non-trivial solutions of waves are obtained for zero determinant in the matrix representation of the dielectric tensor. This is reduced to the following dispersion relation,

$$\frac{\omega^2}{v_A^2 k_\parallel^2} = \frac{1}{2}\frac{\lambda_e^2}{\lambda_p^2}\frac{\beta_e\lambda_p^2 k_x^2}{\left[1+\zeta_e Z\left(\zeta_e\right)\right]e^{-b_e}I_0\left(b_e\right)} + \frac{b_p}{1-e^{-b_p}I_0\left(b_p\right)}. \tag{4.2.12}$$

In the conditions we are interested in this research, we consider the limits of small particle Larmor radii, $b_e \ll b_p \ll 1$, for which $e^{-b_e}I_0(b_e) \approx 1$ and $b_p/[1-e^{-b_p}I_0(b_p)] \approx 1 + 3b_p/4$. Finally, we evaluate the limit of zero electron mass. Thus, the KAWs frequency is obtained,

$$\omega_{\mathrm{KAW}} = v_A k_\parallel \sqrt{1+\frac{3}{8}\frac{k_x^2 v_A^2}{\Omega_p^2}\beta_p}. \tag{4.2.13}$$

We note that the frequencies (4.2.9) and (4.2.13) differ by a factor 3/4 in the transverse wavenumber k_x inside the square root. The group velocity associated

with this frequency is

$$\mathbf{v}_{g,\mathrm{KAW}} = \omega_{\mathrm{KAW}} \left\{ \frac{1}{1+\frac{3}{8}\frac{k_x^2 v_A^2}{\Omega_p^2}\beta_p} \frac{3}{8} \frac{k_x v_A^2}{\Omega_p^2} \beta_p \widehat{\mathbf{x}} + \frac{1}{k_y} \widehat{\mathbf{y}} \right\}.$$

4.2.3 Properties of KAWs

Research based on theoretical predictions of first-order perturbative kinetic and fluid approaches allows us to investigate the properties of KAWs. Kinetic Alfvén waves are labeled as quasi-electrostatic modes due to the development of an electrostatic electric field along the wave-vector direction [130, 134] as small-scale fluctuations are developed in the direction transverse to the wave-vector. This is quantified by the ratio R_E

$$R_E = \frac{\langle |\mathbf{k} \times \delta\mathbf{E}_\mathbf{k}| \rangle_\mathbf{k}}{\langle |\mathbf{k} \cdot \delta\mathbf{E}_\mathbf{k}| \rangle_\mathbf{k}}, \tag{4.2.14}$$

where $\langle \ldots \rangle_\mathbf{k}$ is the wave-vector average, with the Fourier transform obtained on a specific space domain. This ratio compares the electric field component induced by charge separation ($\mathbf{k} \cdot \delta\mathbf{E}_\mathbf{k}$) against the component related to electromagnetic induction ($\mathbf{k} \times \delta\mathbf{E}_\mathbf{k}$). The magnetic compressibility is measured by the ratio

$$C_B = \frac{\left\langle \delta B_\parallel^2 \right\rangle}{\langle \delta B^2 \rangle}, \tag{4.2.15}$$

where $\langle \ldots \rangle$ is space average on a specific domain, and $\delta B^2 = \delta B_\parallel^2 + \delta B_{\perp,1}^2 + \delta B_{\perp,2}^2$. This ratio is the order of $10^{-3} - 10^{-1}$ [134] for highly oblique wave-vector ($\theta \geq 80^\mathrm{o}$). This ratio is in the order of the unity for the Kinetic Slow mode and the whistler

mode for the same range of wavenumbers.

Kinetic Alfvén waves are characterized for having right-hand polarization in the plasma physics sense [135] for β_p in the range of values of interest ($\beta_p \sim 10^{-2}$) and for highly oblique wave-vector ($|k_{\perp,1}| \gg |k_{\parallel}|$) [136–138]. The wave polarization is related to the magnetic helicity σ_m [139],

$$\sigma_m = \delta \mathbf{A}_{\mathbf{k}} \cdot \delta \mathbf{B}_{\mathbf{k}}, \tag{4.2.16}$$

where $\mathbf{A}$ is the magnetic potential. This quantity provides information about the helical structure of the electromagnetic fields of the waves in space with respect to the wave-vector direction. For $\sigma_m > 0$ means left-hand helicity whereas $\sigma_m < 0$ means right-hand helicity. This is illustrated in Fig. 4.1. The sign of the magnetic

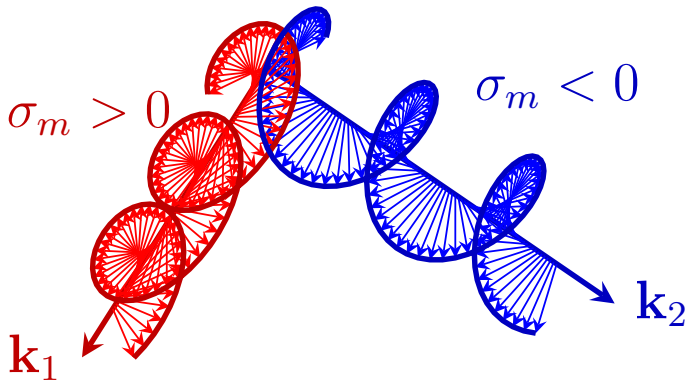

Figure 4.1: Scheme of two circularly-polarized waves having left-hand helicity (red wave $\sigma_m > 0$), and right-hand helicity (blue wave, $\sigma_m < 0$), with their respective wave-vectors.

helicity σ_m also provides the orientation of the rotation depending on the direction of propagation $\mathbf{k}$ and on the background magnetic field $\mathbf{B}_0$. Right-hand polarized

waves follow the signature $\sigma_m > 0$ for forward propagation ($\mathbf{k}\cdot\mathbf{B}_0 > 0$), and $\sigma_m < 0$ for backward propagation ($\mathbf{k}\cdot\mathbf{B}_0 < 0$) [135, 138, 140]. Normalized cross-correlations σ_c show correlations between the magnetic field and bulk-velocity of protons [135, 139],

$$\sigma_c = \frac{2\mathrm{Re}\left\{\delta\mathbf{u}_{p\mathbf{k}}\cdot\delta\mathbf{b}^*_{\mathbf{k}}\right\}}{\left|\delta\mathbf{u}_{p\mathbf{k}}\right|^2 + \left|\delta\mathbf{b}_{\mathbf{k}}\right|^2}, \tag{4.2.17}$$

where $\delta\mathbf{b}_{\mathbf{k}} = \delta\mathbf{B}_{\mathbf{k}}/\sqrt{4\pi n_0 m_p}$. This quantity is characteristic of Alfvén waves, $\sigma_c = -1$ for forward propagation ($\sigma_c = +1$ for backward propagation), and is inherited by KAWs for a broad range of wavenumbers [137, 139]. This means that proton bulk-velocity fluctuations and magnetic field fluctuations are anti-correlated in space. Other transport ratios are the proton compressibility [141],

$$C_p = \frac{\left|\delta n_{p\mathbf{k}}\right|^2}{\left|\delta\mathbf{B}_{\mathbf{k}}\right|^2}. \tag{4.2.18}$$

which measures the ratio of density fluctuations against magnetic fluctuations. Kinetic Alfvén waves have density fluctuations such that this ratio is in the range $\sim 10^{-2} - 1$ for $\beta_p \sim 10^{-2}$ [137]. This means that KAWs exhibit density fluctuations that are smaller or in the order of the magnetic fluctuations. Another ratio is the Alfvén ratio r_{Alfven} [137, 142],

$$r_{\mathrm{Alfven}} = \frac{\left|\delta\mathbf{u}_{p\mathbf{k}}\right|^2}{\left|\delta\mathbf{B}_{\mathbf{k}}\right|^2}. \tag{4.2.19}$$

This quantity measures the magnitudes of bulk-velocity fluctuations against magnetic field fluctuations. Alfvén waves and KAWs are characterized by a value $r_{\mathrm{Alfven}} = 1$ for a wide range of values of β_p [137]. This ratio is used to distinguish

Alfvénic fluctuations from other modes [143].

Chapter 5
Equations, Discretization, Numerical Algorithms, and Parameters

5.1 System of Equations

We choose a PIC-hybrid model, because we are focused on the low-frequency kinetics of protons while ignoring further details of the electrons dynamics.

This model is collisionless. Although collisions are much more frequent in a coronal plasma than in the solar wind [106], the order of magnitude of the electromagnetic scales (Larmor radii and inertial lengths) remains much smaller than the collisional ones (discussion in subsection 2.1). Non-thermal features may arise in the coronal plasma, such as thermal anisotropies, suprathermal particles, and beams [80, 144]. Thus, we choose a kinetic model.

Furthermore, since we are interested in the transition from MHD phenomena to kinetic phenomena, proton kinetics becomes relevant. Accordingly, the scales we consider are far from the scales where electron kinetics becomes relevant. Thus, we choose hybrid model.

The kinetic component can be modeled through a particle model (PIC, particle equations of motion) or a distribution function model (Vlasov equation). The numerical resolution of the Vlasov equation introduces an object that has dimensions $N_x \times N_y \times N_{v_x} \times N_{v_y} \times N_{v_z}$ at each iteration, which is computationally demanding. It

is more convenient to solve the equations of motion for each particle composing the plasma for positions x, y, and velocities v_x, v_y, v_z. With regard of the distribution function, this quantity is necessary to analyze the plasma kinetically. This object is not solved directly by a PIC model, but it can be constructed approximately from particle data. Therefore, we choose a PIC model for the kinetic component.

The PIC-hybrid model in 2 spatial dimensions and 3 velocity dimensions [48, 64–67, 145–147] consists of a kinetic component modeled as individual particles distributed on a discretized spatial grid. Particles are moved by the Lorentz force (in CGS units).

$$\frac{\mathrm{d}\mathbf{r}_s}{\mathrm{d}t} = \mathbf{v}_s, \tag{5.1.1}$$

$$\frac{\mathrm{d}\mathbf{v}_s}{\mathrm{d}t} = \frac{q_s}{m_s}\left[\mathbf{E}\left(\mathbf{r}_s, t\right) + \frac{\mathbf{v}_s \times \mathbf{B}\left(\mathbf{r}_s, t\right)}{c}\right], \tag{5.1.2}$$

where the electromagnetic fields are evaluated at the particle position $\mathbf{r}_s$. The electric and magnetic fields are self-consistent with the particle dynamics. The second component of the model is given by the fluid electron momentum Equation (2.3.2) and assuming an isotropic stress tensor without shear or viscous effects,

$$n_e m_e \frac{\mathrm{d}\mathbf{u}_e}{\mathrm{d}t} = q_e n_e \left[\mathbf{E} + \frac{\mathbf{u}_e \times \mathbf{B}}{c}\right] - \nabla p_e. \tag{5.1.3}$$

The electron density n_e is obtained by introducing the condition of quasi-neutrality (2.3.4), $n_e = n_p$. With regard of time-scales, the electrons dynamics occur on time scales much shorter than those of protons (see subsection 2.3.3), due to the mass difference with protons, $m_e/m_p = 5.44662 \times 10^{-4} \ll 1$. Thus, we neglect the contribution of the electron mass.

Since electrons respond faster compared with the proton time-scales, they rapidly achieve equilibrium. This implies that any possible gradient of electron temperature is rapidly relaxed. Electrons heat conduction is fast [105]. Due to quasi-neutrality, the electrons density evolves in a time-scale in the order of proton time scales. Thus, electron compression is slower than the thermal conduction. Accordingly, electron temperature is set as uniform (adiabatic heating involves the opposite scale-ordering) [105], and following the isothermal closure relation (2.3.5), $p_e = n_e T_e$. For the scales of interest, energy variations are not expected to affect electrons. Therefore, the electron temperature is set as constant in time.

By introducing the Ampère-Maxwell law without the displacement current, and in the limit of zero electron mass, Equation (5.1.3) can be used to model the electric field,

$$\mathbf{E} = -\frac{1}{q_e n_e}\left\{\frac{1}{c}\left[\nabla \times \mathbf{B} - \mathbf{j}_i\right] \times \mathbf{B}\right\} + \frac{T_e}{q_e n_e}\nabla n_e, \tag{5.1.4}$$

where $\mathbf{j}_i$ is the ionic density current obtained as

$$\mathbf{j}_i = \sum_{s,\,\text{ions}} \mathbf{j}_s = \sum_{s,\,\text{ions}} q_s n_s \mathbf{u}_s.$$

This equation is entirely defined on the spatial grid. In this assumption, electrons respond instantaneously in the time-scales we consider in the simulations. Finally, the model requires the induction law (8.2.11) for the evolution of the magnetic field having the electric field (5.1.4).

5.2 Discretization of the Equations

The discretization and general implementation of the Equations (5.1.1), (5.1.2), and (5.1.4) is presented and fundamented. The discretized equations are solved for a time-step $\Delta\bar{t}$. The spatial domain is defined in the plane xy, given the lengths of the system, L_x and L_y. The domain is discretized into $N_x \times N_y$ cells, where N_x is the number of cells along x and N_y is the number of cells along y.

The number of spatial cells, the size of the domain, and the time-step must obey the CFL condition [148]. For a 2D setting, this condition is given by

$$v_A^2 \Delta t^2 \left[\frac{1}{\Delta x^2} + \frac{1}{\Delta y^2} \right] \leq 1, \tag{5.2.1}$$

where v_A is the Alfvén speed. This condition comes from the discretization of the wave equation [148, 149]. In this case, it is a wave propagating at the Alfvén speed. Here, $\Delta x = L_x/N_x$ and $\Delta y = L_y/N_y$. Physically, this condition requires that the time-step is capable of solving the time-scales that can develop in the system [149]. Otherwise, non-physical fluctuations may grow [148].

The space discretization is schematized in Figure 5.1. Particles move and field quantities are defined on each cell of the grid (blue cells, physical grid). They are defined from cell 1 to N_x or N_y. In order to handle boundary conditions, *ghost* cells (gray cells) are defined around the physical grid. These cells have indices 0, $N_x + 1$, and $N_y + 1$. Therefore, all of the grid-defined arrays have $N_x + 2 \times N_y + 2$ components.

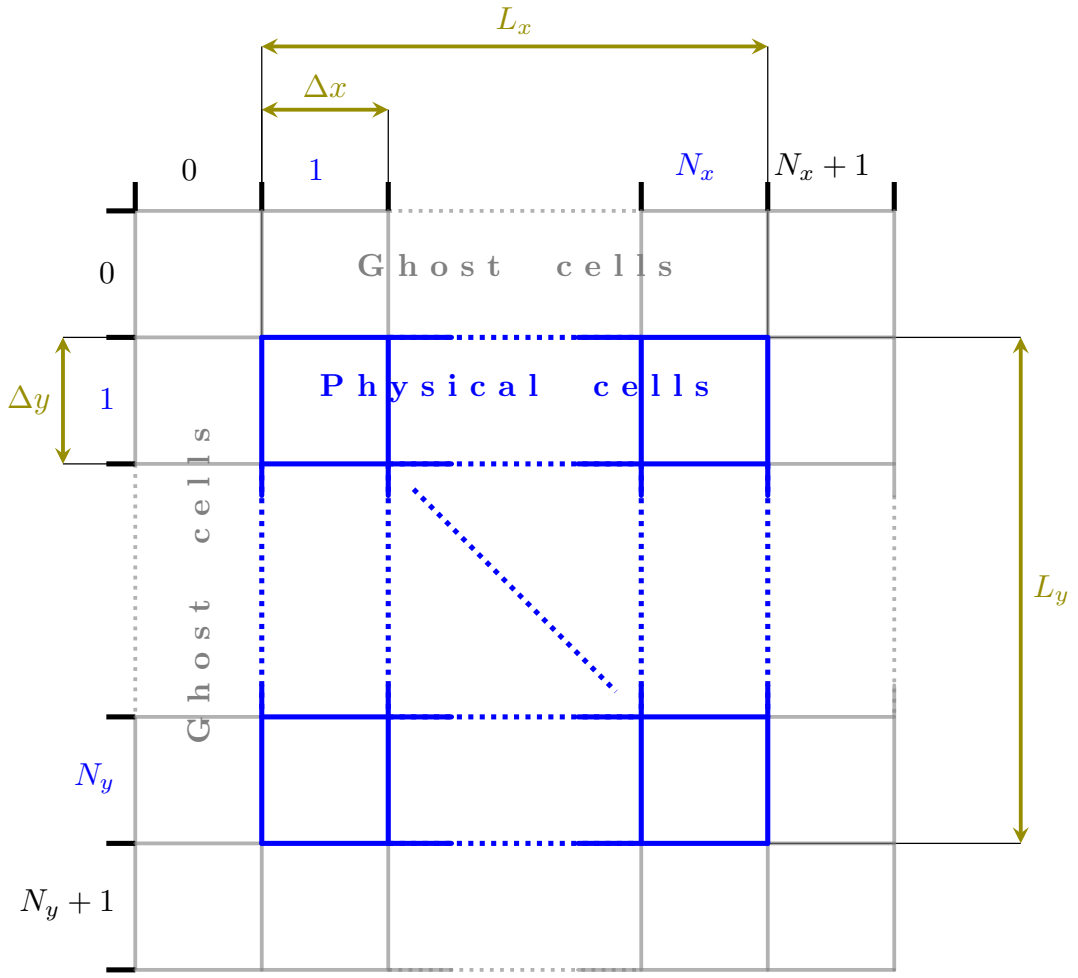

Figure 5.1: Scheme of the space discretization used in the simulation. Physical cells are shown in blue (indices 1 to N_x, and 1 to N_y). Ghost cells, used to handle boundary conditions, are shown in gray (indices 0, $N_x + 1$, and $N_y + 1$). Cell widths and length domains are indicated (green).

5.2.1 Normalization of Variables

This research works with non-dimensional variables. For this purpose, we introduce the following normalizations

- Particle charge q_s is normalized with the proton charge q_p, $\overline{q}_s \equiv q_s/q_p$.
- Particle mass m_s is normalized with the proton mass, $\overline{m}_s \equiv m_s/m_p$.
- Time t, time-step, frequencies ω, ω_r, damping/growth rates γ are normalized with the proton cyclotron frequency $\Omega_p = q_p B_0/m_p c$, $\bar{t} \equiv \Omega_p t$, $\Delta\bar{t} \equiv \Omega_p \Delta t$, $[\overline{\omega}, \overline{\omega}_r, \overline{\gamma}] \equiv [\omega, \omega_r, \gamma]/\Omega_p$.
- Particle density with the total ionic density $n_0 \equiv \sum_{s,\,\text{ions}} n_{0s} m_s/m_p$, $\overline{n}_p \equiv n_p/n_0$. A similar normalization is used for the mass density, $\rho_0 \equiv m_p n_0$.
- Particle velocities and bulk-velocity components are normalized with the Alfvén speed $v_A = B_0/\sqrt{4\pi n_0 m_p}$, $\overline{v}_j \equiv v_j/v_A$, $\delta\overline{u}_{pj} \equiv \delta u_{pj}/v_A$. Here, j is a specific component of the vector.
- Position, lengths, and wave-vectors are normalized with the proton inertial length $\lambda_p \equiv v_A/\Omega_p$, $\overline{\mathbf{r}} \equiv \mathbf{r}\Omega_p/v_A$, $\overline{L} \equiv L\Omega_p/v_A$, $\overline{\mathbf{k}} \equiv \mathbf{k} v_A/\Omega_p$.
- Magnetic field components are normalized with respect to the background magnetic field B_0, $\overline{B}_j \equiv B_j/B_0$.
- Electric field components are normalized with respect to the factor $v_A B_0/c$, $\overline{E}_j \equiv E_j c/B_0 v_A$.
- Temperatures are normalized with the factor $B_0^2/4\pi n_0$, $\overline{T}_{pj} \equiv 4\pi n_0 T_{pj}/B_0^2$.

For the sake of completeness of the quantities we use in this research, we define thermal speed of the species s as $v_{\text{th}s} = \sqrt{2T_s/m_s}$, and the parameter β of the species s as follows, $\beta_{sj} = 8\pi n_s T_{sj}/B_0^2$. For convenience, we introduce the parameter β_e in with the density n_0 as $\beta_e = 8\pi n_0 T_e/B_0^2$ in the equations of motion. This is noted because we use the hypothesis of quasi-neutrality in the PIC-hybrid equations, and the electron density is not uniform.

5.2.2 Shape Functions, Moments of the Distribution Function, and Source Terms

In principle, it is possible to define the kinetic species as point-particles via a distribution of finite N_p particles on the discretized spatial domain [147]

$$f(\mathbf{r}, \mathbf{v}, t) = \sum_{i=1}^{N_p} \delta\left[\mathbf{r} - \mathbf{r}_i(t)\right] \delta\left[\mathbf{v} - \mathbf{v}_i(t)\right].$$

The number of particles N_p in an actual plasma is in the order of the Avogadro number. This is not computationally feasible. Therefore, a reduced number of particles N_p is used. The use of such a distribution may lead to spatial discontinuities due to the possibility of empty cells or abrupt spatial variations in particle densities between cells. Such discontinuities lead to a noisy distribution and divergent fields, introducing effects caused by the very discrete nature of the particles [147, 148]. To avoid such problems, articles are defined with finite size, physically representing a cloud of particles or a macro-particle.

Macro-particles are defined by shape functions S, which are evaluated at a position $\mathbf{r}$ on the grid, given the position $\mathbf{r}_i$ of the macro-particle i, $S = S(\mathbf{r} - \mathbf{r}_i)$. Typically, shape functions are piecewise and defined by polynomials of degree n. The

larger n is, the more the numerical noise on the densities and fields is reduced [148]. However, it requires a larger number of evaluations and a higher consumption of computational resources per macro-particle. Nevertheless, noise is still generated in the simulation. In one spatial dimension, the shape functions are defined as $S_x = S_x(x - x_i)$. For higher dimensions, is possible to use multilinear shape functions. In particular, for two dimensions [148, 150],

$$S(\mathbf{r} - \mathbf{r}_i) \equiv S_x(x - x_i) S_y(y - y_i). \tag{5.2.2}$$

Shape functions are defined in such a way that the integration over the spatial domain yields $\int S(\mathbf{r} - \mathbf{r}_i) \mathrm{d}^2 r = 1$. They are used to compute the moments of the distribution function of the species s by interpolating the particle contribution at a position $\mathbf{r}_i$ to the closest grid cell at $\mathbf{r}$. This is achieved as follows,

$$n_s(\mathbf{r}) = F_s \sum_{j=1}^{N_p/N_s} S\left(\mathbf{r} - \mathbf{r}_{js}\right), \tag{5.2.3}$$

$$\mathbf{u}_s(\mathbf{r}) = \frac{F_s}{n_s(\mathbf{r})} \sum_{j=1}^{N_p/N_s} S\left(\mathbf{r} - \mathbf{r}_{js}\right) \mathbf{v}_{js}, \tag{5.2.4}$$

$$T_{ls}(\mathbf{r}) = \frac{1}{2} m_s \frac{F_s}{n_s(\mathbf{r})} \sum_{j=1}^{N_p/N_s} S\left(\mathbf{r} - \mathbf{r}_{js}\right) \left[v_{l,js} - u_{l,s}(\mathbf{r})\right]^2, \tag{5.2.5}$$

where F_s is a normalization factor which considers the number of particles per cell,

$$F_s = \frac{1}{\max\left[\Pi_s(\mathbf{r})\right]} \frac{n_{0s}}{\sum_{l,\,\mathrm{ions}} m_l n_{0l}}, \tag{5.2.6}$$

where Π_s is the unnormalized particle density,

$$\Pi_s(\mathbf{r}) = \sum_{j=1}^{N_p/N_s} S\left(\mathbf{r} - \mathbf{r}_{js}\right),$$

and the factor involves the maximum number of particles per cell. This factor is necessary in inhomogeneous plasmas, in order to have the correct particle density per species. In the case of homogeneous plasmas, this term is reduced to

$$\max\left[\Pi_s\right] = \frac{N_p/N_s}{N_x N_y},$$

where N_s is the number of species in the plasma.

The source terms are the ionic charge and current densities, ρ_c and $\mathbf{j}_i$, respectively. They are also computed via the shape functions.

$$\rho_c(\mathbf{r}) = \sum_{s,\,\text{ions}}^{N_s} q_s F_s \sum_{j=1}^{N_p/N_s} S\left(\mathbf{r} - \mathbf{r}_{js}\right), \tag{5.2.7}$$

$$\mathbf{j}_i(\mathbf{r}) = \sum_{s,\,\text{ions}}^{N_s} q_s F_s \sum_{j=1}^{N_p/N_s} S\left(\mathbf{r} - \mathbf{r}_{js}\right) \mathbf{v}_{js}. \tag{5.2.8}$$

In this research, we use shape functions of order $n = 2$, requiring 3 nodes in one dimension. For the macro-particle j of the species s we have

$$S_x(x - x_{js}) = \begin{cases} \dfrac{1}{2}\left(\dfrac{3}{2} - \xi_{js}\right)^2, & -\dfrac{3}{2} \le \xi_{js} < -\dfrac{1}{2}, \\ \dfrac{3}{4} - \xi_{js}^2, & -\dfrac{1}{2} \le \xi_{js} < \dfrac{1}{2}, \\ \dfrac{1}{2}\left(\dfrac{3}{2} + \xi_{js}\right)^2, & \dfrac{1}{2} \le \xi_{js} \le \dfrac{3}{2}, \end{cases} \tag{5.2.9}$$

where $\xi_{js} = (x_{js} - x)/\Delta x$, being x_{js} the position of the center of the macro-particle and x is the position of the center of a cell. This is illustrated in Fig. 5.2. A macro-particle at x_p on the grid-axis x interpolates a physical quantity via the function S to the center of the cells the macro-particle spans (black dots and dash-dotted black lines). Considering the 2D shape function (5.2.2), the shape function we use in our research is symmetric and involves 9 cells.

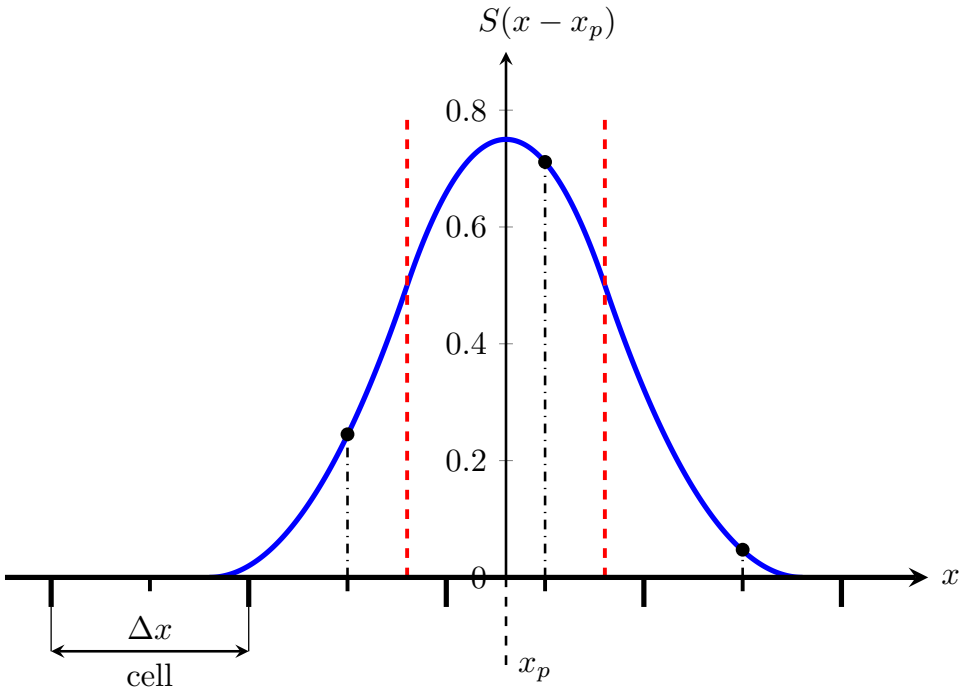

Figure 5.2: Scheme of shape function of order 2 (blue) on the domain x of a particle with position x_p. Cells limits and middle points are indicated. Black dash-dotted lines indicate the value of the shape function associated to a cell. Red dashed lines indicate the nodes of the piece-wise function (5.2.9).

5.2.3 Initialization

Inhomogeneous Density Profile

The initial distribution of particles following an arbitrary mass density profile $\rho_{0p} = \rho_{0p}(x, y)$ is achieved by using a method typically used to load particles in the velocity dependency given a velocity distribution [147, 148]. First, particles are uniformly distributed along y. Then, for fixed positions y_0, the position x_i for the particle i is determined by making the relative number of particles R_i along x equal to the relative accumulative density. This is achieved by solving the equation

$$\frac{P_{0p}(x_i, y_0, 0)}{P_{0p}(L_x, y_0, 0)} = R_i, \tag{5.2.10}$$

where y_0 is a fixed section in y, and P_{0p} is the accumulative mass-density given by

$$P_{0p}(x_i, y_0, 0) = \int_0^{x_i} \rho_{0p}(x, y_0, 0)\mathrm{d}x. \tag{5.2.11}$$

In particular, Equation (5.2.10) is solved via the secant method. The ratio R_i ranges from 0 to 1, and is estimated as follows: For a fixed section y_0 along x, each particle is labeled with a number i in increasing order. The ratio R_i is then computed as the ratio between the number of the particle i and the total number of particles along x for fixed y_0.

Particle Distribution Function

For the initialization of the velocity dependency of the particle distribution (3.2.12), a pseudo-random number generator function is used to provide numbers with a

Gaussian distribution for the partcle velocities. In this way, a seed for the velocity magnitude of a particle at the position (x_0, y_0) within the space-domain is obtained straightforwardly from a Maxwellian distribution.

$$f = \sqrt{-\ln\left[F\left(\text{rand}\right)\right]}, \tag{5.2.12}$$

where F is the function providing pseudo-random numbers. The velocities are computed in the axes of the background magnetic field (2.3.10), because it requires the use of the thermal velocities at (x_0, y_0) using the temperature (2.3.11). Typically, distribution functions are characterized by thermal velocities defined with respect to the background magnetic field. The proton temperatures defined on the space grid are given by

$$\begin{aligned} T_{p\parallel}(x) &= \frac{B_0^2}{8\pi n_0}\frac{n_0}{n_p(x_0)}\left\{\beta_{0p} + \beta_{e0}\left[1 - \frac{n_p(x)}{n_0}\right]\right\}, \\ T_{p\perp}(x) &= T_{p\parallel}(x), \end{aligned}$$

due to the isotropic initialization. The grid-defined thermal speeds are

$$\overline{v}_{\text{th}p\parallel}(\overline{x}) = \sqrt{2\overline{T}_{p\parallel}(\overline{x})}, \tag{5.2.13}$$

$$\overline{v}_{\text{th}p\perp}(\overline{x}) = \overline{v}_{\text{th}p\parallel}(\overline{x}). \tag{5.2.14}$$

The thermal speeds at the position of the particle $(\overline{x}_0, \overline{y}_0)$ are interpolated via the shape functions (5.2.2) from the thermal speeds defined at the grid (5.2.13)

and (5.2.14).

$$\overline{v}_{\mathrm{thp}j}\left(\mathbf{r}_{is}\right) = \sum_{l,\,\mathrm{cells}}^{N_c} \overline{v}_{\mathrm{thp}j}(\overline{x}_l) S\left(\mathbf{r}_l - \mathbf{r}_{is}\right). \tag{5.2.15}$$

The combination of Equations (5.2.12) to (5.2.15) allows us to compute the magnitude of the particle velocities in the directions parallel and perpendicular for a particle at the position $(\overline{x}_0, \overline{y}_0)$. These numbers are strictly positive. The velocity components for the equilibrium are obtained by inserting sines and cosines of pseudo-random phases, θ_{random} and ϕ_{random}, as follows.

$$\overline{v}_{p\parallel} = \overline{v}_{\mathrm{thp}\parallel} f \cos\theta_{\mathrm{random}}, \tag{5.2.16}$$

$$\overline{v}_{p\perp,1} = \overline{v}_{\mathrm{thp}\perp} f \cos\phi_{\mathrm{random}}, \tag{5.2.17}$$

$$\overline{v}_{p\perp,2} = \overline{v}_{\mathrm{thp}\perp} f \sin\phi_{\mathrm{random}}. \tag{5.2.18}$$

Finally, the velocities (5.2.16) to (5.2.18) from each particle are rotated to the axes of the simulation, (x, y, z) via the inverse rotation matrix (A.1.5).

Initial Perturbation

The initial perturbation is set considering the bulk-velocity fluctuation caused by a superposition left- and right-hand polarized Alfvén waves (4.1.10). Considering that such fluctuations are feasible, we choose the perturbation in the component x, transverse to the background magnetic field (2.3.10) and fully contained in the plane of the simulation.

$$\delta\mathbf{u}_{px}(y) = u_0 \sin\left(k_{y0} y\right) \widehat{\mathbf{x}}, \tag{5.2.19}$$

where u_0 is the perturbative amplitude, and k_{y0} is the perturbed mode. The mode is chosen to involve the largest scales along y, therefore, $k_{y0} = 2\pi/L_y$. In order to implement the initial perturbation in Equation (5.2.19), it is necessary to add a drift to the particle velocities (5.2.16) to (5.2.18) based on the particle location. The perturbation is a grid-defined quantity. Therefore, the drift added to each particle velocity must be interpolated to the particle position using the shape functions (5.2.2),

$$\overline{\mathbf{u}}_{p0}\left(\mathbf{r}_{is}\right) = \sum_{l,\,\text{cells}}^{N_c} \overline{\mathbf{u}}_{p0}\left(\mathbf{r}_l\right) S\left(\mathbf{r}_l - \mathbf{r}_{is}\right). \tag{5.2.20}$$

5.2.4 Discretization of the Field Equations

The electromagnetic fields are solved by a 2D finite difference scheme. The Equations (5.1.4) and (8.2.11) are discretized in time in 2nd-order in the time-step. Given the initial magnetic field of the plasma and the initial density of the species, the corresponding electric field is obtained by the following equation. All of the quantities are normalized following subsection 5.2.1.

$$\overline{\mathbf{E}}(0) = \frac{1}{\overline{\rho}_c(0)}\left\{\left[\overline{\nabla}\times\overline{\mathbf{B}}(0) - \overline{j}_i(0)\right]\times\overline{\mathbf{B}}(0)\right\} - \frac{1}{2}\frac{\beta_e}{\overline{\rho}_c(0)}\overline{\nabla}\overline{\rho}_c(0).$$

Then, the following iterations are computed using the iterative Horowitz method [151]. The method is implicit in time, and uses a corrector-predictor approach [152] to solve the fields at each time-step. Given the electromagnetic fields for a time-step n, the fields for the time-step $n+1$ is obtained via iterations of the discretized equations (5.1.4) and (8.2.11). Auxiliary fields are used, which correspond to the fields at half time-step, $n+1/2$. The discretized equations are shown below. For an iteration

$k \geq 0$, the magnetic field is obtained via the induction law,

$$\overline{\mathbf{B}}_{n+1}^{(k)} = \overline{\mathbf{B}}_n - \Delta\bar{t}\overline{\nabla} \times \overline{\mathbf{E}}_{n+1/2}^{(k)}, \tag{5.2.21}$$

$$\overline{\mathbf{E}}_{n+1/2}^{(k)} = \frac{1}{2}\left[\overline{\mathbf{E}}_{n+1}^{(k)} + \overline{\mathbf{E}}_n\right]. \tag{5.2.22}$$

For $k = 0$, the algorithm defines $\mathbf{E}_{n+1}^{(0)} = \mathbf{E}_n$. For the advance of the electric field, we have the following equation,

$$\overline{\mathbf{E}}_{n+1}^{(k)} = \frac{2}{\overline{\rho}_{c,n+1/2}}\left\{\left[\overline{\nabla} \times \overline{\mathbf{B}}_{n+1/2}^{(k)} - \bar{j}_{i,n+1/2}\right] \times \overline{\mathbf{B}}_{n+1/2}^{(k)}\right\} - \frac{\beta_e}{\overline{\rho}_{c,n+1/2}}\overline{\nabla}\overline{\rho}_{c,n+1/2} - \overline{\mathbf{E}}_n, \tag{5.2.23}$$

$$\overline{\mathbf{B}}_{n+1/2}^{(k)} = \frac{1}{2}\left[\overline{\mathbf{B}}_{n+1}^{(k)} + \overline{\mathbf{B}}_n\right]. \tag{5.2.24}$$

The electromagnetic fields converge to the solution through successive iterations, taking the fields of the iteration k as a correction of the predicted in the iteration $k-1$. This is achieved with Equations (5.2.21) to (5.2.24). The method provides a good estimation of the fields by $4-9$ iterations [151]. In this research, we use 15 iterations. Note that the electromagnetic fields at the steps $n+1$ and $n+1/2$ vary with the iterations. The fields at the time-step n and the source terms are not modified. Periodic conditions are enforced in the calculation of the derivatives involved in the curl of the electric field, and by equating the fields with their opposite borders. This is applied to the fields after each calculation, including the half-step fields.

5.2.5 Discretization of the Spatial Partial Derivatives

Partial derivatives in space are computed by a centered, 4th order in $\Delta\overline{x}$ and $\Delta\overline{y}$ scheme using periodic boundary conditions. Given a grid of N nodes, the derivative of the array $\overline{A}$ at a node m such that $3 \leq m \leq N-2$ is given by

$$\frac{\partial \overline{A}(\overline{x}_m)}{\partial \overline{x}} = \frac{\overline{A}\left(\overline{x}_{m-2}\right) - 8\overline{A}\left(\overline{x}_{m-1}\right) + 8\overline{A}\left(\overline{x}_{m+1}\right) - \overline{A}\left(\overline{x}_{m+2}\right)}{12\Delta\overline{x}}. \tag{5.2.25}$$

For nodes m out of that range, the calculation is as follows.

$$\frac{\partial \overline{A}(\overline{x}_{N-1})}{\partial \overline{x}} = \frac{\overline{A}\left(\overline{x}_{N-3}\right) - 8\overline{A}\left(\overline{x}_{N-2}\right) + 8\overline{A}\left(\overline{x}_{N}\right) - \overline{A}\left(\overline{x}_{1}\right)}{12\Delta\overline{x}}, \tag{5.2.26}$$

$$\frac{\partial \overline{A}(\overline{x}_{N})}{\partial \overline{x}} = \frac{\overline{A}\left(\overline{x}_{N-2}\right) - 8\overline{A}\left(\overline{x}_{N-1}\right) + 8\overline{A}\left(\overline{x}_{1}\right) - \overline{A}\left(\overline{x}_{2}\right)}{12\Delta\overline{x}}, \tag{5.2.27}$$

$$\frac{\partial \overline{A}(\overline{x}_{1})}{\partial \overline{x}} = \frac{\overline{A}\left(\overline{x}_{N-1}\right) - 8\overline{A}\left(\overline{x}_{N}\right) + 8\overline{A}\left(\overline{x}_{2}\right) - \overline{A}\left(\overline{x}_{3}\right)}{12\Delta\overline{x}}, \tag{5.2.28}$$

$$\frac{\partial \overline{A}(\overline{x}_{2})}{\partial \overline{x}} = \frac{\overline{A}\left(\overline{x}_{N}\right) - 8\overline{A}\left(\overline{x}_{1}\right) + 8\overline{A}\left(\overline{x}_{3}\right) - \overline{A}\left(\overline{x}_{4}\right)}{12\Delta\overline{x}}. \tag{5.2.29}$$

The derivatives are also defined on the *ghost* cells for periodic boundary conditions.

$$\frac{\partial \overline{A}(\overline{x}_{N+1})}{\partial \overline{x}} = \frac{\partial \overline{A}(\overline{x}_{1})}{\partial \overline{x}},$$
$$\frac{\partial \overline{A}(\overline{x}_{0})}{\partial \overline{x}} = \frac{\partial \overline{A}(\overline{x}_{N})}{\partial \overline{x}}.$$

5.2.6 Discretization of the Particle Equations

The particle Equations (5.1.1) and (5.1.2) are solved using the Boris algorithm with gyrophase correction. This method is second-order in the time-step $\Delta\bar{t}$, non-

symplectic, and phase-space volume conservative [148, 153, 154]. The algorithm updates the velocity by splitting the advance by electric field forcing and magnetic field forcing into three steps: one advance by half-step with the electric field, a rotation with the magnetic field, and the remaining half-step with the electric field [148, 150]. Such splitting and ordering of the stages allows for the algorithm to be reversible in time, aside from numerical imprecisions [155]. For this purpose, we redefine the electromagnetic fields as

$$\mathbf{e}_s \equiv \frac{\Delta\bar{t}}{2}\frac{\overline{q}_s}{\overline{m}_s}\overline{\mathbf{E}},$$
$$\mathbf{b}_s \equiv \frac{\Delta\bar{t}}{2}\frac{\overline{q}_s}{\overline{m}_s}\overline{\mathbf{B}}.$$

for the advance of particles of the species s. Note that these fields are evaluated at the particle position. This is made by interpolating the electromagnetic fields at the position of the particle i of the species s, $\mathbf{r}_{is}$, by using the shape functions (5.2.2),

$$\overline{\mathbf{E}}\left(\mathbf{r}_{is}\right) = \sum_{l,\,\text{cells}}^{N_c} \overline{\mathbf{E}}\left(\mathbf{r}_l\right) S\left(\mathbf{r}_l - \mathbf{r}_{is}\right), \tag{5.2.30}$$

$$\overline{\mathbf{B}}\left(\mathbf{r}_{is}\right) = \sum_{l,\,\text{cells}}^{N_c} \overline{\mathbf{B}}\left(\mathbf{r}_l\right) S\left(\mathbf{r}_l - \mathbf{r}_{is}\right), \tag{5.2.31}$$

where N_c is the number of cells covered by the shape function representing a macro-particle and $\mathbf{r}_l$ is the position of a cell l in which the macro-particle is located. The shape functions in the field interpolations (5.2.30) and (5.2.31) is of the same order as that used in moments (5.2.3) to (5.2.5), and in the source terms (5.2.7) and (5.2.8). This choice avoids introducing non-physical effects such as particle self-forcing [148]. Given the electromagnetic fields, the velocity advance in a time-step for the velocity

of a particle i of the species s at the step $n-1/2$,

$$\overline{\mathbf{u}}_{si} = \overline{\mathbf{v}}_{si,n-1/2} + \mathbf{e}_{s,n}, \tag{5.2.32}$$

$$\overline{\mathbf{w}}_{si} = \overline{\mathbf{u}}_{si} + \mathbf{F}\left(\overline{\mathbf{u}}_{si}; \mathbf{b}_{s,n}\right), \tag{5.2.33}$$

$$\overline{\mathbf{v}}_{si,n+1/2} = \overline{\mathbf{w}}_{si} + \mathbf{e}_{s,n}, \tag{5.2.34}$$

where $\mathbf{F}$ is a function representing the rotation by the magnetic field forcing in a half-step. For the case of the gyrophase correction the rotation [154] is given by

$$\mathbf{F}\left(\overline{\mathbf{u}}_{si}; \mathbf{b}_{s,n}\right) = \frac{2}{1+\tan^2|\mathbf{b}_{s,n}|}\left[\overline{\mathbf{u}}_{si} + \overline{\mathbf{u}}_{si} \times \frac{\mathbf{b}_{s,n}}{|\mathbf{b}_{s,n}|}\tan|\mathbf{b}_{s,n}|\right] \times \frac{\mathbf{b}_{s,n}}{|\mathbf{b}_{s,n}|}\tan|\mathbf{b}_{s,n}|. \tag{5.2.35}$$

This rotation is an approximation to the exact rotation of the particle velocity during one time-step $\Delta\bar{t}$. A scheme is shown in Fig. 5.3. The magnetic forcing rotates the velocity by an angle $\theta = 2|\mathbf{b}_{s,n}|$ with unitary vector $\mathbf{b}_{s,n}/|\mathbf{b}_{s,n}|$, out of the plane (green in Fig. 5.3) of the velocity $\overline{\mathbf{u}}_{si}$ (blue in Fig. 5.3). The rotation is separated into two stages with angles $\theta/2$ [148, 153, 156]. The first stage rotates the vector $\mathbf{u}_{si}$ with magnitude $\tan|\mathbf{b}_{s,n}|$ (solid, black in Fig. 5.3),

$$\overline{\mathbf{u}}_{si}^{-} = \overline{\mathbf{u}}_{si} + \overline{\mathbf{u}}_{si} \times \frac{\mathbf{b}_{s,n}}{|\mathbf{b}_{s,n}|}\tan|\mathbf{b}_{s,n}|. \tag{5.2.36}$$

The second stage rotates $\overline{\mathbf{u}}_{si}^{-}$ to the vector $\overline{\mathbf{w}}_{si}$ (solid, red in Fig. 5.3) by obtaining the rotated vector $\mathbf{F}$ with magnitude $\sin 2|\mathbf{b}_{si}|$ (dash-dotted, red in Fig. 5.3). The vector $\overline{\mathbf{w}}_{si}$ is an approximation to the exact vector $\overline{\mathbf{w}}_{si}^{\text{exact}}$ (solid, dark red in Fig. 5.3).

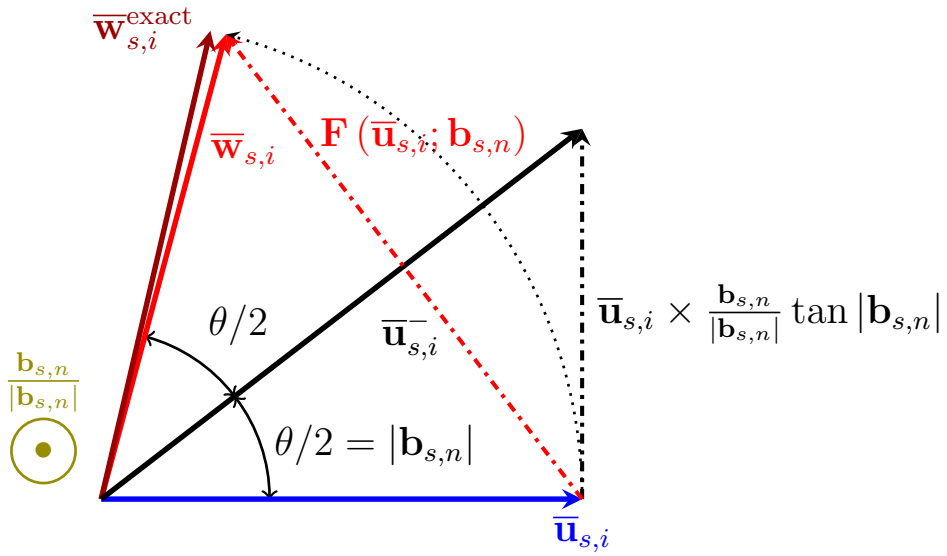

Figure 5.3: Scheme of the magnetic rotation of the velocity vector in the plane transverse to the normalized, local magnetic field $\mathbf{b}_{n,s}$ of the Boris algorithm with gyrophase correction. Intermediate vectors and rotations in Equations (5.2.32), (5.2.33), (5.2.35), and (5.2.36) are shown.

By using the trigonometrical identity,

$$\sin 2\,|\mathbf{b}_{s,n}| = \frac{2\tan|\mathbf{b}_{s,n}|}{1+\tan^2|\mathbf{b}_{s,n}|}.$$

Equation (5.2.35) is obtained, completing the rotation by magnetic field forcing. Finally, the position advance is made with the velocity $\overline{\mathbf{v}}_{si,n+1/2}$ from the position $\overline{\mathbf{r}}_{si,n}$ to $\overline{\mathbf{r}}_{si,n+1}$,

$$\overline{\mathbf{r}}_{si,n+1} = \overline{\mathbf{r}}_{si,n} + \Delta\bar{t}\overline{\mathbf{v}}_{si,n+1/2}. \tag{5.2.37}$$

The property of phase-space volume conservation leads to bounded variations in

the total energy in a conservative system. The Boris algorithm in Equations (5.2.32), (5.2.33), (5.2.34), and (5.2.37), can be defined as a one-step map $\psi_B : \mathbf{z}_k \equiv \left(\overline{\mathbf{r}}_k, \overline{\mathbf{v}}_{k-1/2}\right) \rightarrow \mathbf{z}_{k+1} \equiv \left(\overline{\mathbf{r}}_{k+1}, \overline{\mathbf{v}}_{k+1/2}\right)$ [153]. The properties of non-symplecticity and phase-space volume conservation can be deduced from the Jacobian matrix of the map ψ_B, $\partial\psi_B/\partial\mathbf{z}_k$. This matrix does not verify

$$\left[\frac{\partial\psi_B}{\partial\mathbf{z}_k}\right]^T \mathbf{J} \left[\frac{\partial\psi_B}{\partial\mathbf{z}_k}\right] = \mathbf{J},$$

where $\mathbf{J}$ is the 6×6 symplectic matrix, given by

$$\mathbf{J} = \begin{bmatrix} \mathbf{0} & \mathbb{I} \\ -\mathbb{I} & \mathbf{0} \end{bmatrix},$$

with $\mathbf{0}$ being a 3×3 matrix of zeros, and $\mathbf{I}$ being a 3×3 identity matrix. Therefore, the map is not symplectic at each time-step. However, the determinant of the transformation is equal to the unity, so that the phase-space volume is conservative for each time-step, although it is not symplectic [153].

5.2.7 Digital Filter

As mentioned in subsection 5.2.2, a PIC code introduces intrinsecal numerical noise due to the discreteness of the particles. Without control, noise may grow to large amplitudes and dominate the dynamics of the simulation at the expense of the actual physical processes. This issue can be minimized by **(i)** increasing the order of the shape functions, **(ii)** applying filters to grid-defined quantities, or **(iii)** increasing the number of particles per cell.

In this subsection we focus on the specific use of digital filters applied to the

source terms, the charge density (5.2.7) and the current density (5.2.8). The choice is made based on using less computationally demanding methods.

Source terms are filtered with the purpose of reducing the numerical noise, smoothing the quantities, and for compensation [148]. Smoothing reduces the amplitudes of small-scale fluctuations caused by numerical noise. However, this may affect quantities at large scales, eliminating actual physical processes of the simulation. Thus, compensation is used to reduce this effect. In order to discuss the filtering, we consider a one-dimensional, grid-defined quantity $\Phi(x)$ at a cell j with characteristic weight W constant [148]. Generally, a filter may be defined with several nodes. For the sake of brevity, we focus only on the filter used in this research, a three-node filter,

$$\Phi^{\text{filtered}}(x_j) = \frac{W\Phi\left(x_{j-1}\right) + \Phi\left(x_j\right) + W\Phi\left(x_{j+1}\right)}{1+2W}. \tag{5.2.38}$$

The filter (5.2.38) is symmetric for momentum conservation. The filter is Fourier-transformed to obtain the coefficients W, considering that the system has periodic boundary conditions.

$$\Phi^{\text{filtered}}(k) = \left[\frac{1+2W\cos\left(k\Delta x\right)}{1+2W}\right]\Phi(k) \equiv \ M_W(k\Delta x)\Phi(k).$$

The value $W = 1/2$ leads to an attenuation of order $\mathcal{O}\left[(k\Delta x)^2\right]$, and decays to zero as the argument of the cosine tends to π, which means that small scales are reached. Therefore, small-scale numerical noise is reduced from the simulation. The smoothing filter M_W can be applied several times to the quantity Φ.

To eliminate the residual order of the attenuation, a final compensation filter, M_{W_c} is applied after N successive applications of the smoothing filter. The compen-

sator has the same functional form M_W.

$$\Phi^{\text{fc}}(k) = M_{W_c} M_W^N \Phi(k). \tag{5.2.39}$$

The coefficient of the compensator W_c depends on N. It is obtained by expanding the resulting numerator of the filters with compensation in Taylor series. Here, W_c is the value that eliminates the second order term in $k\Delta x$. For this research, we use $N = 5$, leading to $W_c = -5/14$. We apply the filters for quantities defined on a 2D grid as

$$M_W = \frac{W\Phi\left(x_j, y_{l-1}\right) + W\Phi\left(x_{j-1}, y_l\right) + 2\Phi\left(x_j, y_l\right) + W\Phi\left(x_{j+1}, y_l\right) + W\Phi\left(x_j, y_{l+1}\right)}{2\left(1 + 2W\right)}, \tag{5.2.40}$$

centered at a node $[x_j, y_l]$. We note that this filter can be improved. Birdsall and Langdon [148] develops a 2D formalism which also includes the corner cells around the center. Not just the side cells. We currently do not have an estimation of the difference in applying that filter compared to the one in Equation (5.2.40).

5.3 Spectral Analysis

5.3.1 Damping Time-rate from Simulations

In order to compute the damping time-rate from simulation data, it is necessary to estimate the oscillation frequency $\omega_{\text{SIM}}/\Omega_p$, and the damping rate γ/Ω_p used to

derive Eq. (2.2.17),

$$\frac{\tau_{\rm D}}{\tau_{\rm P}} = \frac{\omega_{\rm SIM}}{2\pi\,|\gamma|}. \tag{5.3.1}$$

In this work, we estimate the oscillation frequency $\omega_{\rm SIM}$ from the kink oscillations of the slab in a domain in x restricted to the oscillatory slab, including the inhomogeneous layers in density fluctuations $\delta n_p = n_p - n_{p0}$, and the oscillating frequency of the perturbed bulk-velocity component δu_{px} (5.2.19). The frequency is obtained from the dispersion relation in both spaces $\omega_r - k_y$ or $\omega_r - k_x$ during the time-interval where damping is observed. This is supported by the analysis of the spectra in both decompositions.

The damping rate γ is estimated from a spectral analysis of the perturbed bulk-velocity (5.2.19). This component is decomposed in wavenumber k_y at different sections x within one of the inhomogeneous layers. Then γ is estimated from the envelope of the time-evolution of the perturbed mode k_y of δu_{px}.

5.3.2 Wave Polarization in the Plasma Physics Sense

In plasmas, the particle gyromotion with respect to a background or mean magnetic field $\mathbf{B}_0$ is relevant to describe the underlying physics. Therefore, the polarization of the electromagnetic waves in the plasma physics sense is measured with respect to the direction of the background magnetic field $\mathbf{B}_0$ [135].

In order to determine the polarization of the waves we find in the electromagnetic fields, we use the dispersion relation plots in $\omega_r - k_x$ and $\omega_r - k_y$ spaces at specific

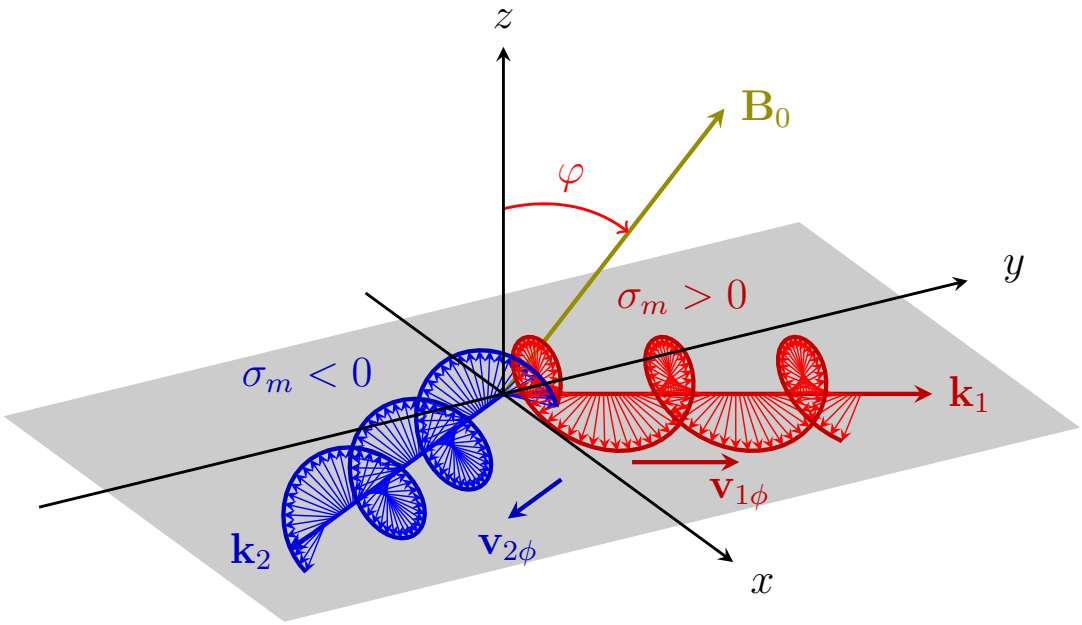

Figure 5.4: Scheme of two circularly-polarized waves counter-propagating in the direction y on the plane xy (gray surface) with opposite magnetic helicity (red for forward propagation, and blue for backward propagation). The background magnetic field $\mathbf{B}_0$ (green) and the direction of the phase velocities $\mathbf{v}_\phi$.

regions of the plasma, the phase velocity $\mathbf{v}_\phi$ [157] given by

$$\mathbf{v}_\phi = \frac{\omega_r}{k^2}\mathbf{k}, \tag{5.3.2}$$

and the spatial helical structure given by the spectral magnetic helicity σ_m (4.2.16), which is measured with respect to the wave-vector direction. Circularly polarized waves counter-propagating in y, constrained to the plane xy are shown in Fig. 5.4 along with their respective phase velocity vectors. Their helicity determines their spatial structure ($\sigma_m > 0$ left-hand helicity, red wave; and $\sigma_m < 0$ right-hand helicity,

blue wave).

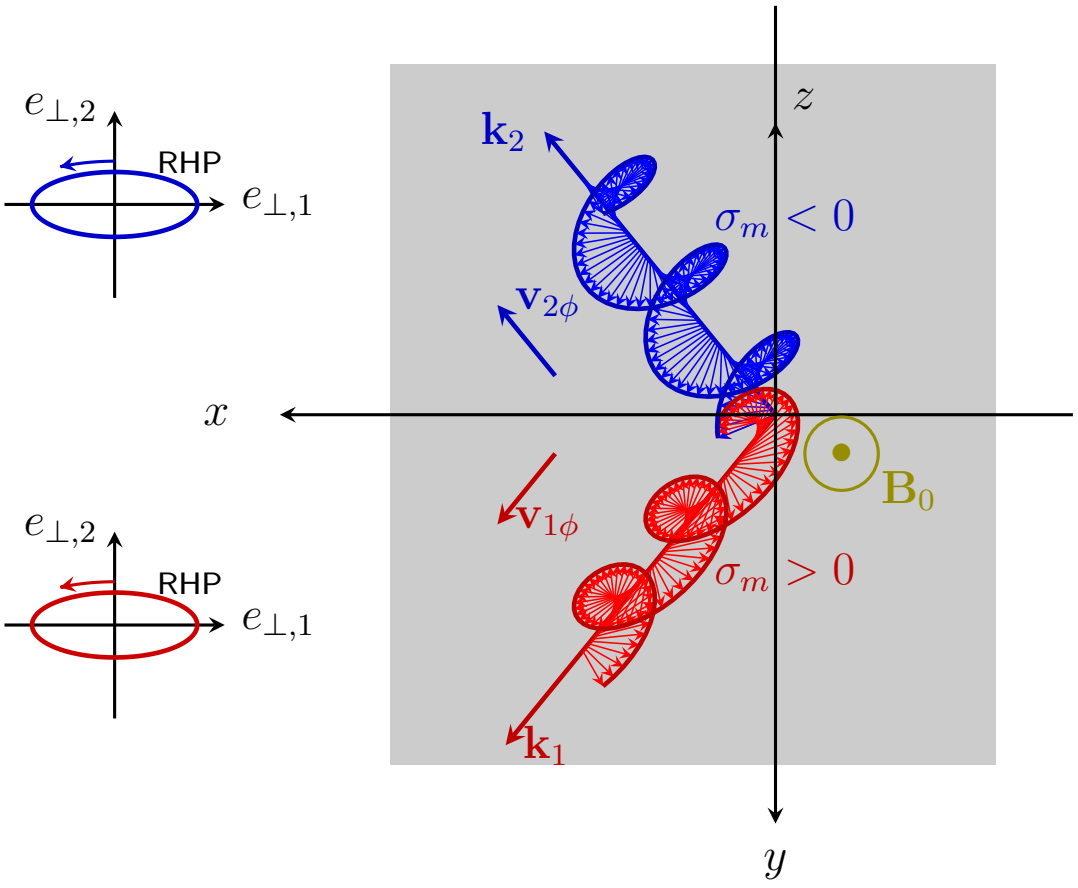

Figure 5.5: Same as Fig. 5.4 but with the observer facing the background magnetic field $\mathbf{B}_0$ (green). The plots at the left-hand show the sense of polarization of the waves in the plasma-physics sense using the axes provided by the rotation (A.1.4). Wave vectors $\mathbf{k}_1$ and $\mathbf{k}_2$ are contained in the plane xy (gray surface).

The phase velocity components are estimated by using the dispersion relation plots. This gives the direction of propagation of the signals in x and y. The phase velocity indicates in which direction the helical structure provided by σ_m is traveling.

Then, the sense of polarization of the wave is determined by an observer pointing opposite to the background magnetic field $\mathbf{B}_0$ as shown in Fig. 5.5 from Fig. 5.4. The rotation of the fields projected onto the plane of observation corresponds to the sense of the polarization. In the example of Fig. 5.5, the forward propagating wave with $\sigma_m > 0$ (red wave) has a right-hand polarization (RHP) as seen by the observer. On the other hand, the wave with $\sigma_m < 0$ (blue wave) seen by the same observer measures the same sense of rotation as the red wave. Therefore, both waves are RHP in the plasma physics sense.

A more straightforward method is proposed by Smith et al. [135] which requires only the magnetic helicity σ_m and normalized cross-correlation σ_c. However, this method is proposed for Alfvén waves in homogeneous plasmas only. These results do not necessarily follow for KAWs in inhomogeneous plasmas. The more generic result using the product $B_0\sigma_m\omega_r/k_\parallel$ (being > 0 for right-hand polarized waves and < 0 for left-hand polarized waves).

5.4 Construction of the Particle Distribution Functions and Temperatures

The distribution functions and phase-space portraits are constructed as 2D-histograms of the particle data, which consists of the particle positions (x_p, y_p), and the velocities ($v_{p\parallel}$, $v_{p,\perp,1}$, $v_{p,\perp,2}$), aligned with the background magnetic field $\mathbf{B}_0$. Histograms are constructed using the package `StatsBase.jl` of the `Julia` programming language.

The perpendicular directions are defined such that ($\perp_1$) is aligned with x and ($\perp_2$) is contained in the plane $y-z$ and perpendicular to $\mathbf{B}_0$ [transformation is given explicitly in Appendix A.1, Equation (A.1.3)]. Each histogram captures a pair of

variables, averaging over the remaining ones. Since the proton distribution functions vary throughout the space domain, specific spatial domains are selected to analyze the local kinetic features of the plasma.

For the averaged space variable, small sampling domains are selected. In $x-$domain, we examine two regions: inside one of the inhomogeneous layers at $x = x_1$, $R_{x1} = [x_1 - \Delta l_x, x_1 + \Delta l_x]$ [inside region (**III**) in Fig. 2.3]; and at the center of the slab, $x = x_2 = L_x/2$, $R_{x2} = [x_2 - \Delta l_x, x_2 + \Delta l_x]$ [inside region (**I**) in Fig. 2.3]. The domain width Δl_x sampled varies from 2 ($l/R = 0.2$) to 4 cells ($l/R = 0.5$). These widths allow us to sample enough particles to construct the distribution functions and to capture small-scale features of the distributions.

In the $y-$domain, the important regions are: $y = y_1 = 3L_y/4$, $R_{y1} = [y_1 - \Delta l_y, y_1 + \Delta l_y]$; and $y = y_2 = L_y/2$, $R_{y2} = [y_2 - \Delta l_y, y_2 + \Delta l_y]$. The width Δl_y of this region is 13 cells, covering the cavity and the winglet separately. This regions are found relevant in the analysis of results prior to the study of the phase-space portraits and velocity distribution functions.

The velocity distribution functions are computed as 2D-histograms of the particle data. The histograms use a pair of velocity components, averaging over the remaining one. Sampling regions in the space domain follow those used in the phase-space analysis. In x, the domain is restricted to the left-inhomogeneous layer R_{x1}. The domains in y are restricted to $R_{x1} \times R_{y1}$, and to $R_{x1} \times R_{y2}$.

We track the temperatures in the background magnetic field-axes, $T_{p\parallel}$, $T_{p\perp,1}$, and $T_{p\perp,2}$ using the same spatial domains employed for the phase-space portraits and the velocity distribution functions. Thus, we examine a density cavity ($R_{x1} \times R_{y1}$) and a density winglet ($R_{x1} \times R_{y1}$). Temperatures are space-averaged in these domains to characterize their time evolution.

5.5 Parameters used in the Simulations and Limitations

5.5.1 Parameters used for the Simulation

The dimensions of the system we use and the parameters we use in this research are discussed in regard of realistic parameters measured in coronal environments. The simulations consider a spatial domain of lengths $L_x\Omega_p/v_A = 170$ and $L_y\Omega_p/v_A = 251.32$ as in the previous works studying resonant absorption with a PIC-hybrid model [37, 38], where $\Omega_p = q_pB_0/m_pc$ is the proton cyclotron frequency and $v_A = B_0/\sqrt{4\pi n_0 m_p}$ is the Alfvén speed inside of the of the slab at the initial instant.

The spatial grid is defined with 256×256 nodes, having an improved resolution in the direction of the density gradient. On this grid, 1024 macro-particles per cell are used. Both the resolution and the number of macro-particles per cell are higher than those used in the cited works. With these conditions, we choose the time step $\Omega_p\Delta t = 0.05$ so that it verifies the CFL condition (5.2.1).

The density profile in Equation (2.2.16) has fixed parameters $\rho_{\text{in}}/\rho_0 = 1, \rho_{\text{en}}/\rho_0 = 0.5$ and $R\Omega_p/v_A = 40$, so that the slab and the inhomogeneous layers are totally contained within the domain in x and away from the boundaries. We briefly refer to the spatial lengths of our system. Particle density in coronal loops is found to be at most $\sim 10^8$ cm^{-3} [73, 74, 83–85]. This allows for the largest proton inertial lengths to be in the order of 23 m. Therefore, the size of the plasma we use is both smaller than a coronal loop (spatial scales in the order of $1 - 100$ Mm [27, 83]), and smaller than what can be measured with the current technology (SolO allows for a spatial resolution in the order of $100 - 200$ km [90, 91]). Thus, the size of the spatial domain and of the inhomogeneities we consider may not represent observable structures in the solar corona.

Observational research finds that quantities such as the background magnetic field and the particle density vary along a whole coronal loop, but they remain nearly uniform in a range of ~ 40 Mm around the apex [83]. Therefore, the configuration we use corresponds to a short section around the apex of the loop. In any case, it allows us to investigate the physics of resonant absorption from a multifluid perspective, including kinetic effects when fluctuations reach spatial scales in the order of the proton inertial length.

5.5.2 Closeness of the Initial Distribution to Exact Equilibrium

As discussed in Chapter 2, the system in MHD equilibrium is not an exact equilibrium condition from a kinetic framework, but it is possible to consider it as close enough to such a condition for our research.

A simulation test is conducted to verify that the system with the conditions given by Equations (2.3.10) and (2.3.11) behaves as an equilibrium state without external perturbations. We track the fluctuations of the total energy of the system, the magnetic field fluctuations, distribution functions, and the density profile for a range of time $\Omega_p t_{\text{test}} = 2400$ with parameters such that the distribution (3.2.12) deviates the most from the exact distribution ($l/R = 0.2$). These quantities remain identical to the initial condition except for noisy fluctuations throughout the space domain, with amplitudes $\sim 10^{-3} B_0$. This supports the conclusion that the distribution (3.2.12) is an equilibrium state, or at least as a quasi-stationary state for long periods of time before the perturbation $\delta \mathbf{u}_{px}$ (5.2.19) is applied.

The chosen parameters lead to a proton gyroradius in the order of 10^{-1} proton inertial lengths, smaller than the width of a spatial cell, whereas the order of magnitude of the length of the inhomogeneity is at least in the order ot 10 proton inertial

lengths. By evaluating the series expansion of the exact stationary distribution up to first-order in the parameter r_p/l_{ih}, we find that the first order term is inversely proportional to the inhomogeneity scale, so that the ratio $l/R = 0.2$ provides the largest first-order term. The ratio between the first- and zeroth-order terms is at most 1.5×10^{-3} at the bulk of the distribution function, favouring the zeroth-order term, Equation (3.2.12). The same conclusion is found at the tail of the distribution, $[-v_y \cos\varphi + v_z \sin\varphi] \simeq 4v_{\text{th}p}$, with the ratio growing up to 1.5×10^{-2} at most. Noisy fluctuations are in the order of the distribution fluctuations at the equilibrium. Therefore, it is possible that such fluctuations dampen deviations of the zeroth order term (3.2.12).

This explains the absence of variations in the test simulation, and allows us to use it as a state quasi-stationary enough for our research, despite the fact that it is not an exact equilibrium solution of the Vlasov equation.

5.5.3 Validation of the Approximation for Non-linear Coupling

Comparison of Rotations with Electric Field Data

In order to check the applicability of the approach of Mottez [47], it is necessary to test the transversality of the electric field fluctuations with respect to the axes of the magnetic field lines **B**. This means to test $\delta E_{\parallel}^{L} = 0$ by using the electric field data from simulations and the rotations with the transformation (8.2.3). This is done by checking how close to zero $\left|\delta E_{\parallel}^{L}\right|$ is, and tracking its maximum value in time.

Then, the parallel component $\delta E_{\parallel}^{\text{Mottez}}$ caused by the non-linear coupling is computed from the simulation data using the unit vector (8.2.6) under the assumption of $\delta E_{\parallel}^{L} = 0$. This equation requires computing the transverse components in the

axes of the magnetic field line, $\delta E^L_{\perp,i}$, with the unit vectors (8.2.4) and (8.2.5) to first order in the angles $\theta_{\perp,i}$. Then, the closeness of this approximation is tested by computing the difference between the parallel field data and the rotation of Mottez [47] $\left|\delta E_\parallel - \delta E_\parallel^{\text{Mottez}}\right|$, and tracking the maximum value in time.

Approximations for the Analytical Calculations

In this research, the angle φ is different from 90°. Thus, the components of the induction laws related to the transverse components (8.2.13) and (8.2.14) involve gradients of the components $\delta E_\parallel$ in both x and y, which are neglected in the calculations. These terms are explicitly computed from simulation data considering the mode $k_y = 2k_{y0}$ (dominant mode in k_y in gradients of $\delta E_\parallel$), and compared with the respectives gradients of the transverse components considering the mode $k_y = k_{y0}$ (dominant mode in k_y in gradients of $\delta E_{\perp,1}$) at a section x at the center of the left inhomogeneous layer, where the largest fluctuations occur. This comparison aims to provide an estimation of the difference in orders of magnitude of the neglected terms with respect to retained terms.

We proceed with the partial derivatives with respect to time t of the amplitudes of the transverse magnetic field components in the induction law [second line in Equation (8.2.15)]. The mode $k_y = k_{y0}$ is tracked in both components $\delta B_{\perp,1}$ and $\delta B_{\perp,2}$ taking simulation data in the same section x. The idea is to obtain the growth/damping rate to compare it with the frequency ω^j in Equation (8.2.15). This rate is obtained as follows for magnetic field amplitude $B^\sigma_{\perp,i}$ of the component

i with propagation j,

$$\gamma_{B\perp,i} = \frac{\partial B^{\sigma}_{\perp,i}/\partial t}{B^{\sigma}_{\perp,i}}. \tag{5.5.1}$$

The component $B_{\perp,1}$ is related to resonant absorption and its damping rate is used as the characteristic time-scale. The component $B_{\perp,2}$ represents the growth of localized fluctuations, and does not exhibit an exponential growth rate. Equation (5.5.1) is applied to this component.

5.5.4 Closeness of Cross-field Drift to Proton Bulk Velocity

The analysis conducted regarding the dynamics in the direction transverse to the background field (2.3.10) considers a comparison between the bulk velocity and the cross-field drift components. This is made by evaluating the maximum value of $|\delta u_{p\perp,j} - v_{\mathrm{EM}\perp,j}|$ as a function of time.

Chapter 6
Multifluid Resonant Absorption on a Slab Geometry

The simulation setting corresponds to a magnetized 2D plasma slab with density profile (2.2.16) [Fig. 2.4], and a uniform background magnetic field (2.3.10). The fluid quantities are set with a pressure-balanced condition, leading to a proton temperature profile (2.3.11). The slab is perturbed with bulk velocity (5.2.19) in the fundamental mode in y with amplitude $u_0/v_A = 0.1$.

Other parameters are $\beta_e = 0.005$, $\beta_{0p} = 0.01$. The grid is defined with $N_x \times N_y = 256 \times 256$ nodes, lengths $\Omega_p L_x/v_A = 170$, $\Omega_p L_y/v_A = 251.32$. The total number of particles considers 1024 macro-particles per cell before initialization with the density profile (2.2.16).

Simulation settings consider: **1.** Fixed angle $\varphi = 45°$ with different ratios $l/R = 0.2$, 0.3, 0.4, and 0.5; **2.** Fixed ratios $l/R = 0.2$ and 0.5, with different angles $\varphi = 10°$, 22.5°, 33.75°, 45°, 56.25°, 67.5°, and 80°.

6.1 Resonant Absorption in the Plasma

The process of resonant absorption is observed in the plasma slab during the evolution of the system. The zones that are resonant with the perturbation excited at the initial instant are located in the inhomogeneous layers between the slab and

the tenuous medium. This is observed in Fig. 6.1, which shows the evolution of the proton density n_p at five different instants of the simulation for the ratio $l/R = 0.4$.

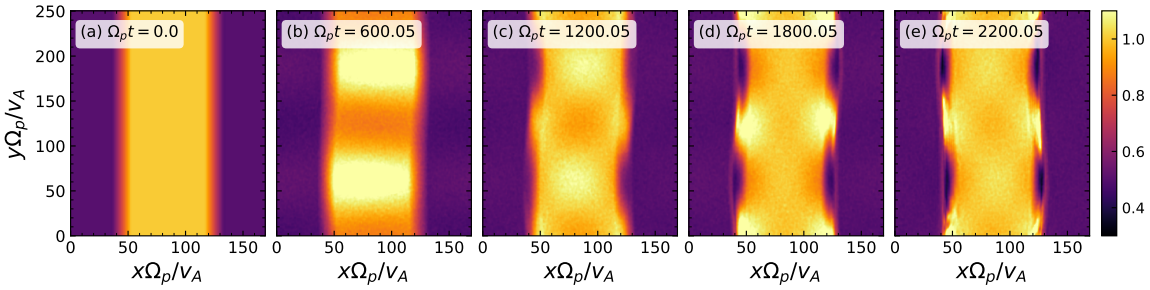

Figure 6.1: Evolution of the proton density n_p as function of x and y at five different instants. Ratio $l/R = 0.4$ and $\varphi = 45^{\circ}$.

The perturbation (5.2.19) causes the whole slab to oscillate in the direction transverse to the background magnetic field. These correspond to kink oscillations. The amplitude of the perturbation allows the slab structure to persist during the evolution of the plasma. The oscillations of the slab have nodes at $y = 0$, $L_y/2$, and L_y, and antinodes at $y = L_y/4$ and $3L_y/4$. During the evolution of the plasma, zones of enhanced density are developed around the antinodes, caused by ponderomotive forces [gradient-driven forces; see Fig. 6.1 (b)] which are typical in low beta plasmas [48, 158, 159]. This is identified in the enhanced density at the antinodes of the slab undergoing kink oscillations [48, 158].

As the large-amplitude oscillations cease, they become localized at the layers (around $x = x_0 \pm R$), where small-scale structures form around the nodes. They correspond stationary to density holes, where there are depletions of protons. At later times, the density enhancements at the antinodes are displaced from within the slab to the nodes and towards the boundaries of the slab. We label these structures as winglets. Both the holes and the winglets persist in the simulations. Their formation

involves kinetic features which will be studied in Chapter 8.

For other ratios l/R, density holes and winglets are also formed in the inhomogeneous layers. Although not shown here, the widths of these structures at the layers grow proportional to the value of l/R. Therefore, these strutures are formed for different ratios l/R, suggesting that the width of the layers does not alter the physics significantly for fixed angle φ.

6.1.1 Resonant Absorption Observed in Vector Quantities

Resonant absorption is also observed in the vector quantities. To analyze vector quantities, the bulk velocity and the magnetic field fluctuations are rotated from the system of axes of the simulation, $x - y - z$, to a system of axes aligned with the background magnetic field $\mathbf{B}_0 \parallel, \perp_1, \perp_2$. This rotation is given by the transformation (A.1.3). Since magnetic fluctuations are such that $\delta B/B_0 \sim 0.1$, the mean magnetic field in space is aligned with the background magnetic field $\mathbf{B}_0$ at all times. Therefore, the transformation (A.1.3) is constant for all the simulations.

Figure 6.2 shows the evolution of the fluctuations of the magnetic field components $\delta\mathbf{B} = \mathbf{B} - \mathbf{B}_0$ during the resonant absorption process found for $l/R = 0.4$. In the component $\delta B_\parallel$, small-scale structures are formed around the zones of the inhomogeneous layers, at the zones where the proton density holes are formed. The amplitude of these fluctuations is smaller than that of the other components of the fluctuating magnetic field. In the component $\delta B_{\perp,1}$, variations occur mostly along the dependency on y mostly in the mode associated with the excited large-scale mode (5.2.19), with decreasing amplitude as the resonant absorption occurs. Similarly, small-scale fluctuations are formed in the zones of the inhomogeneous layers, which become noticeable around instant $\Omega_p t = 960.05$. In the component $\delta B_{\perp,2}$,

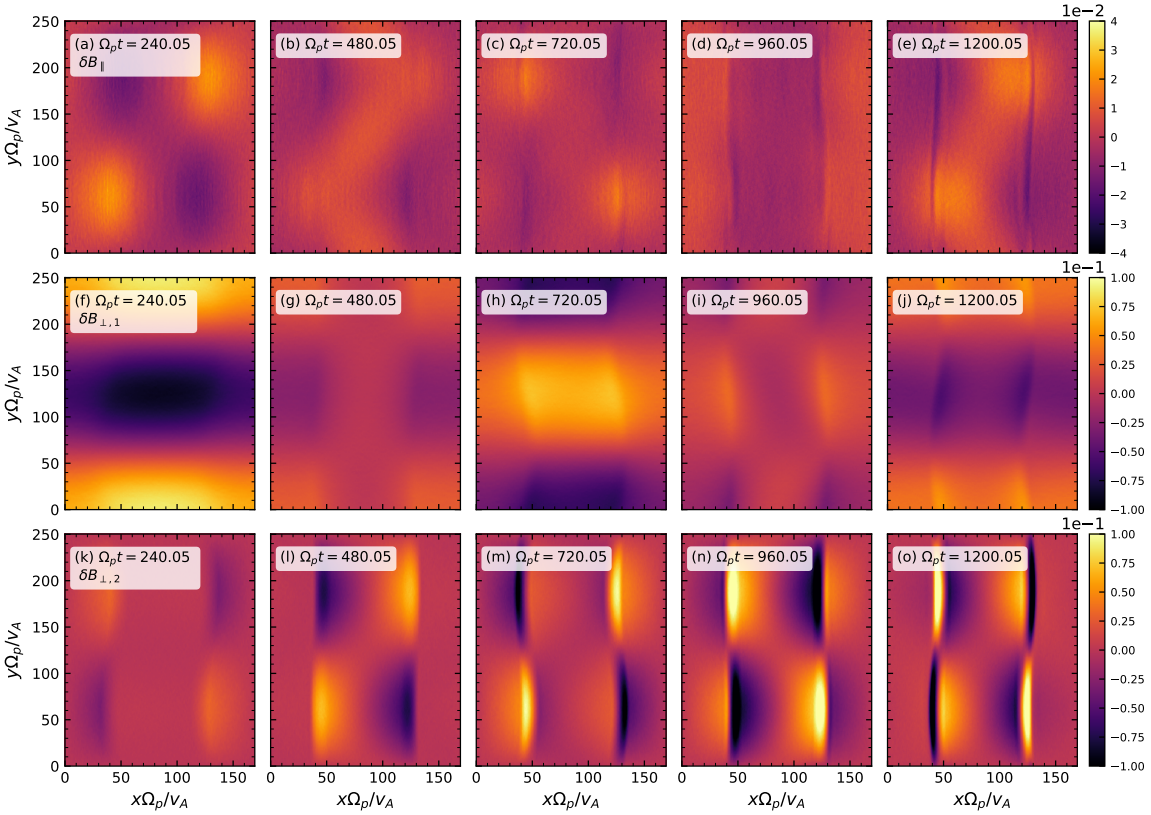

Figure 6.2: Evolution of the magnetic field fluctuations $\delta B_\parallel$ [(a) to (e)], $\delta B_{\perp,1}$ [(f) to (j)], $\delta B_{\perp,2}$ [(k) to (o)] as function of x and y at five different instants. Ratio $l/R = 0.4$ and $\varphi = 45^o$.

small-scale fluctuations grow in amplitude during this process in the zones of the inhomogeneous layers, where the proton density holes are formed, having extreme amplitudes in the zones of the density minima. This indicates that there is energy transfer between the perpendicular components of the magnetic field fluctuations during resonant absorption from scales in the order of the size of the system, $\sim L_y$, to scales in the order of the width of the inhomogeneous layer around the resonant magnetic field lines, $\sim l$. The comparison between the components $\delta B_{\perp,1}$ and $\delta B_{\perp,2}$ indicates that the excited waves have changed their direction of propagation, and

localized within the layers.

Figure 6.3 shows the evolution of the energies associated with the perpendicular components $\delta B_{\perp,1}$ [frame (a)] and $\delta B_{\perp,2}$ [frame (b)] for different ratios l/R. The component $\delta B_{\perp,1}$ is associated with the large-scale, global mode, whereas $\delta B_{\perp,2}$ is associated to localized, small-scale fluctuations. Both energies are computed considering a domain in x restricted to the oscillating inhomogeneous layers around $x\Omega_p/v_A = 45$. The energies of the components $\delta B_{\perp,1}$ decrease in time with increasing magnitude damping rate for thicker layers. After time $\Omega_p t \simeq 900$, the energy becomes more damped with a larger ratio l/R. In the component $\delta B_{\perp,2}$, fluctuations grow in time during the damping of the energy in $\delta B_{\perp,1}$ with the energy for a smaller ratio l/R having smaller amplitudes. Then, the energy in $\delta B_{\perp,2}$ reaches a saturation, with the energy in smaller ratios l/R exhibiting the smallest mean value. Accordingly, there is less energy contained in the small-scale structures for thinner layers. This is in agreement with the theoretical interpretation of the damping due to resonant absorption with the efficiency in transferring energy to small scales from the global mode [9, 15].

Because energy is being transferred to the component $\delta B_{\perp,2}$ and small-scale structures are developed in it, we follow the spectral fluctuations $\delta B_{\perp,2}$ in wavevector $\mathbf{k}-$space at five instants during the damping in $\delta B_{\perp,1}$ caused by resonant absorption for ratios $l/R = 0.2$ and 0.4 (Fig. 6.4). Signals with a wide range in wavenumber k_x having quasi-perpendicular wavevector are generated in all of the cases. This is consistent with the structures in $\delta B_{\perp,2}$ at the layers [Figs. 6.2 (k) to (o)]. The spectra in k_x are obtained by restricting the domain in x in a way such that it involves the plasma slab with the oscillating inhomogeneous layers. In all of the cases of l/R, the amplitude of signals grows toward smaller scales, predominantly in k_x. This range

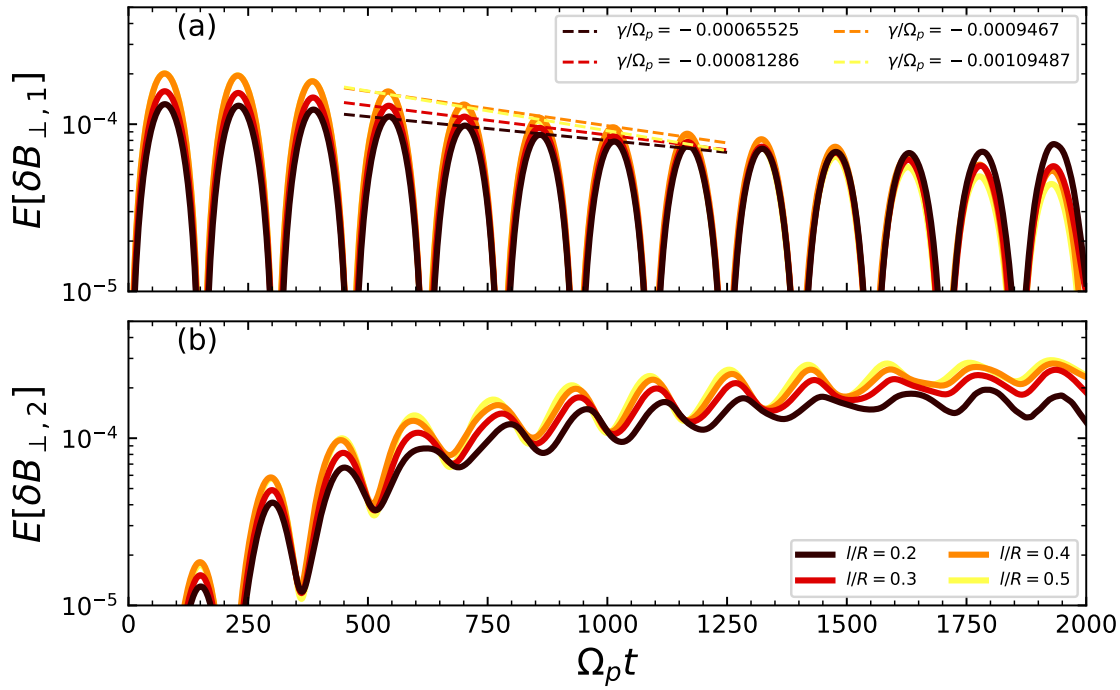

Figure 6.3: Evolution of the magnetic energies of the components (a) $\delta B_{\perp,1}$, $E\left[\delta B_{\perp,1}\right]$, associated to the large-scale mode, and (b) $\delta B_{\perp,2}$, $E\left[\delta B_{\perp,2}\right]$, associated to the small-scale luctuations in the inhomogeneous layers for different ratios l/R and fixed angle $\varphi = 45^{\text{o}}$. Their calculation involves only a domain containing the inhomogeneous layers. A damping-rate is estimated for the energy $E[\delta B_{\perp,1}]$.

is broader in $l/R = 0.2$ and decreases with wider inhomogeneous layers. Fluctuations in a smaller space domain involve a large number of Fourier modes in the overall waves. The scales reached during resonant absorption and at further times are discussed in a forthcoming section of this research.

According to the wavevector decomposition shown in Fig. 6.4, although the damping is stronger and energy is larger in small scales both for larger ratios l/R, the energy transfer reaches the smallest scales for smaller l/R. By taking $l/R = 0.2$, we observe that although the less amount of energy is transferred from the large-scale

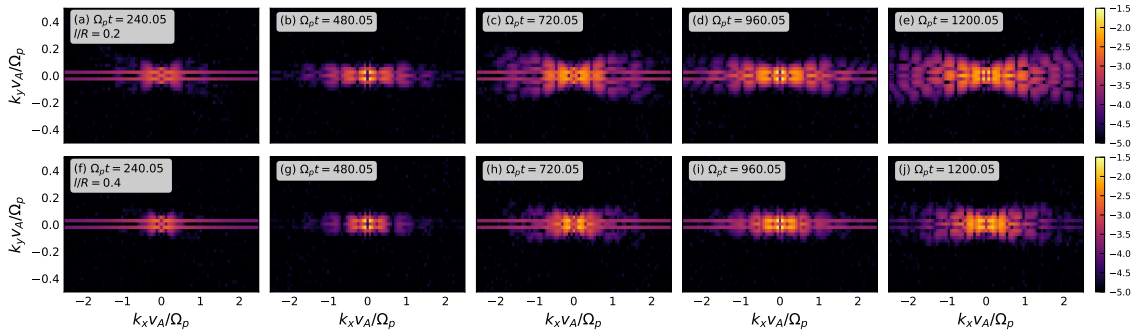

Figure 6.4: Evolution of the 2D magnetic spectrum $|\delta B_{\perp,2}(\mathbf{k})|^2$ in log-scale for $l/R = 0.2$ [(a) to (e)] and 0.4 [(f) to (j)] as function of k_x and k_y at five different instants during the process of damping. Case of $\varphi = 45^{\text{o}}$.

mode in $\delta B_{\perp,1}$, the closer to kinetic scales ($v_A k_x/\Omega_p \gtrsim 1$) are small-scale fluctuations in $\delta B_{\perp,2}$.

Figure 6.5 shows the evolution of the proton bulk-velocity components [computed as in Equation (5.2.4)] during the process of resonant absorption for $l/R = 0.4$. These components are rotated to the axes aligned with $\mathbf{B}_0$. The spatial dependency of the components is similar to that found in the magnetic field fluctuations in Fig. 6.2. In the component $\delta u_{p\parallel}$, fluctuations develop within the plasma slab, indicating a flow of plasma with sinusoidal variations along y due to the projection of $\mathbf{B}_0$ along the axis of the slab. In the component $\delta u_{p\perp,1}$, the initial perturbation (5.2.19) is observed mostly within the plasma slab oscillating in time whose amplitude is reduced during the process of damping in the same way as in the magnetic field component $\delta B_{\perp,2}$. The component $\delta u_{p\perp,2}$ develops small-scale fluctuations of growing amplitude in the inhomogeneous layers around the resonant magnetic field lines. Accordingly, the flow of the plasma occurs mainly in the direction of the kink oscillations in the initial instants to the other transverse direction, localized in the inhomogeneous layers and the density holes. Zones of zero flow in $\delta u_{p\perp,2}$ occur at the zones of largest width

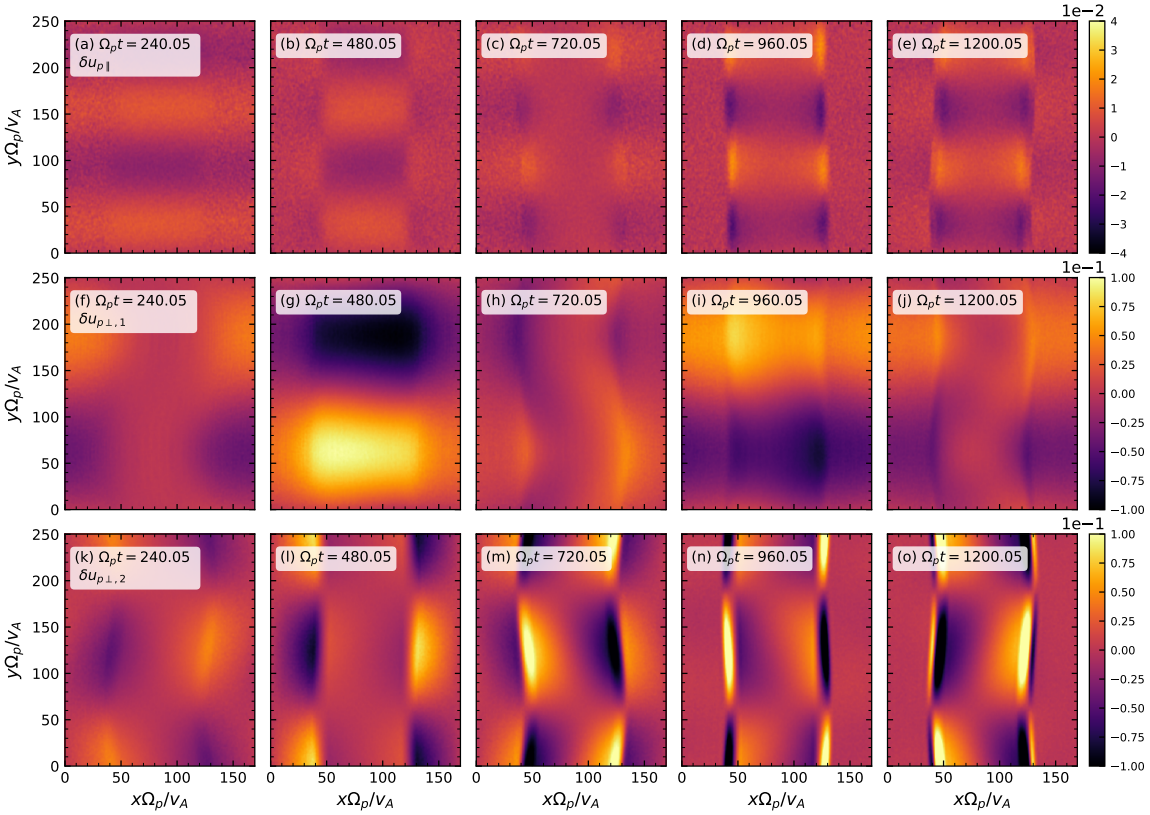

Figure 6.5: Evolution of the proton bulk-velocity fluctuations $\delta u_{p\parallel}$ (amplitude scale factor 10^{-2}) [(a) to (e)], $\delta u_{p\perp,1}$ (amplitude scale factor 10^{-1}) [(f) to (j)], $\delta u_{p\perp,2}$ (amplitude scale factor 10^{-1}) [(k) to (o)] as function of x and y at five different instants during the process of damping. Ratio $l/R = 0.4$ and $\varphi = 45^{\circ}$.

in x of the holes. The largest flows occur in the winglets limiting the holes. These features are observed in all of the simulated ratios l/R, differing in the width of the region where the fluctuations develop along x.

In summary, during resonant absorption in both the proton bulk velocity and the magnetic field fluctuations, large-scale waves propagating with direction y are refracted around the resonant magnetic field lines. These fluctuations acquire wave-vector mostly aligned with x. In the axes of the background magnetic field $\mathbf{B}_0$, their

wavevectors change from the plane $e_{\parallel} - e_{\perp,2}$ (y) to the direction $e_{\perp,1}$ (x). Energy is deposited at small spatial scales in the direction parallel to the proton density gradient. This process is observed in the damping of large-scale fluctuations in the magnetic field component $\delta B_{\perp,1}$ [Figs. 6.2 (f) to (j)] and the simultaneous growth of small-scale fluctuations in the component $\delta B_{\perp,2}$ [Figs. 6.2 (k) to (o)] and in their respective energies (Fig. 6.3).

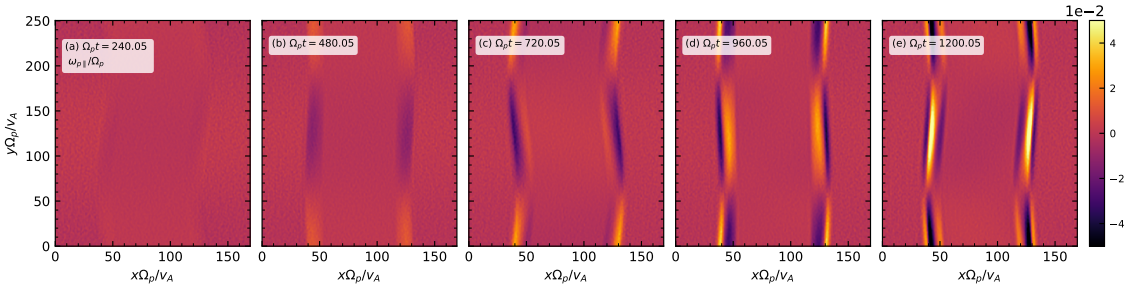

Figure 6.6: Evolution of the parallel proton vorticity $\omega_{p\parallel}$ as function of x and y at five different instants. Ratio $l/R = 0.4$ and $\varphi = 45^{\circ}$.

The proton vorticity $\boldsymbol{\omega}_p = \nabla \times \delta \mathbf{u}_p$ has been studied with regard of resonanty absorption. Theoretical research of resonant absorption of kink-modes in cylindrical plasma columns based on single-fluid MHD models [16, 17] predict that the component parallel to $\mathbf{B}_0$ is enhanced with respect to the transverse componnts. This occurs in the resonant regions. The vorticity is zero everywhere else.

The parallel component $\omega_{p\parallel}$ is shown in Fig. 6.6 for the ratio $l/R = 0.4$. The parallel vorticity is enhanced at the inhomogeneous layers where resonant absorption occurs. The zones of maximum amplitude correspond to the winglets observed in the proton density at the nodes of the slab having the same sign in $y = 0$ and L_y, and opposite with respect to $y = L_y/2$, allowing the flow of particles from one winglet to the other via the density holes. The parallel vorticity is nearly zero at

the center of the density holes observed in Fig. 6.1. As resonant absorption occurs, the vorticity continues to be enhanced, remaining nearly zero anywhere else in the plasma. The perpendicular components of the vorticity remain at low amplitude in all of the plasma, even in the inhomogeneous layers. Numerically, we find the ratio $|\boldsymbol{\omega}_{p\perp}|^2 / |\omega_{p\parallel}|^2 \sim 10^{-2}$, where $|\boldsymbol{\omega}_{p\perp}|^2 = \omega^2_{p\perp,1} + \omega^2_{p\perp,2}$. It also indicates that the large-scale fluctuations excited in the inhomogeneous layers are of Alfvénic nature. This feature provides further features of these simulations consistent with resonant absorption at the inhomogeneous layers. We observe this feature for all of the simulated ratios l/R.

6.1.2 Mode Decomposition of $\delta u_{p\perp,1}$

Further analysis shows the Fourier decomposition of the bulk-velocity component $\delta u_{p\perp,1}$, in which the perturbation is set and energy is injected at large scales.

We are interested in characterizing the decay of large- to small-scale fluctuations during resonant absorption. The procedure is described in subsection 5.3.1. The component $\delta u_{p\perp,1}(\mathbf{r},t) = -\delta u_{px}(\mathbf{r},t)$ is Fourier-decomposed in wavenumber space k_y at fixed sections x, considering the whole domain in y. Figure 6.7 (a) shows the evolution of the density fluctuations for modes in k_y of the plasma slab for the ratio $l/R = 0.4$ at the section $x = L_x/4$ inside the inhomogeneous layer, where the absorption is expected to occur. The first mode of the plasma slab in y, $k_y = k_{y0}$, exhibits an exponential decay during the time-interval $450 \leq \Omega_p t \leq 1300$. By repeating this analysis across the whole plasma slab, we find that the damping of the excited mode is highly non-uniform. We focus on the inhomogeneous layers, where resonant absorption occurs [Fig. 6.7 (b)]. By repeating the analysis for other layer thicknesses, $l/R = 0.2$, 0.3, and 0.5, on $\delta u_{p\perp,1}$, it is found that the space-dependency

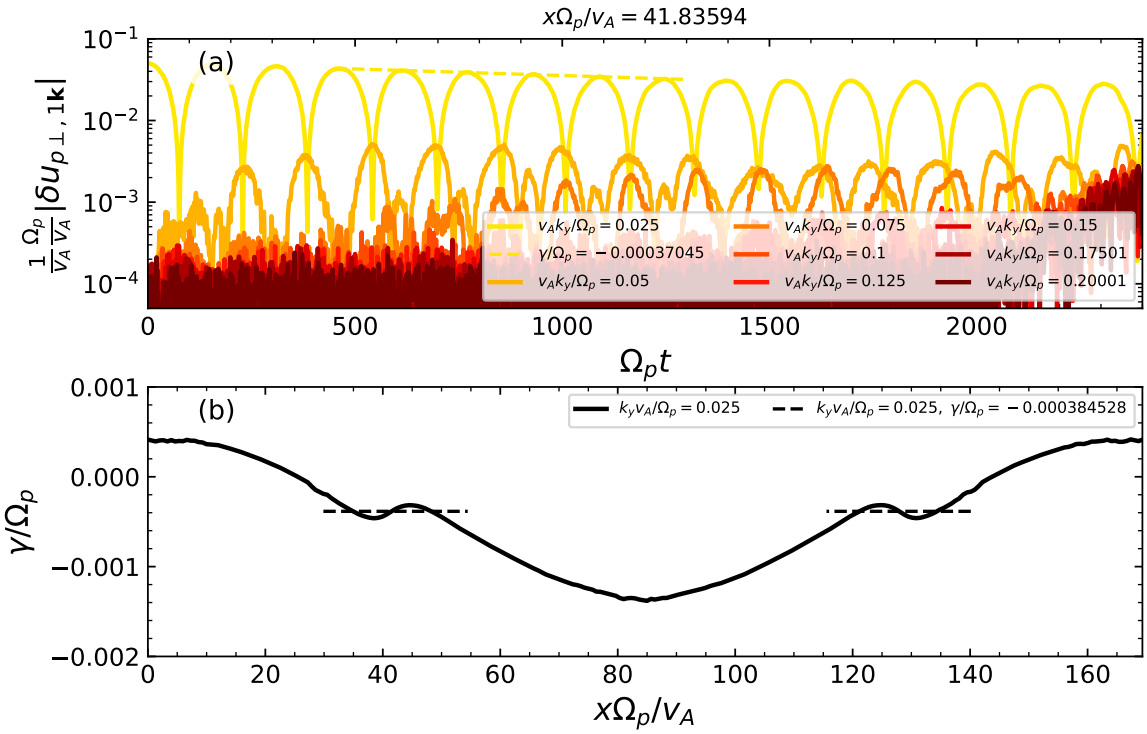

Figure 6.7: (a) Mode decomposition of the bulk-velocity component $\delta u_{p\perp,1}$ in k_y for the domain in y comprising the plasma slab at the fixed section $x\Omega_p/v_A = 41.83594$ inside the left inhomogeneous layer. Mode 1 (solid lines) with the estimated damping rate (dashed lines). (b) Evaluation of the damping rate for modes 1 in k_y across the whole plasma slab. Ratio $l/R = 0.4$ and $\varphi = 45^o$.

on x is similar within the inhomogeneous layers during the same time interval.

Figure 6.8 shows the damping rates associated with resonant absorption [frame (a)], the oscillation frequencies of the slab compared with the left- and right- mode frequencies [frame (b)], and the damping time-rate [frame (c)]. These quantities are shown for different l/R. Generally, the magnitudes of the obtained damping rates decrease with the thickness of the inhomogeneous layers [Fig. 6.8 (a)]. This tendency is expected from single-fluid MHD theory on resonant absorption in the case of weakly damped fluctutuations [7, 9, 13, 160, 161]. This occurs because the

phase of the oscillations of the local magnetic field lines varies the most for smaller ratios l/R, thus for thin layers there are fewer magnetic field lines in phase close to the resonant layer than for larger l/R, making the energy-transfer process to take longer for smaller l/R [161].

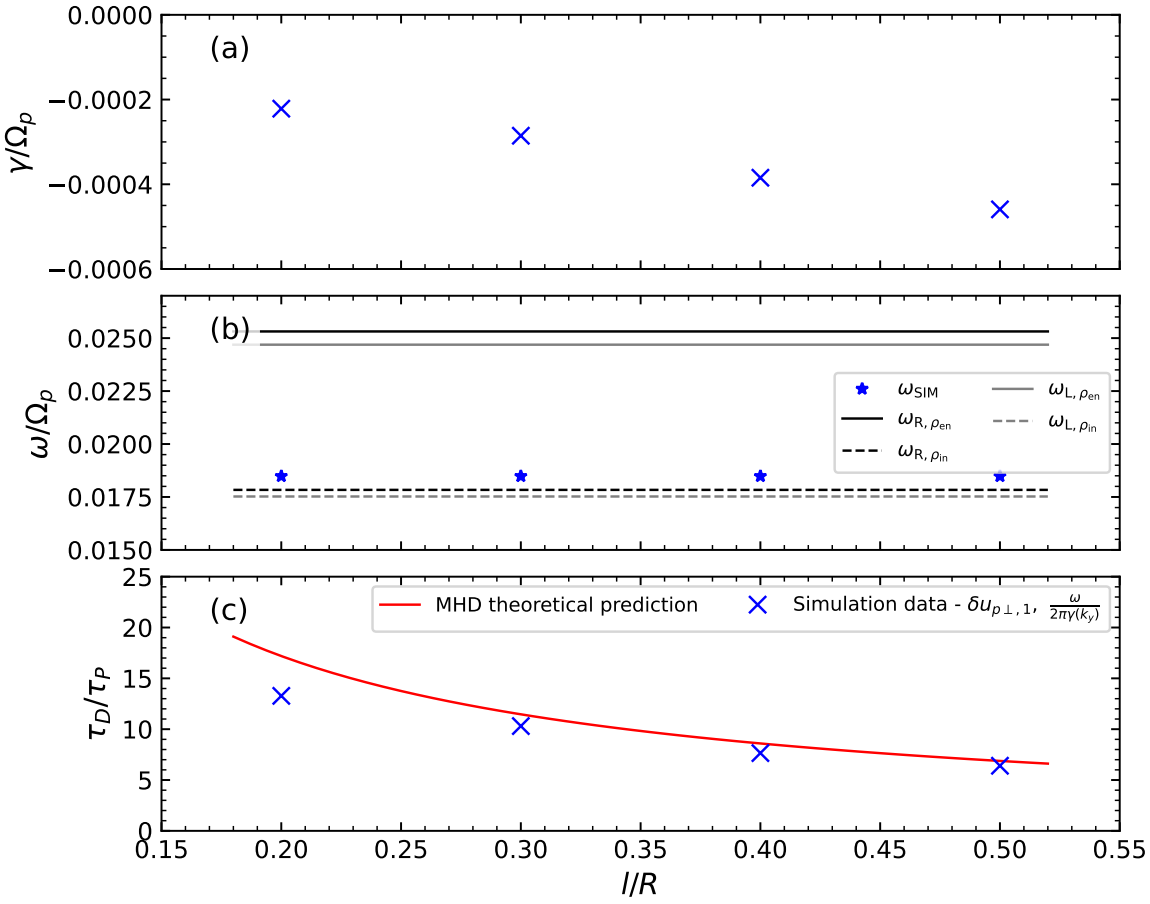

Figure 6.8: Oscillating properties of the plasma column for different ratios l/R based on the component $\delta u_{p\perp,1}$ in the inhomogeneous layers. (a) Damping rate γ/Ω_p; (b) oscillation frequency $\omega_{\mathrm{SIM}}/\Omega_p$ of the plasma columns estimated from the simulations (blue) and the extreme values of the left and right mode frequencies (6.1.1) and (6.1.2); and (c) calculation of the damping time-rate $\tau_{\mathrm{D}}/\tau_{\mathrm{P}}$ for different ratios l/R based on MHD theory (2.2.17) and on simulation data (5.3.1).

By following the dispersion relation in $\omega_r - k_x$ of the proton density fluctuations for the same domain used in x, the frequency of oscillation of the plasma slab can be obtained. The dispersion relation is obtained for the instant t_0 considering a variable time-window Δt_w depending on the ratio l/R, so that the time-Fourier transform considers a time-range $t_0 - \Delta t_w \leq t \leq t_0$. The frequency is solved initially in the same time range used to estimate the damping rate. By extending the time-window to involve previous instants, it is noted that the most intense signals observed in the dispersion relation remain mostly unchanged but with less uncertainty in frequency. Therefore, we use a time-window $\Omega_p \Delta t_w = 1020$ for all of the cases. The oscillation frequency remains mostly independent of l/R and corresponds to $\omega_r/\Omega_p = 1.84799 \times 10^{-2}$. This oscillation frequency is compared with the frequencies of the left- and right-modes frequencies in homogeneous plasmas for parallel propagation [48], using the parameters from the slab and the tenouous medium. In such a case, they obey the dependency in Eqs. (6.1.1) and (6.1.2), obtained from the general Equation (4.1.9). These frequencies use local parameters of Alfvén speed, and density

$$\frac{\omega_{\mathrm{L}}(x)}{\Omega_p} = \frac{k_\parallel^2 v_A^2}{2\Omega_p^2} \frac{v_{Ap}^2(x)}{v_A^2} \left[-1 + \sqrt{1 + 4 \frac{\Omega_p^2}{k_\parallel^2 v_A^2} \frac{v_A^2}{v_{Ap}^2(x)}} \right], \tag{6.1.1}$$

$$\frac{\omega_{\mathrm{R}}(x)}{\Omega_p} = \frac{k_\parallel^2 v_A^2}{2\Omega_p^2} \frac{v_{Ap}^2(x)}{v_A^2} \left[1 + \sqrt{1 + 4 \frac{\Omega_p^2}{k_\parallel^2 v_A^2} \frac{v_A^2}{v_{Ap}^2(x)}} \right], \tag{6.1.2}$$

where the Alfvén speeds ratio considers the Alfvén speed is $v_A = B_0/\sqrt{4\pi m_p n_0}$ computed with the normalization density n_0, and $v_{Ap} = B_0/\sqrt{4\pi m_p n_{0p}(x)}$ is the local Alfvén speed computed with the local proton density. Due to the angle of the magnetic field with respect to the plane of the simulation, the perturbation (5.2.19)

with wavenumber k_{y0} means that the excited waves propagate with wavevector given by Equation (2.2.5) based on the transformation in Eq. (A.1.5), which means that perturbations propagate along the background magnetic field $\mathbf{B}_0$ and in the perpendicular direction $\widehat{\mathbf{e}}_{\perp,2}$. Therefore, the use of Eqs. (6.1.1) and (6.1.2) in the analysis is for comparison purposes only.

The frequencies measured from the simulation are located within the range of the left and right modes frequency (6.1.1) and (6.1.2) respectively, as observed in Fig. 6.8 (b). The frequency uncertainty in the order of 6×10^{-4}. Therefore, the closeness to the theoretical frequencies using the parameters of the inside of the slab is not significant.

With the damping rate γ/Ω_p [Fig. 6.8 (a)] and the oscillation frequency $\omega_{\mathrm{SIM}}/\Omega_p$ [Fig. 6.8 (b)], it is possible to compute the damping time rate which is a quantity predicted by MHD theory for the transverse oscillations of a plasma slab with inhomogeneous layers given by a linear profile under a single-fluid, ideal plasma with no background flow and uniform background, pressure-balanced magnetic field under the condition of thin transition layer approximation, $l/R \ll 1$, [13–15]. The damping time-rate $\tau_{\mathrm{D}}/\tau_{\mathrm{P}}$ under such conditions is given by Eq. (2.2.17) (see section 2.2 for further details),

$$\frac{\tau_{\mathrm{D}}}{\tau_{\mathrm{P}}} = \frac{1}{|\sin\chi|}\frac{4}{\pi^3}\frac{\rho_{\mathrm{in}}+\rho_{\mathrm{en}}}{|\rho_{\mathrm{in}}-\rho_{\mathrm{en}}|}\frac{L_y/R}{l/R}. \tag{6.1.3}$$

The damping time rate obtained from the damping rate γ and oscillation frequency ω_r from the spectral analysis of the fluctuations of the proton density or the perturbed bulk-velocity component (5.3.1). A comparison between these estimations is shown in Fig. 6.8 (c) for $l/R = 0.2$, 0.3, 0.4, and 0.5. The damping time rate from

the simulations deviates continuously for smaller ratios l/R, being more accurate for the ratios $l/R = 0.3$ to 0.5. Generally, deviations increase for thinner inhomogeneous layers. It is interesting to note that although the used ratios l/R do not verify the condition of thin layers strictly, the MHD damping time-rate (6.1.3) is a good estimation of the damping for thicker layers.

The thin transition layer approximation remains valid as long as the relative size between the inhomogeneous layers and kinetic scales is large, that is, strictly MHD-scales are involved. In these simulations, kinetic effects may be triggered for thinner layers, contributing to the discrepancies. Numerical effects may also be acting when fluctuations achieve lengths close to the grid-lengths.

In the next section, the scales reached by resonant absorption in the simulations are discussed and shown to reach the wavenumber associated with the ion inertial length.

6.1.3 Scales Reached by Resonant Absorption

The development of small-scale fluctuations in the spectral densities of the magnetic field, and proton bulk-velocity fluctuations is observed in k_x within the domain of the plasma slabs for all of the simulated ratios l/R. Both quantities exhibit a similar spatial dependency in both coordinates x and y for components in the same direction. Therefore, only the spectral densities of the magnetic field fluctuations are followed. Figure 6.9 shows the evolution of the spectral power density of magnetic fluctuations of each of the components of the magnetic field as functions of k_x averaged over k_y, during the process of damping observed in the spectral decomposition of $\delta n_p = n_p - n_{0p}$. The Fourier transform in x considers a domain that comprises the plasma slab and the oscillating inhomogeneous layers.

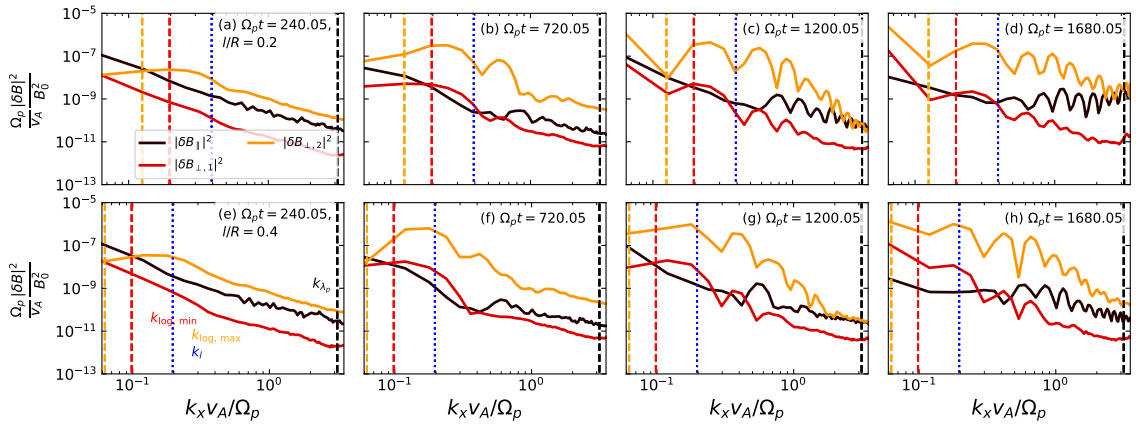

Figure 6.9: Evolution of the spectral density of magnetic field energy fluctuations of the component $\left|\delta B_\parallel\right|^2$(solid black line), $\left|\delta B_{\perp,1}\right|^2$ (solid red line), and $\left|\delta B_{\perp,2}\right|^2$ (solid orange line) for ratios $l/R = 0.2$ and 0.4 (ratio varying along columns) at four instants (time-varying across columns) during the process of damping due to resonant absorption ($\Omega_p t \leq 720.05$), and and at the end and longer times ($\Omega_p t \geq 1200.05$). Important scales are shown for each ratio, k_l (dashed blue line, associated with the length of the inhomogeneity), k_{λ_p} (dashed black line, associated with the proton inertial length), and $k_{\log,\max}$, $k_{\log,\min}$ (dotted orange line and dashed red line, respectively, showing the range of characteristic scales of the density gradient). Case of $\varphi = 45^o$.

Important scales for each ratio l/R are shown for comparison as wavenumber k_x: the proton inertial length, $k_{\lambda_p} = \pi/d_p$ where $d_p = v_A/\Omega_p$; the length of the inhomogeneous layers, $k_{\lambda,p} = \pi/l$, the lengths associated to the density gradient, important in the kinetic theory of inhomogeneous plasmas [123, 162], computed as

$$\lambda_{\log} = \left[\frac{1}{n_p}\frac{\mathrm{d}n_p}{\mathrm{d}x}\right]^{-1}. \tag{6.1.4}$$

In particular, we identify the maximum value where $n_p = n_{\mathrm{en}}$, $k_{\log,\max} = \pi/\left.\lambda_{\log}\right|_{n_{\mathrm{en}}}$ and the minimum value at $n_p = n_{\mathrm{in}}$, $k_{\log,\min} = \pi/\left.\lambda_{\log}\right|_{n_{\mathrm{in}}}$; the proton gyroradius is also considered and is given by $k_{\rho_p} = \pi/\rho_p$, where $\rho_p = \sqrt{\beta_{p\perp}}v_A/\Omega_p$. Due to the

range of values considered for $\beta_{p\perp} = \beta_p$, these scales are not reached in the simulation ($\rho_p \Omega_p / v_A \simeq 0.1 - 0.316228$).

The condition of closeness to the proton gyroradius scale of the slab or the tenuous medium, $k\rho_p \sim 1$ (equivalent to $k\lambda_p \sim 8{-}10$), is not reached either. The wavenumber associated with the proton inertial length is fixed for all of the simulations, and it is close to the upper boundary of the wavenumber domain, $k_{\lambda_p} v_A / \Omega_p = \pi$.

Figure 6.9 shows that the scales associated with the inhomogeneities are much larger than that of the proton inertial length. Initially, at $\Omega_p t = 240.05$, the spectra exhibit a two-range power-law dependency, changing slope within the range of scales comprised by $k_{\log,\min}$ and $k_{\log,\max}$ in all of the cases of l/R. The slopes of the spectra at scales smaller than $k_{\log,\max}$ are larger up to kinetic scales. Peaks arise in the spectra in the component $\delta B_{\perp,2}$ from $k_{\log,\max}$ toward kinetic scales in the order of $k_x v_A / \Omega_p \simeq 1$ during the damping caused by resonant absorption (observe instant $\Omega_p t = 720.05$). Successive peaks are observed toward $k_x v_A / \Omega_p \simeq 2$. These peaks are more evident in the case of $l/R = 0.2$ and 0.3, showing energy transfer toward kinetic scales for thinner inhomogeneous layers. With the growth of fluctuations, the amplitude of the component $\delta B_{\perp,2}$ becomes larger than that of the components $\delta B_{\perp,1}$ and $\delta B_{\parallel}$. Peaks are also formed in the component $\delta B_{\parallel}$ at scales $k_x v_A / \Omega_p \sim 1$ as large-scale fluctuations are damped, more evident for smaller ratios l/R.

By the end of resonant absorption and at further times,the energy peaks continue to ever smaller scales, eventually reaching the proton inertial length scale. This is most evident for the ratios $l/R \leq 0.3$, as noted in Fig. 6.9 at times $\Omega_p t \geq 1200.05$, as time advances. Nevertheless, the level of fluctuations at smaller scales for the cases of $l/R = 0.4$ and 0.5 still increases, although peaks of smaller amplitude are observed in the spectral density. Therefore, perturbations at scales in the order of

the size of the system have been transferred to kinetic scales. Here, to the proton inertial length via the process of resonant absorption at the inhomogeneous layers of a plasma slab. The efficiency of this transfer to small scales is determined by the thickness of these layers. Even though the transverse displacements of the slab may exceed the condition of small-amplitude perturbation of the inhomogeneous layers, resonant absorption is observed in these simulations.

6.2 Resonant Absorption for Different Angles φ

The effects of different angles φ between the plane of the plasma and the background magnetic field $\mathbf{B}_0$ (measured from axis z) for a fixed ratio $l/R = 0.5$ are addressed. Simulations for the same angles with ratio $l/R = 0.2$ are analyzed for comparison. We use angles $\varphi = 0$, 10^o, 22.5^o, 33.75^o, 45^o, 56.25^o, 67.5^o, and 80^o. By changing the angle φ, the local left and right mode frequencies (6.1.1) and (6.1.2) change in magnitude in all of the cases. In particular, for more magnetized plasma slabs (φ approaching to 90^o), the frequencies reach their maximum values, whereas for less magnetized slabs (φ approaching to 0^o), the frequencies of the modes left and right tend to become smaller because of the projection of the perturbative wavenumber k_y on the parallel direction tends to zero, eventually reducing the propagation in the direction parallel to $\mathbf{B}_0$.

6.2.1 Effects on the Proton Density

Transverse kink oscillations develop in the slab for all of the cases. The evolution of the proton density is shown for the angles $\varphi = 22.5^o$, 45^o, and 80^o in Fig. 6.10. The degree of magnetization of the plasma affects the formation of local density

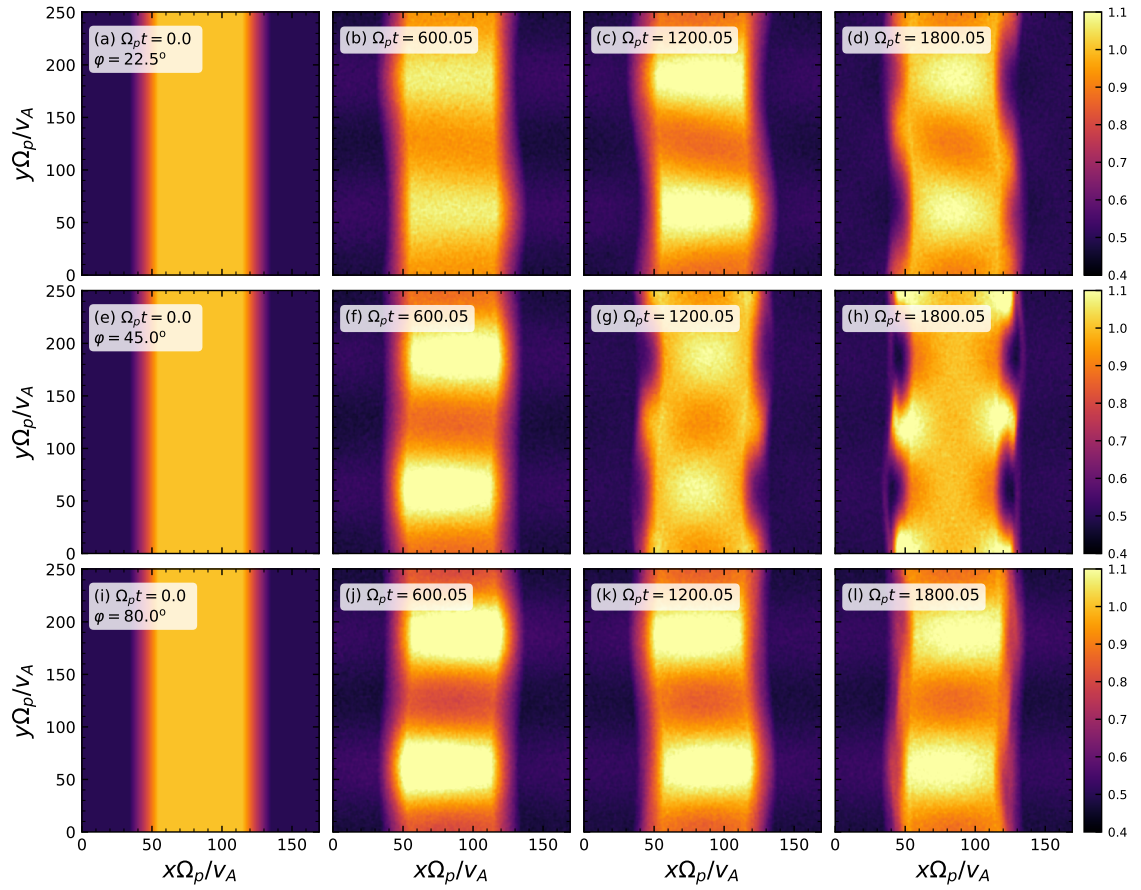

Figure 6.10: Evolution of the proton density during the simulation for angles $\varphi = 22.5^o$ [(a) to (d)], 45^o [(e) to (h)], and 80.0^o [(i) and (l)] at four instants (time-varying across columns). Case of $l/R = 0.5$.

enhancements. Therefore, the magnitude of ponderomotive forces acting along the plasma slabs. The enhancement is larger for larger φ. With regard of the small-scale structures and density holes formed in the inhomogeneous layers, their formations occurs earlier for angles far from $\varphi = 0^o$ and $\varphi = 90^o$ during resonant absorption. The formation of the density holes at the inhomogeneous layers of the slab is also altered by the change in the angle. For angles φ below 33.75^o, the holes take longer

times to be formed ($\varphi = 22.5°$) or are not formed during the simulation ($\varphi = 10°$). For angles close to $\varphi = 90°$, the holes exhibit less depletion, eventually reducing their size, as observed for $\varphi = 80°$ in Figs. 6.10 (i) to (l).

6.2.2 Damping-rate due to Resonant Absorption in $\delta u_{p\perp,1}$

A mode decomposition analysis on the bulk-velocity component $\delta u_{p\perp,1}$ is carried out to determine the damping rate-time using the same analysis presented before for fixed angle $\varphi = 45°$, described in subsection 5.3.1.

Figure 6.11 shows the same as Fig. 6.8 but for different angles φ. The fundamental mode of the plasma slab in k_y exhibits exponential damping, exhibiting a change in the tendency in the inhomogeneous layers. The magnitude of the damping rate γ/Ω_p along the slab increases toward both $\varphi = 0°$ and $90°$, having a maximum arround $\varphi = 33.75°$. A similar behavior is observed for the damping rate γ for the ratio $l/R = 0.2$, but with a smaller magnitude [Fig. 6.11 (a)]. The dispersion relation in $\omega_r - k_x$ space of the density fluctuations evaluated with time-windows chosen for each angle φ shows that the frequency of oscillation of the plasma slab increases with φ [Fig. 6.11 (b)] and in all of the simulations, this frequency is between the extreme values of eqs. (6.1.1) and (6.1.2), indicating that the resonant surfaces are located within the inhomogeneous layers.

By repeating the analysis in simulations for all of the angles for the ratio $l/R = 0.2$, it is observed that the most excited frequencies of oscillation remain mostly unaltered. The ratio τ_D/τ_P is computed from the simulations using Eq. (5.3.1) and is compared with the theoretical prediction based on MHD theory, Eq. (2.2.17) for ratios $l/R = 0.2$ and 0.5. It is observed that the damping time-rates in Fig. 6.11 (c) computed from the simulations agree reasonably with the theoretical prediction

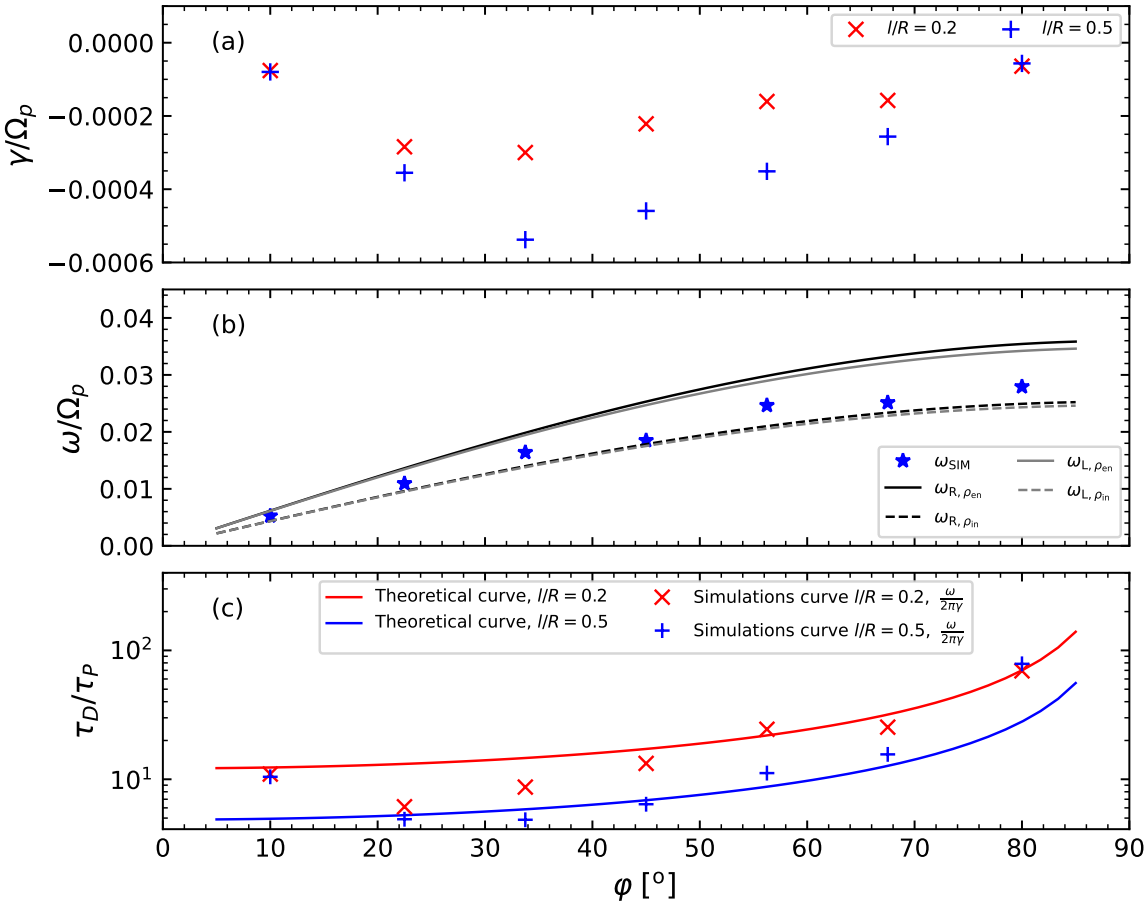

Figure 6.11: Oscillating properties of the plasma slab for different angles φ and fixed ratios $l/R = 0.2$ and 0.5 based on the component $\delta u_{p\perp,1}$ in the inhomogeneous layers. (a) Damping rate γ/Ω_p ($l/R = 0.2$ ex marks, 0.5 crosses); (b) oscillation frequency $\omega_{\mathrm{SIM}}/\Omega_p$ obtained from the simulations (blue) and extreme values of the left and right modes frequencies (6.1.1) and (6.1.2) of the plasma columns; and (c) calculation of the damping time rate $\tau_{\mathrm{D}}/\tau_{\mathrm{P}}$ for different angles φ for fixed ratios l/R based on MHD theory (2.2.17) and on simulation data (5.3.1).

for angles $22.5^{\mathrm{o}} \leq \varphi \leq 67.5^{\mathrm{o}}$ for the ratio $l/R = 0.5$. For angles close to 0^{o} or 90^{o}, deviations occur. For simulations with $l/R = 0.2$, the damping time rates reasonably agree with theoretical MHD predictions for angles $56.25^{\mathrm{o}} \leq \varphi \leq 80^{\mathrm{o}}$. For increasing

angle φ, the tendency of increasing damping time-rate is maintained.

As in the simulations with fixed angle $\varphi = 45^{o}$, we computed the vorticity of the proton bulk velocity for the plasmas with fixed ratios $l/R = 0.2$ and 0.5, with different angles φ. The behavior of the vorticity components is the same as that described for fixed angle (see Fig. 6.6). The vorticity component parallel to the background field has the largest amplitude localized in the inhomogeneous layers for all of the angles from $\varphi = 10^{o}$ to 80^{o}, and nearly zero magnitude in the perpendicular components. The magnitude of the vorticity is the largest at angles $\varphi = 45^{o}$ and is reduced towards angles close to 0^{o} or to 90^{o}. We observe these features in Fig. 6.12 for angles $\varphi = 22.5^{\circ}$, 45°, and 80°.

This tendency is correlated with the formation of holes in the proton density. In the simulations with angles close to 0^{o} the holes are not formed, whereas in the angles close to 80^{o}, the depth of the holes is smaller compared to that observed for angles around $\varphi = 45^{o}$. For larger angles, this can be partially explained with the projection of vorticity on the plane: the closer φ is to 90^{o}, the rotation of the proton bulk velocity is more contained in the perpendicular plane.

Thus, the effect observed in the proton density becomes weaker [compare Figs. 6.10 (h) for $\varphi = 45^{o}$ and (l) for $\varphi = 80^{o}$]. Nevertheless, this feature indicates that the large-scale fluctuations localized in the inhomogeneous layers are of Alfvénic nature [16, 17] regardless of the effectiveness of resonant absorption in transferring energy toward small scales.

6.2.3 Resonant Absorption in Magnetic Field Fluctuations

The structures observed in the magnetic field components for different angles φ are similar to those found for different cases of l/R shown in Figs. 6.2 and 6.5. We

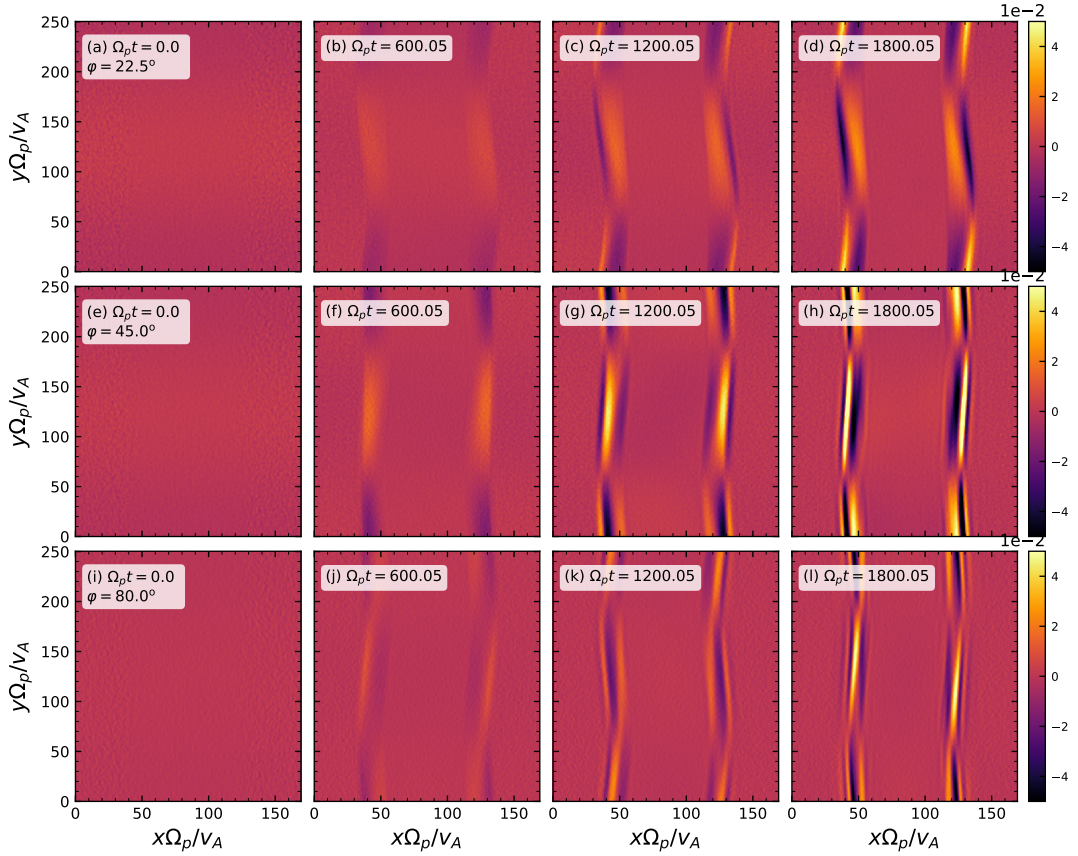

Figure 6.12: Evolution of the parallel proton vorticity $\omega_{p\parallel}$ as function of x and y at five different instants. Fixed ratio $l/R = 0.5$ and three angles φ.

track the evolution of the magnetic energies for different angles. Figure 6.13 shows the magnetic energies of the resonant left layer associated with the components $\delta B_{\perp,1}$ [frame (a)] and $\delta B_{\perp,2}$ [frame (b)] for $l/R = 0.5$. By tracking the energy of the magnetic field fluctuations in the components $\delta B_{\perp,1}$ [Fig. 6.13 (a)] where most of the large-scale fluctuations are observed, and $\delta B_{\perp,2}$ [Fig. 6.13 (b)] where the small-scale fluctuations are developed (also developed in $\delta u_{p\perp,2}$), it is observed that in the extreme cases $\varphi = 10^o$ and 80^o, there is less transferred energy to the

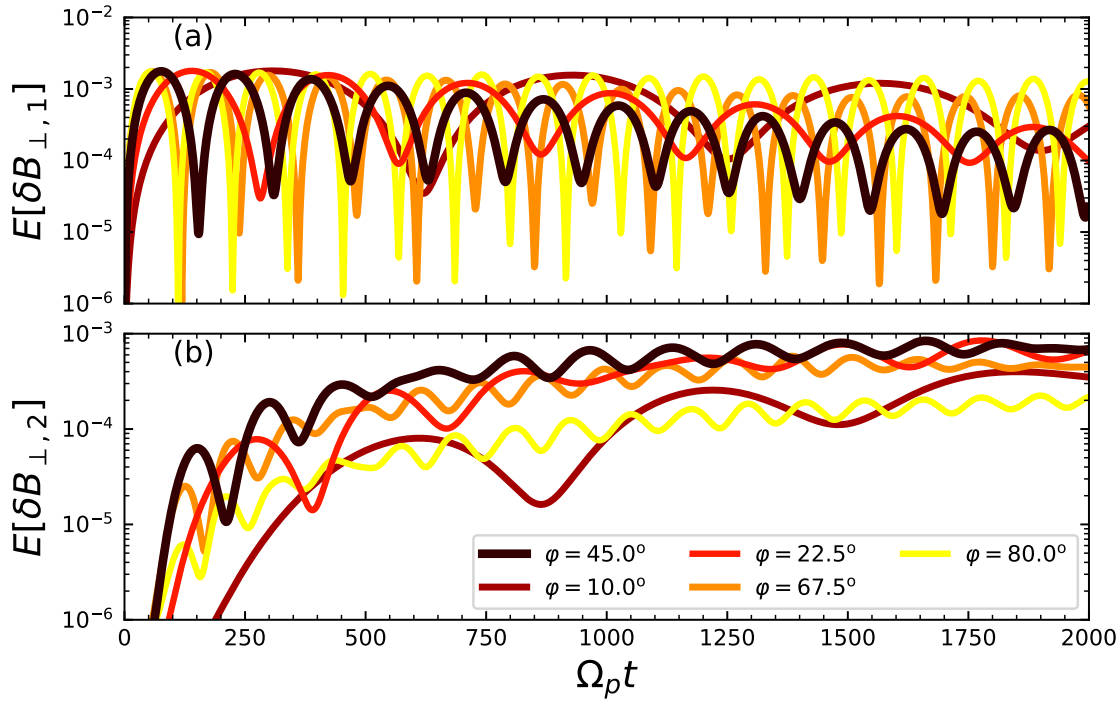

Figure 6.13: Evolution of the magnetic energies of to the components (a) $\delta B_{\perp,1}$, $E\left[\delta B_{\perp,1}\right]$, associated to the large-scale mode, and (b) $\delta B_{\perp,2}$, $E\left[\delta B_{\perp,2}\right]$, associated to the small-scale fluctuations in the inhomogeneous layers for different angles and fixed ratio $l/R = 0.5$, restricting the domain in x to only one of the inhomogeneous layers.

component $\delta B_{\perp,2}$. The energy in the component $\delta B_{\perp,1}$ exhibits the least decay, by the damping rate and the damping time rate estimated from the density fluctuations [Figs. 6.11(a) and (c)], when compared with the intermediate cases of $\varphi = 22.5°$, $45°$, and $67.5°$, where the saturation level for the energy associated to $\delta B_{\perp,2}$ is larger, with a stronger damping in the component $\delta B_{\perp,1}$. This means that magnetic energy is being transferred less efficiently from the large, global scale for the cases with close to zero magnetization and maximum magnetization of the plasma slab.

Further differences are found in the spectral decomposition of the magnetic field

component $\delta B_{\perp,2}$. Signals with a wide range in k_x in the first mode of k_y at $\Omega_p t = 240.05$ in all of the cases of φ are found in the spectra. As the plasmas evolve, signals at larger modes in k_y along with amplitudes growing along k_x appear. The most intense signals are found in the first mode of k_y. During damping, it takes less time for angles close to $\varphi = 45^{\rm o}$ for this range in k_x to extend than for other cases, which agrees with the observed tendency found for the damping time-rate $\tau_{\rm D}/\tau_{\rm P}$ from the simulations [Fig. 6.11 (c)] and with the fast growth in energy in the component $\delta B_{\perp,2}$ [Fig. 6.13 (b)]. Toward the end of the damping, fluctuations at scales with wavenumber $|k_x v_A/\Omega_p| \geq 1$ are present in all of the cases. For $l/R = 0.2$, the range of scales in k_x reached by fluctuations rapidly expands to larger values, $|k_x v_A/\Omega_p| > 1$, at $\Omega_p t = 480.05$.

For angle $\varphi = 80^{\rm o}$ fluctuations reach scales as small as in the case of $\varphi = 45^{\rm o}$ even though the damping time rate is smaller than for the angle $\varphi = 22.5^{\rm o}$ [Fig. 6.11 (c)], and the level of amplitudes observed in the energy of the components $\delta B_{\perp,1}$ and $\delta B_{\perp,2}$ is similar to that for the angle $\varphi = 10^{\rm o}$. As ϕ decreases, a perturbation transverse to the slab causes larger amplitude oscillations than for a more magnetized slab using the same perturbative amplitude $u_0/v_A = 0.1$. Displacements are in the order of the width of the inhomogeneous layers, generating fluctuations with a characteristic scale larger than the length of the layers, rendering the damping of fluctuations as slower.

Regarding the wavenumber range in k_x for signals in the wavevector spectra compared with larger angles φ, the range is reduced, suggesting that resonant absorption is limited and that other processes of non-linear nature may alter the dynamics of the system. Thus, for a fixed perturbative amplitude and if the plasma slab is weakly magnetized, resonant absorption becomes inhibited or rendered less efficient

in transporting energy toward small scales. In the case of a strongly magnetized slab, resonant absorption occurs and energy is transported toward small scales, but most of the energy remains in the large-scale motions. Another factor that may influence the dynamics is that by varying the angle φ, the effective β_p in the plasma changes by a factor $1/\sin^2\varphi$, so that a smaller angle leads to a finite, large β_p, introducing thermal effects in the dynamics.

6.2.4 Scales Reached by Resonant Absorption

Differences in the development of the small-scale fluctuations for different angles φ are observed in the wavevector representations of density fluctuations, the proton bulk velocity, and the magnetic field fluctuations. Figure 6.14 shows the spectral density of the magnetic field energies for the dependency on k_x within the domain of the plasma slabs for the simulated angles φ averaged over k_y, along with the same characteristic scales described for Fig. 6.9 for the ratio $l/R = 0.5$ and instants close to the end and after resonant absorption. As in the case of different ratios l/R, the spatial dependencies of the magnetic field fluctuations and of the proton bulk velocity are similar, so that only the magnetic fluctuations are discussed here. The spectral densities show that peaks appear in the component $\delta B_{\perp,2}$ at scales below the characteristic scales of the density gradient (6.1.4) by the end of damping [instant $\Omega_p t \simeq 1200.05$ in Fig. 6.14] and at times close to the saturation in the energy of the component $\delta B_{\perp,2}$ [Fig. 6.13 (b)].

Fluctuations reach scales in the order of the proton inertial length, being of larger amplitude for angles around $\varphi = 45^{\circ}$. In the component $\delta B_{\perp,1}$, fluctuations tend to be comparable to those of the component $\delta B_{\parallel}$ at scales $k_x v_A/\Omega_p < 1$, and comparable to those of the component $\delta B_{\perp,2}$ at kinetic-scales. In all of the cases, the component

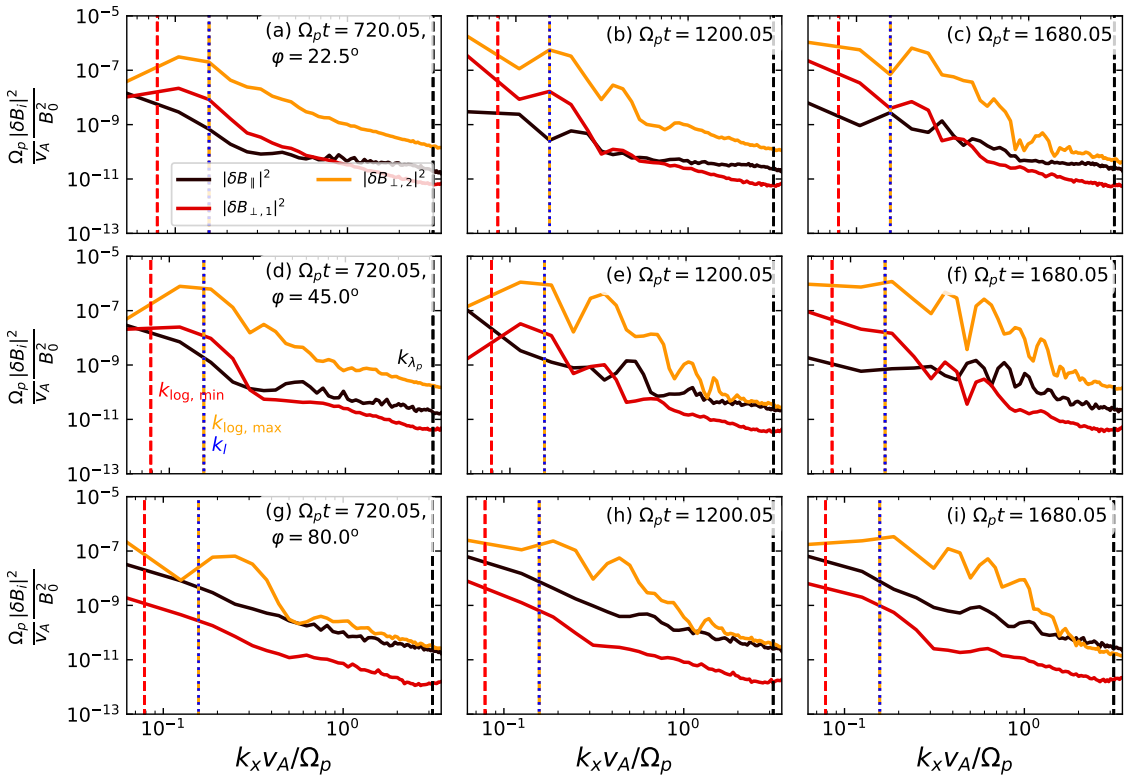

Figure 6.14: Evolution of the spectral density of magnetic field energy fluctuations in the components $\left|\delta B_\parallel\right|^2$ (solid black line), $\left|\delta B_{\perp,1}\right|^2$ (solid red line), and $\left|\delta B_{\perp,2}\right|^2$(solid orange line) for three of the simulated cases of φ (angle varying along columns) at three instants (time-varying across columns) during the process of damping due to resonant absorption. Important scales are shown for each ratio, k_l (dashed blue line, associated with the length of the inhomogeneity), k_{λ_p} (dashed black line, associated with the proton inertial length), and $k_{\log,\max}$, $k_{\log,\min}$ (dotted orange line and dashed red line, respectively, showing the range of scales of the logarithmic derivative). Case of $l/R = 0.5$.

$\delta B_{\perp,1}$ does not exhibit significant features at the end and after resonant absorption. The spectra of the component $\delta B_\parallel$ exhibit peaks growing around scales in the order of the proton inertial length for the intermediate cases $\varphi = 45°$ and $67.5°$. For the case of $l/R = 0.2$ in Fig. 6.15, the spectral densities exhibit features similar to

those observed in the case of $l/R = 0.5$, but with the components $\delta B_{\perp,2}$ and $\delta B_{\parallel}$ exhibiting far more peaks that reach kinetic scales in all of the cases by the end of and after resonant absorption, indicating that more energy has been transferred to scales below and in the order of the proton inertial length, $k_x v_A/\Omega_p = 1$. Therefore, it is observed that most of the energy in the spectra is contained in the component $\delta B_{\perp,2}$, where the level of energy reaching scales in the order of the proton inertial length increases with thinner ratios l/R. In scales such that $k_x v_A/\Omega_p < 1$, both components $\delta B_{\perp,1}$ and $\delta B_{\parallel}$ are of the similar level and below that of the fluctuations in $\delta B_{\perp,2}$; however, at kinetic-scales, the component $\delta B_{\parallel}$ may become relevant and comparable to $\delta B_{\perp,2}$.

Finally, the angle φ also limits the amplitude of the fluctuations reaching kinetic scales, being larger for angles φ far from both 0^{o} and 90^{o}, which coincide with the increase in energy observed in the component $\delta B_{\perp,2}$ in Fig. 6.13 (b). In any case, fluctuations reach kinetic scales after resonant absorption, particularly, scales in the order of the proton inertial length.

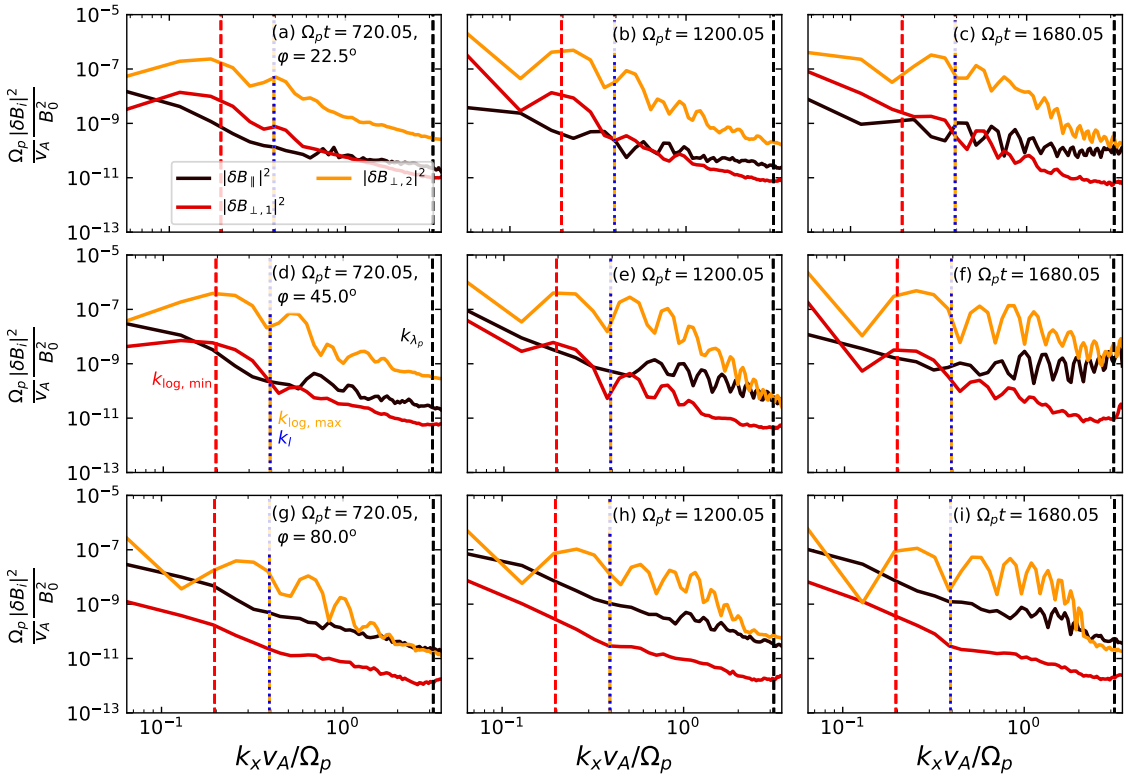

Figure 6.15: Evolution of the spectral density of magnetic field energy fluctuations in the components $\left|\delta B_\parallel\right|^2$(solid black line), $|\delta B_{\perp,1}|^2$(solid red line), and $|\delta B_{\perp,2}|^2$(solid orange line) for three of the simulated cases of φ (angle varying along columns) at three instants (time-varying across columns) during the process of damping due to resonant absorption. Important scales are shown for each ratio, k_l (dashed blue line, associated with the length of the inhomogeneity), k_{λ_p} (dashed black line, associated with the proton inertial length), and $k_{\log,\max}$, $k_{\log,\min}$ (dotted orange line and dashed red line, respectively, showing the range of scales of the logarithmic derivative). Case of $l/R = 0.2$.

Chapter 7

Kinetic Alfvén Waves Induced by Resonant Absorption

7.1 Characterization of Fluctuations at the Layers

7.1.1 Electric and Magnetic Field Fluctuations

Fluctuations generated in the inhomogeneous layers due to resonant absorption are characterized. Among all of the observed cases with fixed angle $\varphi = 45^{\circ}$ and variable ratio l/R, and fixed ratios $l/R = 0.2$ and 0.5 and variable angle φ, it is possible to pin down common features in the observed signals. From the evolution of the magnetic field components (Fig. 6.2), proton bulk-velocity (Fig. 6.5), and of the spectral decompositions of the component $\delta B_{\perp,2}$ (Figs. 6.4, 6.14, and 6.15), it is observed that the fluctuations generated in both inhomogeneous layers are of a wavevector quasi-perpendicular with respect to the background magnetic field $\mathbf{B}_0$, mostly along x. Figure 7.1 shows the evolution of the ratio between the electrostatic to electromagnetic components of the electric field R_E given by Eq. (4.2.14) and the magnetic compressibility C_B, given by Eq. (4.2.15). These quantities are evaluated only on one of the inhomogeneous layers for fixed angle $\varphi = 45^{\circ}$ and variable ratio l/R. It is observed that the electrostatic component of the electric field is larger in all of the cases, with the ratios R_E within the range $0.5 \leq R_E \leq 0.75$, evolving identically for

all of the simulated ratios l/R, differing from each other once resonant absorption has taken place, decreasing in time at a faster rate with smaller ratios l/R. On the other hand, the magnetic compressibility remains small in all the cases, achieving values below $C_B = 0.1$, and increases after resonant absorption has occurred. The rate of this growth is faster for a smaller ratio l/R. Therefore, the fluctuations observed in the inhomogeneous layers are mostly electrostatic and magnetically incompressible, with the electrostatic component and the parallel magnetic fluctuations increasing after resonant absorption has taken place.

For varying angle φ (Fig. 7.2), the same features are observed in the sense of the time-evolution. That is, electric field fluctuations become more electrostatic. On the other hand, magnetic field fluctuations become incompressible after resonant absorption has occurred. In regard with the change in the angle φ, fluctuations become more magnetically compressible and less electrostatic with increasing angle φ, with R_E increasing from ~ 0.4 to 0.9.

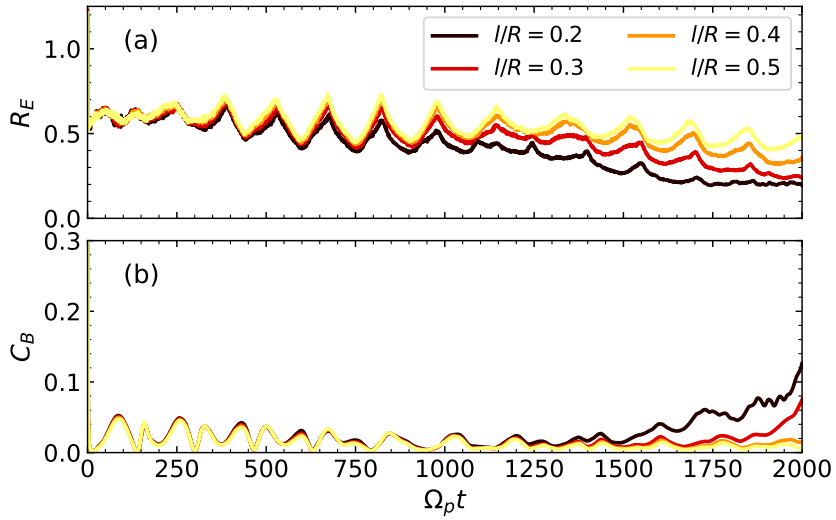

Figure 7.1: Evolution of (a) the averaged ratio R_E (4.2.14) and (b) the averaged magnetic compressibility C_B (4.2.15) for the cases of fixed angle $\varphi = 45^o$ and different ratios l/R. These quantities are evaluated considering only the left inhomogeneous layer of the plasma slab.

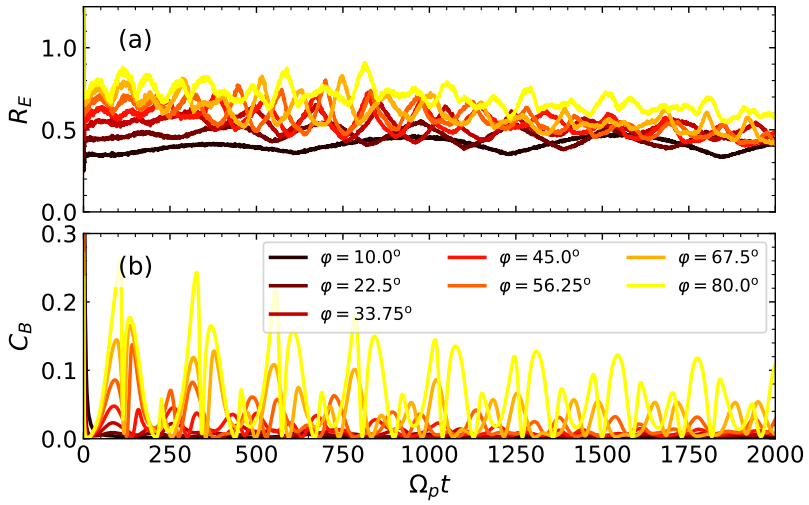

Figure 7.2: Evolution of (a) the averaged ratio R_E (4.2.14) and (b) the averaged magnetic compressibility C_B (4.2.15) for the cases of fixed ratio $l/R = 0.5$ and different angles φ. These quantities are evaluated considering only the left inhomogeneous layer of the plasma slab.

7.1.2 Spectral Analysis of Fluctuations

The structure of the waves can be further decomposed by studying the magnetic helicity of the fluctuations in wavevector space, $\sigma_m(\mathbf{k})$ (4.2.16) [135, 139], at specific instants. The meaning of the signature of the magnetic helicity is illustrated in subsection 4.2, for KAWs properties, and schematically shown in Fig. (4.1).

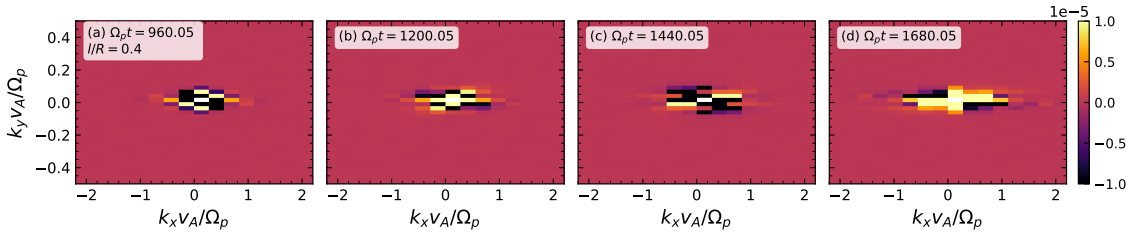

Figure 7.3: Spectral density of the magnetic helicity in wavevector space (4.2.15) considering a range which involves only the left inhomogeneous layer of the plasma slab for the Fourier transform in k_x. Four instants are shown (time-varying across columns) during and after resonant absorption for fixed angle $\varphi = 45^{\text{o}}$ and ratio $l/R = 0.4$.

The spectral density of the magnetic helicity is shown in Fig. 7.3 for a domain in x considering only the left inhomogeneous layer for $\varphi = 45^{\text{o}}$ and $l/R = 0.4$. It indicates that most of the fluctuations acquire a distinctive pattern. The quasi-perpendicular fluctuations in quadrants I ($k_x, k_y > 0$) and III ($k_x, k_y < 0$) have $\sigma_m > 0$. Those in quadrants II ($k_x < 0$, $k_y > 0$) and IV ($k_x > 0$, $k_y < 0$) have $\sigma_m < 0$, in the layer. This pattern is observed in all of the cases of fixed angle $\varphi = 45^{\text{o}}$ and variable ratio l/R, with stronger signatures at larger wavenumbers k_x and k_y. For different angles φ, this pattern is fully developed for angles $33.75^{\text{o}} \leq \varphi \leq 80^{\text{o}}$ for both ratios $l/R = 0.2$ and 0.5. The intensity of the helicity of waves in quadrants I and III becomes smaller for larger angles.

Because most of the fluctuations in the magnetic field related to small-scale propagating structures within the inhomogeneous layers of the plasma slab are found in the component $\delta B_{\perp,2}$, it is possible to associate the previously observed features to this component. The direction of propagation of each of the waves composing those structures, and thus the polarization of those waves can be determined by studying the dispersion relation of the component $\delta B_{\perp,2}$ in the space $\omega_r - k_x$ averaged over k_y (Fig. 7.4 for fixed angle $\varphi = 45^{\text{o}}$ and variable ratio l/R). The frequency domain is constructed in the same way as in the analyses of previous sections, but using a time-window $\Omega_p \Delta t_w = 800$. Based on the procedure described in subsection 5.3.2, the waves found in the inhomogeneous layers have a direction of propagation predominantly in the direction of the equilibrium density gradient on each layer ($\omega_r k_x/k^2 > 0$ in the left layer, and $\omega_r k_x/k^2 < 0$ in the right layer). In the cases of $l/R \leq 0.3$, fluctuations grow which propagate in the opposite direction ($\omega_r k_x/k^2 < 0$ in the left layer, and $\omega_r k_x/k^2 > 0$ in the right layer). Because the averaging over k_y is performed over strictly positive quantities, the dispersion relation plots indicate that the sign of the frequency depends mainly on the sign of k_x. We focus on the left layer. Fluctuations projected in the wavevector plane with $k_x > 0$ propagate parallel to $\mathbf{B}_0$ for $k_\parallel = k_y \sin\varphi > 0$ (quadrant I) and antiparallel to $\mathbf{B}_0$ for $k_y \sin\varphi < 0$ (quadrant IV). The opposite picture is observed for $k_x < 0$ (quadrants II and III, respectively).

The same analysis on fluctuations in the right layer provides (see Fig. 7.5, which shows the same as Fig. 7.4 but for a domain in x restricted to the right layer) the interpretation of waves with identical properties, with propagation in the direction of $-x$. In this sense, the fluctuations in the inhomogeneous layers are mainly described by waves which propagate quasi-perpendicularly along x, parallel to the density gradient, being counterpropagating along $\mathbf{B}_0$. Based on these results, we verify the

relation $B_0\sigma_m(\mathbf{k})(\omega_r/k_\parallel) > 0$, which means that most of these signals have right-hand polarization in the plasma physics sense [with respect to the direction of $\mathbf{B}_0$] [135]. This discards the left-hand polarized kinetic slow mode (KSM) [134, 137, 141, 143] as a major constituent of the fluctuations.

Concerning the frequency, the dispersion relation plots show signals of nearly constant frequency at $|\omega_r/\Omega_p| \simeq 2\times10^{-2}$ caused by the dependency on k_y (not shown here). In these regions, we observe signals with the highest intensities in the first modes in k_x. As the plasmas evolve, the lines are overshadowed by other fluctuations. These features are also observed in the dispersion relation plots of the component $\delta B_{\perp,2}$ for fixed ratios $l/R = 0.2$ and 0.5 and angles in the range $22.5^\text{o} \leq \varphi \leq 80^\text{o}$ (see Fig. 7.6 for $l/R = 0.5$ and the left inhomogeneous layer). Signals at $\omega_r = \omega_\text{KAW}$ become weaker at $\varphi = 80^\text{o}$, which is consistent with the less pronounced structures in the layers. Because these fluctuations have quasi-perpendicular wavevectors and most of these plasmas involve low β_p, we compare these signals with the frequency predicted for KAWs in the limit of low β_p and neglecting the effect of electrons [130],

$$\frac{\omega_\text{KAW}}{\Omega_p} = \frac{v_{Ap}(x)}{v_A}\frac{k_{y0}v_A}{\Omega_p}\sin\varphi\sqrt{1+\frac{k_x^2v_A^2}{2\Omega_p^2}\beta_p}. \tag{7.1.1}$$

This frequency is shown as a function of k_x in the dispersion relation plots (white dashed lines), considering propagation parallel and antiparallel to $\mathbf{B}_0$. The frequency is evaluated with densities, Alfvén speeds, and β_p of the external medium and the plasma slab, separatedly. The used parameters are $1 \leq v_{Ap}/v_A \leq \sqrt{2}$, $0.01 \leq \beta_p \leq 0.0125$, and wavenumber $k_{y0} = 2\pi/L_y$, where most of the energy is stored in k_y. The plots show that these intense signals have frequencies which can be described by Equation (7.1.1). This discards the presence of other right-hand polarized waves,

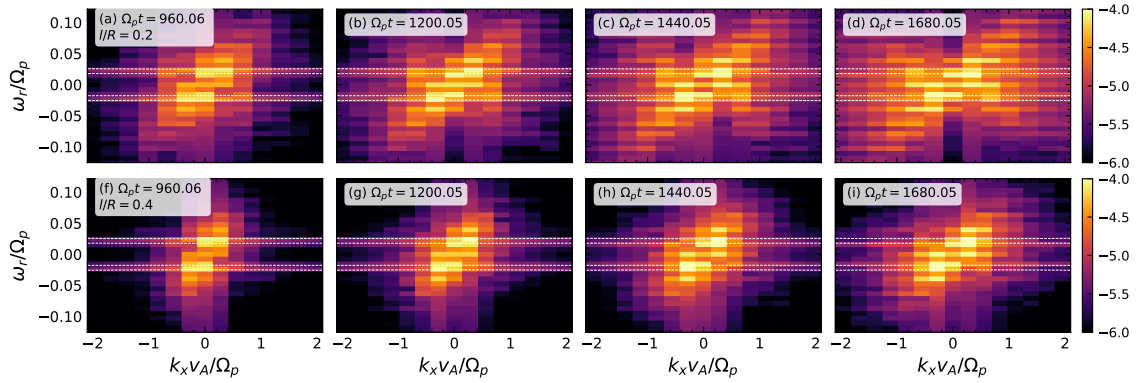

Figure 7.4: Dispersion relation of the component $\delta B_{\perp,2}$ of the magnetic field fluctuations in $\omega_r - k_x$ space, averaged over k_y. The domain in x considers only the left inhomogeneous layer in all of the cases. Four instants are shown (time-varying across columns) during and after resonant absorption for fixed angle $\varphi = 45^{\circ}$ and ratios $l/R = 0.2$, 0.4 (ratio varying along columns). Dashed, white lines represent frequencies given by the KAW dispersion relation (7.1.1).

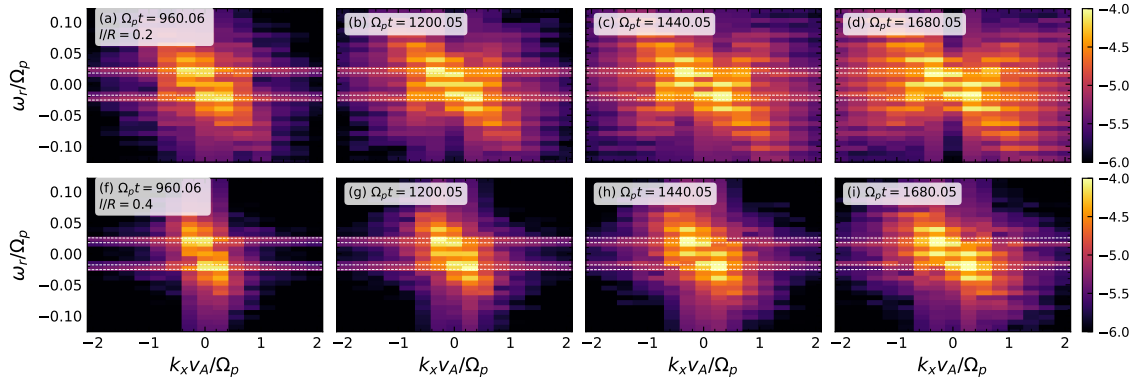

Figure 7.5: Dispersion relation of the component $\delta B_{\perp,2}$ of the magnetic field fluctuations in $\omega_r - k_x$ space, averaged over k_y. The domain in x considers only the right inhomogeneous layer in all of the cases. Four instants are shown (time-varying across columns) during and after resonant absorption for fixed angle $\varphi = 45^{\circ}$ and ratios $l/R = 0.2$, 0.4 (ratio varying along columns). Dashed, white lines represent frequencies given by the KAW dispersion relation (7.1.1).

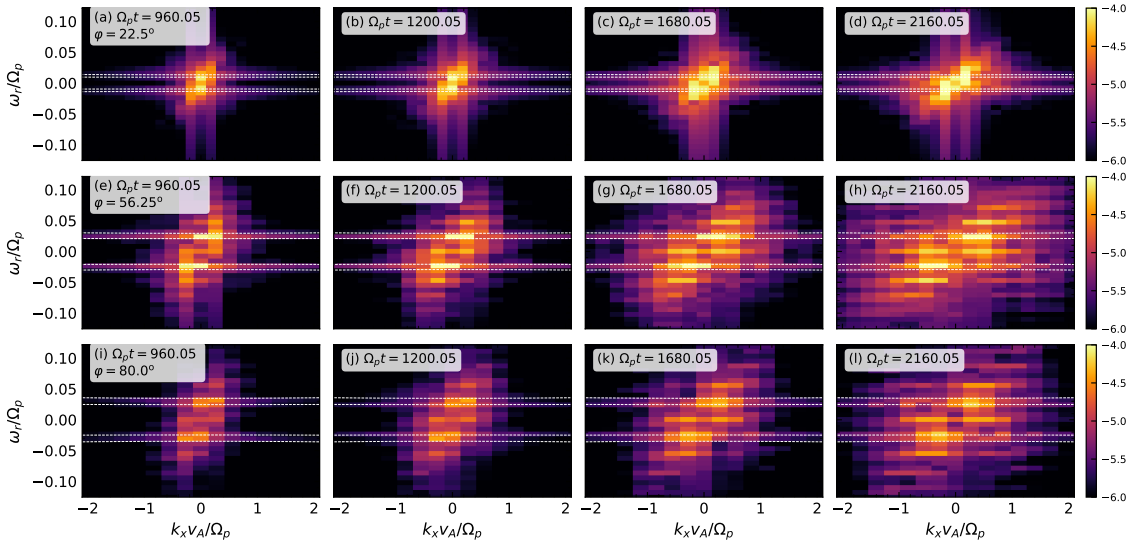

Figure 7.6: Dispersion relation of the component $\delta B_{\perp,2}$ of the magnetic field fluctuations in $\omega_r - k_x$ space, averaged over k_y. The domain in x considers only the left inhomogeneous layer in all of the cases. Four instants are shown (time-varying across columns) during and after resonant absorption for fixed ratio $l/R = 0.5$ and angles $\varphi = 22.5°$, $56.25°$, and $80°$ (angle varying along columns). Dashed, white lines represent frequencies given by the KAW dispersion relation (7.1.1).

such as the fast/magnetosonic mode, of higher frequency. By changing the angle φ, discrepancies are found for linear prediction, particularly with angles $\varphi < 33.75°$.

We compute the group velocity associated to Eq. (7.1.1), $\mathbf{v}_{g,\mathrm{KAW}} = \nabla_{\mathbf{k}} [\pm\omega_{\mathrm{KAW}}]$ given explicitly by Eq. (4.2.10). We find that wave-packets of KAW nature on each layer have non-zero group velocity along x, $|v_{gx,\mathrm{KAW}}| \sim 10^{-4} v_A$ moving inward the slab, which is consistent with the fluctuations in $\delta B_{\perp,2}$ remaining fairly localized within the inhomogeneous layers during the whole simulation [Figs. 6.2 (k) to (o)]. The group velocity along y is also non-zero, but the counter-propagating nature of the waves leads to structures stationary in y.

The signals propagating in the direction $-x$ ($\omega_r k_x/k^2 < 0$) for $l/R \leq 0.3$ in

Fig. 7.4 are not represented by KAWs in the same way as those propagating in the direction $+x$. For variable angle, the regions with the most intense signals are well represented as structures associated with a main KAW mode only for the range $33.75^{\circ} \leq \varphi \leq 80^{\circ}$ [Figs. 7.6 (e) to (l)]. At $\varphi = 22.5^{\circ}$ signatures are not fully developed and appear latter ($\Omega_p t > 1200.05$) [Figs. 7.6 (a) to (d)].

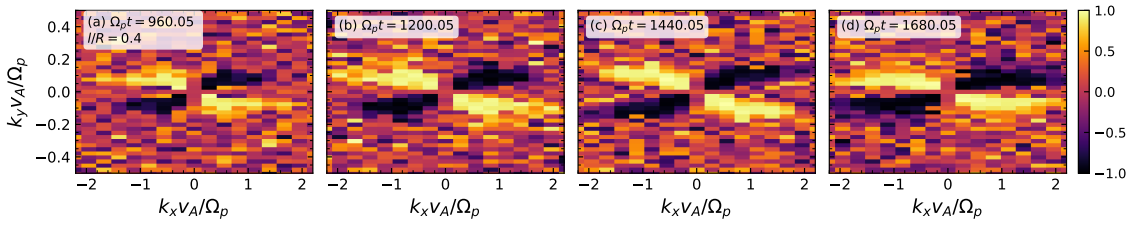

Figure 7.7: Spectral density of the normalized cross helicity in wavevector space (4.2.17) considering a range which involves only the left inhomogeneous layer of the plasma slab for the Fourier transform in k_x. Four instants are shown (time-varying across columns) during and after resonant absorption for fixed angle $\varphi = 45^{\circ}$ and ratio $l/R = 0.4$.

The properties computed for the observed fluctuations strongly suggest that KAWs [130, 137, 140, 163] are being generated in the inhomogeneous layers due to resonant absorption. Other correlation quantities are studied to confirm the nature of the fluctuations, such as the normalized cross helicity σ_c (4.2.17), proton compressibility C_p (4.2.18), and the Alfvén ratio r_{Alfven} (4.2.19) in the wavevector space. These quantities are respectively shown in Figs. 7.7, 7.8, and 7.9 at the same instants for fixed angle $\varphi = 45^{\circ}$ and ratio $l/R = 0.4$ in the left inhomogeneous layer.

Coherent signatures are observed in the normalized cross-helicity (Fig. 7.7) in the range where the quasi-perpendicular fluctuations appear. For all l/R, the waves located in the quadrants I and III have negative cross-helicity, meaning that the proton bulk velocity fluctuations and the magnetic field fluctuations are anti-correlated.

Signals in the quadrants II and IV have positive cross-helicity, but the interpretation is the opposite because of fluctuations in this quadrant propagate antiparallel to $\mathbf{B}_0$ [135]. These values are characteristic of quasi-perpendicular KAWs [137] and sustain the relation $\sigma_m\sigma_c < 0$ for waves with right-hand polarization in the plasma physics sense [135].

Signals in the proton compressibility (Fig. 7.8) indicate that the quasi-perpendicular fluctuations generated in the inhomogeneous layer have compressibility C_p ranging in the order of ~ 0.1 to 1, which is fairly within the range provided for KAWs [137]. The pattern observed for different ratios l/R with fixed angle $\varphi = 45^{\text{o}}$ is extended toward larger wavenumbers k_x as the plasmas evolve, occupying a wide range after resonant absorption has occurred. The pattern does not exhibit significant differences by fixing the ratio l/R and changing the angle φ within the range $33.75^{\text{o}} \leq \varphi \leq 80^{\text{o}}$.

The Alfvén ratio r_{Alfven} is shown in Fig. 7.9 for fixed angle φ and variable ratio l/R. It is found that for the fluctuations that are observed in the wavevector spectra of $\delta B_{\perp,2}$, the Alfvén ratio ranges from ~ 0.3 to 3, suggesting that fluctuations are of Alfvénic nature [134, 137, 142]. The values of these ratios are far from those of other modes, such as the KSM [134, 137, 141, 143]. The same conclusions are drawn for the right inhomogeneous layer in all of the other cases. Based on this analysis, we conclude that within both inhomogeneous layers of the plasma slab associated to the proton density holes, KAWs are the main constituent of the fluctuations that are generated once resonant absorption has occurred and energy has reached kinetic scales.

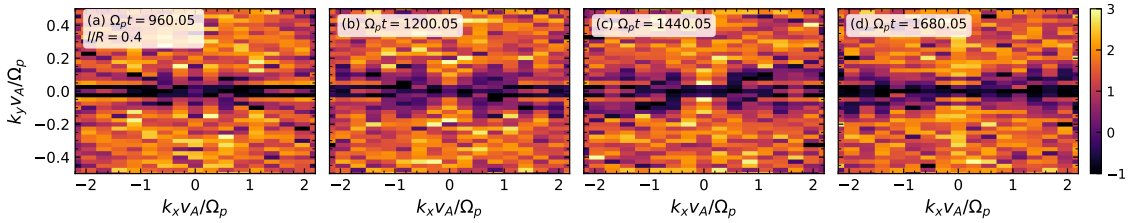

Figure 7.8: Spectral density of the proton compressibility in log-scale in wavevector space (4.2.18) considering a range which involves only the left inhomogeneous layer of the plasma slab for the Fourier transform in k_x. Four instants are shown (time-varying across columns) during and after resonant absorption for fixed angle $\varphi = 45^{\text{o}}$ and ratio $l/R = 0.4$.

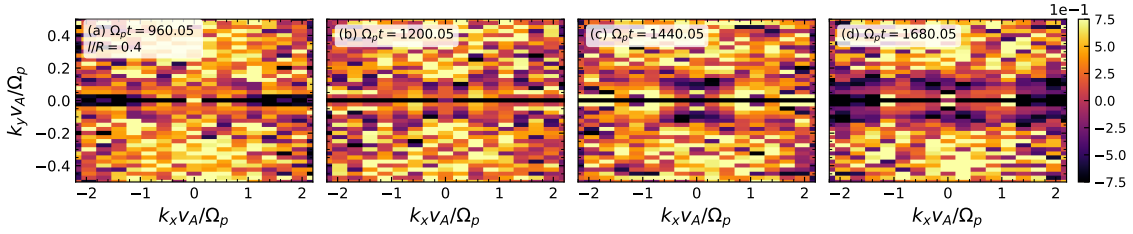

Figure 7.9: Spectral density of the Alfvén ratio in log-scale in wavevector space (4.2.19) considering a range which involves only the left inhomogeneous layer of the plasma slab for the Fourier transform in k_x. Four instants are shown (time-varying across columns) during and after resonant absorption for fixed angle $\varphi = 45^{\text{o}}$ and ratio $l/R = 0.4$.

7.1.3 Kink Oscillations and KAWs

Two different wave modes linked by resonant absorption are found to be linked: kink oscillations, which occur transverse to the background magnetic field at large scales, and KAWs associated with small-scale fluctuations excited in the zones of resonance. We also found that the frequency of the kink oscillations [Fig. 6.8 (b) for fixed angle $\varphi = 45^{\rm o}$, and Fig. 6.11 (b) for fixed ratios l/R] and the frequency measured in the dispersion relation plots ($\omega_r - k_x$) of the magnetic field fluctuations $\delta B_{\perp,2}$ associated to KAWs are identical in time (Fig. 7.4 for the left and Fig. 7.5 for the right layers for angle $\varphi = 45^{\rm o}$ and different ratios l/R, and Fig. 7.6 for $l/R = 0.5$ and different angles). This means that resonant absorption leads to both large-scale kink oscillations and to small-scale fluctuations of a different nature and oscillation phase, but with the same frequency. In the following discussions, these frequencies will be referred to as $\omega_{\rm kink}$ and $\omega_{\rm KAW}$, which are the most important frequencies in the simulations.

The coincidence of these frequencies is shown in Fig. 7.10. This corresponds to dispersion relation of δn_p in $\omega_r - k_y$ averaged on k_x considering a domain containing the slab and both layers for angle $\varphi = 45^{\rm o}$ and different ratios l/R. The signals of the excited mode k_{y0} (fundamental mode) are well represented by the frequencies $\omega_{\rm KAW}$ of the KAWs (4.2.9). This frequency uses k_x as computed for Fig. 7.4. The same is shown in Fig. 7.11 for fixed ratio $l/R = 0.5$ for three angles φ. These plots use $\omega_{\rm KAW}$ with k_x as computed for Fig. 7.6. This coincidence occurs for the dispersion relation $\omega_r - k_y$ of δu_{px}. The time-domains $\Omega_p \Delta t_w$ in both Figures is the same used to determine the frequency $\omega_{\rm SIM}$ in Figs. 6.8 (b) and 6.11 (b).

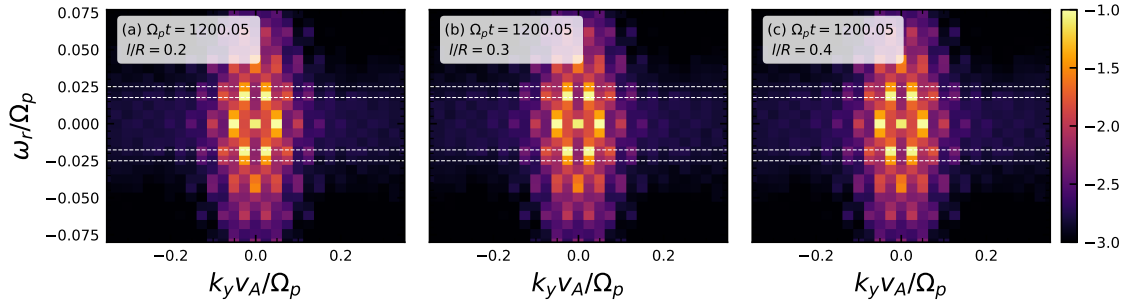

Figure 7.10: Dispersion relation of the component δn_p of the magnetic field fluctuations in $\omega_r - k_y$ space, averaged over k_y. The domain in x considers the slab with both inhomogeneous layers. The time-domain considers the instants where resonant absorption occurs. Three ratios l/R are shown (ratio varying across columns) for fixed angle $\varphi = 45^o$. Dashed, white lines represent frequencies given by the KAW dispersion relation (7.1.1).

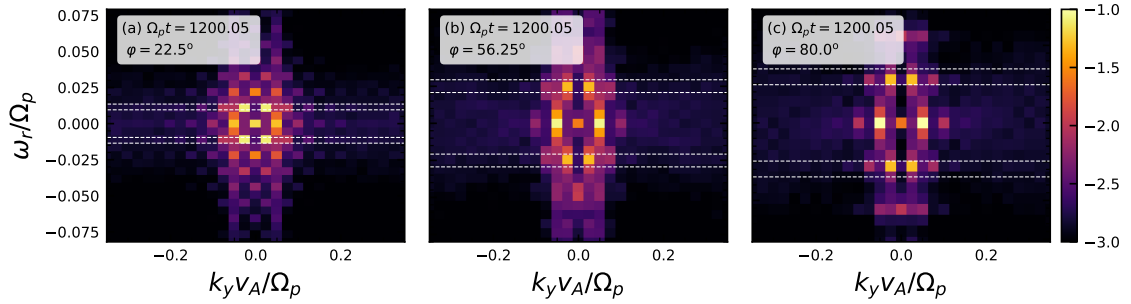

Figure 7.11: Dispersion relation of the component δn_p of the magnetic field fluctuations in $\omega_r - k_y$ space, averaged over k_y. The domain in x considers the slab with both inhomogeneous layers. The time-domain considers the instants where resonant absorption occurs. Three angles φ are shown (angles varying across columns) for fixed ratio $l/R = 0.5$. Dashed, white lines represent frequencies given by the KAW dispersion relation (7.1.1).

Chapter 8

Kinetic Processes Induced by Resonant Absorption - Parallel Dynamics

8.1 Parallel Fluctuations

Resonant absorption generates small-scale structures around the resonant magnetic field lines in the inhomogeneous layers. They appear as density holes or cavities, and density enhancements or winglets in the proton density. They are commonly associated with particle acceleration, heating, and the localization of magnetic fluctuations [11, 49, 51]. For $l/R = 0.4$, Fig. 8.1 (a) shows a Fourier decomposition of the density fluctuations $\delta n_p = n_p - n_{0p}$ in k_y at section x in the middle of the inhomogeneous layer, $x\Omega_p/v_A \simeq 46$. We find that fluctuations at wavenumber $2k_{y0}$ emerge around $\Omega_p t \simeq 800$. They appear while the mode k_{y0} decays exponentially due to resonant absorption of kink oscillations. Mode $2k_{y0}$ is coincident with structures repeated twice along y, which is consistent with the pattern of the cavities and winglets in density. This behavior is present in all the simulations for different ratios l/R.

Electric field fluctuations $\delta E_\parallel$ parallel to $\mathbf{B}_0$ are observed to be confined to the inhomogeneous layers. The largest amplitudes occur at the density winglets ($y = y_2$) and at the density cavities ($y = y_1$). Thus, they are likewise associated with the mode $2k_{y0}$. The Fourier decomposition in k_x of $\delta E_\parallel$ in Fig. 8.1 (b), taken at a winglet of

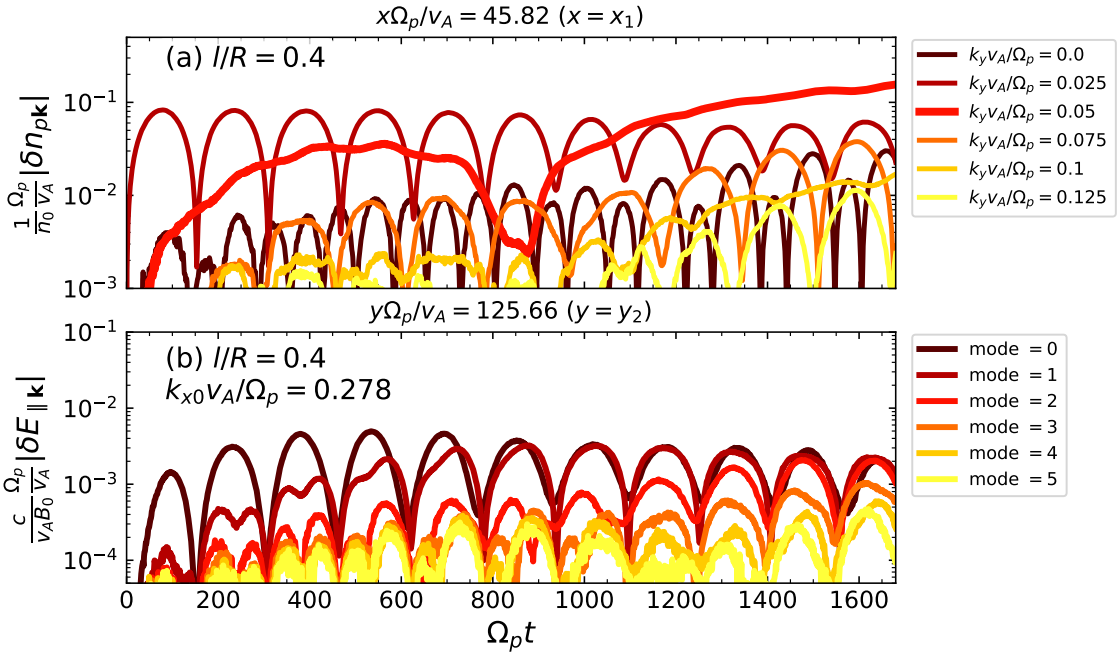

Figure 8.1: Fourier decomposition in (a) k_y of the density fluctuations $\delta n_p = n_p - n_{0p}$ at a fixed location $x = x_1$ in the left inhomogeneous layer, and (b) in k_x of the parallel electric field fluctuations $\delta E_\parallel$ at the left inhomogeneous layer for a fixed section $y = y_2$ at the center of a density winglet. Here, $l/R = 0.4$. The mode of interest are $k_y v_A/\Omega_p = 2k_{y0}v_A/\Omega_p = 0.05$, and the modes 0 and 1 in k_x.

the left layer, shows the fundamental mode k_{x0} growing. This mode reaches the same amplitude as the mean value ($k_x = 0$). The mode $2k_{x0}$ begins to grow at $\Omega_p t \simeq 800$, corresponding to the signature of the formation of small-scale electric field structures inside the layers, concurrent with the density structure driven by resonant absorption.

Now, we investigate the origin of $\delta E_\parallel$. Figure 8.2 shows dispersion relation diagrams in $\omega_r - k_y$ for δn_p [(a) to (c)], $\delta E_\parallel$ [(d) to (f)], and the parallel bulk velocity $\delta u_{p\parallel}$ [(g) to (h)]. The domain in x is restricted to the left layer. The k_{y0} mode component

of the density fluctuations, associated to exponentially damped kink oscillations, has frequency $|\omega_r| = \omega_{\text{kink}}$. At later times, nonpropagating modes at $|k_y| = 2k_{y0}$ grow, consistent with the formation of density structures. In $\delta E_\parallel$, four dominant nonpropagating signals with zero frequency and wavenumber $|k_y| = 2k_{y0}$, and signals with frequency $|\omega_r| = 2\omega_{\text{KAW}}$, and wavenumber $k_y = 0$. The decomposition of $\delta u_{p\parallel}$ has the strongest power in the same modes, $2k_{y0}$.

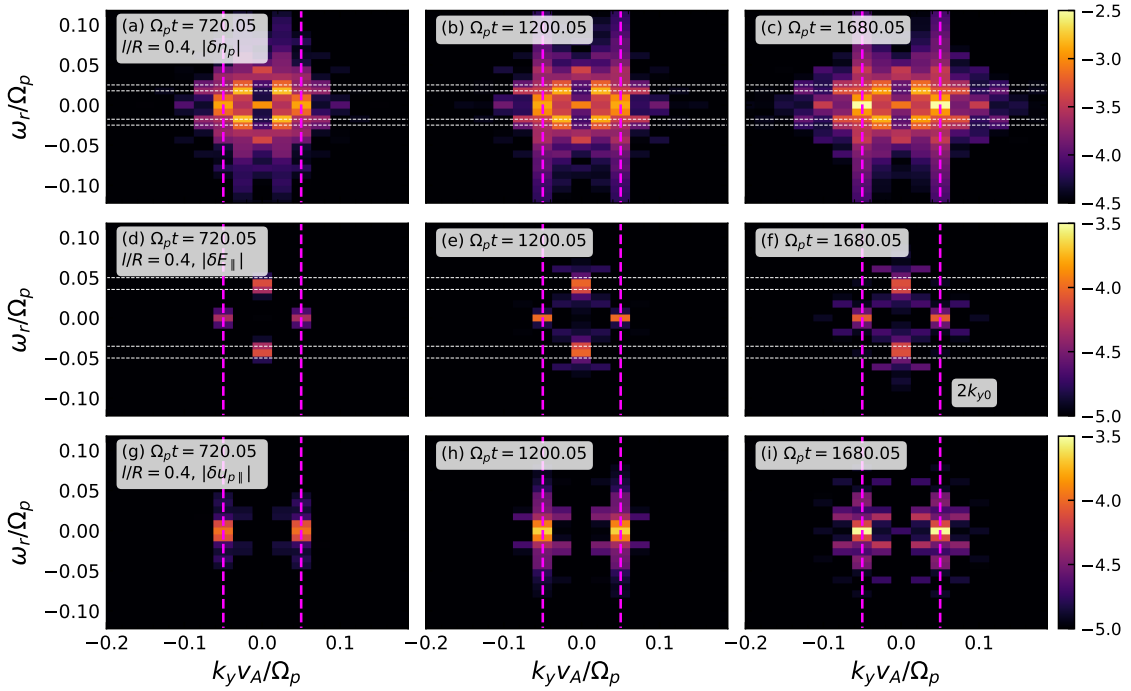

Figure 8.2: Fourier decomposition in $\omega_r - k_y$ space for (a)–(c) density fluctuations $\delta n_p = n_p - n_{0p}$, (d)–(f) parallel electric field fluctuations $\delta E_\parallel$, and (g)–(i) proton parallel-bulk velocity component $\delta u_{p\parallel}$. The Fourier transform in k_x is restricted to a domain containing solely the left side of the inhomogeneous layer, averaged over k_x. Pink lines indicate the mode $k_y = 2k_{y0}$. White lines indicate frequencies (a)–(c) ω_{KAW}, and (d)–(f) $2\omega_{\text{KAW}}$. The frequency ω_{KAW} is the theoretical frequency of KAWs from the Hall-MHD model, Equation (7.1.1).

Similar signals are found in studies of non-linear interaction of counterpropa-

gating circularly-polarized Alfvén waves in homogeneous plasmas [46, 47]. Following Mottez [47], we show that electric fields transverse to the local field lines $\mathbf{B}$ generate a field $\delta E_{\parallel}$ when projected onto $\mathbf{B}_0$. The fields are associated to counterpropagating waves along the background field. Then, we estimate the expected spectral content of $\delta E_{\parallel}$ in $\omega_r - k_y$ space analytically, and compare it with Figs. 8.2 (d) to (f). The agreement suggests that the parallel electric field is predominantly generated by such coupling. Simultaneously, the non-linear coupling leads to the formation of the density structures. This mechanism is operative for all the tested ratios l/R. Finally, the effects of $\delta E_{\parallel}$ on the proton distribution functions are examined.

Because the analysis of Mottez [47] applies to elliptically polarized waves of any mode of parallel propagation, a more detailed characterization of the electromagnetic field in the layers is required.

8.2 Non-linear Wave Coupling

8.2.1 Definition of the Magnetic Field and Rotations

We present the calculations of Mottez [47] and adapt them to the present oblique, and inhomogeneous configuration. We implement the rotations between the axes aligned with the background magnetic field $\mathbf{B}_0$ ($e_{\parallel}$, $e_{\perp,1}$, $e_{\perp,2}$; see Appendix A.1 for the definition of these three directions) and the local total magnetic field line $\mathbf{B} = \mathbf{B}_0 + \delta\mathbf{B}$ ($e^L_{\parallel}$, $e^L_{\perp,1}$, $e^L_{\perp,2}$; superscript L), as shown in Fig. 8.3.

8.2.2 Definition of the Magnetic Field and Rotations

In the derivation by Mottez [47], they considered parallel propagating waves. Here, we consider oblique propagation and dependency on x due to the presence of a

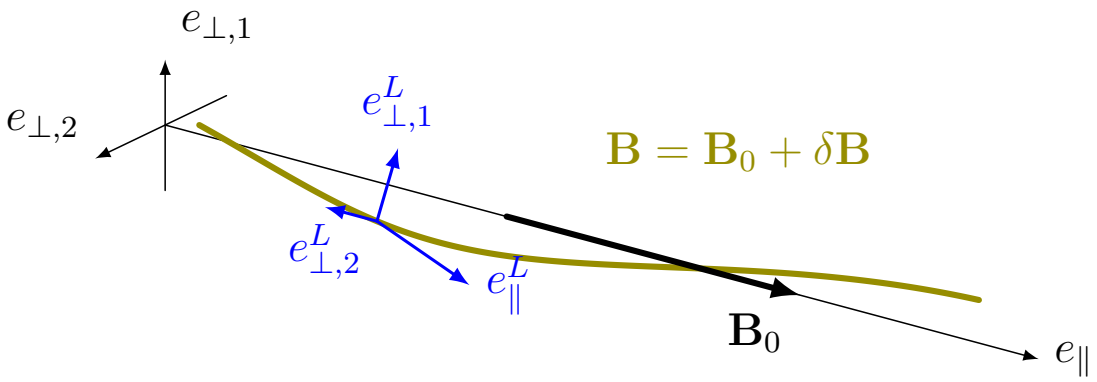

Figure 8.3: Scheme of the axes aligned with the background magnetic field $\mathbf{B}_0$ (black, $e_\parallel$, $e_{\perp,1}$, $e_{\perp,2}$) and the local axes of the magnetic field lines $\mathbf{B}$ (blue, $e^L_\parallel$, $e^L_{\perp,1}$, $e^L_{\perp,2}$) used to study the non-linear coupling of counterpropagating waves based on Mottez [47].

density gradient in that direction. The magnetic field components in the axes of the field $\mathbf{B}_0$ for an elliptically polarized wave are

$$
\begin{aligned}
B_\parallel &= B_0 + \delta B_\parallel(x,y,t), \\
\delta B_{\perp,1} &= \sum_\sigma B^\sigma_{\perp,1}(x)\cos\left[\omega^\sigma(x)t - k^\sigma_y y + \phi^\sigma_{B\perp,1}\right], \qquad (8.2.1)\\
\delta B_{\perp,2} &= \sum_\sigma B^\sigma_{\perp,2}(x)\cos\left[\omega^\sigma(x)t - k^l_y y + \phi^\sigma_{B\perp,2}\right], \qquad (8.2.2)
\end{aligned}
$$

where the sum is over forward propagation in y ($\sigma = A$) and backward proapgation in y ($\sigma = B$). Generally, they have different wavenumbers k_y and frequencies $\omega(x)$ from each other. Here, $\phi^\sigma_{B\perp,2} = \phi^\sigma_{B\perp,1} + n_\sigma\pi/2$, $B^\sigma_{\perp,1} \neq B^\sigma_{\perp,2}$, and $n_\sigma = \pm 1$ depending on the sense of polarization in the plasma physics sense. Geometrically, displacements along a magnetic field line satisfy

$$\frac{\mathrm{d}r_{\parallel}}{B_{\parallel}} = \frac{\mathrm{d}r_{\perp,1}}{\delta B_{\perp,1}} = \frac{\mathrm{d}r_{\perp,2}}{\delta B_{\perp,2}},$$

where $\mathrm{d}r_{\parallel}$ is an infinitesimal displacement along the direction aligned with $B_{\parallel}$ ($e_{\parallel}$ in Fig. 8.3), $\mathrm{d}r_{\perp,1}$ is directed along the density gradient ($e_{\perp,1}$ in Fig. 8.3), and $\mathrm{d}r_{\perp,2}$ is aligned in the remaining perpendicular direction ($e_{\perp,2}$ in Fig. 8.3). Following Mottez [47], the angles of such rotation $\theta_{\perp,i}$ are given by,

$$\frac{\mathrm{d}r_{\perp,1}}{\mathrm{d}r_{\parallel}} = \frac{\delta B_{\perp,1}}{B_{\parallel}} = \tan\theta_{\perp,1},$$
$$\frac{\mathrm{d}r_{\perp,2}}{\mathrm{d}r_{\parallel}} = \frac{\delta B_{\perp,2}}{B_{\parallel}} = \tan\theta_{\perp,2}.$$

In the case of negligible curvature, the transverse magnetic field components implies that $|\delta B_{\perp,i}| \ll B_{\parallel}$, and small angles $\theta_{\perp,j}$. Furthermore, we consider $\left|\delta B_{\parallel}\right| \ll B_0$. This transforms the element $\mathrm{d}r_{\parallel}$ to a displacement in the direction of the background field $\mathbf{B}_0$. The unit vectors for the transformations are defined to first order in $\theta_{\perp,j}$,

$$\widehat{\mathbf{e}}^{L}_{\parallel} = \widehat{\mathbf{e}}_{\parallel} + \theta_{\perp,1}\widehat{\mathbf{e}}_{\perp,1} + \theta_{\perp,2}\widehat{\mathbf{e}}_{\perp,2}, \tag{8.2.3}$$
$$\widehat{\mathbf{e}}^{L}_{\perp,1} = \widehat{\mathbf{e}}_{\perp,1} + \theta_{\perp,1}\widehat{\mathbf{e}}_{\parallel}, \tag{8.2.4}$$
$$\widehat{\mathbf{e}}^{L}_{\perp,2} = \widehat{\mathbf{e}}_{\perp,2} + \theta_{\perp,2}\widehat{\mathbf{e}}_{\parallel}. \tag{8.2.5}$$

These vectors provide the rotation needed to project the local-field quantities (superscript L) onto the backgroind field axes. The inverse transformations of the unitary

vectors are

$$\widehat{\mathbf{e}}_{\parallel} = \widehat{\mathbf{e}}^{L}_{\parallel} - \theta_{\perp,1}\widehat{\mathbf{e}}^{L}_{\perp,1} - \theta_{\perp,2}\widehat{\mathbf{e}}^{L}_{\perp,2}, \tag{8.2.6}$$

$$\widehat{\mathbf{e}}_{\perp,1} = \widehat{\mathbf{e}}^{L}_{\perp,1} - \theta_{\perp,1}\widehat{\mathbf{e}}^{L}_{\parallel}, \tag{8.2.7}$$

$$\widehat{\mathbf{e}}_{\perp,2} = \widehat{\mathbf{e}}^{L}_{\perp,2} - \theta_{\perp,2}\widehat{\mathbf{e}}^{L}_{\parallel}. \tag{8.2.8}$$

from the axes defined along the magnetic field lines $\mathbf{B}$, to the axes of the background magnetic field $\mathbf{B}_0$.

8.2.3 Definition of the Electric Field

Mottez [47] studied the mechanism of parallel acceleration by Alfvén waves [46, 164, 165]. In this case, the electric and magnetic fields are orthogonal. We expand such electric field in the local-field axes

$$\begin{aligned}
\delta E^{L}_{\parallel} &= 0, \\
\delta E^{L}_{\perp,1} &= \sum_{j} E^{Lj}_{\perp,1}(x) \cos\left[\omega^{j}(x)t - k^{j}_{y}y + \phi^{j}_{E\perp,1}\right], \qquad (8.2.9) \\
\delta E^{L}_{\perp,2} &= \sum_{j} E^{Lj}_{\perp,2}(x) \cos\left[\omega^{j}(x)t - k^{j}_{y}y + \phi^{j}_{E\perp,2}\right]. \qquad (8.2.10)
\end{aligned}$$

This electric field is also a superposition of forward- and backward- propagating waves.

8.2.4 General Component Equations

The amplitudes can be written in terms of the magnetic field amplitudes in the axes of $\mathbf{B}_0$ by using the induction law,

$$\frac{1}{c}\frac{\partial \mathbf{B}}{\partial t} = -\nabla \times \mathbf{E}. \tag{8.2.11}$$

The components yield

$$\frac{1}{c}\frac{\partial B_{\parallel}}{\partial t} = \frac{\partial \delta E_{\perp,2}}{\partial x} - \cos\varphi \frac{\partial \delta E_{\perp,1}}{\partial y}, \tag{8.2.12}$$

$$\frac{1}{c}\frac{\partial \delta B_{\perp,1}}{\partial t} = \cos\varphi \frac{\partial \delta E_{\parallel}}{\partial y} + \sin\varphi \frac{\partial \delta E_{\perp,2}}{\partial y}, \tag{8.2.13}$$

$$\frac{1}{c}\frac{\partial \delta B_{\perp,2}}{\partial t} = -\frac{\partial \delta E_{\parallel}}{\partial x} - \sin\varphi \frac{\partial \delta E_{\perp,1}}{\partial y}. \tag{8.2.14}$$

For the time derivatives, we consider that there is a process of damping in $\delta B_{\perp,1}$ and localization in $\delta B_{\perp,2}$, but their time-scale is different than that in the oscillations in y, both due to resonant absorption. The derivatives of the transverse components yield

$$\begin{aligned}\frac{\partial}{\partial t}\delta B_{\perp,i}(x,y,t) = &-\sum_{\sigma} \omega^{\sigma}(x) B^{\sigma}_{\perp,i}(x,t) \sin\left[\omega^{\sigma}(x)t - k^{\sigma}_{y} y + \phi^{\sigma}_{B\perp,i}\right] \\ &+ \sum_{\sigma} \frac{\partial}{\partial t} B^{\sigma}_{\perp,i}(x,t) \cos\left[\omega^{\sigma}(x)t - k^{j}_{y} y + \phi^{\sigma}_{B\perp,i}\right]. \end{aligned} \tag{8.2.15}$$

8.2.5 Calculations of Mottez [47]

The results from Mottez [47] follow from the assumption of an in-place background magnetic field ($\varphi = 90^{\text{o}}$), parallel propagation, and uniform plasma. The latter yields identically zero derivatives with respect to x. Since resonant absorption is not taking place in the plasma, there is no localization of fluctuations anywhere in the plasma. Thus, the amplitudes of the electromagnetic fields do not depend on time. Equations (8.2.12) to (8.2.15) become

$$\begin{aligned}
\frac{1}{c}\frac{\partial B_{\parallel}}{\partial t} &= 0, \\
\frac{1}{c}\frac{\partial \delta B_{\perp,1}}{\partial t} &= \frac{\partial \delta E_{\perp,2}}{\partial y}, \\
\frac{1}{c}\frac{\partial \delta B_{\perp,2}}{\partial t} &= -\frac{\partial \delta E_{\perp,1}}{\partial y}, \\
\frac{\partial}{\partial t}\delta B_{\perp,i}(y,t) &= -\sum_{\sigma} \omega^{\sigma} B^{\sigma}_{\perp,i} \sin\left[\omega^{\sigma} t - k^{\sigma}_{y} y + \phi^{\sigma}_{B\perp,i}\right].
\end{aligned}$$

To determine the transverse components of the electric field in the axes of the background magnetic field $\mathbf{B}_0$ for the induction law, we transform the electric field components in the axes of the magnetic field lines $\mathbf{B}$ (8.2.9) and (8.2.10) by using the unit vectors (8.2.7) and (8.2.8) to first order in the angles $\theta_{\perp,i}$.

$$\begin{aligned}
\delta E_{\perp,1} &= \delta E^{L}_{\perp,1}, \\
\delta E_{\perp,2} &= \delta E^{L}_{\perp,2}.
\end{aligned}$$

From the induction law it is found that

$$
\begin{aligned}
E^{L\sigma}_{\perp,2} &= -\frac{\omega^\sigma}{ck^\sigma_y} B^\sigma_{\perp,1}, \\
E^{L\sigma}_{\perp,1} &= \frac{\omega^\sigma}{ck^\sigma_y} B^\sigma_{\perp,2}, \\
\phi^\sigma_{E\perp 2} &= \phi^\sigma_{B\perp 1}, \\
\phi^\sigma_{E\perp 1} &= \phi^\sigma_{B\perp 2}.
\end{aligned}
$$

Accordingly, the electric field components transverse to the magnetic field lines $\mathbf{B}$ are given by

$$
\begin{aligned}
\delta E^L_{\perp,1} &= -\sum_\sigma \frac{\omega^\sigma}{ck^\sigma_y} B^\sigma_{\perp,2} \cos\left[\omega^\sigma t - k^\sigma_y y + \phi^\sigma_{B\perp,2}\right], \\
\delta E^L_{\perp,2} &= \sum_\sigma \frac{\omega^\sigma}{ck^\sigma_y} B^\sigma_{\perp,1} \cos\left[\omega^\sigma t - k^\sigma_y y + \phi^\sigma_{B\perp,1}\right].
\end{aligned}
$$

We use (8.2.6), and the fields eqs. (8.3.3) and (8.3.4) to compute the component $\delta E_\parallel$ as seen in the axes of the background magnetic field $\mathbf{B}_0$,

$$
\begin{aligned}
\delta E_\parallel &= -E^L_{\perp,1}\theta_{\perp,1} - E^L_{\perp,2}\theta_{\perp,2} \\
&\simeq -E^L_{\perp,1}\frac{B_{\perp,1}}{B_0} - E^L_{\perp,2}\frac{B_{\perp,2}}{B_0}.
\end{aligned}
$$

This transformation yields

$$\delta E_{\parallel} = \left[\frac{\omega^B}{ck_y^B} - \frac{\omega^A}{ck_y^A}\right] B^A_{\perp,1} B^B_{\perp,2} \cos\left[\omega^A t - k_y^A y + \phi^A_{B\perp,1}\right] \cos\left[\omega^B t - k_y^B y + \phi^B_{B\perp,1} + n_B \frac{\pi}{2}\right]$$
$$- \left[\frac{\omega^B}{ck_y^B} - \frac{\omega^A}{ck_y^A}\right] B^A_{\perp,2} B^B_{\perp,1} \cos\left[\omega^A t - k_y^A y + \phi^A_{B\perp,1} + n_A \frac{\pi}{2}\right] \cos\left[\omega^B t - k_y^B y + \phi^B_{B\perp,1}\right].$$

We note that waves propagating in the same direction yield zero parallel component, in the phase-velocity factors ω^σ/k_y^σ. This field is solely caused by counterpropagating waves. For such waves with propagation in y, we set $\omega^A = \omega^B = \omega$. The parallel component can be rewritten as

$$\delta E_{\parallel} = \frac{2\omega}{ck_y} B^A_{\perp,1} B^B_{\perp,2} \left\{\cos\left[2\omega t + \phi_+ + n_B \frac{\pi}{2}\right] + \cos\left[-2k_y y + \phi_- - n_B \frac{\pi}{2}\right]\right\}$$
$$- \frac{2\omega}{ck_y} B^A_{\perp,2} B^B_{\perp,1} \left\{\cos\left[2\omega t + \phi_+ + n_A \frac{\pi}{2}\right] + \cos\left[-2k_y y + \phi_- + n_A \frac{\pi}{2}\right]\right\},$$

where $\phi_\pm = \phi^A_{B\perp 1} \pm \phi^B_{B\perp 1}$. The result is simplified by assuming circular polarization, $B^l_{\perp,1} = B^l_{\perp,2} = B^l_\perp$ for both counterpropagating waves. If waves have opposite polarization, $n_B = -n_A$, we find that

$$\delta E_{\parallel} = \frac{4\omega}{ck_y} B^A_\perp B^B_\perp \sin\left[n_A \frac{\pi}{2}\right] \sin\left[2\omega t + \phi_+\right]. \tag{8.2.16}$$

For the same polarization, $n_A = n_B = n$,

$$\delta E_{\parallel} = \frac{4\omega}{ck_y} B^A_\perp B^B_\perp \sin\left[n \frac{\pi}{2}\right] \sin\left[-2k_y y + \phi_-\right]. \tag{8.2.17}$$

These results correspond to the derivations of Mottez [47]. Counterpropagating, purely transverse waves with respect to the local magnetic field $\mathbf{B}$ interact in a way such that components of the transverse electric field have a non-zero electric field component projected along the background magnetic field $\mathbf{B}_0$, which interacts with the particle distribution in this direction.

8.3 Analysis of the Electromagnetic Fields

8.3.1 Features of the Electromagnetic Fields

The magnetic field fluctuations within the inhomogeneous layers verify the conditions of negligible curvature. Accordingly, the transverse components with respect to $\mathbf{B}_0$ of finite amplitude verify $|\delta B_{\perp,i}| \ll \left|B_{\parallel}\right|$, where $B_{\parallel} = B_0 + \delta B_{\parallel}$. Furthermore, the parallel fluctuations verify $B_0 \gg \left|\delta B_{\parallel}\right|$. These conditions hold for all of the simulated ratios l/R, and allow us to define the local angles associated with the magnetic field line $\mathbf{B}_0$ in the limit of small-angles [47],

$$\tan\theta_{\perp,i} \simeq \theta_{\perp,i} = \frac{\delta B_{\perp,i}}{B_{\parallel}} \simeq \frac{\delta B_{\perp,i}}{B_0}. \tag{8.3.1}$$

We now define the magnetic field lines geometrically based on the field $\mathbf{B}_0$ (see further details in subsection 8.2.1). Using the angles (8.3.1), we rotate from $\mathbf{B}_0$ field-axes to those of the local $\mathbf{B}$ field-axes. The rotations are approximated to first order in $\theta_{\perp,i}$ (here, $i = 1$ and 2 correspond to either of the two transverse components relative to $\mathbf{B}_0$) [47].

Applying the transformations (8.2.3) to (8.2.5) to the electric field components from simulation data $\delta E_{\perp,i}$ (in the axes of $\mathbf{B}_0$), leads to $\delta E_{\parallel}^{L} \simeq 0$ (in the local axes

of **B**). The magnitude of this field remains three to four orders of magnitude below the magnitude of $\delta E^L_{\perp,i}$. It is also two to three orders of magnitude smaller than the parallel field $\delta E_\parallel$, along $\mathbf{B}_0$, through most of our simulations for all l/R. The largest deviations occur within the layers and grow slowly by instant $\Omega_p t \simeq 1700$. Despite this, the electric field fluctuations are predominantly transverse to the local magnetic field lines **B**. We show sections of the component $\delta E^L_\parallel$ in the axes of the local magnetic field in Fig. 8.4 for $l/R = 0.4$, with the other components of the electric field defined on the axes of the local magnetic field lines **B**. Sections of the center of a density cavity, $y = y_1$ [Figs. 8.4(a)–(d)], and at the center of a density winglet $y = y_2$ [Figs. 8.4(e)–(h)] are shown.

This analysis for Alfvén waves is developed for ideal MHD or Hall MHD models, where the condition $\delta E^L_\parallel = 0$ or equivalently $\mathbf{E} \cdot \mathbf{B} = 0$ [46] is automatically satisfied [47]. Here, we verify the same feature in electromagnetic fluctuations generated in kinetic simulations. Moreover, it holds in inhomogeneous plasmas with transverse spatial dependency on x, with quasiperpendicular, elliptically polarized waves (KAWs), and oblique background magnetic field $\mathbf{B}_0$. This extends the conditions under which the analysis of Mottez [47] applies.

8.3.2 Projections of the Transverse Electric Fields

Through the inverse rotation (shown in subsection 8.2.1), we recover the electric field parallel to $\mathbf{B}_0$ from the transverse electric field components:

$$\delta E^{\text{Mottez}}_\parallel = -\,\delta E^L_{\perp,1}\theta_{\perp,1} - \delta E^L_{\perp,2}\theta_{\perp,2}, \tag{8.3.2}$$

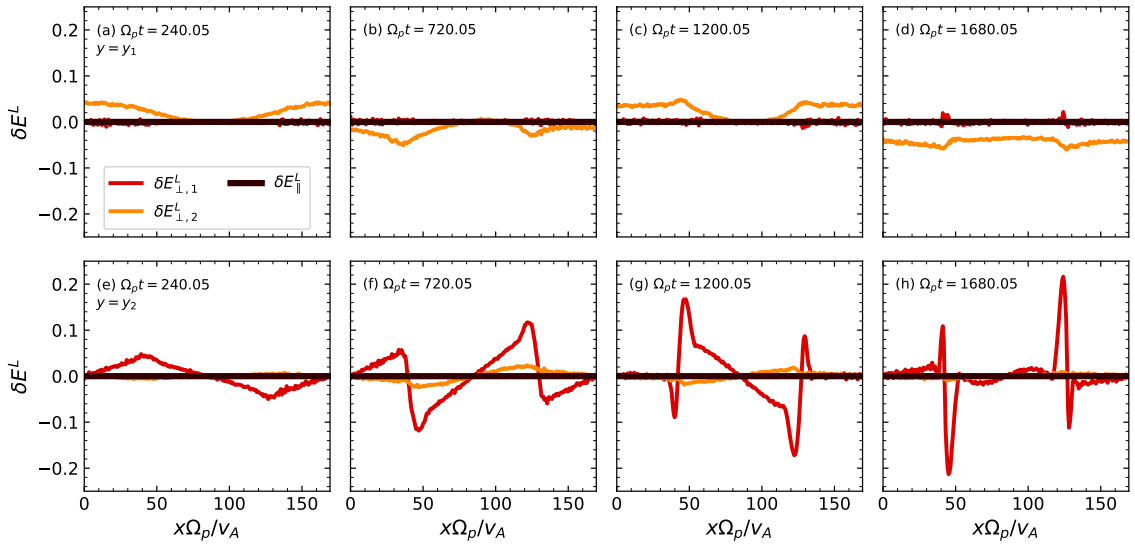

Figure 8.4: Sections of the electric field components in the axes of the local magnetic field $\mathbf{B}$. We show components $\delta E^L_{\parallel} = 0$ (black solid line), and the transverse components $\delta E^L_{\perp,1}$ (solid red line), $\delta E^L_{\perp,2}$ (solid orange line) at four selected times. Sections correspond to (a)–(d) $y = y_1$ at the center of a density hole, and (e)–(h) $y = y_2$ at the center a density winglet. Here, $l/R = 0.4$.

valid to first order in $\theta_{\perp,i}$. This reconstruction matches the field $\delta E_{\parallel}$ from the simulations in Fig. 8.5, where data from the simulations and the projection given by Eq. (8.3.2) are compared at four selected times for $l/R = 0.4$.

The difference $\left|\delta E_{\parallel} - \delta E^L_{\parallel}\right|$ remains at least two orders of magnitude smaller than $|\delta E_{\parallel}|$ in the layers during the formation of density structures, for all l/R. Therefore, the parallel electric field arises primarily from the projection of electric field fluctuations transverse to the magnetic field lines $\mathbf{B}$. After resonant absorption has acted, this field is produced by KAWs with wavenumber k_{y0}. Thus, the localization of these fluctuations implies the localization of $\delta E_{\parallel}$ (for this discussion, we use subsection 5.5.3).

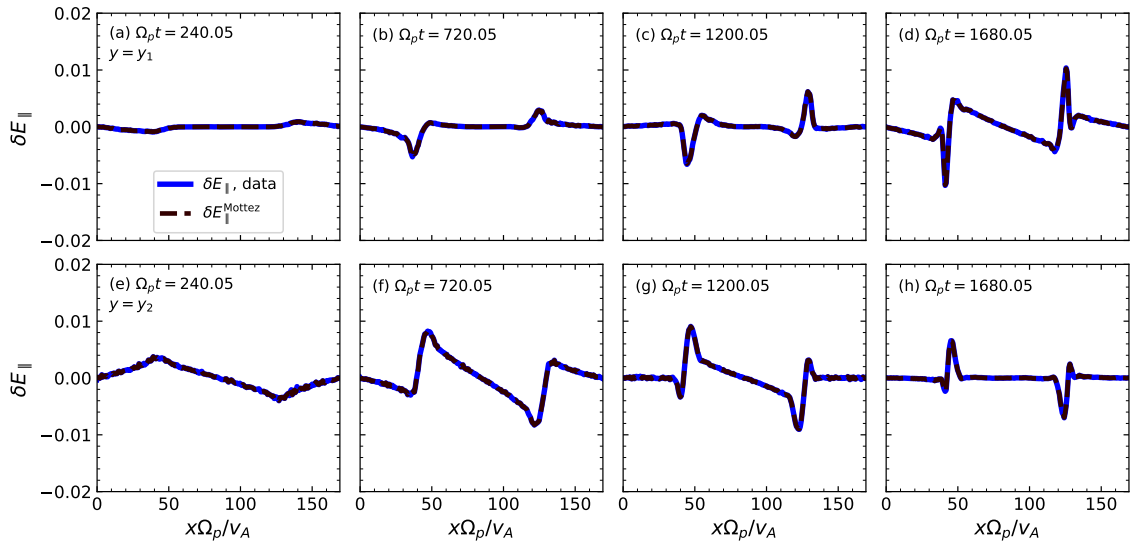

Figure 8.5: Sections of the parallel electric field $\delta E_\parallel$ in the axes of the background magnetic field $\mathbf{B}_0$ at four selected times. Sections correspond to (a)–(d) $y = y_1$ at the center of a density hole, and (e)–(h) $y = y_2$ at the center of a density winglet. Here, $l/R = 0.4$. A comparison is shown between data (solid blue lines) and the projection of Mottez [47] Eq. (8.3.2) (dashed black lines).

8.3.3 Analytical Estimation of the Field $\delta E_\parallel$

The amplitudes of the transverse electric field components in the field line are obtained in terms of the magnetic field components defined on the axes of $\mathbf{B}_0$. We consider pairs of counterpropagating waves along $\mathbf{B}$ that have magnetic field components $B_\parallel \simeq B_0$. The transverse components are given by Equations (8.2.1) and (8.2.2) defined on the axes of $\mathbf{B}_0$, and considering forward ($\sigma = A$) and backward ($\sigma = B$) propagation which may have different wavenumbers k_y and frequencies $\omega(x)$. The phases satisfy $\phi^\sigma_{B\perp,2} = \phi^\sigma_{B\perp,1} + n_\sigma \pi/2$. Generally, $B^\sigma_{\perp,1}$ and $B^\sigma_{\perp,2}$ are different.

The following results are derived from Equation (8.2.11), in subsection 8.2.4. Unlike the analysis in Mottez [47], the amplitudes $B^\sigma_{\perp,j}(x,t)$ depend on both x and time

t. This is due to the density gradient and the progressive localization of fluctuations by resonant absorption. The dominant frequencies ω^σ remain nearly constant for the strongest peaks, but may depend on x due to the density inhomogeneity.

We use the inverse transformation from Eqs. (8.2.4) and (8.2.5), and the induction law (8.2.11) to relate the amplitudes of the magnetic field and the transverse electric field.

Calculation of the Transverse Components

Simulation diagnostics show that the field $\delta E_\parallel$ is typically one order of magnitude smaller than the transverse components. For the principal spectral components (modes k_{y0} in $\delta E_{\perp,i}$ and $2k_{y0}$ in $\delta E_\parallel$), the time derivative $\partial \delta E_\parallel / \partial y$ is $1-2$ orders of magnitude smaller than $\partial \delta E_{\perp,2}/\partial y$ in Equation (8.2.13) (for $\varphi = 45°$ and all l/R). Thus, the derivative of $\delta E_\parallel$ is neglected when convenient, recovering the components of the induction law of [47].

A similar comparison for Equation (8.2.14) shows that the derivative $\partial \delta E_\parallel / \partial x$ is generally smaller than the derivative $\partial \delta E_{\perp,1}/\partial y$. This occurs for $l/R \geq 0.4$. For smaller ratios, their amplitudes are comparable, specifically for $l/R = 0.2$ with any φ. The difference, when it exists, is about one order of magnitude. For other l/R and different φ, $\partial \delta E_\parallel / \partial x$ is surpassed by the other derivative when resonant absorption is operating. Nevertheless, for analytical traceability, we neglect the derivatives of $\delta E_\parallel$ where justified by spectral analysis.

For the time derivatives (8.2.15), we proceed as described in subsection 5.5.3. We compare the oscillatory term ($\propto \omega^\sigma B^\sigma_{\perp,i}$) with the slow amplitude evolution $\partial \delta B_{\perp,i}/\partial t$. For the damped mode k_{y0} by resonant absorption, $B^\sigma_{\perp,1}$, we use damping rates $|\gamma_{B\perp,1}/\Omega_p| \leq 4 \times 10^{-4}$ (for different φ and l/R). For the localized component

$\delta B^j_{\perp,2}$, a growth rate is estimated for mode k_{y0} with Equation (5.5.1). Here, we find growth rates $|\gamma_{B\perp,2}| \sim 10^{-4} - 10^{-3}$ depending on the case. These slow rates justify neglecting the slow amplitude term in Equation (8.2.15) in favor of the oscillatory term for the analytical estimate.

The rotation of the electric field components (8.2.9) and (8.2.10) to the background field-axes yields $\delta E_{\perp,i} \approx \delta E^L_{\perp,i}$, to first order in the angles $\theta_{\perp,i}$. We now determine the locally transverse components of the electric field in the local field axes from the induction law. We obtain the following relations with the magnetic field amplitudes and phases.

$$
\begin{aligned}
E^{L\sigma}_{\perp,2}(x,t) &= -\frac{\omega^\sigma}{ck^\sigma_y}\frac{B^\sigma_{\perp,1}(x,t)}{\sin\varphi}, \\
E^{L\sigma}_{\perp,1}(x,t) &= \frac{\omega^\sigma}{ck^\sigma_y}\frac{B^\sigma_{\perp,2}(x,t)}{\sin\varphi}, \\
\phi^\sigma_{E\perp 2} &= \phi^\sigma_{B\perp 1}, \\
\phi^\sigma_{E\perp 1} &= \phi^\sigma_{B\perp 2}.
\end{aligned}
$$

Using these relations, the electric field components locally transverse to $\mathbf{B}$ are

$$
\delta E^L_{\perp,1} = -\sum_\sigma \frac{\omega^\sigma(x)}{ck^\sigma_y}\frac{B^\sigma_{\perp,2}(x,t)}{\sin\varphi}\cos\left[\omega^\sigma(x)t - k^\sigma_y y + \phi^\sigma_{B\perp,2}\right], \tag{8.3.3}
$$

$$
\delta E^L_{\perp,2} = \sum_\sigma \frac{\omega^\sigma(x)}{ck^\sigma_y}\frac{B^\sigma_{\perp,1}(x,t)}{\sin\varphi}\cos\left[\omega^\sigma(x)t - k^\sigma_y y + \phi^\sigma_{B\perp,1}\right]. \tag{8.3.4}
$$

8.3.4 Calculation of the Parallel Component

Inserting the resulting electric field components into Equation (8.3.2) leads to

$$\delta E_{\parallel} = \frac{2\omega(x)}{ck_y}\frac{B^A_{\perp,1}(x.t)B^B_{\perp,2}(x.t)}{\sin\varphi}\left\{\cos\left[2\omega(x)t+\phi_+ + n_B\frac{\pi}{2}\right]+\cos\left[-2k_{y0}y+\phi_- - n_B\frac{\pi}{2}\right]\right\} - \frac{2\omega(x)}{ck_y}\frac{B^A_{\perp,2}(x,t)B^B_{\perp,1}(x,t)}{\sin\varphi}\left\{\cos\left[2\omega(x)t+\phi_+ + n_A\frac{\pi}{2}\right]+\cos\left[-2k_{y0}y+\phi_- + n_A\frac{\pi}{2}\right]\right\}, \tag{8.3.5}$$

for counterpropagating waves with identical frequencies ω and wavenumbers $|k_y| = k_{y0}$. This result is similar to that for parallel propagating and circularly polarized Alfvén waves. However, since the waves in this work are elliptically polarized, identical (in our case, $n_A = n_B$),

$$\delta E_{\parallel} = \frac{2\omega}{ck_y}\frac{B^A_{\perp,1}(x)B^B_{\perp,2}(x)}{\sin\varphi}\sin\left[n\frac{\pi}{2}\right]\left\{-\sin\left[2\omega t+\phi_+\right]+\sin\left[-2k_y y+\phi_-\right]\right\} + \frac{2\omega}{ck_y}\frac{B^A_{\perp,2}(x)B^B_{\perp,1}(x)}{\sin\varphi}\sin\left[n\frac{\pi}{2}\right]\left\{\sin\left[2\omega t+\phi_+\right]+\sin\left[-2k_y y+\phi_-\right]\right\}. \tag{8.3.6}$$

or opposite ($n_A = -n_B$) polarizations of the waves, nonpropagating waves with frequencies and wavenumbers $2\omega_{\mathrm{KAW}}$ and $2k_{y0}$ are present in the electric field. This is in line with the spectral decomposition of the parallel electric field $\delta E_{\parallel}$ observed in Figs. 8.2 (d)–(f) and supports the interpretation that the parallel electric field is predominantly due to the non-linear coupling of counterpropagating waves.

The signals in Equation (8.3.5) appear at the first stages of the simulation, as seen in Fig. 8.1 (b), indicating that before the generation of the KAWs, the coupling is initially driven by kink oscillations. These signatures become more relevant once

KAWs are generated.

8.4 Particle Drifts

A particle motion analysis following Mottez [47] provides further physical interpretation. We estimate the particle drifts transverse to the total magnetic field line $\mathbf{B}$ projected onto the direction parallel to $\mathbf{B}_0$. The drift considers cross-field, polarization, and the magnetic field gradient drifts. In consistency with the assumptions used to derive the parallel field $\delta E_\parallel$, curvature effects are neglected. Therefore, curvature drift is not considered here, in accordance with the small-angle approximation used in section 8.3.1.

$$\widehat{\mathbf{e}}_\parallel \cdot \mathbf{v}_{p\perp}^{L} = c\widehat{\mathbf{e}}_\parallel \cdot \left[\frac{\mathbf{E}\times\mathbf{B}}{B^2}\right] + \frac{m_p}{q_p B^2}\frac{\mathrm{d}\delta E_\parallel}{\mathrm{d}t} + \frac{m_p v_\perp^2}{2q_p B^3}\widehat{\mathbf{e}}_\parallel \cdot [\nabla B \times \mathbf{B}]\,. \tag{8.4.1}$$

8.4.1 Cross-field Drift

The parallel projection is

$$\widehat{\mathbf{e}}_\parallel \cdot \left[\frac{\mathbf{E}\times\mathbf{B}}{B^2}\right] = \frac{B_{\perp,1}E_{\perp,2} - B_{\perp,2}E_{\perp,1}}{B^2},$$

Corrections to the cross-field drift due to inhomogeneities [166] involve second-order gyroradius terms and are negligible for the parameters used here. Using explicit field components yields combinations of $\cos^2\Phi^\sigma$ and $\sin^2\Phi^\sigma$, where the phases $\Phi^\sigma = \omega(t)t \pm k_y y + \phi^\sigma_{B\perp,i}$. The elliptical polarization prevents the reduction of this drift to constants as in the case of circularly polarized waves [47]. Trigonometric identities

lead $\cos^2\Phi^\sigma$ and $\sin^2\Phi^\sigma$ to harmonic terms involving mixed signals 2ω and $2k_y$.

These signals appear weakly in the dispersion relation plots of $\delta u_{p\parallel}$ [Figs. 8.2 (h) to (j)]. The strongest parallel signals are rather nonpropagation modes with $k_y = \pm 2k_{y0}$. Thus, the cross-field drift alone does not yield significant proton transport in our simulations.

8.4.2 Polarization Drift

The time derivative of $\delta E_\parallel$ Eq. (8.3.5) is evaluated for the polarization drift, using particle positions for dependence on x and y,

$$\frac{\mathrm{d}\delta E_\parallel}{\mathrm{d}t} = \frac{\partial \delta E_\parallel}{\partial t} + v_x \frac{\partial \delta E_\parallel}{\partial x} + v_y \frac{\partial \delta E_\parallel}{\partial y}.$$

We apply derivatives to the parallel field in Equation (8.3.6). By neglecting the slow time variations of the magnetic field amplitudes ($\partial B^\sigma_{\perp,i}/\partial t$), several harmonic terms with 2ω and $2k_y$ are obtained. There are no mixed space and time dependencies. These signals match the nonpropagating modes $\pm 2k_{y0}$ and $\pm 2\omega_{\mathrm{KAW}}$ seen in the dispersion relation plots $\omega_r - k_y$ in density fluctuations, parallel bulk-velocity, and parallel electric field (Fig. 8.2). Accordingly, the polarization drift contributes to the harmonics observed in the proton parallel bulk velocity. This drift is a significant component of the parallel particle response. The polarization drift provides the main contribution to particle motion parallel to the field $\mathbf{B}_0$. To avoid secular growth, we assume that the frequency ω is approximately uniform in the layers.

8.4.3 Gradient Magnetic Field Drift

The parallel projection of the gradient magnetic field drift is

$$v_{\mathrm{G}\parallel} = \frac{m_p v_\perp^2}{2q_p B}\left[\frac{B_{\perp,1}}{B^2}\cos\varphi\frac{\partial B}{\partial y} + \frac{B_{\perp,2}}{B^2}\frac{\partial B}{\partial x}\right].$$

The derivatives $\partial B/\partial y$ and $\partial B/\partial x$ in terms of the derivatives of $\delta B_{\perp,i}$, lead to several non-cancelling terms. The elliptical polarization mixes counterpropagating and copropagating waves. The terms associated with copropagating waves generate harmonic terms $\sin 2\Phi^\sigma$ and $\cos^2\Phi^\sigma$. These are weak or not seen in the parallel fields or bulk velocities. Terms associated with counterpropagating waves yield purely temporal or spatial oscillations with 2ω and $2k_y$. These are consistent with the signals seen in the parallel fields and bulk velocities.

Thus, this drift contains the expected spectral content. However, we can at most state that the fluctuations associated with the counterpropagating waves are more intense. The effect of other terms has a negligible net contribution in the performed analyses.

8.4.4 Diamagnetic Drift

This drift involves the pressure gradient, rather than particle data. Thus, it was not included in Equation (8.4.1). This drift is given by

$$\mathbf{v}_{\mathrm{DM}} = -\frac{1}{q_p n_p B^2}\nabla p_p \times \mathbf{B}.$$

The proton pressure p_p is $p_p = k_B n_p T_p$ requires knowledge of the density n_p and

the temperature T_p. We use harmonic dependencies from dispersion relations plots to estimate the order of the involved harmonics. The spectra of the three temperatures show strong power at $\omega_{\mathrm{KAW}} - \omega_{\mathrm{kink}}$ and k_{y0}, with nonpropagating signals at $2k_{y0}$. The temperature $T_{p\parallel}$ additionally has frequencies $2\omega_{\mathrm{KAW}}$ and k_{y0}. The proton density has strongest signals at ω_{kink} and k_{y0}, and nonpropagating signals at $2k_{y0}$.

The projection of the drift onto $\mathbf{B}_0$ is

$$v_{\mathrm{DM}\parallel} = -\frac{1}{q_p n_p B^2}\left[B_{\perp,2}\frac{\partial}{\partial r_{\perp,1}}\left(n_p k_B T_p\right) - B_{\perp,1}\frac{\partial}{\partial r_{\perp,2}}\left(n_p k_B T_p\right)\right].$$

The signals contained by n_p and T_p lead to a drift with higher harmonics of k_{y0} and ω_r. These signals are not consistent with the modes associated with the structures we observe in density and phase-space portraits $y - v_\parallel$. This drift does not significantly contribute to parallel heating and acceleration.

We conclude that the polarization drift through the field $\delta E_\parallel$ and the magnetic field gradient contribute most to particle acceleration and to a depletion of protons in the antinodes of kink oscillations. Simultaneously, protons are displaced toward the nodes. The dispersion relations plots of δn_p and $\delta u_{p\parallel}$ [Figs. 8.2 (g)–(i)], show that most of the density and flux variations depend only on space. This is consistent with the physical picture of counterpropagating Alfvén waves driving particle motion of Mottez [47].

In relation to resonant absorption, because fluctuations are localized in x, the resulting field $\delta E_\parallel$ is also localized. Thus, particle acceleration effects occur only within the inhomogeneous layers. Other non-linear terms or interactions may also contribute, because the condition for total transverse fields $\delta E_\parallel^L = 0$ and the differ-

ence $\left|\delta E_{\parallel} - \delta E_{\parallel}^{\text{Mottez}}\right| = 0$ are not strictly verified. However, we provide reasonable evidence that the non-linear interaction between the waves generated at the layers represents the most relevant signals we observe in the electromagnetic fields.

8.5 Phase-space Portraits along $y - v_{\parallel}$ Plane

We follow the phase-space portraits in the $y - v_{\parallel}$ plane in Fig. 8.6 in the region R_{x1} [frames (e) to (h)], and in R_{x2} [frame (i) to (l)] for $l/R = 0.4$. These regions are shown in white dotted lines in the proton density [frames (a) to (d)]. At the onset of resonant absorption, $\Omega_p t = 240.05$, the distributions exhibit sinusoidal oscillations in $v_{\parallel}$ along y [Figs. 8.6 (e) and (i)]. The oscillations persist at $\Omega_p t = 720.05$ both inside the slab and at the left layer. By $\Omega_p t = 1200.05$, the deformations of the distribution inside the slab become filamentary structures in phase-space [Fig. 8.6 (k) and (l)]. This structure indicates that particles move nearly force-free. This is in agreement with the localization of the electric field fluctuations only within the layers.

At the layers, there is a flux of particle-density toward velocities larger than $\left|v_{\parallel}\right| = u_0$. The flux transports protons from regions around $y = L_y/4$ and $3L_y/4$ to the regions around $y = 0$ and $L_y/2$ [see Figs. 8.6 (c) and (d)]. This is consistent with particle flux along $\mathbf{B}_0$ and the signals observed in the dispersion relation of $\delta E_{\parallel}$ and $\delta u_{p\parallel}$ [see Figs. 8.2 (d) to (i)], driven by the projection of the KAWs fields onto the parallel direction. At $\Omega_p t = 1680.05$, the distributions at the layer exhibit a strong deformation, depleting regions around $y = L_y/4$ and $3L_y/4$, where proton density cavities are formed. Protons are displaced toward $y = 0$, $L_y/2$, and L_y, locally enhancing the particle density and forming the winglets. In this process, the width of the distribution function in $v_{\parallel}$ increases at these locations, see Fig. 8.6(h).

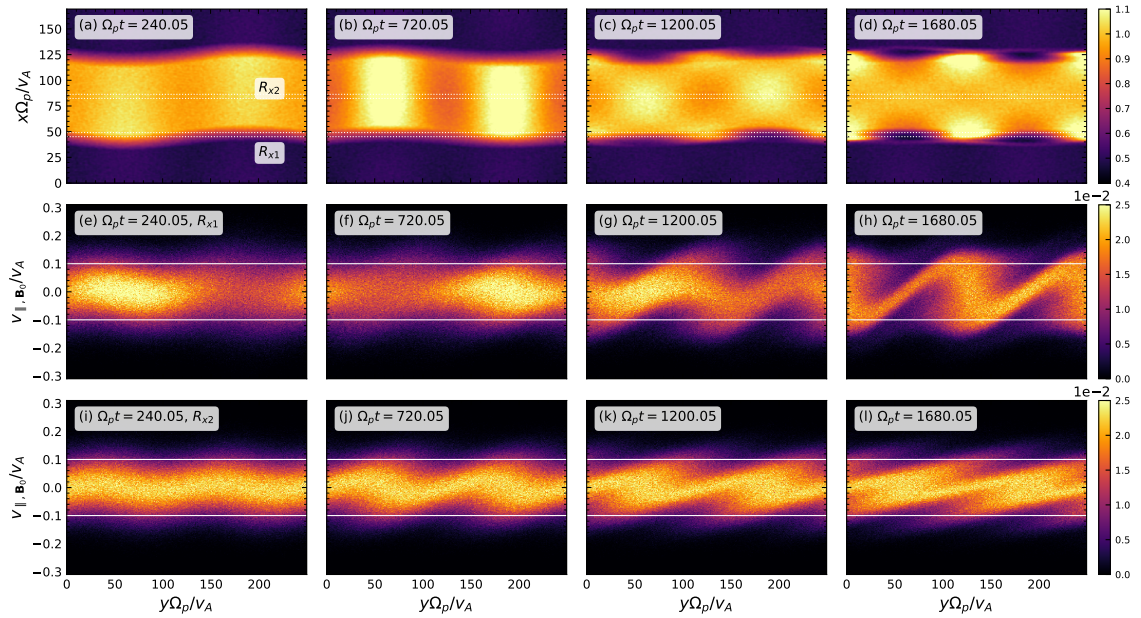

Figure 8.6: Evolution of (a)–(d) the proton density indicating boundaries of regions R_{x1} and R_{x2} (white dotted lines), and phase-space portraits $y - v_\parallel$ at regions (e)–(h) R_{x1} in the inhomogeneous layer, and at (i)–(l) R_{x2} at the center of the slab. Velocities are shown in the phase-space portraits (e)–(l): $v_\parallel = \pm u_0$ (solid white line). Here, $l/R = 0.4$.

No particular velocity $v_\parallel$ shows signatures of resonant interactions at the cavities. The density depletion spans a wide range of velocities, suggesting a non-resonant interaction [47]. Intermediate snapshots of the phase-space portraits in region R_{x1} (Fig. 8.7) show that the overall structures rotate around $v_\parallel = 0$, suggesting trapping of protons at longer times. For ratios $l/R \leq 0.3$, these structures are disrupted beyond $\Omega_p t = 1680$, when spatial scales reach the grid resolution and numerical noise grows.

Figure 8.8 shows sections of the distribution functions extracted from the phase-space contours of Fig. 8.6. Frame (a) shows sections in the region R_{x1} and the left

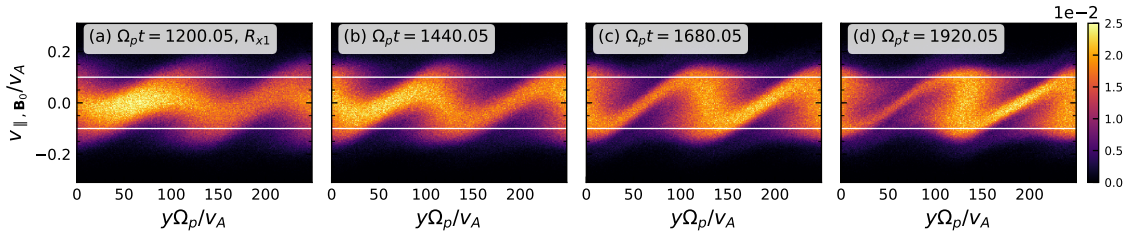

Figure 8.7: Evolution of the phase-space portraits $y - v_{\parallel}$ at region R_{x1} in the inhomogeneous layer for four selected long times. Velocities $\left|v_{\parallel}\right| = u_0$ are shown in the phase-space portraits as solid white lines. Here, $l/R = 0.4$.

layer and $y = y_1$ in the center of a density cavity. Frame (b) shows sections in the region R_{x2} in the center of the slab, in the same y. In both cases, there is a narrowing in $v_{\parallel}$ due to particle depopulation. The strongest narrowing occurs at R_{x1} due to the parallel electric field. Frames (c) and (d) show the same regions, respectively, both at $y = y_2$, the center of the density winglet. At the layer, the distributions widen toward velocities $\left|v_{\parallel}\right| = u_0$ and flatten significantly around $v_{\parallel} = 0$ after resonant absorption. This is consistent with the proton flux caused by the parallel field $\delta E_{\parallel}$. In contrast, the distribution at the center of the slab shows weaker diffusion.

Across all of the simulated cases with fixed angle $\varphi = 45°$ and varying l/R, the spatial dependence on y is qualitatively similar. However, in the region R_{x1}, the projections in $y - v_{\parallel}$ plane systematically broaden in $v_{\parallel}$. Larger ratio l/R yields increasingly flat distributions around $v_{\parallel} = 0$, as in Fig. 8.8 (c). These flat-topped distributions resemble those reported in electron populations in the Earth's magnetosphere downstream of the bow shock [167–170], and near reconnection sites [171–173]. This signature indicates strong heating. In our simulations, such heating is caused by the KAW fluctuations via the field $\delta E_{\parallel}$.

We conclude that the non-linear coupling between the counterpropagating KAWs

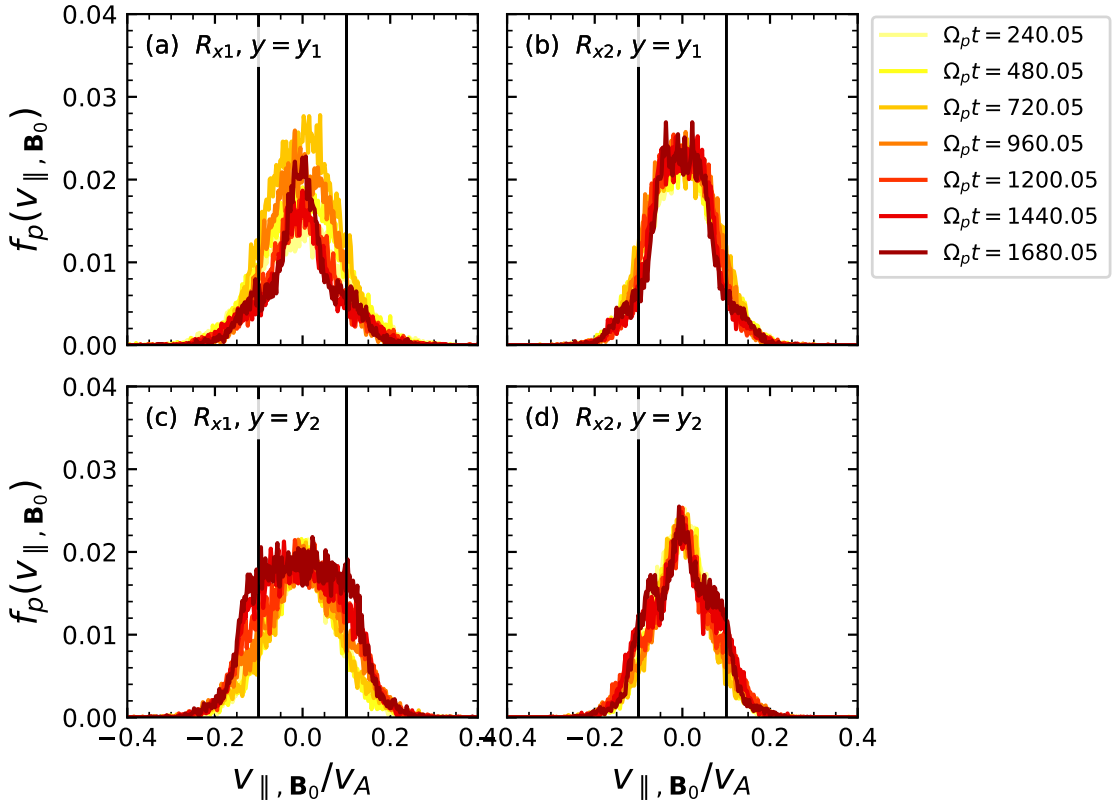

Figure 8.8: Evolution of the distribution function obtained from the phase-space portraits projected on $y - v_{\parallel}$ evaluated at section (a)–(b) $y = y_1$, and (c)–(d)] at $y = y_2$. Velocities $\left|v_{\parallel}\right| = u_0$ are shown with solid black lines. Here, $l/R = 0.4$.

generated by resonant absorption leads to non-resonant wave-particle interaction. Here, protons are accelerated, forming regions of minimum density and enhancing heating of the distribution at the newly formed regions of maximum density, both in the direction parallel to $\mathbf{B}_0$.

Previous interpretations in research attributed density structures generated by resonant absorption to dispersive effects triggered by cross-field oscillations of Alfvén waves near resonant lines [38]. These processes involve frequencies near the pro-

ton cyclotron frequency, perpendicular heating, and parallel heating by transit-time damping. In contrast, in our simulations, the density enhancements arise from non-resonant particle acceleration driven by KAWs through the parallel field $\delta E_{\parallel}$. Cross-field modulation does not occur here because the density gradient is orthogonal to $\mathbf{B}_0$ [37]. The fluctuations we identify are low-frequency, by two orders of magnitude below Ω_p. The heating occurs predominantly in the parallel direction, without resonant damping of fluctuations.

8.6 Proton Parallel Temperatures

Temperature variations are concentrated at the layers for all values of l/R. At the center of the density winglet ($R_{x1} \times R_{y2}$), the parallel temperature $\langle T_{p\parallel} \rangle$ [Fig. 9.4 (a)] initially decreases up to instant $\Omega_p t \simeq 250$. This is consistent with the particle acceleration out of the density cavities by the parallel electric field generated by the KAWs. Subsequently, $\langle T_{p\parallel} \rangle$ increases in time for all ratios l/R. Their growth rate slows near $\Omega_p t \simeq 1000$ and acquires similar values across cases by $\Omega_p t = 1700$.

At the center of the cavity ($R_{x1} \times R_{y1}$), for all ratios l/R the temperature $\langle T_{p\parallel} \rangle$ evolve in phase with the kink oscillations throughout the simulation. Their fluctuation frequency matches ω_{kink}. As in the winglets, smaller l/R produces larger temperature oscillations, indicating a stronger reversible field-particle power exchange at smaller transverse scales. The temperature $\langle T_{p\parallel} \rangle$ increases early on and saturates by $\Omega_p t \simeq 350$, then decreases to lower values by $\Omega_p t \simeq 1200$. This cooling is largely driven by particle depletion within the cavity. Afterward, $\langle T_{p\parallel} \rangle$ rises again and returns to near its initial value by $\Omega_p t = 1700$.

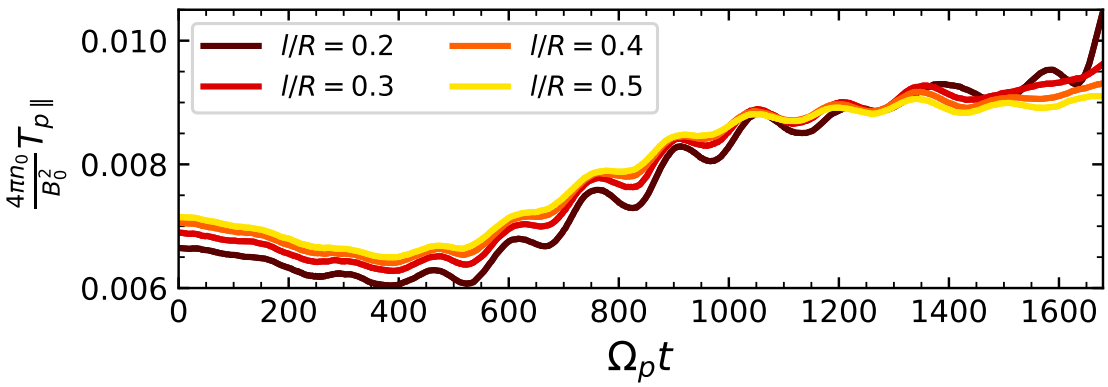

Figure 8.9: Evolution the space-averaged temperature $\langle T_{p\parallel} \rangle$ at the winglet in the left layer, $R_{x1} \times R_{y2}$.

8.7 The Effect of Different Angles φ

8.7.1 Wave-particle Interaction

As in the case $\varphi = 45°$, density structures in the layers are dominated by the second mode $2k_{y0}$. This mode in δn_p grows and eventually exceeds the amplitude of the mode k_{y0}, where resonant absorption occurs [Fig. 8.1 (a)]. For $\varphi = 10°$ (no resonant absorption), and 80° (weak resonant absorption) mode $2k_{y0}$ does not surpass mode k_{y0}. At most, they achieve the same amplitude in $\varphi = 80°$. Repeating the dispersion relation analysis of subsection 8.1, we find that the parallel field $\delta E_\parallel$ develops strong nonpropagating signals as in $l/R = 0.4$ and $\varphi = 45°$ (pairs $|\omega_r| = 2\omega_{\mathrm{KAW}}$, $k_y = 0$, and $\omega_r = 0$, $|k_y| = 2k_{y0}$). This result is extended for all φ and $l/R = 0.2$ and 0.5.

The magnetic field fluctuations are consistent with the hypothesis of negligible curvature (subsection 8.3.1). The electric field remains nearly perpendicular to the magnetic field lines $\mathbf{B}$ (subsection 8.3.1). The longitudinal $\delta E_\parallel^L$ (departure from transversality) is 3 orders of magnitude smaller than the components $\delta E_{\perp,i}^L$, and 2

orders of magnitude below $\delta E_{\parallel}$, for angles near $\varphi = 45°$. The deviations $\delta E_{\parallel}^{L}$ grow more rapidly for $l/R = 0.2$ for all angles by the time $\Omega_p t \simeq 1700$. Despite this, the dominant contribution to $\delta E_{\parallel}$ is the coupling of counterpropagating waves localized within the layers at all φ. This is verified in the dispersion relation plots $\omega_r - k_y$ and coincides with Equation (8.3.5). Rotating the fields as in Eq. (8.3.2) confirms that the field $\delta E_{\parallel}$ in the data originates from this coupling. Thus, we extend the conclusions of subsection 8.1 to other angles of $\mathbf{B}_0$.

Changing the angle φ modifies the degree of localization by resonant absorption [39]. To quantify this effect, we analyze the k_y spectrum of $\delta E_{\parallel}$, focusing on the mode $2k_{y0}$. For $l/R = 0.5$, its temporal evolution is shown in Fig. 8.10. For angles $22.5° \leq \varphi \leq 67.5°$, the amplitude of $2k_{y0}$ grows and saturates at a similar level, consistent with the formation of small-scale structures in the layers.

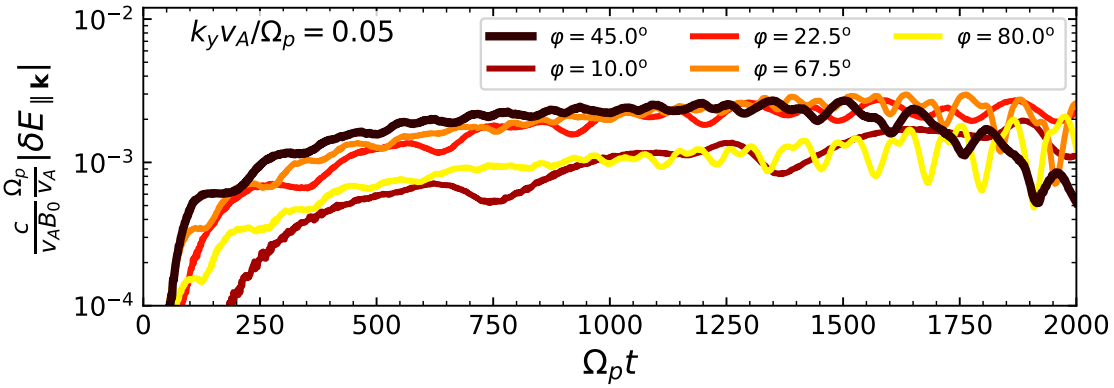

Figure 8.10: Fourier decomposition of the parallel electric field $\delta E_{\parallel}$ in k_y at a section x located at the center of the left inhomogeneous layer. Evolution of the amplitude of mode $2k_{y0}$ for different angles φ.

For $\varphi = 10°$, the mode $2k_{y0}$ has the lowest amplitude, because localization does not occur. For $\varphi = 80°$, resonant absorption is weak. The generated KAWs are

weak and prevent the full formation of structures. These results indicate that producing small-scale structures requires not only localization, but also a large enough amplitude of the mode $2k_{y0}$ in $\delta E_{\parallel}$. The same qualitative behavior is obtained for $l/R = 0.2$.

8.7.2 Phase-space Portraits along $y - v_{\parallel}$ Plane

The phase-space portraits in the projection $y - v_{\parallel}$ at the left inhomogeneous layer (R_{x1}) have a strong dependence on φ. For $33.75° \leq \varphi \leq 56.25°$, the distributions resemble those in Figs. 8.6 (e) to (h) [see Figs. 8.11 (e) to (h) for $\varphi = 56.25°$]. Additionally, the distribution deforms at a faster rate as φ approaches 45°. Regions near $y = L_y/4$, and $3L_y/4$ depopulate rapidly. The displaced particle density piles up around $y = 0$, $L_y/2$, and L_y and broadens the distribution in $v_{\parallel}$, as in Fig. 8.8 (c). At larger times, the structures tend to rotate around $v_{\parallel} = 0$ and suggest proton trapping. These features disappear with angles $\varphi \geq 80°$.

For $\varphi = 80°$, weak filamentary structures are observed [Figs. 8.11 (i) to (l)]. This signals a substantially weaker wave-particle interaction. No significant heating is found at $y = 0$, $L_y/2$, or L_y. This is consistent with the low amplitude KAWs generated at the layers, and the correspondingly weak field $\delta E_{\parallel}$. For $\varphi = 22.5°$, the deformations in the distribution occur, but a slower pace [Figs. 8.11 (a) to (d)]. These trends hold for $l/R = 0.2$ and 0.5.

Phase-space portraits $y - v_{\parallel}$ inside the slab (R_{x2}), show oscillatory structures for $\varphi = 10°$. As the angle φ increases toward 56.25°, filaments develop more rapidly. For $\varphi = 80°$ (Fig. 8.12), the filaments evolve into vortex-like structures centered at $y = L_y/4$ and $3L_y/4$. These structures correlate with the increasing persistence of density enhancement inside the slab at large φ, consistent with ponderomotive forces

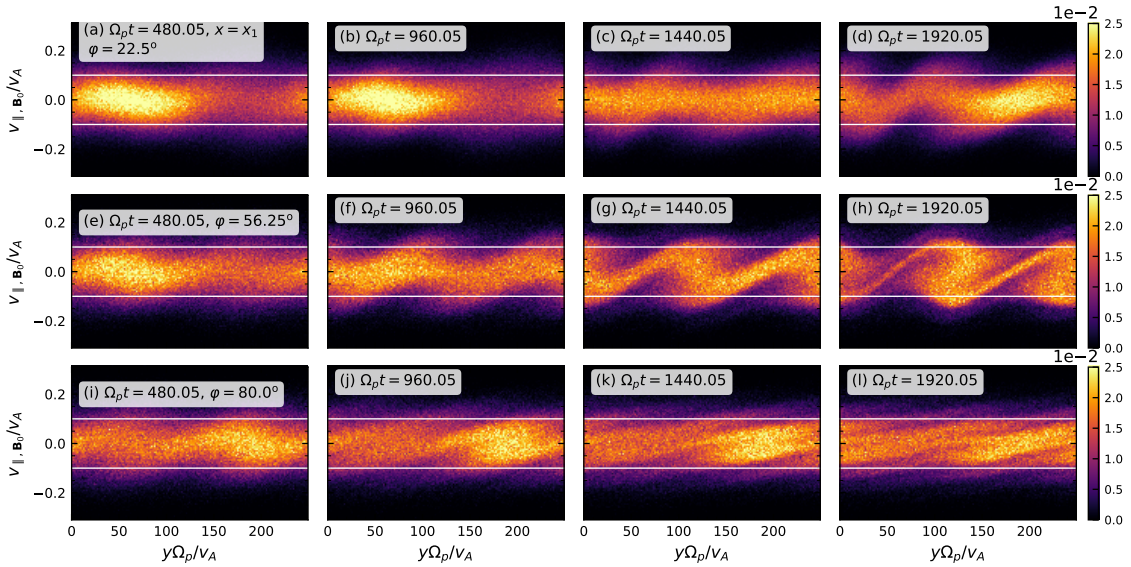

Figure 8.11: Evolution of the phase-space portraits at region R_{x1} for angles (a)–(d) $\varphi = 22.5°$, (e)–(h) $\varphi = 56.25°$, and (i)–(l) $\varphi = 80°$. Velocities are shown in the phase-space portraits (e)–(l): $v_{\parallel} = \pm u_0$ (solid white line). Here, $l/R = 0.5$.

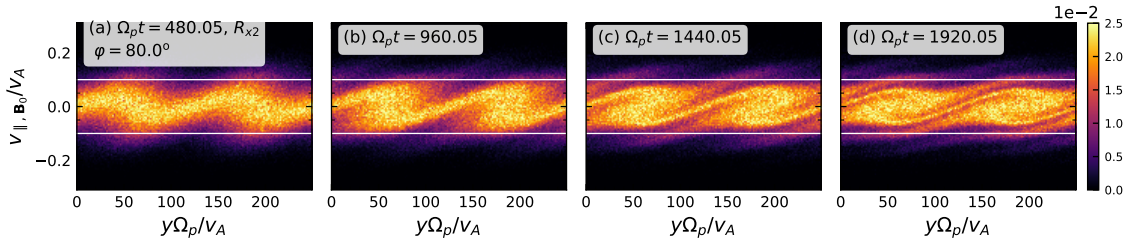

Figure 8.12: Evolution of the phase-space portraits $y - v_{\parallel}$ at region R_{x2} in the center of the slab for the angle [(a) to (d)] 80°. Velocities are shown in the phase-space portraits: $\left|v_{\parallel}\right| = u_0$ (solid white lines). Case of ratio $l/R = 0.5$.

acting parallel to $\mathbf{B}_0$ [33, 48, 158]. Resonant absorption seems to suppress these forces by diverting energy into the layers. Thus, for large angles, the weaker KAWs lead to weaker energy transfer and more pronounced ponderomotive forcing. For $\varphi = 10°$, the dynamics are dominated by kink oscillations, without major distortions in the

structure of the distributions.

8.7.3 Proton Parallel Temperature

Space-averaged temperatures are examined for $l/R = 0.5$ and all φ. Fluctuations occur mainly in the winglets for $22.5° \leq \varphi \leq 80°$, with the strongest increases in $\langle T_{p\parallel} \rangle$.

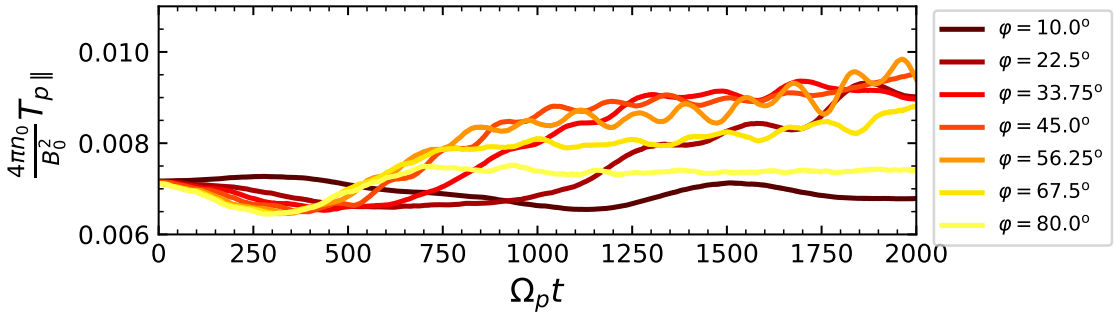

Figure 8.13: Evolution the space-averaged temperature $\langle T_{p\parallel} \rangle$ at the winglet in the left layer, $R_{x1} \times R_{y2}$.

At the winglet region ($R_{x1} \times R_{y2}$), temperature $\langle T_{p\parallel} \rangle$ (Fig. 8.13) exhibits an initial drop followed by an arrest that occurs earlier for larger φ. This arrest marks the onset of resonant absorption and parallel energization driven by the field $\delta E_\parallel$. A sustained increase follows for $22.5° \leq \varphi \leq 56.25°$, with the largest saturation temperature near $\varphi = 45° - 56.25°$. At higher angles, the growth weakens. These trends agree with the phase-space distortions in $y - v_\parallel$, which decrease toward $\varphi = 80°$ as the amplitudes of the KAWs drop.

Around the density cavity ($R_{x1} \times R_{y1}$), all temperatures oscillate at the kink frequency. Their amplitudes decrease with a larger angle φ. Moving averages $\langle T_{p\parallel} \rangle\big|_{\text{mob}}$ for $\varphi \geq 22.5°$ are shown in Fig. 8.14. The average temperature $\langle T_{p\parallel} \rangle$ drops below

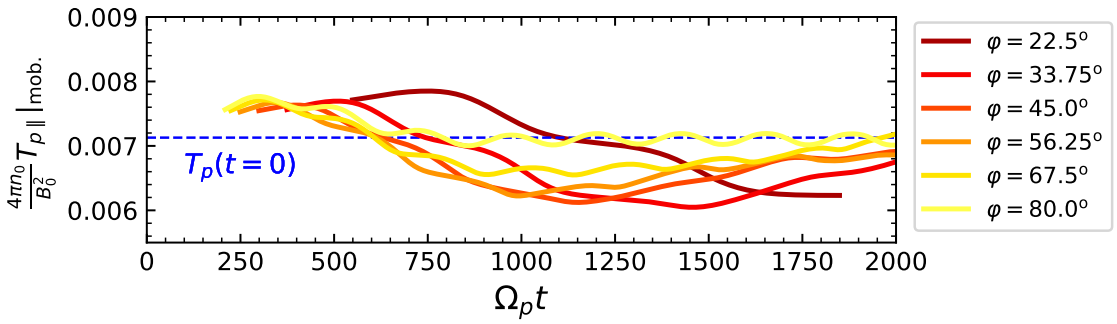

Figure 8.14: Evolution the space-averaged temperature $\langle T_{p\|} \rangle$, and mobile-averaged at a density cavity in the left layer, $R_{x1} \times R_{y2}$.

its initial level after $\Omega_p t \simeq 600$ for angles $\varphi \geq 33.75°$. This is delayed to $\Omega_p t = 1250$ for $\varphi = 22.5°$. The case $\varphi = 80°$ shows the smallest fluctuations.

Chapter 9

Kinetic processes induced by resonant absorption - transverse dynamics

9.1 Transverse Wave-particle Interaction

Kinetic Alfvén waves excited at the layers verify $\left|\omega_r/k_\parallel\right| \sim v_A$, far from the core of the proton distributions. Also, the developed frequencies in the electromagnetic fields are at least two orders of magnitude below that of the proton cyclotron frequency, so that there is no cyclotron resonance. Thus, there are no resonant wave-particle interactions, $\Omega_p \gg \omega_r \gg k_\parallel v_\parallel$ [55]. Therefore, the fluctuations exhibit non-resonant wave-particle interactions.

9.1.1 Cross-field Drift and Bulk-velocity

We now examine the dynamics in the $x-v_{\perp,2}$ phase-space portraits. For this purpose, we consider the transverse components of the cross-field drift $\mathbf{v}_{\mathrm{EM}} = c\mathbf{E} \times \mathbf{B}/B^2$, which is caused by the electromagnetic fields in the plasma. Figure 9.1 compares the transverse bulk velocity fluctuations $\delta u_{p\perp,1}$ and $\delta u_{p\perp,2}$ with the corresponding components of the cross-field drift for $l/R = 0.4$ at $y = y_1$ (center of a density cavity) and $y = y_2$ (center of a density winglet). There is strong agreement, indicating that the transverse proton dynamics are largely driven by the cross-field drift within the inhomogeneous layers.

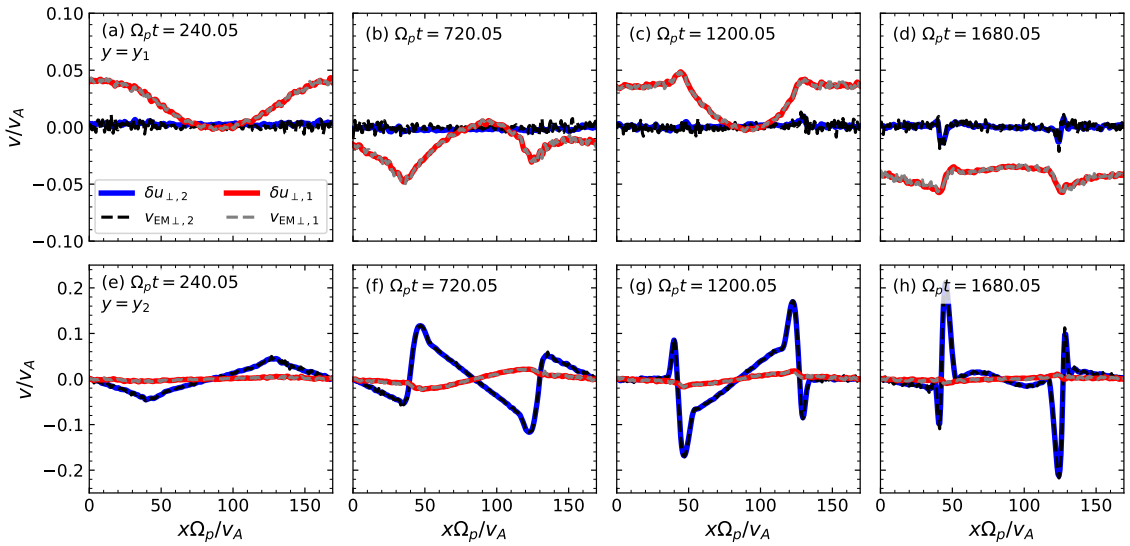

Figure 9.1: Sections of the cross-field drift $\mathbf{v}_{\mathrm{EM}}$ and the bulk-velocity components in the projections transverse to $\mathbf{B}_0$ at four selected times. Sections correspond to (a)–(d) $y = y_1$ at the center of a density hole, and (e)–(h) $y = y_2$ at the center a density winglet. A comparison is shown between data from bulk velocity components (solid, blue and red lines) and components of the cross-field drift (dashed, black and grey lines). Here, $l/R = 0.4$.

For $\varphi = 45°$, the relative deviations $|\delta u_{p\perp,1} - v_{\mathrm{EM},1}|/v_A$ at the layers are of order 10^{-2} for most of the simulations. This deviation is 5×10^{-2} times the maximum value in $|\delta u_{p\perp,1}|$. In $|\delta u_{p\perp,2} - v_{\mathrm{EM},2}|/v_A$, the maximum value is about 1.6×10^{-2}, nearly 9×10^{-2} times the maximum value of $|\delta u_{p\perp,2}|$. The deviations grow in time, more rapidly for smaller ratio l/R. By $\Omega_p t \simeq 1700$, this difference reach ~ 0.25 times the peak amplitude of $|\delta u_{p\perp,2}|$ for $l/R = 0.2 - 0.3$. This difference is $\lesssim 0.15$ the maximum value of this velocity for larger l/R. The largest differences arise at the layers. Yet, the cross-field drift reproduces the overall transverse response of protons, particularly $\delta u_{p\perp,2}$.

The cross-field drift has been associated with perpendicular non-resonant inter-

action [59, 63]. For our purposes, the most important component of this drift is the direction $e_{\perp,2}$,

$$v_{\mathrm{EM}\perp,2} = \frac{\delta E_{\parallel}\delta B_{\perp,1} - \delta E_{\perp,1}B_{\parallel}}{B^2}. \tag{9.1.1}$$

The dominant contribution to this drift is by $\delta E_{\perp,1}$, linked to the KAWs wavepackets. It carries a significant small-scale structure along the density gradient. Thus, the drift in the direction $e_{\perp,2}$ is highly localized. The large magnitude of $B_{\parallel} = B_0 + \delta B_{\parallel}$ causes this term to be dominant.

9.2 Phase-space Portraits along $x - v_{\perp,2}$ plane

The drift leads the proton distribution into an oscillatory motion in $e_{\perp,2}$ in the phase-space portraits $x - v_{\perp,2}$. This is shown in Fig. 9.2 and suggests reversible field-particle energy exchange. The strongest deformations become localized within the layers during and after resonant absorption in R_{y2} (center of a density winglet) [see Figs. 9.2(e)–(h)], coincident with the presence of the localized KAWs. Similar distortions have been reported in non-resonant heating by a spectrum of finite-amplitude Alfvén waves with non-random phases [59] and monochromatic KAWs [63], where the cross-field drift drives the particle motion. Toward the centers of the cavities, the deformations become negligible, suggesting no particle energization. This is consistent with the nearly vanishing amplitude of $v_{\mathrm{EM}\perp,2}$ [see Figs. 9.1(a)–(d) in the same region].

Further works have studied non-resonant interaction in low-β under random-phased Alfvén wave spectra and particle dynamics, finding pitch-angle scattering [56, 174, 175]. This renders particle motion as quasi-random [59]. The localized KAW

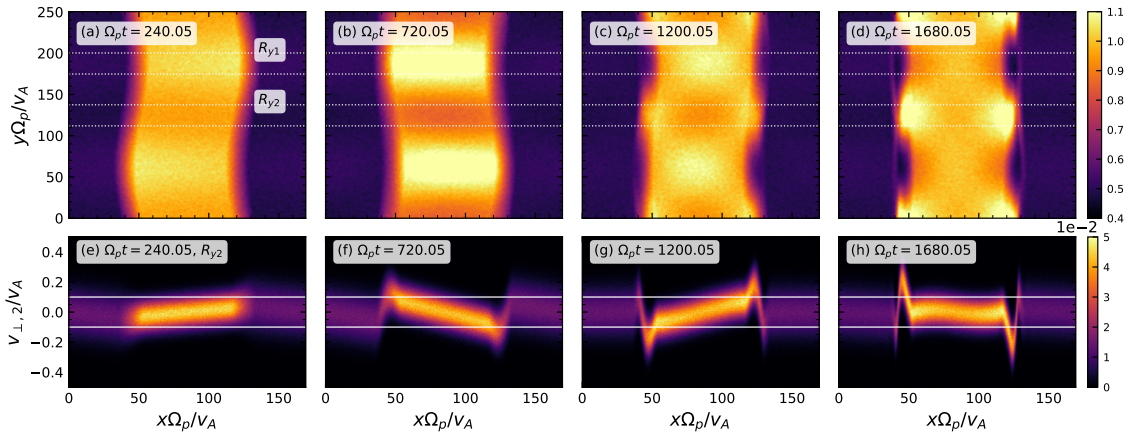

Figure 9.2: Evolution of (a)–(d) the proton density, and phase-space portraits $x-v_{\perp,2}$ at region (e)–(h) R_{y2} at the center of the central winglet. Velocities $|v_{\perp,2}| = u_0$ are shown in the phase-space portraits with solid white lines. Here, $l/R = 0.4$.

wavepackets possess non-random phases, but pitch-angle scattering may still arise within the layers at the winglets, as suggested by works on coherent Alfvén and whistler spectra [176, 177]. A more detailed particle-level analysis is out of the scope of this work.

The mechanism proposed by Vasquez [38] consists of scattering particles' velocity spaces $v_\parallel - v_\perp$, which matches the description of pitch-angle scattering, but they do not specify the underlying dynamical process.

9.3 Velocity Particle Distribution Functions

Figure 9.3 shows the velocity distributions in coordinates $v_\parallel - v_{\perp,2}$ at R_{x1}. At the density cavity, the distributions remain centered near the origin [Figs. 9.3 (a) to (d)]. Their width in $v_\parallel$ evolves consistently with the phase-space portraits $y-v_\parallel$ [Figs. 8.6 (f) to (h)]: bulk narrowing, particle depletion in the cavities transport toward the

winglets driven by the parallel field $\delta E_{\parallel}$. By the end of resonant absorption, diffusion appears around $\left|v_{\parallel}\right| \simeq u_0$ [Fig. 9.3 (d)]. At the winglet [Fig. 9.3 (e) to (h)], strong diffusion occurs across the range $\left|v_{\parallel}\right| \lesssim u_0$.

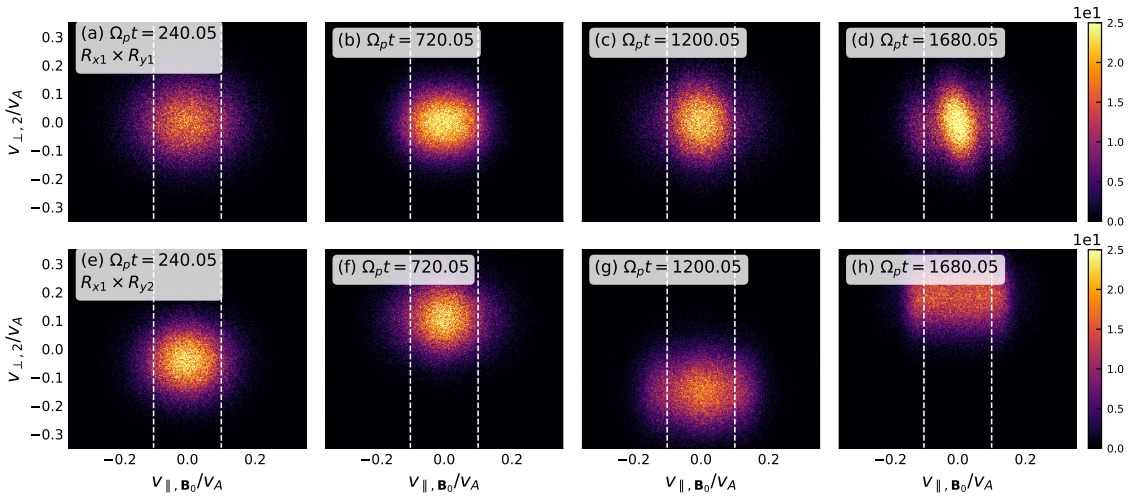

Figure 9.3: Evolution of the velocity distribution function at the region R_{x1} in the left inhomogeneous layer of the slab in coordinates $v_{\parallel} - v_{\perp,2}$ around (a)–(d) the center of a density hole R_{y1}, and (e)–(h) at the center of a winglet R_{y2}. Velocities $\left|v_{\parallel}\right| = u_0$ with dashed white lines are shown for comparison. Here, $l/R = 0.4$.

For the velocity $v_{\perp,2}$, the distributions at the winglet ($R_{x1} \times R_{y2}$) drift alternately in time, as seen in Figs. 9.3 (e)–(h). The drift in $v_{\perp,2}$ becomes negligible toward the cavities [$R_{x1} \times R_{y1}$ in Figs. 9.3(a)–(d)]. These features are in agreement with the phase-space portraits at the layers $x - v_{\perp,2}$ [see Figs. 9.2(e)–(h)] and in the behavior of the component $\delta u_{p\perp,2}$ [shown in Figs. 6.5 (k)–(o)].

With different l/R, distributions in $v_{\parallel} - v_{\perp,2}$ exhibit increasing diffusion in $v_{\perp,2}$ for smaller values of l/R during and after resonant absorption ($\Omega_p t = 1200.05$ and 1680.05). The broadening in velocity $v_{\parallel}$ is larger for the ratio $l/R = 0.2$ and weakens for larger l/R. Inside the slab, the distributions remain without significant features.

9.4 Proton Transverse Temperatures and Temperature Ratios

9.4.1 Transverse Temperatures

As with the parallel temperature, transverse temperatures' variations are concentrated at the layers for all values of l/R. We first address the density winglet ($R_{x1} \times R_{y2}$). The temperature $\langle T_{p\perp,1} \rangle$ [Fig. 9.4 (a)] remains nearly unchanged. In contrast, $\langle T_{p\perp,2} \rangle$ [Fig. 9.4 (b)] is nearly constant until $\Omega_p t \simeq 500$, after which it develops oscillatory peaks once KAWs form at the layers. These peaks follow an exponential envelope whose growth rate increases as l/R decreases. A spectral analysis of $T_{p\perp,2}$ (not shown) confirms that its fluctuations appear together with the KAWs and share the same frequency ω_{KAW}.

A Fourier decomposition of the component $\delta E_{\perp,1}$ in k_x at the winglet (Fig. 9.5) shows growing modes k_{x0}, $2k_{x0}$, and $3k_{x0}$. Their rise in amplitudes, signals the emergence of small-scale structure. Here, peaks in $\langle T_{p\perp,2} \rangle$ (black dashed lines) are concurrent with the growth of those modes. Similar mode amplitudes occur near the inflection points of $\langle T_{p\perp,2} \rangle$, but with opposite spatial distribution. This suggests reversible, non-dissipative apparent heating [59, 175, 178, 179]. The exponential component correlates with KAW localization and the cross-field drift. As l/R decreases, smaller scales dominate and drive faster growth in the envelope of $\langle T_{p\perp,2} \rangle$, consistent with diffusion processes described for weak Alfvénic turbulence [60] and pitch-angle scattering by coherent, non-random phased waves [176, 177].

Perpendicular non-resonant interaction with finite-amplitude Alfvén waves [56, 57, 59] and KAWs [63] based on particle motion leads to fluctuations in perpendic-

ular temperature. These fluctuations depend on the amplitudes of the waves of the spectra. Here, we can only assert that there is a correlation of the amplitudes of modes k_x of the KAWs, with the peaks in temperature $\langle T_{p\perp,2}\rangle$.

Heating in regions of enhanced density has been reported in research about resonant absorption [38], but our results point to a different origin. Parallel heating here arises from non-resonant acceleration by the field $\delta E_{\parallel}$ generated by wave coupling. Perpendicular heating appears only in the direction $e_{\perp,2}$ and exhibits reversibility in time, absent in Vasquez [38].

For all l/R, the three temperatures in the density cavity ($R_{x1} \times R_{y1}$) evolve in phase with the kink oscillations throughout the simulation. Their fluctuation frequency matches ω_{kink}. As in the winglets, smaller l/R produces larger temperature oscillations, indicating a stronger reversible field-particle power exchange at smaller transverse scales.

The time-averaged transverse temperatures $\langle T_{p\perp,1}\rangle$ and $\langle T_{p\perp,2}\rangle$ show small departures from their initial values. This indicates that the transverse field-particle energy exchange remains largely reversible and produces negligible net perpendicular heating when averaged over time in the cavities.

9.4.2 Temperature Ratios

At the density winglet ($R_{x1} \times R_{y2}$), the proton anisotropy remains near unity initially, then exhibits oscillatory deviations in the range $\Omega_p t \approx 240 - 720$. After resonant absorption, the anisotropy becomes localized at the layers, with enhanced temperature $\langle T_{p\parallel}\rangle$ at the winglets [Fig. 9.4 (c)]. All l/R show a long-term bias toward parallel heating, consistent with the broadening of the distributions in $v_{\parallel}$ [coordinates $v_{\parallel} - v_{\perp,2}$ in Figs. 9.3 (e) to (h)]. Smaller ratios l/R exhibit stronger anisotropy.

Deviations from gyrotropy at the winglets grow from $\Omega_p t \simeq 500$ onward [Fig. 9.4 (d)], favouring the broadening of the distributions in $v_{\perp,2}$. The envelope of $\langle T_{p\perp,2}\rangle$ / $\langle T_{p\perp,1}\rangle$ follows an exponential increase [dashed lines in frame (e)] with larger growth rates for smaller ratios l/R. Although the achieved conditions may transiently exceed instability thresholds, determining whether actual kinetic instabilities grow is beyond the scope of the present analysis.

At the density cavity ($R_{x1} \times R_{y1}$), the temperature anisotropy is therefore dominated by the reduction in $\langle T_{p\parallel}\rangle$, which biases the anisotropy to $\langle T_{p\perp}\rangle$. The ratio of transverse temperatures $\langle T_{p\perp,2}\rangle$ / $\langle T_{p\perp,1}\rangle$ remains close to unity through all of the runs, showing no significant non-gyrotropy inside the cavities up to $\Omega_p t \simeq 1700$.

9.5 The Effect of Different Angles φ

9.5.1 Wave-particle Interaction and Phase-space Portraits in $x - v_{\perp,2}$ Plane

In the projection $x - v_{\perp,2}$, the plasma oscillates coherently in $v_{\perp,2}$ at $\varphi = 22.5°$, centered near $x = L_y/2$. The oscillations mildly distort the distribution in the layers. This pattern is also present in $\varphi = 10°$. For larger angles, once fluctuations $\delta B_{\perp,2}$ become localized at the layers, the oscillations in the distribution become similarly localized around the density winglets [as in Figs. 9.2 (e) to (h) for $\varphi = 45°$ and $l/R = 0.4$], and deformations develop smaller-scale features that evolve increasingly rapidly as φ increases.

The magnitudes of the velocities achieved by the distributions at the winglets decrease for $\varphi \geq 67.5°$. This is consistent with the reduced efficiency of resonant absorption at large angles (Chapter 6). The dynamics follow the cross-field drift

described in subsection 9.1, dominated by the drift in Eq. (9.1.1), and the field $\delta E_{\perp,1}$. This holds for all φ and both l/R.

Finally, the maximum difference $|\delta u_{p\perp,2} - v_{\mathrm{EM},2}|/v_A$ at the layers remains small, $\lesssim 0.02$ for $l/R = 0.5$, rising to ~ 0.046 at $\Omega_p t = 2000$ for the range $45° \leq \varphi \leq 67.5°$, being 0.2 times the maximum amplitude of $\delta u_{\perp,2}$; and ~ 0.08 for $l/R = 0.2$ at $\varphi = 56.25°$ by $\Omega_p t = 1680$, being 0.4 times the maximum value of $\delta u_{p\perp,2}$. Despite this, the transverse cross-field drift provides an accurate description of the overall transverse motion. In accordance with this, it supports the interpretation that the phase-space dynamics in $x - v_{\perp,2}$ reflect protons following the drift imposed by the KAWs.

9.5.2 Velocity Distribution Functions

We track the velocity distribution functions in the projection $v_\parallel - v_{\perp,2}$ for fixed ratios $l/R = 0.2$ and 0.5. At the center of the density cavity ($R_{x1} \times R_{y1}$), the distributions evolve similarly to the case $l/R = 0.4$ and $\varphi = 45°$ [Figs. 9.3 (a) to (d)]. The distribution is depleted from the cavity and its core narrows in $v_\parallel$. This behavior is found for all angles $22.5° \leq \varphi \leq 80°$ and agrees with the narrow phase-space structures seen in $y - v_\parallel$ within a layer [Figs. 8.6 (a) to (d)]. For $\varphi = 80°$, both depopulation and narrowing are weakest due to the reduced particle energization.

At the center of the density winglet ($R_{x1} \times R_{y2}$), the distributions have drift in $v_{\perp,2}$ consistent with the cross- field drift component $e_{\perp,2}$. In velocity $v_\parallel$, the distributions broaden for $\varphi \geq 22.5°$, indicating diffusion that produces strong flattening around $v_\parallel = 0$ by time $\Omega_p t = 1200$. The flattening becomes stronger with increasing angle φ up to $\varphi = 56.25°$. For larger angles, it is reduced, again reflecting weaker energization.

For angle $\varphi = 10°$, the distributions remain close to Maxwellians, with minimal distortions. The same holds for the ratio $l/R = 0.2$.

9.5.3 Proton Transverse Temperatures and Temperature Ratios

Space-averaged temperatures have localized fluctuations at the winglets ($R_{x1} \times R_{y2}$), specifically for $22.5° \leq \varphi \leq 80°$. Temperature $\langle T_{p\perp,2} \rangle$ grows the most, but slower than $\langle T_{p\parallel} \rangle$. The temperature $\langle T_{p\perp,1} \rangle$ remains near its initial value and follows the kink oscillations.

The temperature $\langle T_{p\perp,2} \rangle$ [Fig. 9.6 (a)] grows exponentially with oscillations up to $\Omega_p t = 1800$. The growth rate is the smallest for $\varphi = 80°$, as resonant absorption here is the weakest. For the angles $\varphi \geq 22.5°$, the development of small-scale fluctuations in $\delta E_{\perp,1}$ associated with KAWs produces similar behavior, extending the reversibility of the process and the possibility of pitch-angle scattering to configurations with different angles φ.

Proton anisotropy is governed by the temperature $\langle T_{p\parallel} \rangle$ [Fig. 9.6 (b)]. The early saturation follows from the initial arrest, while the later decreases due to parallel heating. Minimum anisotropies occur for $33.75° \leq \varphi \leq 56.25°$. For $\varphi = 67.5°$, anisotropy remains small due to weaker resonant absorption (Chapter 6). Deviations from gyrotropy [Fig. 9.6 (d)], rise with φ and peak at the range $\varphi = 56.25° - 67.5°$, while remaining minimal at $\varphi = 10°$.

Around the density cavity ($R_{x1} \times R_{y1}$), all temperatures oscillate at the kink frequency. Their amplitudes decrease with a larger angle φ. Moving averages $\langle T_p \rangle|_{\text{mob}}$ for the perpendicular temperatures have minimal deviations, implying negligible net heating/cooling of the distributions at the cavities. Oscillatory components dampen weakly, with slower damping at larger angles φ, indicating a decreased field-particle

energy exchange over time and a net narrowing of the distributions in time.

Temperature ratios (no moving average) show that the cavity anisotropy (Fig. 9.7) decreases until resonant absorption begins. The arrest occurs later for smaller angles. At $\varphi = 22.5°$, anisotropy grows in favour of the perpendicular direction due to the decay of $\langle T_{p\|} \rangle$. For larger angles, anisotropy saturates above unity, peaking at $33.75° \leq \varphi \leq 56.25°$ and decreasing for larger angles. The perpendicular temperatures remain essentially gyrotropic for all φ.

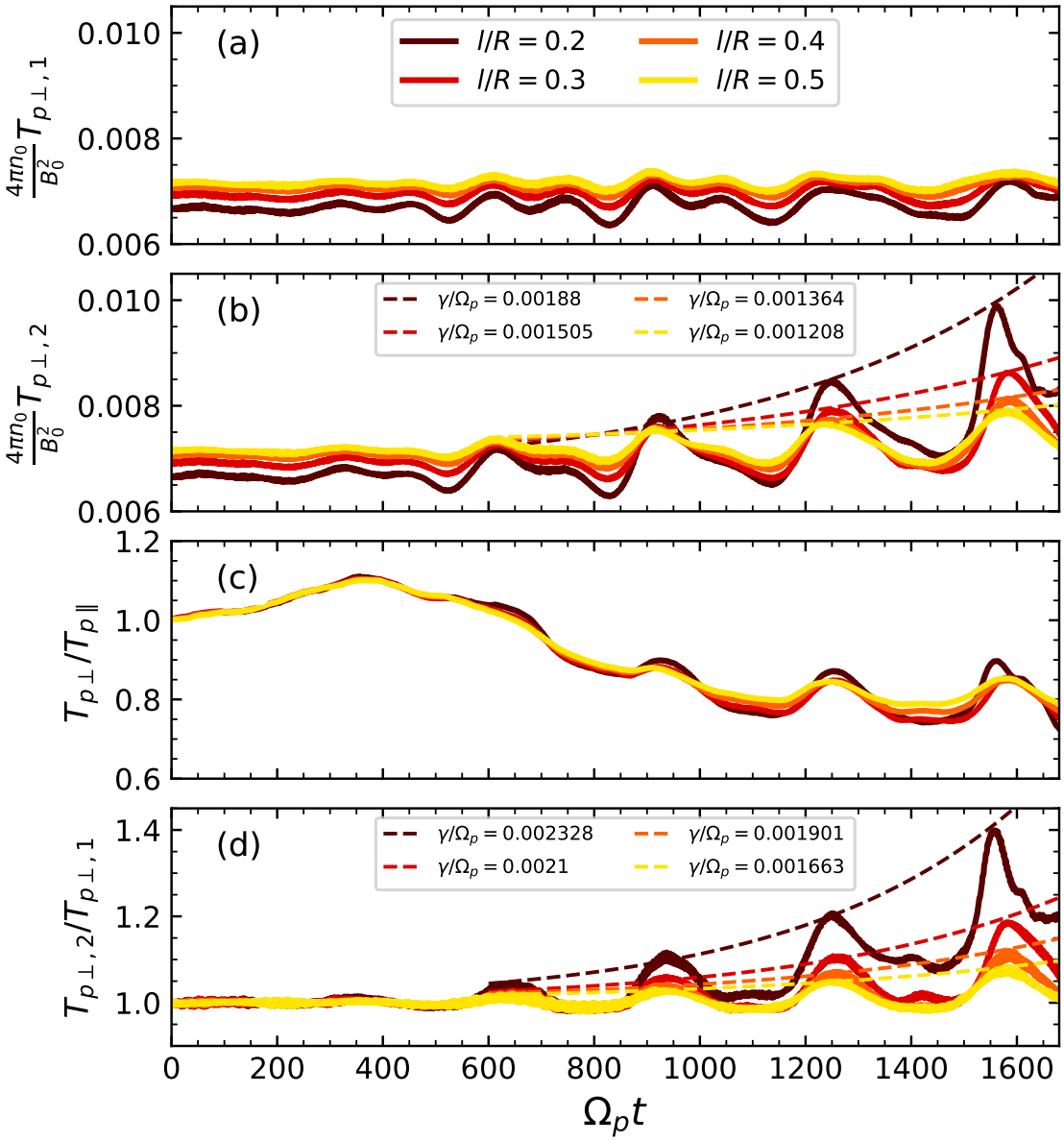

Figure 9.4: Evolution of temperature-related quantities for different l/R. Quantities are averaged in a region corresponding to a density winglet at the left layer, $R_{x1} \times R_{y2}$. Quantities (solid lines) are (a) $\langle T_{p\perp,1} \rangle$, (b) $\langle T_{p\perp,2} \rangle$, (c) anisotropy of space-averaged temperatures, $\langle T_{p\perp} \rangle / \langle T_{p\parallel} \rangle$, and (d) ratio of space-averaged perpendicular temperature, $\langle T_{p\perp,2} \rangle / \langle T_{p\perp,1} \rangle$. Exponential fit to envelopes are shown for $\langle T_{p\perp,2} \rangle$ and $\langle T_{p\perp,2} \rangle / \langle T_{p\perp,1} \rangle$ (dashed lines).

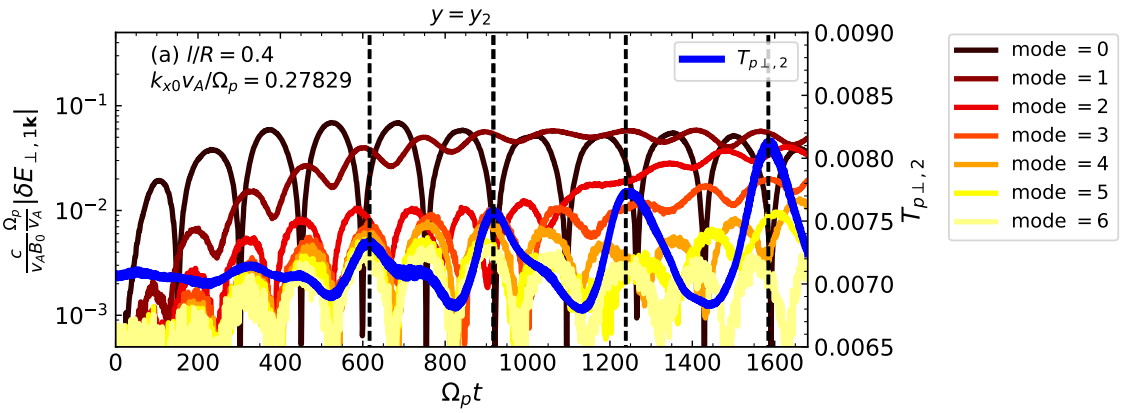

Figure 9.5: Fourier decomposition in k_x of the electric field fluctuations $\delta E_{\perp,1}$ within the left inhomogeneous layer at the section $y = y_2$ around the center of a density winglet, compared with the space-averaged temperature $\langle T_{p\perp,2}\rangle$ at the same location. Here, $l/R = 0.4$.

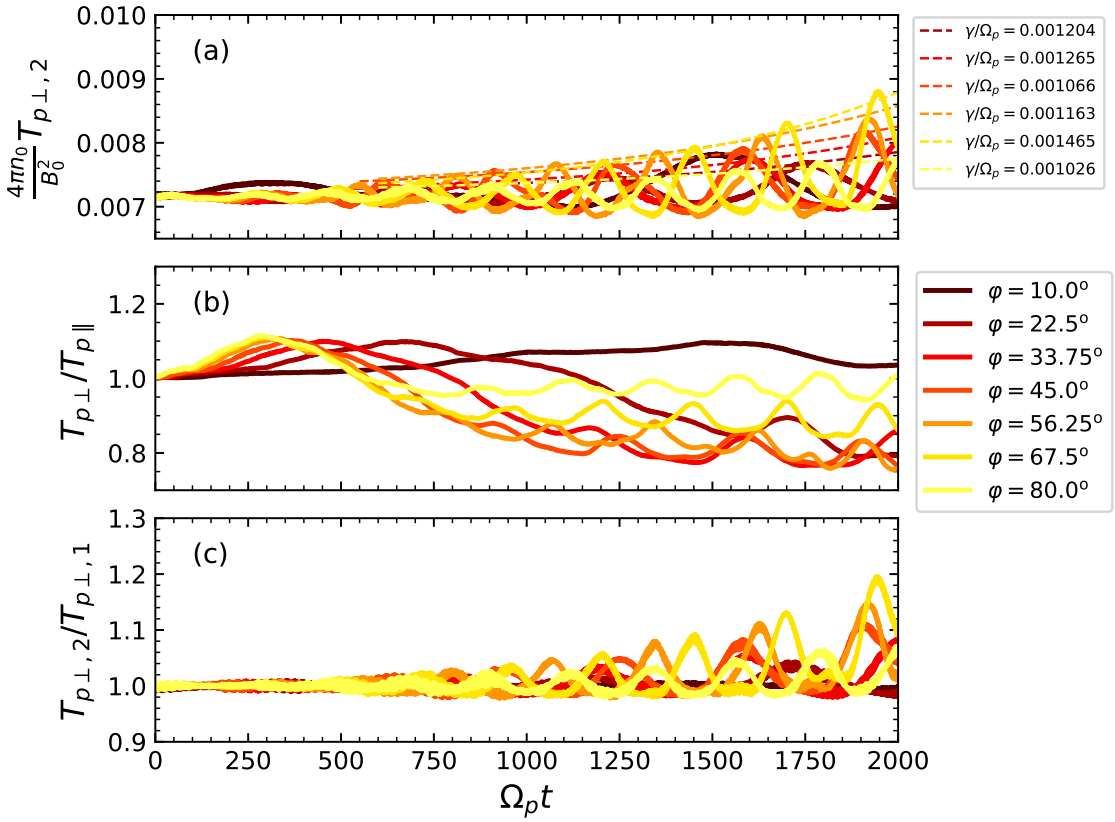

Figure 9.6: Evolution of temperature-related quantities for different angles φ. Quantities are averaged in the region around a density winglet at the left layer, $R_{x1} \times R_{y2}$. Quantities (solid lines) are (a) $\langle T_{p\perp,2} \rangle$, (b) anisotropy of space-averaged temperatures, $\langle T_{p\perp} \rangle / \langle T_{p\parallel} \rangle$, and (b) the ratio of space-averaged transverse temperatures, $\langle T_{p\perp,2} \rangle / \langle T_{p\perp,1} \rangle$. Fixed ratio $l/R = 0.5$.

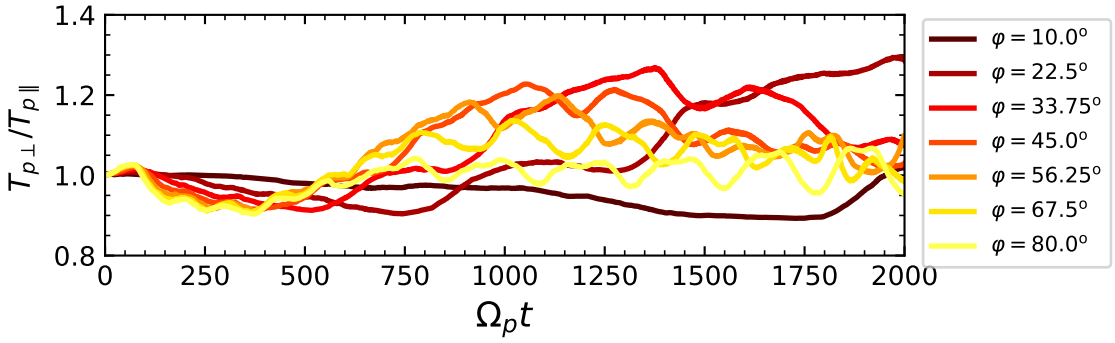

Figure 9.7: Evolution of proton temperature anisotropy, $\langle T_{p\perp} \rangle / \langle T_{p\parallel} \rangle$, for different angles φ. Temperatures are averaged in the region around a density hole at the left layer, $R_{x1} \times R_{y1}$. Fixed ratio $l/R = 0.5$.

Chapter 10
Conclusions

The process of resonant absorption in a plasma composed of kinetic protons and fluid, massless electrons have been studied in a plasma slab with inhomogeneous density layers via 2D−3V PIC-hybrid simulations for different layer thickness ratios l/R and angles of the background magnetic field φ. The initial perturbation consists of a superposition of waves, among which there is a combination of left- and right-hand polarized MHD waves that exhibit oscillations transverse to the y-axis.

10.1 On the Multi-fluid Features of the Resonant Absorption

This work examined the multi-fluid features of resonant absorption in an inhomogeneous plasma slab. They are compared with single-fluid MHD theory. Transverse kink oscillations are localized and refracted in the layers, becoming aligned with the density gradient. The localized fluctuations generate small-scale fluctuations in proton density, transverse bulk velocity, and magnetic field [component $(\perp, 2)$], and parallel vorticity. Such features are consistent with resonant absorption for different l/R and φ. This renders resonant absorption as a robust phenomenon.

The perturbed mode of $\delta u_{p\perp,1}$ exhibits exponential decay with an inhomogeneous damping rate. The damping time rates inferred at the layers, where resonant absorption occurs, generally agree with MHD predictions. However, there are deviations for

smaller l/R, weakly magnetized ($\varphi \leq 33.75°$), and strongly magnetized ($\varphi \geq 67.5°$) slabs. We attribute these discrepancies to kinetic and non-linear effects, which become important when the transverse displacements exceed the length of the layers, or to the effective β_p becoming smaller for small φ. In strong magnetization, a larger fraction of the energy remains stored in the large-scale mode.

The small-scale fluctuations generated by resonant absorption in density, bulk velocity, and magnetic field grow mainly in k_x, and reach scales below the density-gradient scale for all of the cases of φ and l/R. Energy in magnetic field fluctuations is found at scales around the proton inertial length after resonant absorption. Energy analysis confirms that the energy transfer toward smaller scales is more efficient for larger ratios l/R. Conversely, smaller ratios l/R, are capable of redistributing energy closer to kinetic scales. Different angles φ affect the energy transfer toward small scales. Moderately magnetized slabs readily allow reaching the proton inertial length. Strongly magnetized slabs also allow for small-scale fluctuations to develop, but with smaller amplitudes. Weakly magnetized slabs are dominated by large-scale fluctuations. Thus, both l/R and φ affect the efficiency in energy transfer toward kinetic scales and in the development of small-scale fluctuations.

In transverse magnetic field fluctuations, we identify quasi-perpendicular, weakly compressible waves with a strong electrostatic component. Signatures in the dispersion relations of $\delta B_{\perp,2}$, polarization in the plasma physics sense, and other spectral diagnostics allow to characterize them primarily as KAWs, with the possible contribution of other modes at later times. They develop for all ratios l/R, and angles $\varphi \geq 22.5°$.

Finally, in all configurations where resonant absorption operates, the frequency of the global kink mode matches the frequency of the generated KAWs. Thus, small-

scale waves are generated at scales in the order of the proton inertial length with the same frequency of the initial excited mode.

10.2 On the Kinetic Features of Resonant Absorption

Resonant absorption produces spatially localized KAW fluctuations. They interact non-linearly and generate a parallel electric field $\delta E_{\parallel}$. This field is responsible for the formation of small-scale, nonpropagating, and density structures (cavities and winglets). The analytical estimate proposed here reproduces well the main signals of $\delta E_{\parallel}$. This estimate captures the main signatures of the field dispersion relation $\omega_r - k_y$. The spatial component of $\delta E_{\parallel}$ accelerates protons along $\mathbf{B}_0$. For all the parameters in which resonant absorption operates, flat-topped distributions develop at the winglets. Such distributions indicate strong parallel heating. This demonstrates the kinetic impact of resonant absorption of the global kink mode on the proton distribution functions.

In the perpendicular directions, the electromagnetic fields drive cross-field drift. The proton distribution functions develop oscillatory patterns in $v_{\perp,2}$. They are consistent with non-resonant field-particle interactions with Alfvén waves and KAWs. These oscillations gradually localize within the layers. The component $(\perp, 2)$ of the drift is dominant and closely follows the structure of $\delta E_{\perp,1}$. The emergence of small-scale fluctuations in $\delta E_{\perp,1}$ correlates with the exponential increase in the envelope of $T_{p\perp,2}$. This seems consistent with pitch-angle scattering driven by non-random phased KAWs. Its oscillatory component suggests partial reversibility.

These effects appear for all l/R, but may differ in intensity. Larger amplitudes are found for thinner layers whose widths approach the proton inertial length. The

effects are stronger for $22.5° \leq \varphi \leq 56.25°$ and weaken as the projection of the field $\mathbf{B}_0$ on the simulation plane increases. No resonant absorption or associated kinetic activity is observed for $\varphi = 10°$. All the identified energization processes are non-linear and non-resonant. This underlines their relevance for the generation of small-scale structures in space, in the particle distribution functions, and in proton heating for low-β, inhomogeneous plasmas. These mechanisms differ in nature from those proposed by [38].

The interpretations of $\delta E_{\parallel}$ and the drift estimates are limited by the approximations required for analytical traceability. Their applicability to other regimes or parameter choices may be reduced. Nonetheless, the present results show non-linear pathways emerging from resonant absorption to kinetic-scale structures and proton energization.

10.3 General Remarks

As a final remark, we assess the feasibility of the configuration studied in this research. As was noted in the definition of the parameters, the scale-lengths of the system we use (in the order of 5 km with inhomogeneities of length $184\ \text{m} \leq l \leq 460\ \text{m}$ based on observational parameters in coronal loops [73, 74, 83–85]) are much smaller than what can be measured with the current technology in solar corona (SolO [90, 91]). Therefore, the scale-lengths used in this research may not correspond to actual observable structures. Physical quantities such as particle density and magnetic field have been reported as uniform within an extension of 40 Mm around the apex of the coronal loops [83]. In this sense, the configuration we use may be regarded as a small section around the apex of a loop. Another point to be noted is the periodic bound-

ary conditions in both axes. A more realistic setting would consider open boundary along the direction of the density gradient, allowing for particle flux along these directions or to introduce effects which emulate curvature in the slab. Regardless, this configuration provides a clear description of resonant absorption when fluctuations reach spatial scales in the order of the proton inertial length, and presents a contribution to understand both the multifluid feature of resonant absorption, and the kinetic features of the phenomenon when kinetic scales are reached. In any case, if structures whose size is in the order of the 1 km with inhomogeneities of $100 - 500$ m in the solar corona, we would expect to observe the physics we report here. We also expect that the physics of resonant absorption in real-size coronal loops to be qualitatively similar to our results when kinetic-scales are reached, since the process essentially transports fluctuations towards small scales.

Chapter 11

List of Activities

This chapter compiles the academic activities performed during the PhD program, including publications, presentations, and other activities.

11.1 Accepted Publications

2023

- H. A. Carril, J. A. Gidi, R. E. Navarro, A. A. Araneda. "Formation of multiple BGK-like structutres in the time-asymptotic state of collisionless Vlasov-Poisson plasmas". In: *PhRevE* 107, 065203 (June 2023), p. 065203. DOI: 10.1103/PhysRevE.107.065203.

2025

- H. A. Carril, J. Terradas, R. E. Navarro, A. F. Viñas, M. Goossens. "Resonant Absorption and Fluctuations via Hybrid Simulations on Coronal Loops. I. Plasma Multifluid Description". In: *ApJ* 986.1, 40 (June 2025), p. 40. DOI: 10.3847/1538-4357/adceac.

2026

- H. A. Carril, A. F. Viñas, J. Terradas, R. E. Navarro, M. Goossens. "Resonant Absorption and Fluctuations via Hybrid Simulations on Coronal Loops. II. Kinetic Description". In: *ApJ* 999.2 (March 2026), p. 191. DOI: 10.3847/1538-4357/ae394e.

11.2 Presentations

2020

- **Poster** presented online at the **XXII Simposio Chileno de Física** from November 24 to 26. Title: "Coupling of Solitary Ion-Acoustic Waves and Electron Holes in Maxwellian Unmagnetized Plasmas".

2021

- **Poster** presented online at the **XII Conferencia Latinoamericana de Geofísica Espacial, COLAGE** 2021, from November 22 to 26. Title: "Coupling of Solitary Ion-Acoustic Waves and Electron Holes in Maxwellian Unmagnetized Plasmas".

2022

- **Poster** presented at the **XXIII Simposio Chileno de Física**, from November 22 to 24 in Valparaíso, Chile. Title: "Formation of multiple BGK-like structutres in the time-asymptotic state of collisionless Vlasov-Poisson plasmas".

2024

- **Poster** presented at the **XIV Conferencia Latinoamericana de Geofísica Espacial, COLAGE** 2024 from April 9 to 12 in Monterrey, México. Title: "Resonant Absorption via 2D Hybrid-PIC Simulations".

- **Poster** presented at the **XXIV Simposio Chileno de Física** from November 20 to 22 in Temuco, Chile. Title: "Resonant Absorption via 2D Hybrid-PIC Simulations".

2025

- **Talk** presented at the **II Congreso Chileno de Física de Plasmas** from December 1 to 4 in Valparaíso, Chile. Title: "Resonant Absorption via 2D Hybrid-PIC Simulations: Kinetic Description".

11.3 Other Relevant Activities and Outreach

2023

- **Doctoral stay** in Palma, Spain from October 4 2023 to August 31 2024, at the Universitat de les Illes Balears (UIB) under the guidance of Dr. Jaume Terradas Calafell.

2024

- **Monitor** at the **Ciència per a Tothom** 2024, May 9 in Palma, Spain.

Appendices

Appendix A

Mathematical Appendix

A.1 Rotation Matrices for Vector Quantities

The analysis of the vector quantities is made on an orthonormal basis in which one of the axes is alingned with the background magnetic field $\mathbf{B}_0$. The first rotation is in the azimuthal angle θ measured from the axis x, contained in the plane xy and defined by the matrix $R(\theta)$. Explicitly, for a vector $\mathbf{A}$ defined over the axes xyz, this rotation is given by

$$\begin{aligned} \mathbf{A}' &= R(\theta)\mathbf{A} \\ \begin{Bmatrix} A'_x \\ A'_y \\ A'_z \end{Bmatrix} &= \begin{bmatrix} \cos\theta & \sin\theta & 0 \\ -\sin\theta & \cos\theta & 0 \\ 0 & 0 & 1 \end{bmatrix} \begin{Bmatrix} A_x \\ A_y \\ A_z \end{Bmatrix}, \end{aligned} \tag{A.1.1}$$

with unit vectors

$$\begin{aligned} \widehat{\mathbf{x}}' &= \cos\theta\widehat{\mathbf{x}} + \sin\theta\widehat{\mathbf{y}}, \\ \widehat{\mathbf{y}}' &= -\sin\theta\widehat{\mathbf{x}} + \cos\theta\widehat{\mathbf{y}}, \\ \widehat{\mathbf{z}}' &= \widehat{\mathbf{z}}. \end{aligned}$$

This rotation is graphically shown in Fig. A.1. The rotation on φ is performed on

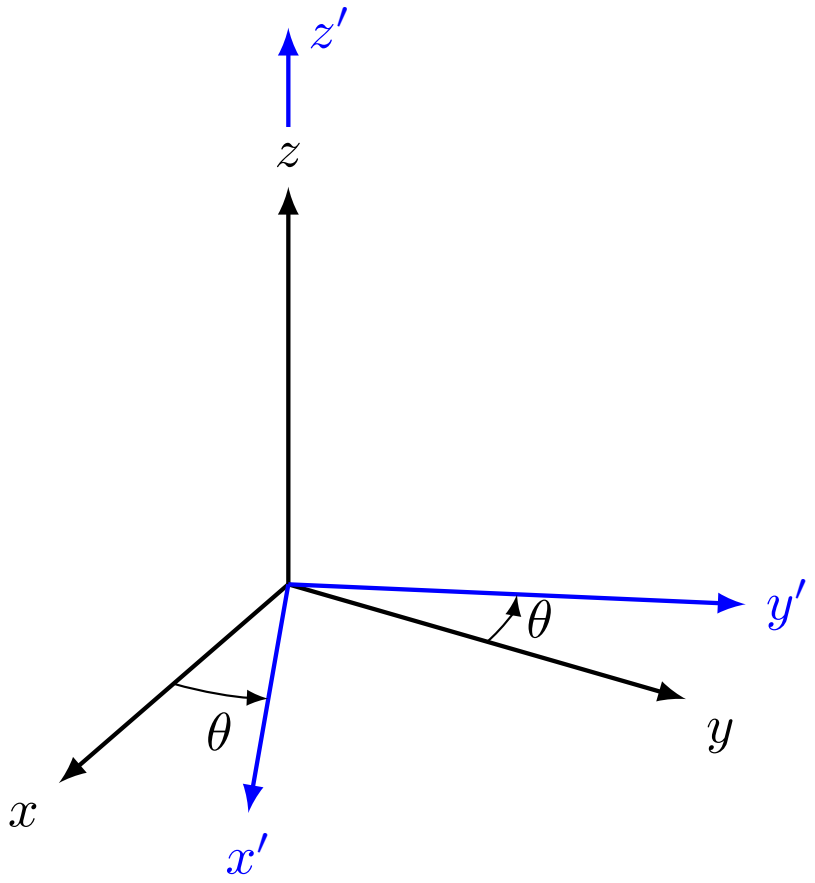

Figure A.1: Rotation of axes xyz (black) to $x'y'z'$ (blue) via the rotation matrix $R(\theta)$ with angle θ.

a vector $\mathbf{A}'$ already rotated by the matrix $R(\theta)$. For such a vector, the rotation is mediated by the matrix $R(\varphi)$, obtaining a vector in the axes $\parallel, \perp 1, \perp 2$. The angle

φ is measured from the axis z. The transformation is explicitly given by

$$\begin{aligned} \mathbf{A}_{\mathbf{B}_0} &= R(\varphi)\mathbf{A}' \\ \begin{Bmatrix} A_{\parallel} \\ A_{\perp,1} \\ A_{\perp,2} \end{Bmatrix} &= \begin{bmatrix} \sin\varphi & 0 & \cos\varphi \\ 0 & 1 & 0 \\ -\cos\varphi & 0 & \sin\varphi \end{bmatrix} \begin{Bmatrix} A'_x \\ A'_y \\ A'_z \end{Bmatrix}, \end{aligned} \tag{A.1.2}$$

with unit vectors

$$\begin{aligned} \widehat{\mathbf{e}}'_{\parallel} &= \sin\varphi\widehat{\mathbf{x}}' + \cos\theta\widehat{\mathbf{z}}', \\ \widehat{\mathbf{e}}'_{\perp,1} &= \widehat{\mathbf{y}}', \\ \widehat{\mathbf{e}}'_{\perp,2} &= -\cos\varphi\widehat{\mathbf{x}}' + \sin\theta\widehat{\mathbf{z}}'. \end{aligned}$$

This rotation is graphically shown in Fig. A.2. Therefore, the rotation from a vector given in the axes xyz to the axes $\parallel, \perp 1, \perp 2$, aligned with the background magnetic field $\mathbf{B}_0$ is given by the matrix $R(\theta,\varphi) = R(\varphi)R(\theta)$. Explicitly,

$$\begin{aligned} \mathbf{A}_{\mathbf{B}_0} &= R(\varphi)R(\theta)\mathbf{A} \\ \begin{Bmatrix} A_{\parallel} \\ A_{\perp,1} \\ A_{\perp,2} \end{Bmatrix} &= \begin{bmatrix} \cos\theta\sin\varphi & \sin\theta\sin\varphi & \cos\varphi \\ -\sin\theta & \cos\theta & 0 \\ -\cos\theta\cos\varphi & -\sin\theta\cos\varphi & \sin\varphi \end{bmatrix} \begin{Bmatrix} A_x \\ A_y \\ A_z \end{Bmatrix}, \end{aligned} \tag{A.1.3}$$

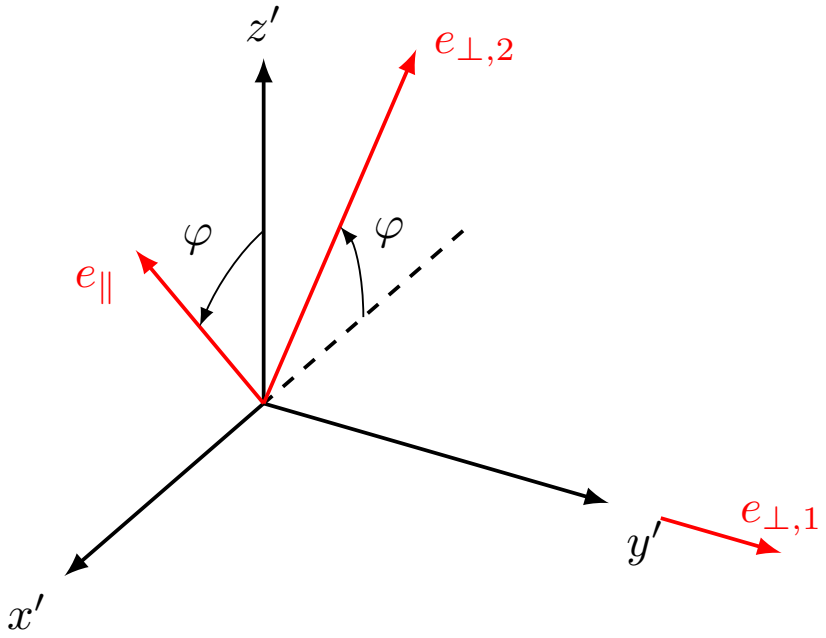

Figure A.2: Rotation of axes $x'y'z'$ (black) to $\parallel, \perp 1, \perp 2$ (red) via the rotation matrix $R(\varphi)$ with angle φ.

with unit vectors

$$\begin{aligned}
\widehat{\mathbf{e}}_{\parallel} &= \cos\theta \sin\varphi \widehat{\mathbf{x}} + \sin\theta \sin\varphi \widehat{\mathbf{y}} + \cos\varphi \widehat{\mathbf{z}}, \\
\widehat{\mathbf{e}}_{\perp,1} &= -\sin\theta \widehat{\mathbf{x}} + \cos\theta \widehat{\mathbf{y}}, \\
\widehat{\mathbf{e}}_{\perp,2} &= -\cos\theta \cos\varphi \widehat{\mathbf{x}} - \sin\theta \cos\varphi \widehat{\mathbf{y}} + \sin\varphi \widehat{\mathbf{z}}.
\end{aligned}$$

Graphically, the combination of rotations is shown in Fig. A.3 for arbitrary angles θ and φ.

In the paper, the field $\mathbf{B}_0$ is given by $\mathbf{B}_0 = B_0(\sin\varphi\widehat{\mathbf{y}} + \cos\varphi\widehat{\mathbf{z}})$, so that the quantities defined in axes xyz are now rotated to $\mathbf{B}_0$, so that $\theta = \pi/2$ and φ. This

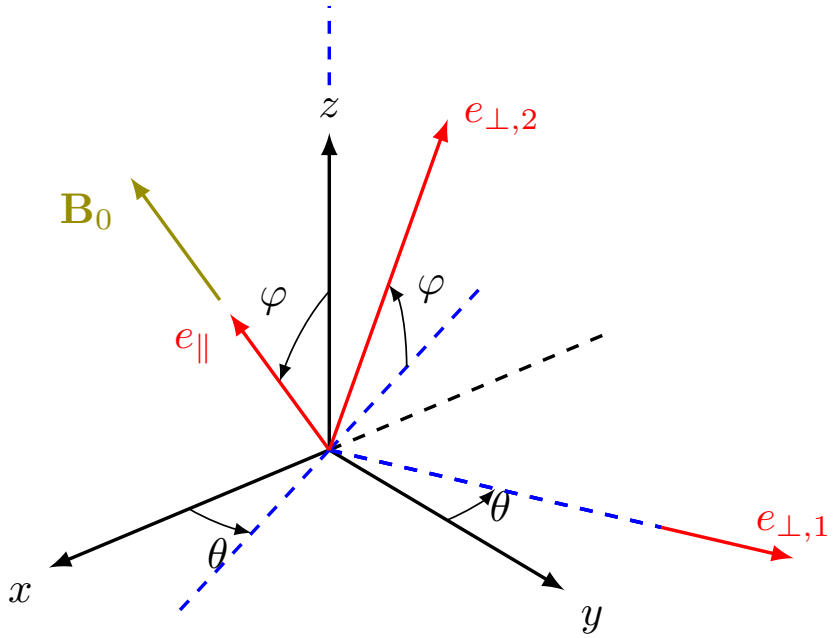

Figure A.3: Rotation of axes xyz (black) to $\parallel, \perp 1, \perp 2$ (red), aligned with the field $\mathbf{B}_0$ (green), via the rotation matrix $R(\theta, \varphi) = R(\varphi)R(\theta)$ with angles θ and φ. Blue dashed lines represent the intermediate axes $x'y'z'$.

transformation is given by

$$\mathbf{A}_{\mathbf{B}_0} = R(\varphi)R(\pi/2)\mathbf{A}$$

$$\begin{Bmatrix} A_{\parallel} \\ A_{\perp,1} \\ A_{\perp,2} \end{Bmatrix} = \begin{bmatrix} 0 & \sin\varphi & \cos\varphi \\ -1 & 0 & 0 \\ 0 & -\cos\varphi & \sin\varphi \end{bmatrix} \begin{Bmatrix} A_x \\ A_y \\ A_z \end{Bmatrix}, \tag{A.1.4}$$

with unit vectors

$$\begin{aligned}\widehat{\mathbf{e}}_{\parallel} &= \sin\varphi\widehat{\mathbf{y}} + \cos\varphi\widehat{\mathbf{z}},\\ \widehat{\mathbf{e}}_{\perp,1} &= -\widehat{\mathbf{x}},\\ \widehat{\mathbf{e}}_{\perp,2} &= -\cos\varphi\widehat{\mathbf{y}} + \sin\varphi\widehat{\mathbf{z}}.\end{aligned}$$

This rotation is graphically shown in Fig. A.4. The inverse transformation is given by the inverse matrix of (A.1.4), given by

$$\begin{aligned}\mathbf{A} &= R^{-1}(\pi/2,\varphi)\mathbf{A}_{\mathbf{B}_0}\\ \begin{Bmatrix} A_x \\ A_y \\ A_z \end{Bmatrix} &= \begin{bmatrix} 0 & -1 & 0 \\ \sin\varphi & 0 & -\cos\varphi \\ \cos\varphi & 0 & \sin\varphi \end{bmatrix} \begin{Bmatrix} A_{\parallel} \\ A_{\perp,1} \\ A_{\perp,2} \end{Bmatrix}.\end{aligned} \tag{A.1.5}$$

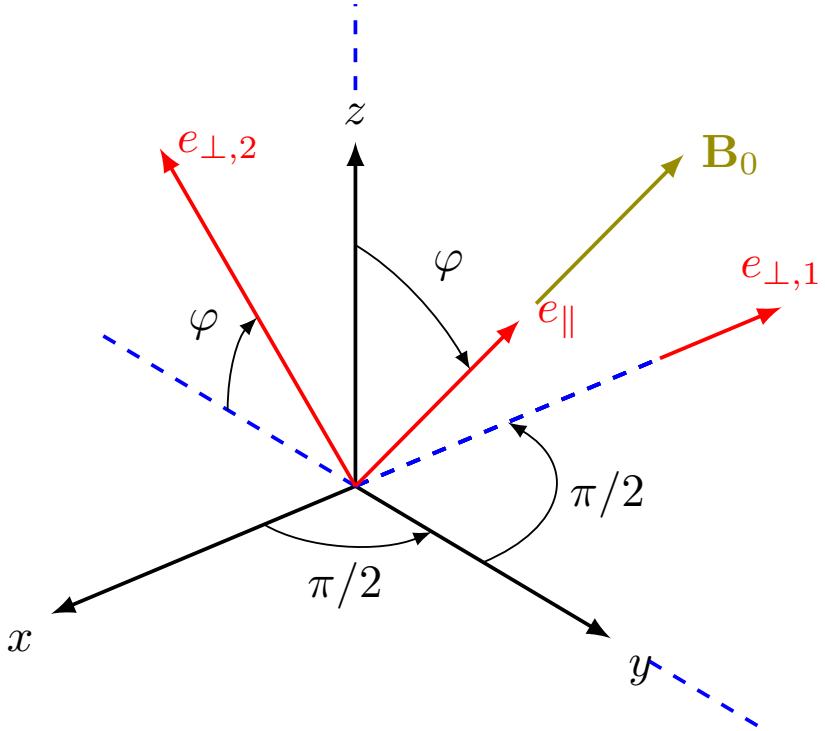

Figure A.4: Rotation of axes xyz (black) to $\parallel, \perp 1, \perp 2$ (red), aligned with the field $\mathbf{B}_0$ (green), via the rotation matrix $R(\theta, \varphi) = R(\varphi)R(\theta)$ with angles $\theta = \pi/2$ and φ. Blue dashed lines represent the intermediate axes $x'y'z'$.

A.2 Complex Integration

The integration of Equation (2.2.11) with the approximation of Equation (2.2.12) leads to an integral of the form

$$\lim_{\delta \to 0^+} \int_{x_A-\delta}^{x_A+\delta} \frac{F(x)}{x - x_A} \mathrm{d}x, \tag{A.2.1}$$

in the limit of thin inhomogeneous layer. Here, $F(x)$ is an analytic function of x everywhere in the complex plane. The argument of the integral (A.2.1) has a simple pole at $x = x_A$, which is within the integration domain. Therefore, complex calculus methods are required to solve it properly. This task requires to introduce a contour of integration around the simple pole. A semicircunference contour $\mathcal{C}_\epsilon$ of radius ϵ such that $\delta > \epsilon > 0$. Two other contours are defined on the real axes, $\mathcal{C}_1$ and $\mathcal{C}_2$. The overall contour $\mathcal{C} = \mathcal{C}_\epsilon \cup \mathcal{C}_1 \cup \mathcal{C}_2$ is shown in Fig. A.5.

Thus, the integral becomes

$$\int_{\mathcal{C}} \frac{F(\eta)}{\eta - x_A} \mathrm{d}\eta = \int_{x_A-\delta}^{x_A-\epsilon} \frac{F(x)}{x - x_A} \mathrm{d}x + \int_{x_A+\epsilon}^{x_A+\delta} \frac{F(x)}{x - x_A} \mathrm{d}x + \int_{\mathcal{C}_\epsilon} \frac{F(\eta)}{\eta - x_A} \mathrm{d}\eta.$$

The integral over $\mathcal{C}_\epsilon$ is parametrized as $\eta - x_A = \epsilon e^{-i\theta}$.

$$\int_{\mathcal{C}_\epsilon} \frac{F(\eta)}{\eta - x_A} \mathrm{d}\eta = -i \int_0^\pi F\left(\epsilon e^{-i\theta} + x_A\right) \mathrm{d}\theta. \tag{A.2.2}$$

The integrals defined on the real axis only, become the principal value of the integral.

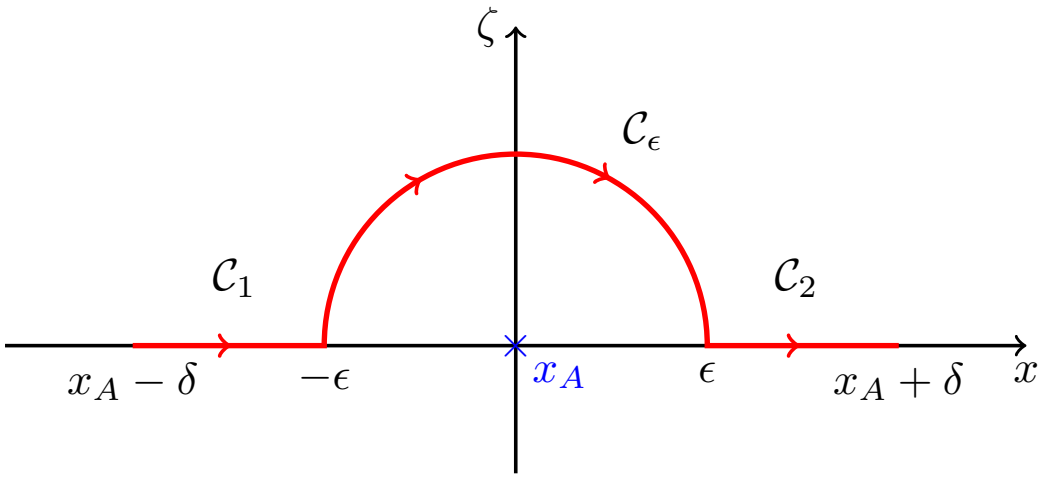

Figure A.5: Scheme of the integration contours for Equation (A.2.1) in the complex plane around the simple pole at $x = x_A$.

The function $F(x)$ can be expanded in Taylor series around x_A.

$$\int_b^a \frac{F(x)}{x - x_A}\mathrm{d}x = \int_b^a \frac{F(x_A)}{x - x_A}\mathrm{d}x + \sum_{n=1}^{\infty} \int_b^a (x - x_A)^{n-1} \left.\frac{\mathrm{d}^n F}{\mathrm{d}x^n}\right|_{x=x_A} \mathrm{d}x \tag{A.2.3}$$

In the limit of $\epsilon \to 0^+$, the integral along $\mathcal{C}_\epsilon$, we consider that the function F is entire, in particular at $x = x_A$. This leads to a zero principal value. Accordingly, it is found that the integral converges to

$$\int_{\mathcal{C}} \frac{F(\eta)}{\eta - x_A}\mathrm{d}\eta = -\, i\pi F(x_A). \tag{A.2.4}$$

Since this result does not depend on δ, the evaluation of the integral in the limit of thin layer, $\delta \to 0^+$, still yields (A.2.4). In this way, the condition for the lagrangian displacements ξ_x (2.2.13) is obtained.

Appendix B
Dictionary

B.1 Abbreviations

AIA: Atmospheric Imaging Assembly (instrument aboard SDO).

BBGKY: Bogoliubov-Born-Green-Kirkwood-Yvon (hierarchy of equations in statistical mechanics).

CFL: Courant-Friederichs-Lewy (condition for differential equations).

CoMP: Coronal Multichannel Polarimeter (ground-based telescope).

EM: Electromagnetic.

IRIS: Infrared Interferometer in Space (instrument).

KAW/s: Kinetic Alfvén wave/s.

KHI: Kelvin-Helmholtz instability.

LHP: Left hand polarization/polarized.

MHD: Magnetohydrodynamics.

PIC: Particle in cell.

RHP: Right hand polarization/polarized.

SDO: Solar Dynamics Observatory (mission).

SIM: From simulation (used in ω_{SIM}).

SolO: Solar Orbiter (mission).

SOT: Solar Optical Telescope (instrument aboard Hinode).

TRACE: Transition Region and Coronal Explorer (mission).

Bibliography

[1] L. Chen and A. Hasegawa. "Plasma heating by spatial resonance of Alfvén wave". In: *PhFl* 17.7 (July 1974), pp. 1399–1403. DOI: 10.1063/1.1694904 (cit. on p. 1).

[2] Akira Hasegawa and Lui Chen. "Kinetic process of plasma heating due to Alfvén wave excitation". In: *PhRvL* 35.6 (Aug. 1975), pp. 370–373. DOI: 10.1103/PhysRevLett.35.370 (cit. on p. 1).

[3] A. Hasegawa and L. Chen. "Kinetic processes in plasma heating by resonant mode conversion of Alfvén wave". In: *PhFl* 19.12 (Dec. 1976), pp. 1924–1934. DOI: 10.1063/1.861427 (cit. on p. 1).

[4] R. J. Morton et al. "Alfvénic waves in the inhomogeneous solar atmosphere". In: *RvMPP* 7.1, 17 (Dec. 2023), p. 17. DOI: 10.1007/s41614-023-00118-3 (cit. on pp. 1, 2, 45).

[5] B. Inhester. "Resonance absorption of Alfvén oscillations in a nonaxisymmetric magnetosphere". In: *JGR* 91.A2 (Feb. 1986), pp. 1509–1518. DOI: 10.1029/JA091iA02p01509 (cit. on p. 1).

[6] P. S. Cally and Z. Sedláček. "Phase mixing and surface-wave decay in an inhomogeneous plasma". In: *JPlPh* 48.1 (Aug. 1992), pp. 145–158. DOI: 10.1017/S0022377800016433 (cit. on p. 1).

[7] J. Terradas et al. “Resonant Absorption in Complicated Plasma Configurations: Applications to Multistranded Coronal Loop Oscillations”. In: *ApJ* 679.2 (June 2008), pp. 1611–1620. DOI: 10.1086/586733 (cit. on pp. 1, 11, 102).

[8] Roberto Soler and Jaume Terradas. “Magnetohydrodynamic Kink Waves in Nonuniform Solar Flux Tubes: Phase Mixing and Energy Cascade to Small Scales”. In: *ApJ* 803.1, 43 (Apr. 2015), p. 43. DOI: 10.1088/0004-637X/803/1/43 (cit. on p. 1).

[9] M. S. Ruderman and B. Roberts. “The Damping of Coronal Loop Oscillations”. In: *ApJ* 577.1 (Sept. 2002), pp. 475–486. DOI: 10.1086/342130 (cit. on pp. 1, 2, 15, 21, 96, 102).

[10] Tom Van Doorsselaere et al. “Coronal Heating by MHD Waves”. In: *SSRv* 216.8, 140 (Dec. 2020), p. 140. DOI: 10.1007/s11214-020-00770-y (cit. on pp. 1, 15).

[11] J. A. Ionson. “Resonant absorption of Alfvénic surface waves and the heating of solar coronal loops.” In: *ApJ* 226 (Dec. 1978), pp. 650–673. DOI: 10.1086/156648 (cit. on pp. 1, 15, 134).

[12] M. Goossens et al. “On the nature of kink MHD waves in magnetic flux tubes”. In: *A&A* 503.1 (Aug. 2009), pp. 213–223. DOI: 10.1051/0004-6361/200912399 (cit. on pp. 1, 15, 22).

[13] Roberto Soler et al. “The Behavior of Transverse Waves in Nonuniform Solar Flux Tubes. I. Comparison of Ideal and Resistive Results”. In: *ApJ* 777.2, 158 (Nov. 2013), p. 158. DOI: 10.1088/0004-637X/777/2/158 (cit. on pp. 1, 15, 102, 105).

[14] Joseph V. Hollweg and G. Yang. "Resonance absorption of compressible magnetohydrodynamic waves at thin "surfaces"". In: *JGR* 93.A6 (June 1988), pp. 5423–5436. DOI: 10.1029/JA093iA06p05423 (cit. on pp. 1, 15, 21, 105).

[15] Hui Yu et al. "Resonant Damping of Kink Modes in Solar Coronal Slabs". In: *SoPh* 296.6, 95 (June 2021), p. 95. DOI: 10.1007/s11207-021-01839-9 (cit. on pp. 1, 11, 15, 20, 21, 96, 105).

[16] M. Goossens et al. "Resonant absorption: Transformation of compressive motions into vortical motions". In: *A&A* 641, A106 (Sept. 2020), A106. DOI: 10.1051/0004-6361/202038394 (cit. on pp. 1, 100, 113).

[17] M. Goossens et al. "Surface Alfvén Waves in Solar Flux Tubes". In: *ApJ* 753.2, 111 (July 2012), p. 111. DOI: 10.1088/0004-637X/753/2/111 (cit. on pp. 1, 15, 100, 113).

[18] J. Terradas et al. "Nonlinear Instability of Kink Oscillations due to Shear Motions". In: *ApJL* 687.2 (Nov. 2008), p. L115. DOI: 10.1086/593203 (cit. on p. 2).

[19] L. Ofman, J. M. Davila, and R. S. Steinolfson. "Coronal Heating by the Resonant Absorption of Alfven Waves: The Effect of Viscous Stress Tensor". In: *ApJ* 421 (Jan. 1994), p. 360. DOI: 10.1086/173654 (cit. on p. 2).

[20] L. Ofman and J. M. Davila. "Nonlinear resonant absorption of Alfvén waves in three dimensions, scaling laws, and coronal heating". In: *JGR* 100.A12 (Dec. 1995), pp. 23427–23442. DOI: 10.1029/95JA01907 (cit. on p. 2).

[21] T. A. Howson et al. "Resonant absorption in expanding coronal magnetic flux tubes with uniform density". In: *A&A* 631, A105 (Nov. 2019), A105. DOI: 10.1051/0004-6361/201936146 (cit. on p. 2).

[22] Patrick Antolin and Tom Van Doorsselaere. "Influence of resonant absorption on the generation of the Kelvin-Helmholtz Instability". In: *FrP* 7, 85 (June 2019), p. 85. DOI: 10.3389/fphy.2019.00085 (cit. on p. 2).

[23] P. Antolin et al. "Resonant Absorption of Transverse Oscillations and Associated Heating in a Solar Prominence. II. Numerical Aspects". In: *ApJ* 809.1, 72 (Aug. 2015), p. 72. DOI: 10.1088/0004-637X/809/1/72 (cit. on p. 2).

[24] N. Magyar and T. Van Doorsselaere. "Damping of nonlinear standing kink oscillations: a numerical study". In: *A&A* 595, A81 (Nov. 2016), A81. DOI: 10.1051/0004-6361/201629010 (cit. on p. 2).

[25] E. N. Parker. "The Phase Mixing of Alfven Waves, Coordinated Modes, and Coronal Heating". In: *ApJ* 376 (July 1991), p. 355. DOI: 10.1086/170285 (cit. on p. 2).

[26] V. M. Nakariakov et al. "TRACE observation of damped coronal loop oscillations: Implications for coronal heating". In: *Sci* 285 (Aug. 1999), pp. 862–864. DOI: 10.1126/science.285.5429.862 (cit. on pp. 2, 14, 15).

[27] Markus J. Aschwanden et al. "Transverse Oscillations in Coronal Loops Observed with TRACE II. Measurements of Geometric and Physical Parameters". In: *SoPh* 206.1 (Mar. 2002), pp. 99–132. DOI: 10.1023/A:1014916701283 (cit. on pp. 2, 87).

[28] R. Erdélyi and Y. Taroyan. "Hinode EUV spectroscopic observations of coronal oscillations". In: *A&A* 489.3 (Oct. 2008), pp. L49–L52. DOI: 10.1051/0004-6361:200810263 (cit. on p. 2).

[29] Richard J. Morton et al. "Weak Damping of Propagating MHD Kink Waves in the Quiescent Corona". In: *ApJ* 923.2, 225 (Dec. 2021), p. 225. DOI: 10.3847/1538-4357/ac324d (cit. on p. 2).

[30] C. R. Goddard et al. "A statistical study of decaying kink oscillations detected using SDO/AIA". In: *A&A* 585, A137 (Jan. 2016), A137. DOI: 10.1051/0004-6361/201527341 (cit. on pp. 2, 15).

[31] Alena Nechaeva et al. "Catalog of Decaying Kink Oscillations of Coronal Loops in the 24th Solar Cycle". In: *ApJL* 241.2, 31 (Apr. 2019), p. 31. DOI: 10.3847/1538-4365/ab0e86 (cit. on pp. 2, 14, 15).

[32] Takenori J. Okamoto et al. "Resonant Absorption of Transverse Oscillations and Associated Heating in a Solar Prominence. I. Observational Aspects". In: *ApJ* 809.1, 71 (Aug. 2015), p. 71. DOI: 10.1088/0004-637X/809/1/71 (cit. on p. 2).

[33] M. Goossens, J. Andries, and M. J. Aschwanden. "Coronal loop oscillations. An interpretation in terms of resonant absorption of quasi-mode kink oscillations". In: *A&A* 394 (Nov. 2002), pp. L39–L42. DOI: 10.1051/0004-6361:20021378 (cit. on pp. 2, 15, 164).

[34] G. Verth, J. Terradas, and M. Goossens. "Observational Evidence of Resonantly Damped Propagating Kink Waves in the Solar Corona". In: *ApJL* 718.2 (Aug. 2010), pp. L102–L105. DOI: 10.1088/2041-8205/718/2/L102 (cit. on p. 2).

[35] Iñigo Arregui et al. "Damping of Fast Magnetohydrodynamic Oscillations in Quiescent Filament Threads". In: *ApJL* 682.2 (Aug. 2008), p. L141. DOI: 10.1086/591081 (cit. on p. 2).

[36] Ajay K. Tiwari et al. “Damping of Propagating Kink Waves in the Solar Corona”. In: *ApJ* 876.2, 106 (May 2019), p. 106. DOI: 10.3847/1538-4357/ab164b (cit. on p. 2).

[37] Bernard J. Vasquez and Joseph V. Hollweg. “Cross-field energy transfer of a body Alfvén wave propagating along and across a pressure-balanced structure”. In: *GeoRL* 31.14, L14803 (July 2004), p. L14803. DOI: 10.1029/2004GL019746 (cit. on pp. 3, 87, 160).

[38] Bernard J. Vasquez. “Resonant absorption of an Alfvén wave: Hybrid simulations”. In: *JGRA* 110.A10, A10S02 (Oct. 2005), A10S02. DOI: 10.1029/2004JA010872 (cit. on pp. 3, 5, 87, 159, 170, 173, 185).

[39] Hugo A. Carril et al. “Resonant Absorption and Fluctuations via Hybrid Simulations on Coronal Loops. I. Plasma Multifluid Description”. In: *ApJ* 986.1, 40 (June 2025), p. 40. DOI: 10.3847/1538-4357/adceac (cit. on pp. 3, 24, 162).

[40] C. L. Vásconez et al. “Kinetic Alfvén Wave Generation by Large-Scale Phase Mixing”. In: *The Astrophysical Journal* 815.1 (2015), p. 7. DOI: 10.1088/0004-637X/815/1/7. URL: https://dx.doi.org/10.1088/0004-637X/815/1/7 (cit. on p. 3).

[41] F. Pucci et al. “From Alfvén waves to kinetic Alfvén waves in an inhomogeneous equilibrium structure”. In: *JGRA* 121.2 (Feb. 2016), pp. 1024–1045. DOI: 10.1002/2015JA022216 (cit. on p. 3).

[42] Teresa Maiorano et al. “Kinetic Alfvén wave generation by velocity shear in collisionless plasmas”. In: *JPlPh* 86.2, 825860202 (Apr. 2020), p. 825860202. DOI: 10.1017/S002237782000032X (cit. on p. 3).

[43] Robert L. Lysak and Yan Song. "Development of parallel electric fields at the plasma sheet boundary layer". In: *JGRA* 116, A00K14 (Sept. 2011), A00K14. DOI: 10.1029/2010JA016424 (cit. on p. 3).

[44] L. Xiang et al. "Mode Conversion of Kinetic Alfvén Waves in the Presence of Proton Beams and Its Role in Plasma Heating in the Solar Corona". In: *ApJ* 936.2, 159 (Sept. 2022), p. 159. DOI: 10.3847/1538-4357/ac8a96 (cit. on p. 3).

[45] Yuriy Voitenko and Marcel Goossens. "Cross-Field Heating of Coronal Ions by Low-Frequency Kinetic Alfvén Waves". In: *ApJL* 605.2 (Apr. 2004), pp. L149–L152. DOI: 10.1086/420927 (cit. on p. 3).

[46] F. Mottez. "Non-propagating electric and density structures formed through non-linear interaction of Alfvén waves". In: *AnGp* 30.1 (Jan. 2012), pp. 81–95. DOI: 10.5194/angeo-30-81-2012 (cit. on pp. 3, 137, 140, 146).

[47] F. Mottez. "Plasma acceleration by the interaction of parallel propagating Alfvén waves". In: *JPlPh* 81.1, 325810104 (Jan. 2015), p. 325810104. DOI: 10.1017/S0022377814000580 (cit. on pp. 3, 4, 45, 89, 90, 137–140, 142, 145, 146, 148, 149, 152, 155, 157).

[48] Jaume Terradas, Adolfo F. Viñas, and Jaime A. Araneda. "Excitation of ion-acoustic waves by non-linear finite-amplitude standing Alfvén waves". In: *A&A* 660 (2022), A24. DOI: 10.1051/0004-6361/202141914 (cit. on pp. 4, 9, 46, 48, 61, 93, 104, 164).

[49] P. M. Bellan and K. Stasiewicz. "Fine-Scale Cavitation of Ionospheric Plasma Caused by Inertial Alfvén Wave Ponderomotive Force". In: *PhRvL* 80.16 (Apr.

1998), pp. 3523–3526. DOI: 10.1103/PhysRevLett.80.3523 (cit. on pp. 4, 134).

[50] P. K. Shukla and L. Stenflo. "Generation of localized density perturbations by shear Alfvén waves". In: *PhPl* 7.6 (June 2000), pp. 2738–2739. DOI: 10.1063/1.874124 (cit. on p. 4).

[51] Nagendra Singh, Manish Yeladandi, and Sudeepth Araveti. "Density cavity formation by large-scale shear Alfvén waves". In: *EPL* 91.6 (Sept. 2010), p. 69003. DOI: 10.1209/0295-5075/91/69003 (cit. on pp. 4, 134).

[52] Anju Kumari, R. P. Sharma, and Nitin Yadav. "Study of localized structures of kinetic Alfvén wave and generation of turbulence". In: *PhPl* 22.6, 062304 (June 2015), p. 062304. DOI: 10.1063/1.4922678 (cit. on p. 4).

[53] Sachin Kumar, R. P. Sharma, and H. D. Singh. "Nonlinear excitation of short scale turbulence in solar corona by kinetic Alfvén waves". In: *PhPl* 16.7, 072903 (July 2009), p. 072903. DOI: 10.1063/1.3184826 (cit. on p. 4).

[54] R. P. Sharma and H. D. Singh. "Density cavities associated with inertial Alfvén waves in the auroral plasma". In: *JGRA* 114.A3, A03109 (Mar. 2009), A03109. DOI: 10.1029/2008JA013474 (cit. on p. 4).

[55] Sofiane Bourouaine, Eckart Marsch, and Christian Vocks. "On the Efficiency of Nonresonant Ion Heating by Coronal Alfvén Waves". In: *ApJ* 684.2 (Sept. 2008), p. L119. DOI: 10.1086/592243 (cit. on pp. 4, 167).

[56] C. B. Wang, C. S. Wu, and P. H. Yoon. "Heating of Ions by Alfvén Waves via Nonresonant Interactions". In: *PhRvL* 96.12, 125001 (Mar. 2006), p. 125001. DOI: 10.1103/PhysRevLett.96.125001 (cit. on pp. 4, 169, 172).

[57] Quanming Lu and Xing Li. "Heating of ions by low-frequency Alfven waves". In: *PhPl* 14.4, 042303 (Apr. 2007), p. 042303. DOI: 10.1063/1.2715569 (cit. on pp. 4, 172).

[58] P. H. Yoon, C. B. Wang, and C. S. Wu. "Pitch-angle diffusion of ions via nonresonant interaction with Alfvénic turbulence". In: *PhPl* 16.10, 102102 (Oct. 2009), p. 102102. DOI: 10.1063/1.3236749 (cit. on p. 4).

[59] Chuanfei Dong and Nagendra Singh. "Ion pseudoheating by low-frequency Alfvén waves revisited". In: *PhPl* 20.1, 012121 (Jan. 2013), p. 012121. DOI: 10.1063/1.4789608 (cit. on pp. 4, 169, 172).

[60] Benjamin D. G. Chandran et al. "Perpendicular Ion Heating by Low-frequency Alfvén-wave Turbulence in the Solar Wind". In: *ApJ* 720.1 (Sept. 2010), pp. 503–515. DOI: 10.1088/0004-637X/720/1/503 (cit. on pp. 4, 172).

[61] Jay R. Johnson and C. Z. Cheng. "Stochastic ion heating at the magnetopause due to kinetic Alfvén waves". In: *GeoRL* 28.23 (Dec. 2001), pp. 4421–4424. DOI: 10.1029/2001GL013509 (cit. on p. 4).

[62] S. S. Cerri, L. Arzamasskiy, and M. W. Kunz. "On Stochastic Heating and Its Phase-space Signatures in Low-beta Kinetic Turbulence". In: *ApJ* 916.2, 120 (Aug. 2021), p. 120. DOI: 10.3847/1538-4357/abfbde (cit. on p. 4).

[63] Cheong R. Choi et al. "Proton Perpendicular Heating by Kinetic Alfvén Waves". In: *ApJ* 878.2, 141 (June 2019), p. 141. DOI: 10.3847/1538-4357/ab218b (cit. on pp. 4, 169, 172).

[64] Jaime A. Araneda, Adolfo F. Viñas, and HernáN. F. Astudillo. "Proton core temperature effects on the relative drift and anisotropy evolution of the ion

beam instability in the fast solar wind". In: *JGRA* 107.A12, 1453 (Dec. 2002), p. 1453. DOI: 10.1029/2002JA009337 (cit. on pp. 9, 61).

[65] L. Ofman and A. F. Viñas. "Two-dimensional hybrid model of wave and beam heating of multi-ion solar wind plasma". In: *JGRA* 112.A6, A06104 (June 2007), A06104. DOI: 10.1029/2006JA012187 (cit. on pp. 9, 61).

[66] P. S. Moya et al. "Computational and theoretical study of the wave-particle interaction of protons and waves". In: *AnGp* 30.9 (Sept. 2012), pp. 1361–1369. DOI: 10.5194/angeo-30-1361-2012 (cit. on pp. 9, 61).

[67] Y. G. Maneva et al. "Dissipation of Parallel and Oblique Alfvén-Cyclotron Waves—Implications for Heating of Alpha Particles in the Solar Wind". In: *ApJ* 814.1, 33 (Nov. 2015), p. 33. DOI: 10.1088/0004-637X/814/1/33 (cit. on pp. 9, 61).

[68] F. Otto. *Library FotranFiles.jl*. https://juliadata.org/FortranFiles.jl/stable/. Documentation site. Version 0.6.2 (cit. on p. 9).

[69] M. Frigo and S. G. Johnson. "The Design and Implementation of FFTW3". In: *IEEEP* 93.2 (2005). Special issue on "Program Generation, Optimization, and Platform Adaptation", pp. 216–231. DOI: 10.1109/JPROC.2004.840301 (cit. on p. 9).

[70] D. Widmann. *Library StatsBase.jl*. https://juliastats.org/StatsBase.jl/stable/. Documentation site. Version 0.34.5 (cit. on p. 9).

[71] J. M. White. *Library LsqFit.jl*. https://julianlsolvers.github.io/LsqFit.jl/latest/tutorial/. Documentation site. Version 0.15.1 (cit. on p. 9).

[72] Markus J Aschwanden. *Physics of the solar corona: an introduction with problems and solutions*. Springer, 2006 (cit. on p. 11).

[73] Fabio Reale. "Coronal Loops: Observations and Modeling of Confined Plasma". In: *LRSP* 11.1, 4 (Dec. 2014), p. 4. DOI: 10.12942/lrsp-2014-4 (cit. on pp. 11–14, 87, 185).

[74] G. R. Gupta, Durgesh Tripathi, and Helen E. Mason. "Spectroscopic Observations of a Coronal Loop: Basic Physical Plasma Parameters Along the Full Loop Length". In: *ApJ* 800.2, 140 (Feb. 2015), p. 140. DOI: 10.1088/0004-637X/800/2/140 (cit. on pp. 11, 13, 87, 185).

[75] Ester Antonucci et al. "Observations of the Solar Corona from Space". In: *SSRv* 216.8, 117 (Oct. 2020), p. 117. DOI: 10.1007/s11214-020-00743-1 (cit. on pp. 11, 12).

[76] J. Terradas, M. Goossens, and G. Verth. "Selective spatial damping of propagating kink waves due to resonant absorption". In: *A&A* 524, A23 (Dec. 2010), A23. DOI: 10.1051/0004-6361/201014845 (cit. on p. 11).

[77] Zihao Yang et al. "Global maps of the magnetic field in the solar corona". In: *Sci* 369.6504 (Aug. 2020), pp. 694–697. DOI: 10.1126/science.abb4462 (cit. on p. 12).

[78] Harry P. Warren and David H. Brooks. "THE TEMPERATURE AND DENSITY STRUCTURE OF THE SOLAR CORONA. I. OBSERVATIONS OF THE QUIET SUN WITH THE EUV IMAGING SPECTROMETER ON HINODE". In: *ApJ* 700.1 (2009), p. 762. DOI: 10.1088/0004-637X/700/1/762. URL: https://doi.org/10.1088/0004-637X/700/1/762 (cit. on p. 12).

[79] Thomas Wiegelmann, Gordon J. D. Petrie, and Pete Riley. "Coronal Magnetic Field Models". In: *SSRv* 210.1-4 (Sept. 2017), pp. 249–274. DOI: 10.1007/s11214-015-0178-3 (cit. on p. 12).

[80] Eckart Marsch. "Kinetic Physics of the Solar Corona and Solar Wind". In: *LRSP* 3.1, 1 (Dec. 2006), p. 1. DOI: 10.12942/lrsp-2006-1 (cit. on pp. 12, 60).

[81] I. V. Zimovets and V. M. Nakariakov. "Excitation of kink oscillations of coronal loops: statistical study". In: *A&A* 577, A4 (May 2015), A4. DOI: 10.1051/0004-6361/201424960 (cit. on p. 12).

[82] G. Nisticò, V. M. Nakariakov, and E. Verwichte. "Decaying and decayless transverse oscillations of a coronal loop". In: *A&A* 552, A57 (Apr. 2013), A57. DOI: 10.1051/0004-6361/201220676 (cit. on pp. 12, 14, 15).

[83] G. Y. Chen et al. "Measuring local physical parameters in coronal loops with spatial seismology". In: *A&A* 678, A205 (Oct. 2023), A205. DOI: 10.1051/0004-6361/202346393 (cit. on pp. 12–14, 87, 88, 185).

[84] Markus J. Aschwanden and Carolus J. Schrijver. "Coronal Loop Oscillations Observed with Atmospheric Imaging Assembly—Kink Mode with Cross-sectional and Density Oscillations". In: *ApJ* 736.2, 102 (Aug. 2011), p. 102. DOI: 10.1088/0004-637X/736/2/102 (cit. on pp. 13–15, 87, 185).

[85] J. T. Schmelz et al. "Are Coronal Loops Isothermal or Multithermal?" In: *ApJ* 691.1 (Jan. 2009), pp. 503–515. DOI: 10.1088/0004-637X/691/1/503 (cit. on pp. 13, 87, 185).

[86] V. M. Nakariakov et al. “Kink Oscillations of Coronal Loops”. In: *SSRv* 217.6, 73 (Sept. 2021), p. 73. DOI: 10.1007/s11214-021-00847-2 (cit. on pp. 14, 15).

[87] Markus J. Aschwanden et al. “Coronal Loop Oscillations Observed with the Transition Region and Coronal Explorer”. In: *ApJ* 520.2 (Aug. 1999), pp. 880–894. DOI: 10.1086/307502 (cit. on pp. 14, 15).

[88] S. A. Anfinogentov, V. M. Nakariakov, and G. Nisticò. “Decayless low-amplitude kink oscillations: a common phenomenon in the solar corona?” In: *A&A* 583, A136 (Nov. 2015), A136. DOI: 10.1051/0004-6361/201526195 (cit. on pp. 14, 15).

[89] Yuhang Gao et al. “Decayless Oscillations in Solar Coronal Bright Points”. In: *ApJ* 930.1, 55 (May 2022), p. 55. DOI: 10.3847/1538-4357/ac62cf (cit. on p. 14).

[90] Z. F. Li et al. “Evidence of external reconnection between an erupting mini-filament and ambient loops observed by Solar Orbiter/EUI”. In: *A&A* 673, A83 (May 2023), A83. DOI: 10.1051/0004-6361/202245814 (cit. on pp. 14, 87, 185).

[91] B. Ram et al. “Stereoscopic observations reveal coherent morphology and evolution of solar coronal loops”. In: *A&A* 693, A312 (Jan. 2025), A312. DOI: 10.1051/0004-6361/202452339 (cit. on pp. 14, 87, 185).

[92] Paul Boerner et al. “Initial Calibration of the Atmospheric Imaging Assembly (AIA) on the Solar Dynamics Observatory (SDO)”. In: *SoPh* 275.1-2 (Jan. 2012), pp. 41–66. DOI: 10.1007/s11207-011-9804-8 (cit. on p. 14).

[93] James R. Lemen et al. "The Atmospheric Imaging Assembly (AIA) on the Solar Dynamics Observatory (SDO)". In: *SoPh* 275.1-2 (Jan. 2012), pp. 17–40. DOI: 10.1007/s11207-011-9776-8 (cit. on p. 14).

[94] P. Rochus et al. "The Solar Orbiter EUI instrument: The Extreme Ultraviolet Imager". In: *A&A* 642, A8 (Oct. 2020), A8. DOI: 10.1051/0004-6361/201936663 (cit. on p. 14).

[95] Marcel Goossens. *Linear MHD waves in Cartesian geometry. Transverse inhomogeneity and mixed properties.* 2022 (cit. on pp. 14, 17, 18, 21, 22).

[96] VV Zajtsev and AV Stepanov. "On the origin of pulsations of type IV solar radio emission. Plasma cylinder oscillations (I)." In: *IGAFS* 37 (1975), pp. 3–10 (cit. on p. 15).

[97] Sihui Zhong et al. "30-min decayless kink oscillations in a very long bundle of solar coronal plasma loops". In: *NatSR* 13, 12963 (Aug. 2023), p. 12963. DOI: 10.1038/s41598-023-40063-2 (cit. on p. 16).

[98] Hui Yu et al. "Kink and Sausage Modes in Nonuniform Magnetic Slabs with Continuous Transverse Density Distributions". In: *ApJ* 814.1, 60 (Nov. 2015), p. 60. DOI: 10.1088/0004-637X/814/1/60 (cit. on p. 15).

[99] Jaume Terradas. "Excitation of Standing Kink Oscillations in Coronal Loops". In: *SSRv* 149.1-4 (Dec. 2009), pp. 255–282. DOI: 10.1007/s11214-009-9560-3 (cit. on pp. 15, 50).

[100] Richard D Hazeltine and Francois L. Waelbroeck. *The framework of plasma physics*. CRC Press, 2018 (cit. on p. 17).

[101] W. J. Tirry and M. Goossens. "Quasi-Modes as Dissipative Magnetohydrodynamic Eigenmodes: Results for One-dimensional Equilibrium States". In: *ApJ* 471 (Nov. 1996), p. 501. DOI: 10.1086/177986 (cit. on p. 20).

[102] Sébastien Galtier. *Introduction to Modern Magnetohydrodynamics*. 2016. DOI: 10.1017/CBO9781316665961 (cit. on p. 25).

[103] D. W. Hewett. "A global method of solving the electron-field equations in a zero-inertia-electron-hybrid plasma simulation code". In: *JCoPh* 38.3 (Dec. 1980), pp. 378–395. DOI: 10.1016/0021-9991(80)90155-2 (cit. on p. 28).

[104] Hans Pécseli. *Waves and Oscillations in Plasmas*. 2012. DOI: 10.1201/b12702 (cit. on p. 28).

[105] Robert J Goldston. *Introduction to plasma physics*. CRC Press, 2020 (cit. on pp. 28, 30, 31, 34, 36, 62).

[106] Daniel Verscharen, Kristopher G. Klein, and Bennett A. Maruca. "The multi-scale nature of the solar wind". In: *LRSP* 16.1, 5 (Dec. 2019), p. 5. DOI: 10.1007/s41116-019-0021-0 (cit. on pp. 30, 60).

[107] Donald Gary Swanson. *Plasma kinetic theory*. Crc Press, 2008 (cit. on pp. 30, 34, 37, 54).

[108] JA Bittencourt. "Fundamentals of plasma physics. 3". In: (2008) (cit. on pp. 30, 51).

[109] Nicholas A Krall and Alvin W Trivelpiece. "Principles of plasma physics". In: *American Journal of Physics* 41.12 (1973), pp. 1380–1381 (cit. on pp. 30–32, 35–38).

[110] Stephan Brunner. "Waves and instabilities in inhomogeneous plasmas". In: *3d circle course at Centre de Recherches en Physique des Plasmas, Association Euratom-Confédération Suisse, Ecole Polytechnique Feédérale de Lausanne, Switzerland, https://crppwww. epfl. ch/brunner/inhomoplasma. pdf (entered 01.06. 2018)* (2014) (cit. on pp. 30, 39, 41, 42).

[111] Paul M Bellan. *Fundamentals of plasma physics*. Cambridge university press, 2008 (cit. on pp. 32–34).

[112] Peter Andrew Sturrock. *Plasma physics: an introduction to the theory of astrophysical, geophysical and laboratory plasmas*. Cambridge University Press, 1994 (cit. on pp. 32, 33).

[113] Dwight Roy Nicholson and Dwight R Nicholson. *Introduction to plasma theory*. Vol. 1. Wiley New York, 1983 (cit. on p. 33).

[114] Setsuo Ichimaru. *Statistical plasma physics, volume I: basic principles*. CRC Press, 2018 (cit. on p. 34).

[115] Anatoliĭ Aleksandrovich Vlasov. "The vibrational properties of an electron gas". In: *UFN* 10.6 (1968), p. 721 (cit. on p. 38).

[116] B. U. Ö. Sonnerup and Shin-Yi Su. "Large Amplitude Whistler Waves in a Hot Collision-Free Plasma". In: *PhFl* 10.2 (Feb. 1967), pp. 462–464. DOI: 10.1063/1.1762132 (cit. on p. 39).

[117] F. Malara, O. Pezzi, and F. Valentini. "Exact hybrid Vlasov equilibria for sheared plasmas with in-plane and out-of-plane magnetic field". In: *Phys. Rev. E* 97 (5 2018), p. 053212. DOI: 10.1103/PhysRevE.97.053212. URL: https://link.aps.org/doi/10.1103/PhysRevE.97.053212 (cit. on p. 39).

[118] G. Guzzi et al. “Exact hybrid-kinetic equilibria for magnetized plasmas with shearing flows”. In: *Astronomy & Astrophysics* 645 (2021), A147. DOI: 10.1051/0004-6361/202039656 (cit. on p. 39).

[119] F. Malara et al. “Exact Shearing Flow Magnetized Hybrid Kinetic Equilibria with Inhomogeneous Temperature”. In: *The Astrophysical Journal* 941.2 (2022), p. 201. DOI: 10.3847/1538-4357/aca077. URL: https://dx.doi.org/10.3847/1538-4357/aca077 (cit. on p. 39).

[120] R. E. Navarro et al. “Solar Wind Thermally Induced Magnetic Fluctuations”. In: *PhRvL* 112.24, 245001 (June 2014), p. 245001. DOI: 10.1103/PhysRevLett.112.245001 (cit. on p. 40).

[121] Roberto E. Navarro et al. “Theory of electromagnetic fluctuations for magnetized multi-species plasmas”. In: *PhPl* 21.9, 092902 (Sept. 2014), p. 092902. DOI: 10.1063/1.4894700 (cit. on p. 40).

[122] J. A. Valdivia et al. “Magnetic fluctuations in anisotropic space plasmas: The effect of the plasma environment”. In: *AdSpR* 58.10 (Nov. 2016), pp. 2126–2133. DOI: 10.1016/j.asr.2016.04.017 (cit. on p. 40).

[123] A.B. Mikhailovskii. *Theory of Plasma Instabilities: Volume 2: Instabilities of an Inhomogeneous Plasma*. Springer US, 1995. ISBN: 9780306171819. URL: https://books.google.es/books?id=MbvvAAAAMAAJ (cit. on pp. 41, 42, 107).

[124] H. Naitou, T. Kamimura, and S. Tokuda. “Initial particle loadings for a nonuniform simulation plasma in a magnetic field”. In: *JCoPh* 38.3 (Dec. 1980), pp. 265–274. DOI: 10.1016/0021-9991(80)90149-7 (cit. on p. 41).

[125] D. Cai, L. R. O. Storey, and T. Neubert. "Kinetic equilibria of plasma shear layers". In: *PhFlB* 2.1 (Jan. 1990), pp. 75–85. DOI: 10.1063/1.859541 (cit. on p. 41).

[126] M. Mathioudakis, D. B. Jess, and R. Erdélyi. "Alfvén Waves in the Solar Atmosphere. From Theory to Observations". In: *SSRv* 175.1-4 (June 2013), pp. 1–27. DOI: 10.1007/s11214-012-9944-7 (cit. on p. 45).

[127] M. Velli and F. Pruneti. "Alfvén waves in the solar corona and solar wind". In: *PPCF* 39 (Dec. 1997), B317–B324. DOI: 10.1088/0741-3335/39/12B/024 (cit. on p. 45).

[128] Ildar K. Khabibrakhmanov and Danny Summers. "On the theory of Alfvén waves in the solar wind". In: *JGR* 102.A4 (Apr. 1997), pp. 7095–7104. DOI: 10.1029/96JA03843 (cit. on p. 45).

[129] Robert L. Lysak and William Lotko. "On the kinetic dispersion relation for shear Alfvén waves". In: *JGR* 101.A3 (Mar. 1996), pp. 5085–5094. DOI: 10.1029/95JA03712 (cit. on pp. 45, 54).

[130] Neil F Cramer. *The physics of Alfvén waves*. John Wiley & Sons, 2011 (cit. on pp. 45, 48, 51, 53, 56, 126, 129).

[131] Hans L Pécseli. *Waves and oscillations in plasmas*. CRC Press Boca Raton, 2013 (cit. on p. 51).

[132] Ronald C Davidson. "Kinetic waves and instabilities in a uniform plasma". In: (1981) (cit. on p. 54).

[133] Burton D Fried and Samuel D Conte. *The plasma dispersion function: the Hilbert transform of the Gaussian*. Academic Press, 2015 (cit. on p. 55).

[134] Yasuhito Narita and Eckart Marsch. "Kinetic Slow Mode in the Solar Wind and Its Possible Role in Turbulence Dissipation and Ion Heating". In: *ApJ* 805.1, 24 (May 2015), p. 24. DOI: 10.1088/0004-637X/805/1/24 (cit. on pp. 56, 126, 130).

[135] Charles W. Smith et al. "Erratum: Correction to "Turbulence analysis of the Jovian upstream 'wave' phenomenon"". In: *JGR* 89.A10 (Oct. 1984), pp. 9159–9160. DOI: 10.1029/JA089iA10p09159 (cit. on pp. 57, 58, 82, 85, 124, 126, 130).

[136] Thomas H Stix. *Waves in plasmas*. Springer Science & Business Media, 1992 (cit. on p. 57).

[137] J. S. Zhao et al. "Properties of Short-wavelength Oblique Alfvén and Slow Waves". In: *ApJ* 793.2, 107 (Oct. 2014), p. 107. DOI: 10.1088/0004-637X/793/2/107 (cit. on pp. 57, 58, 126, 129, 130).

[138] Jiansen He et al. "Do Oblique Alfvén/Ion-cyclotron or Fast-mode/Whistler Waves Dominate the Dissipation of Solar Wind Turbulence near the Proton Inertial Length?" In: *ApJL* 745.1, L8 (Jan. 2012), p. L8. DOI: 10.1088/2041-8205/745/1/L8 (cit. on pp. 57, 58).

[139] C. W. Smith, M. L. Goldstein, and W. H. Matthaeus. "Turbulence analysis of the jovian upstream "wave" phenomenon". In: *JGR* 88.A7 (July 1983), pp. 5581–5594. DOI: 10.1029/JA088iA07p05581 (cit. on pp. 57, 58, 124).

[140] S. Y. Huang et al. "Kinetic Scale Slow Solar Wind Turbulence in the Inner Heliosphere: Coexistence of Kinetic Alfvén Waves and Alfvén Ion Cyclotron Waves". In: *ApJL* 897.1, L3 (July 2020), p. L3. DOI: 10.3847/2041-8213/ab9abb (cit. on pp. 58, 129).

[141] S. P. Gary. "Low-frequency waves in a high-beta collisionless plasma: polarization, compressibility and helicity". In: *JPlPh* 35.3 (June 1986), pp. 431–447. DOI: 10.1017/S0022377800011442 (cit. on pp. 58, 126, 130).

[142] Owen W. Roberts, Yasuhito Narita, and C. Philippe Escoubet. "Multi-scale analysis of compressible fluctuations in the solar wind". In: *AnGp* 36.1 (Jan. 2018), pp. 47–52. DOI: 10.5194/angeo-36-47-2018 (cit. on pp. 58, 130).

[143] S. P. Gary and Dan Winske. "Correlation function ratios and the identification of space plasma instabilities". In: *JGR* 97.A3 (Mar. 1992), pp. 3103–3111. DOI: 10.1029/91JA02752 (cit. on pp. 59, 126, 130).

[144] Jaroslav Dudík et al. "Nonequilibrium Processes in the Solar Corona, Transition Region, Flares, and Solar Wind (Invited Review)". In: *SoPh* 292.8, 100 (Aug. 2017), p. 100. DOI: 10.1007/s11207-017-1125-0 (cit. on p. 60).

[145] T. Terasawa et al. "Decay instability of finite-amplitude circularly polarized Alfven waves: A numerical simulation of stimulated Brillouin scattering". In: *JGRA* 91.A4 (Apr. 1986), pp. 4171–4187. DOI: 10.1029/JA091iA04p04171 (cit. on p. 61).

[146] D Winske and Nagendra Omidi. "Hybrid codes: Methods and applications". In: *Presented at the 4th International School for Space Simulation* (1991), pp. 1–5 (cit. on p. 61).

[147] Alexander S. Lipatov. *The hybrid multiscale simulation technology: an introduction with application to astrophysical and laboratory plasmas*. 2002 (cit. on pp. 61, 66, 70).

[148] Charles K Birdsall and A Bruce Langdon. *Plasma physics via computer simulation*. CRC press, 2018 (cit. on pp. 63, 66, 67, 70, 76, 77, 80, 81).

[149] Toshi Tajima. *Computational plasma physics: with applications to fusion and astrophysics*. CRC press, 2018 (cit. on p. 63).

[150] R Hockney and J Eastwood. "Computer simulations using particles mcgraw-hill". In: *New York* 61 (1981) (cit. on pp. 67, 76).

[151] Eric J. Horowitz, Dan E. Shumaker, and David V. Anderson. "QN3D: A Three-Dimensional Quasi-neutral Hybrid Particle-in-Cell Code with Applications to the Tilt Mode Instability in Field Reserved Configurations". In: *JCoPh* 84.2 (Oct. 1989), pp. 279–310. DOI: 10.1016/0021-9991(89)90234-9 (cit. on pp. 73, 74).

[152] D. Winske et al. "Hybrid Simulation Codes: Past, Present and Future - A Tutorial". In: *Space Plasma Simulation*. Ed. by J. Büchner, C. Dum, and M. Scholer. Vol. 615. 2003, pp. 136–165 (cit. on p. 73).

[153] Hong Qin et al. "Why is Boris algorithm so good?" In: *PhPl* 20.8 (2013), p. 084503. DOI: 10.1063/1.4818428 (cit. on pp. 76, 77, 79).

[154] Seiji Zenitani and Takayuki Umeda. "On the Boris solver in particle-in-cell simulation". In: *PhPl* 25.11, 112110 (Nov. 2018), p. 112110. DOI: 10.1063/1.5051077 (cit. on pp. 76, 77).

[155] Jay P Boris et al. "Relativistic plasma simulation-optimization of a hybrid code". In: *Proc. Fourth Conf. Num. Sim. Plasmas*. 1970, pp. 3–67 (cit. on p. 76).

[156] Seiji Zenitani and Tsunehiko N. Kato. "Hyper Boris integrators for kinetic plasma simulations". In: *CoPhC* 315, 109695 (Oct. 2025), p. 109695. DOI: 10.1016/j.cpc.2025.109695 (cit. on p. 77).

[157] John David Jackson and Ronald F Fox. *Classical electrodynamics*. 1999 (cit. on p. 83).

[158] J. Terradas and L. Ofman. "Loop Density Enhancement by Nonlinear Magnetohydrodynamic Waves". In: *ApJ* 610.1 (July 2004), pp. 523–531. DOI: 10.1086/421514 (cit. on pp. 93, 164).

[159] R. Lundin and A. Guglielmi. "Ponderomotive Forces in Cosmos". In: *SSRv* 127.1-4 (Dec. 2006), pp. 1–116. DOI: 10.1007/s11214-006-8314-8 (cit. on p. 93).

[160] Marcel Goossens, Joseph V. Hollweg, and Takashi Sakurai. "Resonant Behaviour of Magnetohydrodynamic Waves on Magnetic Flux Tubes - Part Three". In: *SoPh* 138.2 (Apr. 1992), pp. 233–255. DOI: 10.1007/BF00151914 (cit. on p. 102).

[161] Joseph V. Hollweg. "Resonance Absorption of Magnetohydrodynamic Surface Waves: Physical Discussion". In: *ApJ* 312 (Jan. 1987), p. 880. DOI: 10.1086/164934 (cit. on pp. 102, 103).

[162] A. B. Mikhailovsky. "Instabilities in inhomogeneous plasma". In: *Basic Plasma Physics: Selected Chapters, Handbook of Plasma Physics, Volume 1*. Jan. 1983, p. 299 (cit. on p. 107).

[163] R. Bruno and D. Telloni. "Spectral Analysis of Magnetic Fluctuations at Proton Scales from Fast to Slow Solar Wind". In: *ApJL* 811.2, L17 (Oct. 2015), p. L17. DOI: 10.1088/2041-8205/811/2/L17 (cit. on p. 129).

[164] F. Mottez, V. Génot, and P. Louarn. "Comment on "PIC simulations of circularly polarised Alfvén wave phase mixing: a new mechanism for electron

acceleration in collisionless plasmas" by Tsiklauri et al." In: *A&A* 449.2 (Apr. 2006), pp. 449–450. DOI: 10.1051/0004-6361:20054229 (cit. on p. 140).

[165] D. Tsiklauri. "A mechanism for parallel electric field generation in the MHD limit: possible implications for the coronal heating problem in the two stage mechanism". In: *A&A* 455.3 (Sept. 2006), pp. 1073–1080. DOI: 10.1051/0004-6361:20064816 (cit. on p. 140).

[166] José A Bittencourt. *Fundamentals of plasma physics*. third. Springer Science & Business Media, 2004. ISBN: 0-387-20975-1 (cit. on p. 152).

[167] Harikrishnan Aravindakshan et al. "Theory of ion holes in plasmas with flat-topped electron distributions". In: *PhPl* 30.2 (Feb. 2023), p. 022903. DOI: 10.1063/5.0086613 (cit. on p. 158).

[168] Robert G. (editor) Tsurutani Bruce T. (editor);Stone. *Collisionless Shocks in the Heliosphere: Reviews of Current Research*. Geophysical Monograph Series. American Geophysical Union, 1985. ISBN: 0875900615; 9781118664179; 1118664175; 9780875900612 (cit. on p. 158).

[169] W. Masood et al. "Electron velocity distribution and lion roars in the magnetosheath". In: *AnGp* 24.6 (July 2006), pp. 1725–1735. DOI: 10.5194/angeo-24-1725-2006 (cit. on p. 158).

[170] W. C. Feldman et al. "Electron velocity distributions near the earth's bow shock". In: *JGR* 88.A1 (Jan. 1983), pp. 96–110. DOI: 10.1029/JA088iA01p00096 (cit. on p. 158).

[171] Y. Asano et al. "Electron flat-top distributions around the magnetic reconnection region". In: *JGRA* 113.A1, A01207 (Jan. 2008), A01207. DOI: 10.1029/2007JA012461 (cit. on p. 158).

[172] K.-J. Hwang et al. “Cluster observations near reconnection X lines in Earth’s magnetotail current sheet”. In: *JGRA* 118.7 (2013), pp. 4199–4209. DOI: https://doi.org/10.1002/jgra.50403 (cit. on p. 158).

[173] Mitsuo Oka et al. “Electron energization and thermal to non- thermal energy partition during earth’s magnetotail reconnection”. In: *PhPl* 29.5, 052904 (May 2022), p. 052904. DOI: 10.1063/5.0085647 (cit. on p. 158).

[174] C. S. Wu and P. H. Yoon. “Proton Heating via Nonresonant Scattering Off Intrinsic Alfvénic Turbulence”. In: *PhRvL* 99.7, 075001 (Aug. 2007), p. 075001. DOI: 10.1103/PhysRevLett.99.075001 (cit. on p. 169).

[175] C. B. Wang and C. S. Wu. “Pseudoheating of protons in the presence of Alfvénic turbulence”. In: *PhPl* 16.2, 020703 (Feb. 2009), p. 020703. DOI: 10.1063/1.3068472 (cit. on pp. 169, 172).

[176] P. M. Bellan. “Pitch angle scattering of an energetic magnetized particle by a circularly polarized electromagnetic wave”. In: *PhPl* 20.4, 042117 (Apr. 2013), p. 042117. DOI: 10.1063/1.4801055 (cit. on pp. 170, 172).

[177] Young Dae Yoon and Paul M. Bellan. “Nondiffusive Pitch-Angle Scattering of a Distribution of Energetic Particles by Coherent Whistler Waves”. In: *JGRA* 125.6, e27796 (June 2020), e27796. DOI: 10.1029/2020JA027796 (cit. on pp. 170, 172).

[178] D. Verscharen and E. Marsch. “Apparent temperature anisotropies due to wave activity in the solar wind”. In: *AnGp* 29.5 (May 2011), pp. 909–917. DOI: 10.5194/angeo-29-909-2011 (cit. on p. 172).

[179] Yasuhiro Nariyuki. “On apparent temperature in low-frequency Alfvénic turbulence”. In: *PhPl* 19.8, 084504 (Aug. 2012), p. 084504. DOI: 10.1063/1.4747499 (cit. on p. 172).